Developing a modeling and simulation framework for human thermoregulation for voxelized domains

by

Rohan Amare

B.E., Mumbai University, India, 2015

AN ABSTRACT OF A DISSERTATION

submitted in partial fulfillment of the
requirements for the degree

Doctor of Philosophy

Alan Levin Department of Mechanical and Nuclear Engineering
Carl R. Ice College of Engineering

KANSAS STATE UNIVERSITY
Manhattan, Kansas

2023

Abstract

Since the 1980s, various models have been developed to simulate human thermoregulation. These models have undergone many modifications, maturing from simple geometrical shapes to more advanced polygon meshes. However, state-of-the-art models still lack the flexibility to be person specific and simulate thermoregulation with anatomical accuracy. Computational human phantoms (CHP), such as voxel phantoms, are anthropomorphic models developed from person-specific medical imaging data. These models provide the flexibility to represent a person-specific simulation domain with anatomical accuracy. However, using voxel phantoms for thermoregulation is challenging. This dissertation focuses on the challenges of using voxel phantoms for thermoregulation simulation and proposes solutions to overcome them.

The first challenge associated with voxel phantoms is the stair-step effect introduced due to the cuboidal nature of voxels. To understand and quantify the surface area error due to the stair-step effect, a sphere was used, as a sphere represents the worst-case scenario for 3D curved domains. The overestimation of surface area for a sphere was found to be 50 %. Many solutions are available in the literature to reduce this error, but all of them rely on an unstructured mesh. To maintain the structured nature inherent in voxel phantoms, a structured cleaving method was developed. This method divides a pixel into four triangles and a voxel into 24 tetrahedrons. Using the smoothing method described in this dissertation, the overestimation of the surface area of a sphere was reduced to 16 %. This method was further tested on four tumors obtained from MRI scans. The overestimation of surface area for these tumors was reduced from 47 % to 17 % on average using the structured cleaving method.

The second challenge of thermoregulation models lies in the multiphysics aspect of thermoregulation. Blood flow in vasculature is predominantly modeled as one-dimensional,

whereas the blood flow in capillary beds is modeled as three-dimensional. This results in a mixed-dimensional mesh of vasculature and the tissue-capillary bed. This mixed-dimensional coupling was addressed using the Dirac distribution function and algorithm obtained from the literature. This algorithm was further advanced by adding multiscale coupling due to the difference in mesh resolutions of segmented vasculature and tissue voxels. The mixed-dimensional, multi-scale mesh was used to create a blood flow - heat transfer coupled solver and simulate this multi-physics phenomenon on frog tongue data obtained from the literature. The resulting framework is called the Voxelized Multi-Physics Simulation Framework (VoM-PhyS), which provides a strong foundation for a full-body thermoregulation simulation.

The third challenge with any voxel domain generated from imaging data is associated with voxel resolution. Due to the dimensional scale of blood vessels, not all vessels are captured in a given voxel resolution. This loss of segmentable vascular data results in discontinuous blood vessels. The pre-capillary vessels, like arterioles, provide the highest resistance to blood flow. Due to the resolution limitations, these pre-capillary vessels are modeled with the tissue as a porous domain. In other words, using the porous media method, pre-capillary vessels get modeled with a capillary bed in a tissue voxel. This results in a loss of information that could have been modeled if the pre-capillary vessels were segmented and modeled distinct from capillary bed. These vessels can only be modeled if a very high image resolution is used, which would also increase the computational cost of the entire simulation domain. Instead, a mathematical representation of the pressure drop induced in these unsegmented blood vessels is used. A part of this dissertation focuses on developing a mathematical equation to calculate the pressure drop parameter, which can be used to accurately model the flow resistance offered by pre-capillary vessels and simulate blood flow. This dissertation provides the equations to calculate the pressure drop parameters for any given vasculature and tissue domain, provided the total pressure drop across the simulation domain and the total blood steady-state flow rate are known. These equations provide deeper insight into vascular resistance and strengthen the VoM-PhyS Framework by allowing the flexibility to reduce the mesh size and computational memory requirements. The effect of substituting

segmented vessels with mathematical pressure drop parameters on heat transfer is analyzed by simulating a 3D vascular domain of 32 terminal vessels and five generations of bifurcation. Each generation is successively removed and substituted with the pressure drop parameter to analyze the error in heat transfer due to a lack of segmentation data. To reduce this error, two methods are proposed and demonstrated to show considerable energy error reduction.

Developing a modeling and simulation framework for human thermoregulation for voxelized domains

by

Rohan Amare

B.E., Mumbai University, India, 2015

A DISSERTATION

submitted in partial fulfillment of the
requirements for the degree

Doctor of Philosophy

Alan Levin Department of Mechanical and Nuclear Engineering
Carl R. Ice College of Engineering

KANSAS STATE UNIVERSITY
Manhattan, Kansas

2023

Approved by:

Co-Major Professor
Amir A. Bahadori

Approved by:

Co-Major Professor
Steven J. Eckels

Copyright

Abstract

Since the 1980s, various models have been developed to simulate human thermoregulation. These models have undergone many modifications, maturing from simple geometrical shapes to more advanced polygon meshes. However, state-of-the-art models still lack the flexibility to be person specific and simulate thermoregulation with anatomical accuracy. Computational human phantoms (CHP), such as voxel phantoms, are anthropomorphic models developed from person-specific medical imaging data. These models provide the flexibility to represent a person-specific simulation domain with anatomical accuracy. However, using voxel phantoms for thermoregulation is challenging. This dissertation focuses on the challenges of using voxel phantoms for thermoregulation simulation and proposes solutions to overcome them.

The first challenge associated with voxel phantoms is the stair-step effect introduced due to the cuboidal nature of voxels. To understand and quantify the surface area error due to the stair-step effect, a sphere was used, as a sphere represents the worst-case scenario for 3D curved domains. The overestimation of surface area for a sphere was found to be 50 %. Many solutions are available in the literature to reduce this error, but all of them rely on an unstructured mesh. To maintain the structured nature inherent in voxel phantoms, a structured cleaving method was developed. This method divides a pixel into four triangles and a voxel into 24 tetrahedrons. Using the smoothing method described in this dissertation, the overestimation of the surface area of a sphere was reduced to 16 %. This method was further tested on four tumors obtained from MRI scans. The overestimation of surface area for these tumors was reduced from 47 % to 17 % on average using the structured cleaving method.

The second challenge of thermoregulation models lies in the multiphysics aspect of thermoregulation. Blood flow in vasculature is predominantly modeled as one-dimensional,

whereas the blood flow in capillary beds is modeled as three-dimensional. This results in a mixed-dimensional mesh of vasculature and the tissue-capillary bed. This mixed-dimensional coupling was addressed using the Dirac distribution function and algorithm obtained from the literature. This algorithm was further advanced by adding multiscale coupling due to the difference in mesh resolutions of segmented vasculature and tissue voxels. The mixed-dimensional, multi-scale mesh was used to create a blood flow - heat transfer coupled solver and simulate this multi-physics phenomenon on frog tongue data obtained from the literature. The resulting framework is called the Voxelized Multi-Physics Simulation Framework (VoM-PhyS), which provides a strong foundation for a full-body thermoregulation simulation.

The third challenge with any voxel domain generated from imaging data is associated with voxel resolution. Due to the dimensional scale of blood vessels, not all vessels are captured in a given voxel resolution. This loss of segmentable vascular data results in discontinuous blood vessels. The pre-capillary vessels, like arterioles, provide the highest resistance to blood flow. Due to the resolution limitations, these pre-capillary vessels are modeled with the tissue as a porous domain. In other words, using the porous media method, pre-capillary vessels get modeled with a capillary bed in a tissue voxel. This results in a loss of information that could have been modeled if the pre-capillary vessels were segmented and modeled distinct from capillary bed. These vessels can only be modeled if a very high image resolution is used, which would also increase the computational cost of the entire simulation domain. Instead, a mathematical representation of the pressure drop induced in these unsegmented blood vessels is used. A part of this dissertation focuses on developing a mathematical equation to calculate the pressure drop parameter, which can be used to accurately model the flow resistance offered by pre-capillary vessels and simulate blood flow. This dissertation provides the equations to calculate the pressure drop parameters for any given vasculature and tissue domain, provided the total pressure drop across the simulation domain and the total blood steady-state flow rate are known. These equations provide deeper insight into vascular resistance and strengthen the VoM-PhyS Framework by allowing the flexibility to reduce the mesh size and computational memory requirements. The effect of substituting

segmented vessels with mathematical pressure drop parameters on heat transfer is analyzed by simulating a 3D vascular domain of 32 terminal vessels and five generations of bifurcation. Each generation is successively removed and substituted with the pressure drop parameter to analyze the error in heat transfer due to a lack of segmentation data. To reduce this error, two methods are proposed and demonstrated to show considerable energy error reduction.

Table of Contents

List of Figures

List of Tables

Nomenclature

$(k_{ij})_{eff}$ Anisotropic effective thermal conductivity

α Perfusion parameter

ΔV Voxel volume

Δx Voxel size along x-axis

Δy Voxel size along y-axis

Δz Voxel size along z-axis

$\Delta P_{t \to V,term}$ Pressure drop between venous compartment of tissue and terminal node venous

$\Delta P_{A,term \to t}$ Pressure drop between terminal arterial node and arterial compartment of tissue

ΔP_t Pressure drop between arterial compartment and venous compartment

ϵ Radius of sphere of influence

γ_a Arterial pressure drop parameter

γ_v Venous pressure drop parameter

γ_β Generic pressure drop parameter

$\kappa_{j,i}$ Flow conductivity of vessel between node j and i

$\mathcal{G}_{a,i}$ Arterial volumetric source flow rate at voxel i

$\mathcal{G}_{v,i}$ Venous volumetric sink flow rate at voxel i

$\mathcal{Q}$ Total volumetric blood flow rate in vascular tree

$\mathcal{R}_A$ Equivalent flow resistance of arterial tree

$\mathcal{R}_V$ Equivalent flow resistance of venous tree

$\mathcal{R}_{eq}$ Equivalent flow resistance of vascular tree

$\mathcal{R}_{ji}$ Flow resistance of vessel between node j and i

$\mathcal{X}$ Normalized sensitivity coefficient

K_a Arterial compartment permeaability

K_v Venous compartment permeaability

$\mathrm{L_{j,i}}$ Length of blood vessel between node j and i

$\mathrm{R_{ji}}$ Radius of blood vessel between node j and i

μ Viscosity of blood

Ω Computational domain

ω_b Blood perfusion parameter

ω_{pennes} Pennes blood perfusion parameter

ϕ Porosity

ρ_b Density of blood

ρ_t Density of tissue

τ_{ij} Linear transmisibility between voxel i and voxel j

θ Temperature offset

ξ WJM shape factor

A_c Cross section area

A_s Surface area

A_c Cross-section area

$A_{s,b}$ Surface area of blood vessel

$c_{p,b}$ Specific heat capacity of blood

$c_{p,t}$ Specific heat capacity of tissue

k Thermal conductivity

k_t Thermal conductivity of tissue

k_{bo} Thermal conductivity of bone

m Mass flow rate

$N_{a,i}^T$ Set of arterial terminals supplying blood to voxel i

$N_{v,i}^T$ Set of venous terminals receiving blood from voxel i

$P_{a,i}$ Pressure in i-th arterial compartment

$q_{v,ji}$ Volumetric flow rate in blood vessel between node j and i

r Radius

T Temperature

t Time

U Pseudo-overall heat transfer coefficient

u_{perf} Perfusion flow rate

Δs Δx, Δy or Δz based on the direction

$\dot{q}$ Volumetric generation of heat

h_{amb} Convective heat transfer coefficient of air

h_b Convective heat transfer coefficient of blood

h Convective heat transfer coefficient

p_i Pressure at node i in vasculature

T_{amb} Ambient temperature

T_{in} Inlet temperature

Pe Peclet number

Acknowledgments

I express my deepest gratitude to my advisors- Dr. Amir Bahadori and Dr. Steven Eckels. They not only provided research guidance but have been exemplary mentors who have truly taught me what it means to be an advisor, mentor, guide, and teacher.

I want to thank my Ph.D. Committee, Dr. Bradley Behnke, Dr. Byron Jones, and Dr. Punit Prakash, for their guidance and help on various occasions throughout this journey. They have extended their time and support to me, not only for research queries but also for helping me grow professionally.

My growth would have remained incomplete without Mrs. Meredith Schlabach, under whom I worked as graduate research assistant. I always look up to her to learn professional ethics, professional perfectionism, and reliability. In addition, I am grateful to Mr. Matthew Campbell, who has consistently been one of my loudest cheerleaders. He has continuously provided me with insights, ideas, and invaluable help with debugging my code.

My journey and interest in research couldn't have begun without Dr. Kannan Iyer, who taught me what research truly is and saw potential in a raw student who needed a teacher. I express my deepest and most sincere gratitude to him for imbibing professional ethics, dedication toward research, and curiosity to keep questioning with a critical scientific mind.

I have been fortunate to have been taught by outstanding teachers throughout my academic life. Whether it was my kindergarten or university, I have the happiest memories whenever I look back and think of my teachers. I am indebted to them for being such a revolutionary force in my life that I fell in love with learning and education and decided to pursue the highest degree in my field.

It takes a village, they say, and I have a town to support me! I owe my gratefulness to Savita Adsul, Zubeida Alali, Velmurugan Balaraman, Kaitlin and Seton Bachle, Aaron Cole, Dave Goulart, Niranjan Gudibande, Rushabh Gujarati, Shreeraksha Hegde, Satyajit

Kasar, Anna Kucera, Stephen Kucera, Asawari Kulkarni, Courtney Markle, Kshitija Memane, Garett Mann, Manpreet Singh Minhas, Priyal Parikh, Aravind R., Vishag Rajendra, Avantika Ramekar, Srinivas Ravi, Ranum Family, Reader Family, Sofiya Sabreen, Aashish Salvi, Debarshi Saha, Jay Sheth, Shima Soleimani and SPICMACAY-KSU Chapter.

I am thankful to Mohana Yoganadan for supporting and encouraging me in this journey's most testing and challenging phase. Her encouragement, support, compassion, and confidence in me and my capabilities have helped me to keep working toward my goal.

I especially thank Shelly Reves-Klinker, Debra Wilcox, Stefan Yates, and Cathy Sandoval for being my cheerleaders and letting me vent my heart out. No matter how stressed I was, they always made me smile. Across the KState campus, I am grateful to Barbara Theirer-Larson, Beth Bailey, Daniel Ireton, Dr. Beverly Earles, Dr. Terry Beck, Dr. Mingjun Wei, Dr. Kevin Wanklyn, Dr. Jeremy Roberts, Dr. Sara Thurston, and Dr. Jana Fallin.

This journey has been testing in every possible way. The support and help I have received from my therapist Cristine Glendening and the Lafene Health Centre are enormous. I couldn't have made it here without Cristine. Her advice, guidance, and support have brought me out of very dark phases of my life. No words can express my gratitude towards her.

Finally, this thesis is dedicated to all the parental figures in my life. I want to express my deepest gratitude and love to my parents - Mummy and Pappa, who gave me birth. Their hard work, sacrifices, love, and support have culminated my academic journey. I thank my brother Pritish and my aunt for supporting me in this journey. I am blessed to have received unconditional parental love from people who adopted me as their own in love. My Kaka and Kaki (Mrs. Geeta Amre and Mr. Narendra Amre), Amma and Appa (Mrs. Swarnam Ravi and Mr. Ravi Ramchander), Mom and Dad (Mrs. Robbin Cole and Mr. Terry Cole), Mrs. Brenda Kucera and Ms. Vibhavari Jani. Though they didn't give birth to me, their unconditional love, guidance, and teachings have shaped my life and individuality. I cannot be thankful enough for the contribution of all my parents.

Dedication

I dedicate my dissertation to all the parental figures in my life.

Mummy & Pappa (Mrs. Sudha & Mr. Prabhakar Amare)

Chinta (Mrs. Darshana Waradkar)

Kaki & Kaka (Mrs. Geeta & Mr. Narendra Amre)

Amma & Appa (Mrs. Swarnam & Mr. Ravi)

Mom & Dad (Mrs. Robbin & Mr. Terry Cole)

Mrs. Brenda & Mr. Bill Kucera

Prof. Vibhavari Jani

Without any of them, this dream could not be a reality.

Chapter 1

Introduction

Understanding human thermal response is challenging due to the complex physical, biological, and chemical processes involved. Human thermoregulation models have been used in fields of vehicular comfort[1], biomedical engineering[2], human thermal comfort[3;4], buildings and HVAC[4–6], and medicine[7]. The ability of the human body to regulate its temperature as a response to feedback is amazing and equally complex. The hypothalamus acts as a thermostat that receives input signals from different body parts and responds with control mechanisms to regulate heat exchange and create a homeothermic core. This process of receiving input signals and providing feedback response is called the human thermoregulation mechanism. The models used to simulate these phenomena are termed human thermophysiological or human thermoregulatory models.

Thermophysiological models consist of two main components: the simulation domain, which is the human body, and control equations, which are used to determine sweat rate, shiver rate, changes in respiration rate, and vasomotion. These equations use core temperature, skin temperature, ambient temperature, and other environmental parameters such as humidity and thermal radiation to calculate the human thermal response. Control equations, when coupled with the human anatomical domain for simulation, provide a complete thermophysiological model. Representation of the simulation domain is critical. Greater accuracy in the model's anatomical features can improve the simulation result. In the ther-

moregulation models found in literature, simple geometrical shapes that can be defined by quadratic equations are used to model human anatomy. These models are good for preliminary analysis but suffer major limitations due to the lack of anthropomorphic data in the simulation domain.

Like anatomical accuracy, blood flow modeling affects thermoregulation simulation. Blood flow plays a crucial role in thermoregulation. Vasomotion regulates the blood flow and its redistribution within the domain. This provides required fine-tuning to control heat exchange occurring between the skin and the environment. By varying blood circulation, the human body can remove excess heat from a local tissue experiencing higher temperatures or reduce loss of heat to the environment to conserve heat. Thus, the location of blood vessels, blood flow rate, and heat transfer between blood vessels and tissue must be understood and modeled for a complete thermophysiological simulation.

Computational human phantoms (CHPs) are anthropomorphic models generated from medical imaging data that provide a high-level of accuracy in representing the anatomical features of human organs and tissues. These phantoms are extensively used in research areas like radiation dosimetry and biomedical engineering. Surprisingly, the utilization of these anatomically accurate models in the human thermoregulation field is not reported. This dissertation focuses on the possibility of using CHP for human thermoregulation research and associated challenges.

1.1 Problem Statement and Scope of Research

Fig. 1.1 illustrates the objectives of this dissertation. The simulation domain shown in Fig. 1.1 represents a CHP generated from magnetic resonance imaging (MRI) scans. The ability of CHPs to be person-specific provides the flexibility to make it unique and applicable to each individual's needs and simulate thermoregulation. The control equations to be analyzed in this dissertation include heat exchange with the environment and heat exchange between blood vessels and tissue. For modeling heat transfer between blood vessels and tissue, a mathematical framework to model unsegmented blood vessels is needed in addition

to blood flow coupled heat transfer solver. The distinct objectives of this dissertation are as follows:

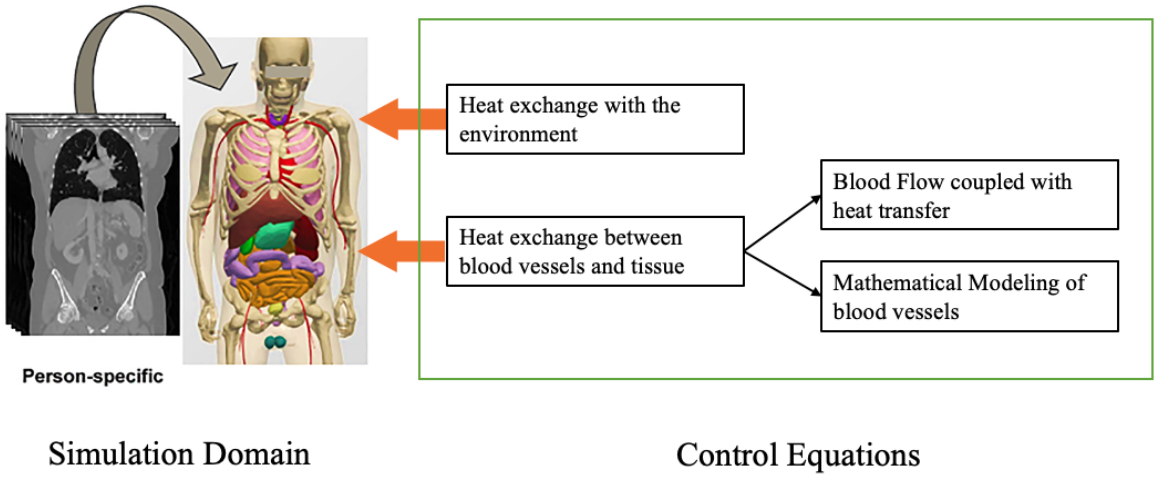

Figure 1.1: Research outline illustration

1. Identifying the challeges with using CHPs for thermoregulation

   Understand the challenges associated with using CHPs for thermoregulation. Conduct literature review to identify possible solutions in literature to overcome the challenges.

2. Simulating heat exchange between CHP and environment.

   Voxel phantoms generated from medical imaging data have incorrect surface areas. The overestimation of surface area results in inaccurate thermal analysis. The solutions found in the literature require surface fitting using modeling tools or surface area correction using a reference domain. An algorithm that smoothens voxelized surfaces without referring to a reference domain is needed to make the simulation truly person-specific with the flexibility to model organs directly from imaging data. This algorithm, its applications, and its drawbacks are covered in this dissertation.

3. Simulating coupled multiphysics equations.

   Thermal regulation in biological domains consists of blood flow coupled with heat transfer. The effect of convective heat exchange between large blood vessels and tissue on bioheat transfer has been debated. Due to the lack of *in-vivo* experimental data, this remains unknown. However, the location of blood vessels and the capillary network is known to help regulate heat transfer using vasomotion. Part of this dissertation focuses on developing a multiscale, multidimensional, multiphysics framework for simulating blood flow coupled with heat transfer. This simulation framework is adaptable to consider heat exchange between large blood vessels and tissue, along with the heat exchange occurring within the unsegmented pre-capillary vessels. The ability of this novel simulation framework to control the location of heat transfer within the vasculature provides a considerable advantage over existing bioheat equations and simulation frameworks.

4. Simulating flow resistance of unsegmented vascular data.

   One of the major drawbacks of voxel phantoms is limitations associated with voxel resolution. Capillary beds in the human body exist on the scale of micrometers. A CHP with micrometer voxel size would require excessive memory due to large mesh size. Thus, obtaining a CHP with vasculature segmented down to capillary bed is a challenge with existing methods. To simulate the unsegmented capillary bed, tissue voxels are modeled as porous media with porosity representing the density of capillary bed in the respective tissues and organs. However, the vasomotion that controls blood flow and resultant heat transfer occurs in pre-capillaries, and so representing them is crucial. Furthermore, the resolution of imaging data may not provide segmentable pre-capillary vessels. Hence, a mathematical model to predict the flow resistances of these pre-capillary vessels is needed. Chapter 5 of this dissertation presents mathematical equations used to calculate the flow resistance of unsegmented pre-capillaries. These equations are one of the major contributions of this dissertation to science.

Chapter 2

Literature Review

This chapter provides a literature review and a more detailed discussion of dissertation aims. The first section of this chapter elaborates on the various human thermoregulation models found in the literature. This review reveals that human thermoregulation research still relies on stylized phantoms to represent the human anatomy. Modern CHPs should be used to advance the field of thermoregulation research. A brief review of CHPs is provided in this chapter.

The other aspect of thermoregulation modeling is the bioheat transfer equations. There are various bioheat transfer models found in the literature. A review of these existing bioheat transfer models and their limitations is provided in a mini-review in this chapter. This mini-review of bioheat transfer equations demonstrates that a simulation framework is required to accommodate the complexities of bioheat transfer and not be restricted to any single bioheat transfer equation.

Following that, the main goal of this dissertation to develop a modeling and simulation framework for thermoregulation for a voxel phantom is emphasized, with three primary challenges elaborated. Finally, the solutions obtained in literature to address these challenges, their limitations, and the novel methods developed as part of this dissertation to address these challenges are introduced.

2.1 Human Thermal Modeling

Thermoregulation is a vital process for the human body to maintain its homeothermic core and not readily reach catastrophic conditions such as hyperthermia or hypothermia. Various attempts to model and simulate this complex phenomenon have been undertaken. The models used for simulating the human body and its thermoregulation have ranged from a single lumped system[8] to highly complex models used with the latest CFD technology[9]. A rough classification scheme divides the existing thermophysiological models into five categories, as elaborated below. A timeline to illustrate the modifications of these models over time is given in Fig. 2.1. This timeline is not exhaustive but attempts to specify important models developed over the course of history.

2.1.1 Single Segment Models

Single-segment models consider the body as a lumped object and do not provide a detailed thermal distribution within the anatomy. They are further divided into one-node or multi-node models, based on the location and number of nodes where temperature is determined.

1. One-Node or Empirical Models

   One-node models are empirical models that consider the entire human body as one lumped object exposed to the environment. Franger[8], and Givoni and Goldman[8] are examples of these models. These models are generated by collecting data on the human thermoregulatory reaction to environmental conditions and fitting a mathematical model. The empirical models are thus applicable only if the exact conditions of the environment and the subject are met. With variations of environmental and biological conditions of the subject, empirical models face challenges if those conditions were not considered when the model was developed.

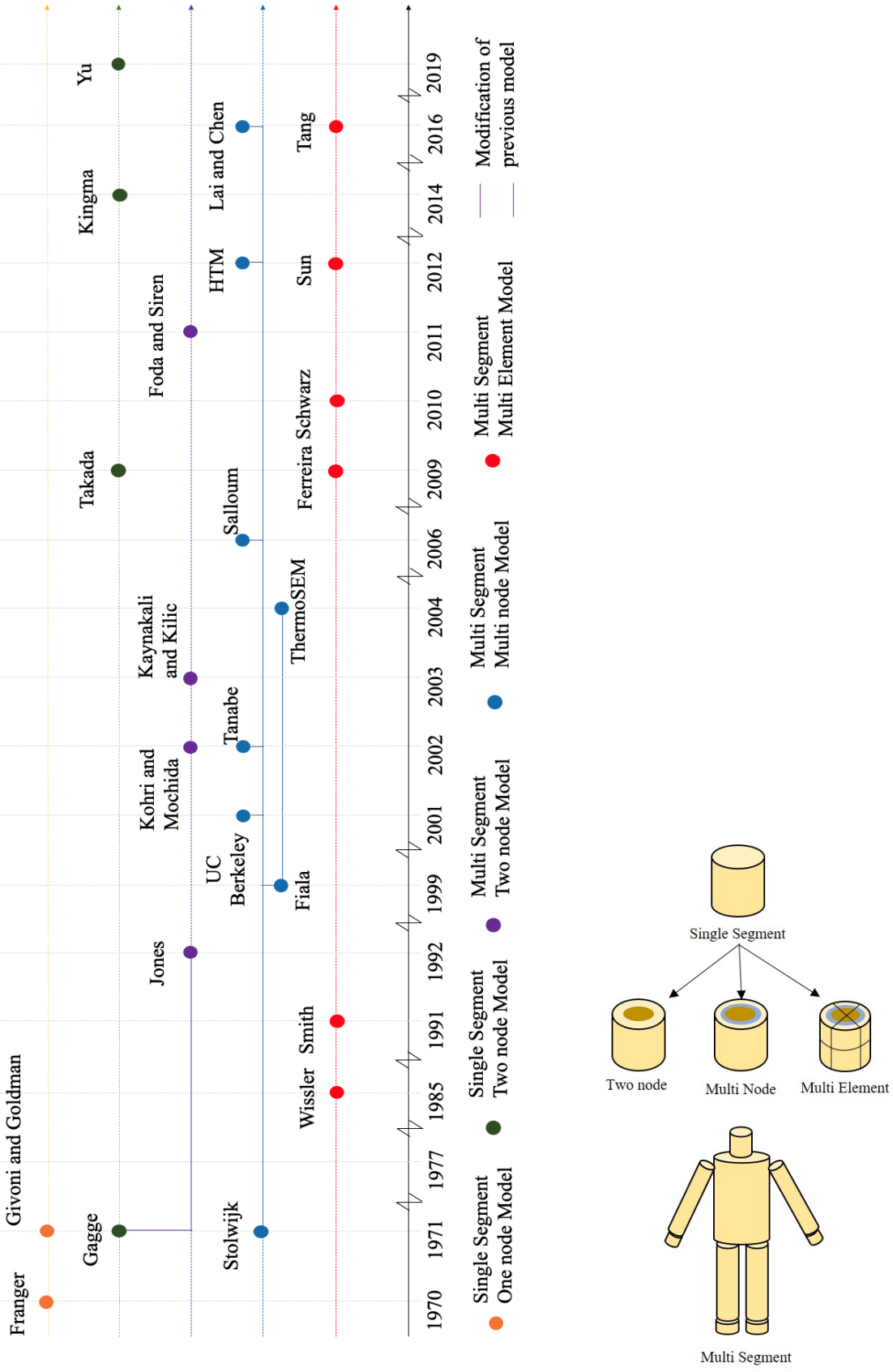

Figure 2.1: Timeline of thermophysiological models

2. Two-Node Models

   Empirical models provide a database of the general response of the human body to certain environmental conditions. The need for a detailed thermal audit provided more insight into thermoregulation mechanisms within the human body, resulting in single-segment, two-node models. Gagge[10] developed the first single-segment, two-node model, which has undergone many modifications. Takada[11], Kingma[11], and Yu[12] are other examples of single-segment two-node models. These models divide the human body in a shell-and-core arrangement where the shell represents the skin layer. Such models helped determine blood flow distribution between the core and skin. However, these models do not address the intricacies of human anatomy and organ placement within the core.

2.1.2 Multi Segment Models

Limitations of single-segment models were overcome by defining different segments allocated to represent different parts of the human body. These multi-segmented models can be further classified as follows:

1. Two-Node Models

   One of the most basic representations of multi-segment, two-node model is the Jones model[13], which is a modification of the Gagge model[10]. The Jones model retains the shell and core structure while dividing the skin further into multiple segments to represent skin over different parts of the body such as head, torso, arms, and legs. Other models shown in Fig 2.1, which belong to multi-segment two-node models, have similar arrangements[11]. One of the latest models developed by Yu et al.[12] uses a two-node model coupled with a nonlinear heart-rate regulation model to determine human thermal behavior.

2. Multi-Node Models

   The multi-node and the multi-element models are the two most well-developed and detailed categories of the human thermal model family. The Stolwijk model[14] divided

the human body into 25 nodes and six segments to predict the thermal response of astronauts in outer space. A central blood pool was used to act as the heart from which the blood circulates to different nodes across the body. The Stolwijk model does not consider crossflow heat exchange between arteries and veins nor the local variation of blood flow and other tissue properties. This model provided a foundation for highly detailed models like Fiala[15–17], Tanabe[18], Salloum[19;20], Lai and Chen[21], and others. The Fiala[15–17] model is a state-of-the-art model used to represent human thermoregulation for subjects exposed to different environments. Tanabe[18] modified the Stolwijk model by increasing the number of nodes from 25 to 65 within 16 body segments. The Lai and Chen[21] model is a modification of the Fiala model that simulates non-uniform thermal environment surrounding the human subject.

3. Multi-Element Models

   Multi-element models are similar to multi-node models, with the major difference being that each element is constrained to have only one location where the quantity is calculated. In other words, multi-node models have sub-layers or sub-sections that divide the element further, whereas in multi-element models, there are no such sub-divisions within the element. The Wissler model[22] is one the most developed multi-element models, consisting of a detailed blood-flow network based on Pennes' bioheat equation[23]. The Smith[24] model and Sun's[25] model are based on Wissler. While Wissler and Smith used cylinders to represent the anatomy, Sun introduced curvature on the cylinders to accurately represent human limbs.

The study of human thermoregulation research reveals the fact that almost all models used are stylized, incorporating geometrical objects such as cylinders and spheres to represent the human anatomy. Recent models like Nelson et al.[26], Tanabe[18], 3-D Virtual Human Model[27;28] and Finite Element Model (FEM)[29] are adding the anatomical complexities required for state-of-the-art simulation tools. A detailed review of thermophysiological models can be found in Refs[11;30;31].

2.2 Computational Human Phantoms (CHPs)

A parallel branch of research that deals with biomedical applications[32] and radiation dosimetry[33–35] makes use of CHPs. A brief overview of the advancement in the CHPs is presented below.

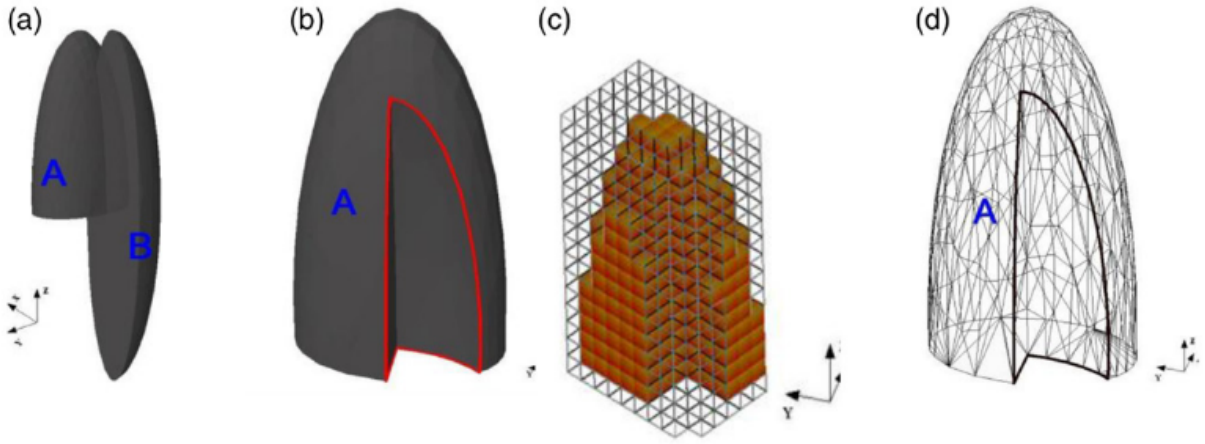

Figure 2.2: Model of the left lung (a) The CSG-type modeling before the boolean operation (subtraction) is performed between two ellipsoids (b) End result after subtraction (c) A voxel representation of the lung (d) A BREP-type of modeling of the same lung using polygon mesh. (Used with permission from Xu.[36])

Advancements in CHPs

Radiation dosimetry aims to determine the amount and spatial distribution of energy deposited in the human anatomy due to exposure to various radiation sources[33–37]. Accurate radiation dosimetry relies on accurate anatomical parameters of the organs and human body for simulation. Anthropomorphic phantoms provide realistic models of human organs and tissues. CHPs can be stylized models developed using solid geometrical shapes like cylinders or ellipsoids, or highly advanced with B-Spline smoothening and mesh surfaces. A brief review of different categories of CHPs is provided below.

- Stylized Phantoms or Constructive Solid Geometry (CSG)

  Stylized phantoms are made using simple geometrical shapes like ellipsoids, spheres,

cuboids, cylinders, etc., that can be defined by quadratic equations. An example of a stylized phantom lung is shown in Fig. 2.2.a and Fig. 2.2.b. These models resemble the initial stylized models used in thermoregulation research described in the prior section. Similar to the challenge experienced for thermoregulation, many of the human body organs and anatomical features cannot be defined using quadratic equations. The Revised ORNL (RORNL)[38;39] phantom series is an example of a group of stylized phantoms.

- Voxel Phantoms

  Voxel phantoms provided a one of its kind anthropomorphic models for computational simulations. Medical imaging data are collected for an individual and used to reconstruct the anatomy[36;40;41] by extruding the pixels to the height of imaging slice thickness. An example of this is shown in Fig. 2.2.c, where a left lung is constructed using voxels. The challenges associated with voxel phantoms are elaborated in Ref[36;42], and will be described later in this chapter. One of the primary limitations of voxel phantoms is associated with the image resolution used to collect medical image data. Recent advancements have resulted in multiscale and multiresolution models[43] to overcome this limitation. In spite of their limitations, voxel phantoms provide major advantages over stylized phantoms as elaborated in Ref[32;36;39;44]. One of the major advantages of the voxel phantom lies in its flexibility and adaptability for existing simulation codes[32;45]. Since voxels represent a finite volume element, they are easily transferable to other finite volume simulations without requiring mesh modifications.

- BREP Phantoms or Mesh Phantoms

  Many challenges associated with voxel phantoms were overcome by using polygon-mesh or NURBS (non-uniform rational B-spline) surfaces[32;36;42;46–48]. In Boundary Representation (BREP) phantoms, the organ's surface is represented using polygon meshes which are easily interchangeable with BREP data structures. Using a surface rendering method, polygon meshes are fitted over the surface of the voxelized organ, and

refinement techniques are used to smoothen the surfaces[42]. Since tetrahedral meshes are more common for simulation purposes, recent advancements have generated algorithms to convert polygon-mesh phantoms to tetrahedral mesh phantoms[49]. However, the major challenge for mesh phantoms is converting complex organs and shapes from voxel phantoms to mesh phantoms. This process requires manual hours to fine-tune the NURBS surfaces on voxelized organs and can be cost and labor intensive if required to be individualized to a specific subject.

2.3 Bioheat Transfer Models

Various models have been developed to simulate the bioheat transfer mechanisms. However, the complexities associated with metabolic heat generation, heat exchange, blood flow, and vasomotion makes it challenging to have one model that explains the bioheat transfer thoroughly. Due to this, many different equations and models can be found in the literature with various assumptions for simplicity and their limitations. A small review of a handful of these models that were considered important is given below. Many more models are available in the literature not covered in this review.

The available bioheat models can be classified into perfusion-based, countercurrent, and porous media-based models. Two other classifications of bioheat models exist: phase lag and statistical models. The physics of phase lag in bioheat equations has been criticized and debated. The research field has no consensus if the phase lag theory is valid. A detail review of experimental and numerical validation of dual phase lag bioheat models can be found in Ref.[50]. Staistical models are considered obsolete with the advancements in computational simulations. Due to these reasons, the phase lag models and statistical models are not considered in this review.

2.3.1 Perfusion-Based Bioheat Models

In perfusion-based models, blood is considered to perfuse the tissue domain once it leaves the segmented blood vessel. Perfusion controlled by the perfusion parameter depends on the type of tissue. The Pennes Bioheat Model[23] is one of the most famous and commonly used models to simulate bioheat transfer using perfusion phenomena.

Pennes Bioheat Equation

Pennes[23] assumes that blood does not exchange heat as it flows in a major supply artery and vein. Instead, the warm blood flowing in an artery reaches the capillary bed and immediately achives thermal equilibrium. Thus, the tissue and blood are considered to be at the same temperature. Once the blood has perfused across the tissue domain, it enters the venous system at tissue temperature. The Pennes bioheat equation (BHE) is shown in Eq. (2.1) where ω_{pennes} represents the Pennes perfusion parameter.

$$\rho_t c_{p,t} \left(\frac{\partial T_t}{\partial t} \right) = \nabla(k_t \nabla T_t) + \omega_{pennes} c_{p,b} [T_a - T_t] + \dot{q} \tag{2.1}$$

The primary challenges with Pennes bioheat equation are intrinsic to the assumptions involved[51]. In the Pennes BHE, the blood perfusion rate is determined via curve-fitting to experimental data. Thus, this perfusion rate can be used for predicting a thermal map for tissue only if the same environmental and biological conditions are met. The other limitation of the Pennes BHE is that the perfusion parameter ω_{pennes} is a scalar quantity. Thus, the Pennes BHE does not account for spatial variation of perfusion but considers it to be uniform in the volume. This assumption is not true, as vasomotion varies the blood perfusion in tissue and organs.

Wulff Continuum Model

Some limitations of the Pennes BHE were overcome by the Wulff Continuum Model[52]. The bioheat equation proposed by Wulff is shown in Eq. (2.2). The Wulff BHE proposes a vectorized perfusion parameter to simulate the convective heat exchange between blood vessels and tissue.

$$\rho c_p \frac{\partial T_t}{\partial t} = k_t \nabla^2 T_t + \rho c_p \vec{v}_b \nabla T_b + \dot{q} \tag{2.2}$$

In Eq. (2.2), the $\vec{v}_b$ represents the blood velocity in capillaries. Similar to Pennes BHE, Wulff assumes thermal equilibrium between tissue and blood in capillary bed. The estimation of local blood velocity is complex and thus makes it difficult to use the Wulff BHE[52–54]. In addition, Wulff does not consider the effect of heat transfer between large vessels and tissue, and assumes heat exchange occurs only in the capillary bed.

Chen and Holmes Model

The Wulff BHE and the Pennes BHE consider thermal equilibrium between tissue and capillary bed, and ignore heat transfer between larger vessels and tissue. Chen and Holmes[55] proposed not to consider a single continuum model to simulate bioheat transfer but rather model it using two separate continuums representing tissue and blood, respectively. Chen and Holmes proposed a model considering larger vessels and their effect on bioheat transfer. The BHE proposed by Chen and Holmes is given in Eq. (2.3a).

$$\rho c_p \frac{\partial T_t}{\partial t} = \nabla \left(k_{eff} \nabla T_t \right) + \omega^* \rho_b c_{p,b} \left[T_a^*(r_{in}) - T_t \right] - \rho_b c_{p,b} \vec{v}_b \nabla T_t + \dot{q} \tag{2.3a}$$

$$k_{eff} = k_t + k_p \tag{2.3b}$$

Chen and Holmes introduced the concept of thermally significant vessels and thermal equilibration length. The thermal equilibration length is defined as the minimum length required for a vessel of a specific diameter to achieve thermal equilibrium with the surrounding. If a blood vessel has a length less than the required thermal equilibration length, the vessel is termed a "thermally significant vessel". This model shows that thermal equilibrium is achieved by blood vessels whose diameter is within 50 µm and 300 µm[54;55].

In Eq. (2.3a), k_{eff} represents the effective thermal conductivity due to tissue k_t and perfused blood k_p. The temperature of blood entering an artery of radius r_{in} is $T_a^*(r_{in})$, and the velocity of blood is $\vec{v}_b$. The perfusion term ω^* represents the perfusion rate for blood vessels with a smaller radius than the arterial blood vessel. A detailed vascular network is required to accurately implement Chen and Holmes method. Thus, the availability of vascular network limits the applicability of this method.

2.3.2 Countercurrent Bioheat Models

Perfusion models focus on the capillary bed and tissue while failing to model the heat exchange between larger vessels and tissues, except the Chen and Holmes[55] model. The counter-current flow behavior of arteries and veins plays a crucial role in bioheat transfer. The major arteries and veins always run in pairs and are in proximity to each other. This results in counter-current heat exchange, where a warm fluid loses heat to a cooler fluid flowing in the opposite direction. This anatomical feature of arteries and veins was studied and considered in bioheat equations. The models that assume countercurrent flow to affect bioheat transfer are classified as countercurrent bioheat models.

Mitchell and Myers

Mitchell and Myers[56] were the pioneers of the theory of counter-current heat exchange in bioheat transfer[54]. Considering control volumes for arterial and venous flow, respectively, and applying the conservation of energy principle, they proposed a two-equation model. In these coupled set of equations, Eq. (2.4) is used to calculate the temperature of arterial blood

and Eq. (2.5) is used to calculate the temperature of venous blood.

$$\frac{T_a(x) - T_t}{T_0 - T_t} = \exp\left(\frac{(N_v - N_a)(x/L)}{2}\right)\left[\frac{B\cosh A(1 - x/L) + \sinh A(1 - x/L)}{B\cosh A + \sinh A}\right] \tag{2.4}$$

$$\frac{T_v(x) - T_t}{T_0 - T_t} = \exp\left(\frac{(N_v - N_a)(x/L)}{2}\right)\left[\frac{B\cosh A(1 - x/L) - \sinh A(1 - x/L)}{B\cosh A + \sinh A}\right] \tag{2.5}$$

where,

$$N_a = \frac{k_a A_a L}{\dot{m}_a c_p}$$
$$N_v = \frac{k_v A_v L}{\dot{m}_v c_p}$$

and

$$A = \sqrt{(N_a + N_v)(N_a + N_v + 4N_i)}/2$$
$$B = \sqrt{(N_a + N_v + 4N_i)/(N_a + N_v)}$$

In Eqs. (2.4) and (2.5), the temperature at a location x is calculated using tissue temperature T_t and temperature at location $x = 0$ (T_0). The temperature at $x = 0$ is considered to be known and provided as a boundary condition to solve the coupled equation set. The nondimensional conductances N_a and N_v are calculated using specific thermal conductivities for arteries and veins, k_a and k_v, respectively, and the mass flow rates $\dot{m}_a$ and $\dot{m}_v$ in arteries and veins, respectively. The nondimensional conductance N_i represents the conductance ratio between arteries and veins. Eqs. (2.4) and (2.5) are difficult to solve. Three different conditions and solutions for each are provided in literature[56], but the complexities of these equations make them difficult to use for simulation in bioheat transfer research.

Keller and Seiler

Keller and Seiler[57] developed a bioheat model for the isothermal subcutaneous layers of tissue. Their model divides the simulation domain into two regions: an isothermal core and a peripheral region where the temperature varies from the core to the periphery (skin). Similar to Chen and Holmes[55], the Keller and Seiler BHE models not only the counter-current heat exchange between arteries and veins but also perfusion in the capillary bed. The Keller and Sieler BHE consists of an energy equation for tissue (Eq. (2.6)), an energy equation for arterial flow (Eq. (2.7)), and an energy equation for venous flow (Eq. (2.8)). Eqs. (2.6) - (2.8) are coupled.

$$k_t \left(\frac{d^2T_t}{d^2x}\right) + \left(h\frac{A_s}{V} + c_p\omega_b\right)[T_a - T_t] + h_b\frac{A_s}{V}[T_v - T_t] + \dot{q} \tag{2.6}$$

$$\left[(\dot{m}_a)_0 - \int_0^x \omega_b dx\right] c_p \left(\frac{dT_a}{dx}\right) + h_b\frac{A_{s,b}}{V}[T_a - T_t] = 0 \tag{2.7}$$

$$\left[(\dot{m}_v)_0 - \int_0^x \omega_b dx\right] c_p \left(\frac{dT_v}{dx}\right) + \left(c_p\omega_b + h_b\frac{A_{s,b}}{V}\right)[T_t - T_v] = 0 \tag{2.8}$$

$$k_{eff} = -\frac{\delta}{T_b - T_s} k_t \left(\frac{dT_t}{dx}\right)_{x=\delta} \tag{2.9}$$

After solving the Eqs. (2.6), (2.7), , and (2.8), the effective thermal conductivity (k_{eff}) of the tissue is calculated using Eq. (2.9). The variable δ represents tissue thickness and at $x = \delta$, the temperature is considered to be skin temperature (T_s). The term $A_{s,b}$ represents the surface area of blood vessel with tissue and V represents the tissue volume. Similar

to Chen and Holmes[55], and Mitchell and Myers[56], the Keller and Seigel coupled BHEs are complex to solve. In addition, Keller and Siegel model is limited by the availability of detailed vascular data required to simulate the BHE.

Simplified Bioheat Equation (WJM)

Weinbaum et al.[58;59] performed anatomical studies on vasculature in a rabbit thigh. In their findings, they suggested that the deep tissue layer, intermediate layer, and cutaneos layer have different thermal interactions at the vessel-tissue interface. These differences in vessel-tissue thermal interactions are due to the variations in vascular geometry, capillary-bed density, and shunting of blood flow to cutaneous layer[58]. They thus proposed a three-layer model, where the cutaneous layer was modeled as a single pair of vessels in the near skin plexus, the intermediate layer was modeled as a counter-current transverse pair of terminal vessels, and deep tissue was modeled as isolated countercurrent large vessels[54;58]. Due to the difficulties in implementing this higly complex system of bioheat equations, Weinbaum and Jiji[60] proposed a simplified BHE (Eq. (2.10a))

$$(\rho\bar{c}_p)\frac{\partial T_t}{\partial t} - \frac{\partial}{\partial x_i}\left[(k_{ij})_{eff}\frac{\partial T_t}{\partial x_j}\right] = -\frac{\pi^2 n A_{s,b}^2 k_b^2}{4k\xi} Pe^2 l_j \frac{\partial l_i}{\partial x_i}\frac{\partial T_t}{\partial x_j} + \dot{q} \tag{2.10a}$$

$$\xi = \frac{\pi}{cosh^{-1}\left(l/2A_{s,b}\right)} \tag{2.10b}$$

$$(k_{ij})_{eff} = k_t\left(\delta_{ij} + \frac{\pi^2}{4\xi k_t^2} n A_{s,b}^2 k_b^2 Pe^2 l_i l_j\right) \tag{2.10c}$$

In the simplified Weinbaum and Jiji BHE (Eq. (2.10a)), Pe represents the nondimensional Peclet number, n represents the number of vessel pairs crossing the suraface of control volume per unit area and ξ is the shape factor given by Eq. (2.10b), l represents the length of a blood

vessel, and $\partial l_i/\partial x_i$ represents the angle between a pair of countercurrent blood vessels. If the blood vessels are perfectly straight, this term is zero. The effective thermal conductivity of tissue, $(k_{ij})_{eff}$, is calculated using Eq. (2.10c). Though Eq. (2.10a) was proposed as a simplified[60] version of previous equations[58], the model demands additional details of the vasculature, which remains a challenge to obtain[54].

2.3.3 Porous Media Based Bioheat Models

Unlike the continuum models, the porous media based bioheat models consider the matrix of capillary bed and tissue to be a porous domain of a given porosity ϕ. The porosity of tissue represents the density of capillary bed in a given tissue or organ. Using the porous-media assumption, the tissue-capillay system is then divided into solid and fluid domains with $0 < \phi < 1$ representing the amount of blood in tissue. The porous media based models that serve as a foundation for other modified versions are described below.

Roetzel and Xuan

Roetzel and Xuan[61] proposed a two equation bioheat model based on the porous media assumption for tissue. The major deviation from the continuum based approach was in their assumption of local non-thermal equilibrium between blood vessels and tissue. The energy equation for tissue (solid region) is given in Eq. (2.11) and for blood (fluid region) is given in Eq. (2.12).

$$(1-\phi)(\rho c_p)\frac{\partial T_t}{\partial t} = k_{t,eff}\nabla^2 T_t + h_b A_{s,b}(T_b - T_t) + (1-\phi)\dot{q} \tag{2.11}$$

$$\phi\rho c_p\left[\frac{\partial T_b}{\partial t} + \vec{v}_b\nabla T_b\right] = k_{b,eff}\nabla^2 T_b + h_b A_{s,b}(T_t - T_b) \tag{2.12}$$

The effective thermal conductivities for tissue ($k_{t,eff}$) and blood ($k_{b,eff}$) are calculated based on the porosity (ϕ) as $k_{t,eff} = (1-\phi)k_t$ and $k_{b,eff} = \phi k_b$. Eqs. (2.11) and (2.12) are coupled via the convective heat exchange between blood and tissue.

If local thermal equilibrium (LTE) between blood and tissue is assumed, then the convective heat exchange term from Eqs. (2.11) and (2.12) equates to zero as T_t equals T_b, and the two equations can be combined to give Eq. (2.13), where $T_b = T_t = T$.

$$\begin{aligned}((1-\phi)(\rho c_p)_t + \phi(\rho c_p)_b)\frac{\partial T}{\partial t} + \phi(\rho c_p)_b \vec{v}_b \nabla T \\ = (k_{t,eff} + k_{b,eff})\nabla^2 T + (1-\phi)\dot{q}\end{aligned} \tag{2.13}$$

The LTE Eq. (2.13) resembles the Wulff BHE with the velocity term vectorizing the perfusion in porous tissue domain.

Nakayama and Kuwahara

Nakayama and Kuwahara[62] formulated a two-energy equation model which was later extended to a three-energy equation model. The three energy equations are for arteries (Eq. (2.14)), veins (Eq. (2.15)), and tissue (Eq. (2.16)), respectively. The two-energy equation model is derived by lumping the arterial and venous system into a single fluid sytem.

$$\begin{aligned}\phi_a (\rho c_p)_b \left[\frac{\partial T_a}{\partial t} + \vec{v}_a \nabla T_a\right] = \phi_a \left[k_b + k_{dis,a}\right] \nabla^2 T_a \\ -A_{s,a} h_b (T_a - T_t) - \omega_a (\rho c_p)_a (T_a - T_t)\end{aligned} \tag{2.14}$$

$$\begin{aligned}\phi_v (\rho c_p)_b \left[\frac{\partial T_v}{\partial t} + \vec{v}_v \nabla T_v\right] = \phi_v \left[k_b + k_{dis,v}\right] \nabla^2 T_v \\ -A_{s,v} h_b (T_v - T_t) - \omega_v (\rho c_p)_v (T_v - T_t)\end{aligned} \tag{2.15}$$

$$(1-\phi_a-\phi_v)(\rho c_p)_t\frac{\partial T_t}{\partial t}=(1-\phi_a-\phi_v)k_t\nabla^2 T_t+A_{s,a}h_b(T_a-T_t)$$
$$+A_{s,v}h_b(T_v-T_t)+(\rho c_p)_b\omega_a(T_a-T_t)+(\rho c_p)_b\omega_v(T_v-T_t)+(1-\phi_a-\phi_v)\dot{q} \tag{2.16}$$

$$k_{dis}=\frac{3\phi_a\left[(\rho c_p)_b\right]^2|\vec{v}_b|^2}{14A_{s,a}h_b} \tag{2.17}$$

The uniqueness of Nakayama and Kuwahara's[62] BHE model is that it can be reduced to Pennes[23] BHE, Chen and Holmes[55] BHE, and Keller and Seiler[57] BHE. The thermal dispersion conductivity, k_{dis}, represents the thermal conductivity due to the tortuosity of blood vessels and is given by Eq. (2.17)[62;63]. For simplicity, the thermal dispersion conductivity can be considered zero if the tortuosity of blood vessels is not significant. Due to the ability of Nakayama and Kuwahara's two-equation model to reproduce other bioheat equations, it is commonly known as a generalized two-equation model.

2.4 Using Voxel Phantoms for Human Thermoregulation

Sections 2.1 and 2.2 in the current chapter show a distinct difference in the simulation domains used. Thermoregulation research relies prominently on stylized phantoms with few exceptions[18;26–29]. Human thermoregulation research can be advanced further by utilizing advanced CHPs as simulation domain rather than stylized models. CHPs have been demonstrated to be person-specific and provide anatomically accurate simulation domains. Thus, using CHPs with thermoregulation control equations can provide a more detailed analysis lacking in other thermoregulation models.

Anatomically accurate CHPs described in section 2.2 consist of voxel phantoms and mesh phantoms. Voxel phantoms are directly generated from medical imaging data, whereas

mesh phantoms use voxel phantoms to fit a surface over the volume. Mesh phantoms offer greater accuracy, but developing a mesh phantom from a voxel phantom is highly complex and requires a lot of pre-processing of each organ to reach an acceptable level[42] of anthropomorphic representation. In recent times, advancements have been made to hasten this process of generating mesh phantoms from voxel phantoms[49], which are promising for future work. A graphical illustration of steps involved in creating a voxel phantom is shown in Fig. 2.3(Adapted from Xu[36]).

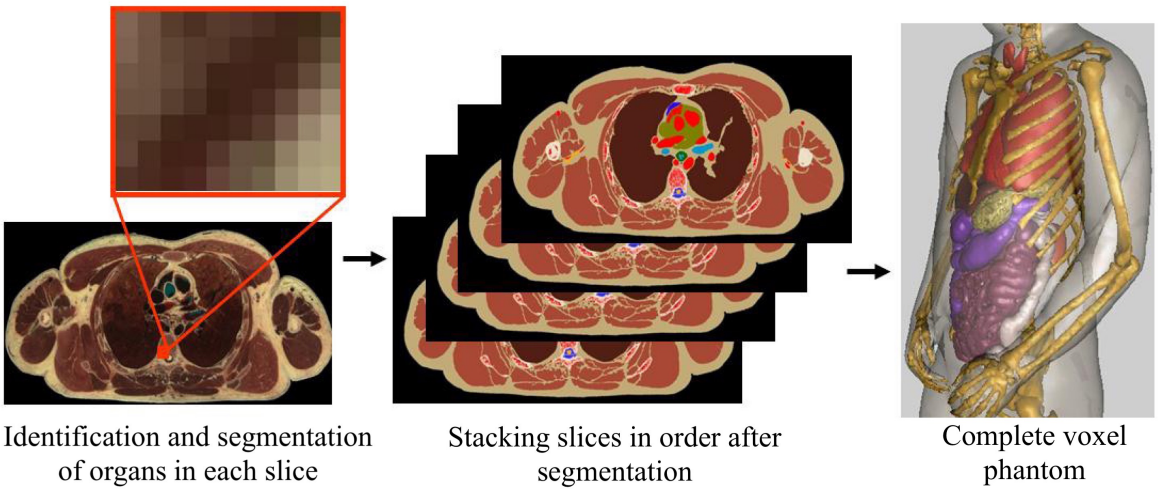

Figure 2.3: Steps to create a voxel phantom. (Adapted from Xu.[36])

An individual mesh phantom represents one body type, reflecting original medical data. A voxel phantom can be generated directly from individual imaging data and is then readily accessible for simulation[32;36;64–66]. This flexibility is absent for mesh phantoms. In addition, voxel phantoms are generally organ volume-conserving when the adequate image resolution is used to capture the organ details. Thus, this dissertation focuses on using voxel phantoms to develop a thermoregulation simulation framework.

The review of bioheat models in section 2.3 demonstrates the variations in the available bioheat equations. The perfusion bioheat models do not consider the effect of large blood vessels on heat transfer, and the countercurrent bioheat models require vascular data which is difficult to obtain. Thus, porous media based models are the best option to be used for developing a thermoregulation simulation framework using voxel phantoms. The proposed

simulation framework must consider the effect of large blood vessels on heat transfer with tissue. Thus a novel framework of porous media based bioheat equations is developed as part of this dissertation.

Challenges associated with using voxel phantoms for thermoregulation

The challenges associated with voxel phantoms are a result voxel resolution and the geometric nature of voxels. The primary challenges are elaborated below.

- Stair-step effect

  Voxels are cuboidal, and cuboidal structures introduce errors in the surface of a curved domain[40;67]. This error or pattern of voxels is known as the stair-step effect[66;68;69]. The stair-step effect cannot be avoided when using a voxel phantom unless one modifies it to a mesh phantom, which is a complicated procedure. A square pixel introduces an error up to 27 % of the total surface area in 2D and a voxel introduces surface area error up to 50 % in 3D. The surface area error is more prominent in smaller and spherical organs like eyeballs, due to the voxel shape[32;36;42;43].

- Blood flow coupled with heat transfer

  Blood flow and vasomotion play a critical role in thermoregulation. The blood flowing from the core to the peripheral skin carries heat and acts as a thermal fluid in the entire human body. In the case of localized heating, local vasomotion helps diffuse heat away from the tissue and avoid overheating the region to the best of its capability[19;70–74]. Compared to spatial variation of temperature in 3D tissue, the flow and thermal variation in a blood vessel is limited to its axial flow direction. Hence it is common to model blood flow as 1D flow. This 1D approximation used in the blood vessels cannot be used for 3D tissue and introduces a multi-dimensional coupling challenge.

- Discontinuous blood vessel network

  Achieving a complete and continuous blood vessel network is difficult when modeling voxelized phantoms. Blood vessel radii span the micrometer to centimeter scales,

with a 1.25 cm radius at the aorta, 3 µm at the capillary bed, and 1.5 cm at vena cava[75]. Currently available *in vivo* imaging technology does not allow micrometer resolution. Clinical scanners typically provide images with voxel dimensions in the range of millimeter.[76]. This resolution cannot represent the finer blood vessel branches, and such anatomical structures are absent in voxel phantoms, resulting in an incomplete and discontinuous blood vessel network. To model the capillary bed and blood flow in such a domain, porous media methods are typically employed[54;61–63;77]. However, the resistances of the pre-capillary vessels regulate vasomotion and hence need to be understood and modeled correctly.

2.5 Stair-Step Effect Rectification

Various methods have been proposed to address the challenge posed by the cuboidal shape. Converting voxel phantoms to polygon mesh phantoms[32;78] provides better accuracy in surface area. Polygon mesh elements can have more than six facets, resulting in highly complex equations to be solved for fluid dynamics and heat transfer. Thus, more computational resources are required to store information and perform calculations on every face of the element. Though polygon meshes provide exceptional representations of complex surfaces, the computational requirements pose a challenge for simulation. Polygon meshes are thus converted to tetrahedral meshes[32;48;49] as the mesh element is reduced to have only four faces, reducing the computational requirements significantly.

Samaras et al.[79] proposed using a surface area correction factor with convective heat transfer coefficient. This correction factor will depend on the overestimation of mesh surface area with respect to the correct surface area. This method works only when the actual area of the organ or the individual subject involved in the simulation is known. The value of the heat transfer coefficient would thus be different for each individual after using the correction factor. The uncertainties and challenges one could encounter in characterizing the actual surface area of each individual subject need to be investigated further. Similar to Samaras[79], Dillard et al.[80] developed a framework to generate a smooth 3D domain from a cartesian

grid. The advantage of Dillard's framework is that it maintains the cartesian grid in which voxels are obtained from the medical imaging data. However, their smoothing framework faces challenges when modeling multiple organs.

An algorithm based on the marching cube method[69] is used to model two adult and two children phantoms[66]. The marching cube method is by far one of the most-used algorithms to smooth a surface represented by cuboidal structures[81]. This method converts the outer layer to a tetrahedral mesh while the internal elements are still hexahedral. In the marching cube method, a scalar value is stored at the lattice point. This scalar value is the pixel information in the case of an image. Each lattice point is a corner vertex of a cube and eight such lattice points define one cubic voxel. This arrangement of information on the vertices of the cube helps to generate the intersection topologies which results in smooth surfaces. Such a mesh with information stored on the vertices is excellent for Finite Element Methods (FEM). Pixels obtained from imaging data can be easily extended to a voxel in 3D with the information stored in the center of the voxel. A voxel domain generated this way can be easily used for finite-volume analysis. Since the finite volume method (FVM) uses flux balance across the faces, the equations are more straightforward and easier to handle for simulation compared to those of the FEM. However, surface-smoothing algorithms used for a FEM mesh cannot be used for an FVM mesh and thus methods such as a marching cube face a challenge. Compared to simulations and models that use FEM, very few models that use FVM for medical applications can be found. Crockett et al.[82] is an example that uses FVM. They use the volume of fluid (VOF) method to smooth the surface under consideration for simulation.

Lattice cleaving, developed by Bronson et al.[83], is another method to smooth an interface of a voxel domain. The method generates a tetrahedral mesh to conform approximately to the surface area interface between materials. The method cuts a body-centered cubic lattice to match the surface, similar to the marching cube method. The generated mesh is tetrahedral, unstructured, and allows mesh element sizes to vary, thus having fewer elements in the region where an interface is not present. The method uses 24 stencil tetrahedrons that vary based on the cuts on the lattice. The lattice cleaving method creates an unstructured

mesh with varying mesh element sizes. It is one of the best methods to utilize for stair-step error rectification. However, the goal of the current dissertation was to create a structured mesh where the original nature of the voxel is maintained to remain close to the medical imaging data. Thus, a structured form of the lattice cleaving method was developed and called as the"Structured Cleaving Method", discussed in Chapter 3.

2.6 Multiphysics Simulation

Multiphysics simulations are rapidly developing and the simulation frameworks used vary from commercial CFD tools like ANSYS[84] to in-house models[85;86] depending on the requirements. However, the major challenge lies in the multi-dimensional aspect of modeling. Blood vessels are highly intricate and form complex patterns[87;88]. Their effect on heat transfer has been studied since the 1940s[23;31;52;54;60;63]. Due to the scale difference between the capillary bed and the simulation domain, porous media models are commonly used to simulate blood flow in tissue[54;62;63;73;89–91], and the density of capillary bed in the tissue is modeled using the porosity parameter.

For modeling large vessels that are segmentable from imaging data or of comparable scale with simulation domain dimensions, blood flow is modeled as 1D flow[92;93] with the vessels considered as 1D pipe segments. The tissue is modeled as a porous domain with porosity representing the capillary density. When dealing with a multi-scale mesh with mixed-dimensional coupling, it is common to use different bioheat transfer models for different dimensional mesh[54;94;95]. Thus, for a 1D mesh of segmented blood vessels countercurrent bioheat models are applicable. For a 3D mesh of tissue and capillaries, porous-media based bioheat transfer models are useful. The challenge in such a mixed-dimensional multiphysics simulation lies in coupling the 1D model with the 3D model[73;96]. The VaPor model developed by Blowers et al.[73] provides a solution for multi-dimensional coupling that can be used for for thermal analysis[97]. The VaPor model employs the Rapidly-exploring Random Tree (RRT) algorithm[98] to generate blood vessels that are not segmented due to limitations in image resolution to simulate counter-current heat exchange at every level of the vasculature.

In VaPor model, all the voxels that intersect a terminal vessel are made to exchange blood with that respective vessel. Other voxels that do not intersect with any terminal vessel rely on perfusion for blood flow. Inter-domain mass transfer thus becomes an important parameter, which is specified at each vessel terminal. In other words, if a terminal vessel is intersecting ten tissue voxels, each voxel receives one-tenth the flow rate flowing through the terminal vessel. The inter-domain mass transfer parameter controls this flow rate between vessel and tissue. This parameter is further used to determine the diameters of blood vessels and to calculate pressure drop across the vessel segments. In human thermal modeling research[11;31;32;99;100], the pressure drop across the cardiovascular domain and blood flow simulation is important in addition to thermal mapping. The VaPor model provides a novel way to simulate heat transfer in a mixed domain but lacks the ability to couple pressure gradient with assigned inter-domain mass transfer[73]. Furthermore, determining the flow rate at every vessel terminal is challenging when simulating a very large domain, such as the human body. Thus, the literature review so far demonstrates a requirement for a framework that can simulate blood flow with correct pressure distribution, and simulate coupled heat transfer for a large scale biological domains like organs and human body.

Hodneland et al.[101] developed a framework that uses the Dirac distribution function to couple a 1D blood flow network with 3D porous tissue. This framework uses the Hagen-Poiseuille equation to model one-dimensional blood flow in large blood vessels and the two-compartment porous model for a three-dimensional tissue. Due to the flexibility and pressure continuity of Hodneland's model, this flow simulation model was used to create a novel multiphysics simulation framework by adding heat transfer capabilities. The resulting multiphysics, multiscale and multidimensional framework is termed as Voxelized MultiPhysics Simulation (VoM-PhyS) framework and will be elaborated further in Chapter 4.

2.7 Pre-Capillary Blood Vessels

Technological advancements enable visualization and modeling of the vasculature[87;88] with the ever-increasing resolution, providing highly detailed blood vessel domains. These domains can be further used to simulate many biophysical mechanisms. When coupled with accurate biophysics simulations, such realistic models can be used to illustrate, understand, and predict biological responses to different environmental conditions. Such tools can predict patient response to medical treatment, changes in blood flow distribution due to burns or clots[102–104], drug distribution, and damage to healthy tissue during hyperthermia treatments[65;94].

However, a very high resolution data is required to visualize vasculature for the entire human body. As described in section 2.4, the resolution of the voxel phantom limits the visualization of blood vessels that can be modeled. Although capillary beds can be modeled using porous media assumption in tissue, pre-capillary vessels that are considered to affect heat transfer by WJM[59;60;105] also play a crucial role in vasomotion. The arterioles, which can vary flow resistance, are present in pre-capillary vessels that often get overlooked in bioheat transfer. For a complete human thermoregulation framework, the ability to simulate vasomotion is important; thus, modeling the pre-capillary network is crucial.

In a voxel domain generated from imaging data, a blood vessel ends where the resolution of the voxel can no longer identify it. One option to simulate the pre-capillary vessels from this point would be the mathematical modeling of blood vessels or an algorithm to simulate vascularization and generate blood vessels. Vascularization and angiogenesis are highly complex phenomena that include chemical, physical, and biological processes[106–110]. Vascular Endothelial Growth Factor (VEGF) signaling released by the tissue cells directs the tip cell to guide vascularization. Various biocomputational models have been developed to simulate vascularization[111–114].

Computational models developed from a biological perspective[114] are different from models developed from an engineering perspective. One of the primary approaches engineers use to model blood vessel growth is modeling blood vessels as fractals[115–120]. The Diffusion

Aggregation Method proposed by Fleury[121–123] is commonly used to model blood vessels as fractals. This is a "random walker" method where a particle is released from the periphery and "walks" randomly until it merges with an existing branch. The challenge with this method is that there is no way to control the dimension of blood vessels. Moreover, a random walker method is highly accurate when an oxygen diffusion map is used to guide the random walker. However, this requires solving mass transfer equations for oxygen concentration after adding every random walker to the existing blood vessel, which is computationally expensive for a large domain like an organ or human body.

Another method that provides a better alternative is called Constrained Constructive Optimization (CCO)[124–127]. In CCO, the main assumption is that blood flow is equally distributed in the specific organ domain. Based on this assumption, the supply blood flow rate in the organ is equally distributed in a given number of terminals. The blood flow rate passing through a single terminal vessel and the pressure drop between the supply node and the terminal of vasculature are provided as constraints. A random point is selected within the domain and a new branch is grown towards the point. The radius of the new branch is calculated such that the total volume of the vasculature is minimized. The CCO method has undergone various modifications such as parallelizing the growth of blood vessels[127–129] to increase computational efficiency.

An example of the application of the CCO model is found in Correa-Alfonso's work of vascularization on mesh liver model[86]. The minimum diameter of a blood vessel in this liver model is 100 µm. The blood vessels in this model are also shunted, i.e., arteries are directly connected with veins. This model lacks blood vessels with diameters less than 100 µm. The shunt between arteries and veins at 100 µm cannot model the time blood spends in the capillary bed. Blood flow is the slowest in the capillary bed and is expected to have a higher energy absorption rate due to the time spent there. The challenge with using the CCO method with voxel phantom is associated with voxel resolution. For example, in the mesh liver model, to model the blood vessels of 100 µm, a voxel resolution of less than 100 µm is required. When a cubodial voxel of size 500 µm is used to voxelize the mesh, the domain has a total of 1.36×10^7 voxels. About 70 % of hepatic arteries are lost in the voxelization

of the liver mesh as they have a diameter of less than 500 µm.

Modeling every blood vessel to the capillary bed is not a feasible solution. Thus, a new method is required to model the flow resistance and heat transfer of blood vessels that exist between the capillary bed and the segmented blood vessels. In Hodneland's model[101], the pressure drop parameter is used to simulate the resistance of the "virtual" blood vessels that are not segmented. Determining the resistance of unsegmented vessels from available vascular data will addresses the challenge of mathematically modeling the pre-capillary vessels. Chapter 5 of this dissertation focuses on mathematical derivation of equations that can be used for modeling virtual blood vessels.

Chapter 3

Structured Cleaving Mesh

One primary challenge with voxelized domains is the stair-step effect resulting from the cuboidal structure of voxels. A detailed review of various methods found in the literature to reduce the surface area error due to stair-step effect is given in Chapter 2. The Lattice cleaving method[83] smoothens the voxel mesh by converting it to an unstructured tetrahedral mesh. This chapter focuses on developing an algorithm that develops a tetrahedral mesh and smoothing technique for a structured mesh, and is termed as the "Structured Cleaving Method".

In this chapter, the amount of error in the surface area of a voxel mesh is quantified using a circle for 2D and a sphere for 3D as a reference domain, respectively. Since the circle and sphere represent the worst-case scenarios for a curved geometry that is represented using voxel mesh, quantifying the surface area error on these geometries represents the maximum possible error. Two surface area smoothing techniques are elaborated – the addition method and the removal method. The application and the effect of these methods on the triangular mesh (2D) and tetrahedral mesh (3D) are described in this chapter. Finally, the application of the structured cleaving method for heat transfer analysis is demonstrated on four mice tumors obtained from MRI scans. These scans were provided by the Biomedical Computing Device Laboratory at Kansas State University.

3.1 2D Analysis

Fig. 3.1.a shows two possibilities of a single pixel representing a circular structure in a course mesh. The pixel can be either larger than the circle, as shown by the blue square, or smaller than the circle, as shown by the green square. Fig. 3.1.b shows the comparison of a finer (green) and coarser mesh (blue). As the mesh is refined, a stair-step path is followed along the surface (circumference) of the circle. As will be shown later, this limits surface area convergence and is a major source of error.

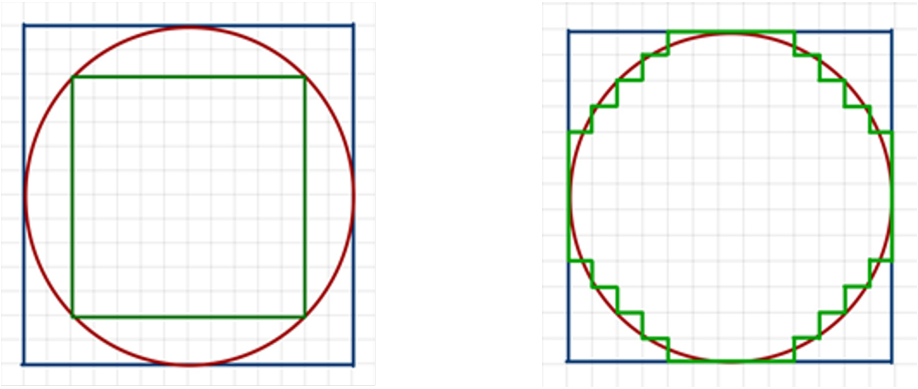

(a) courser mesh (b) courser and finer mesh

Figure 3.1: Square pixel representation of a circle

Consider a mesh grid shown in Fig. 3.2. The mesh cell "i,j" is surrounded by four rectangles as shown. Heat transfer interactions that take place within the domain are shown with red arrows. The steps taken to obtain a discrete heat diffusion equation are as follows:

A general 2D heat diffusion equation for a heat generating domain is shown in Eq. (3.1).

$$\frac{\partial}{\partial x}\left(k\frac{\partial T}{\partial x}\right)+\frac{\partial}{\partial y}\left(k\frac{\partial T}{\partial y}\right)+\dot{q}=0 \tag{3.1}$$

The terms k, T, and $\dot{q}$ represent thermal conductivity, temperature and volumetric heat generation rate, respectively, at a point x, y.

Integrating Eq. 3.1 over the volume $\Delta x \times \Delta y$, Eq (3.2) and Eq. (3.3) are derived.

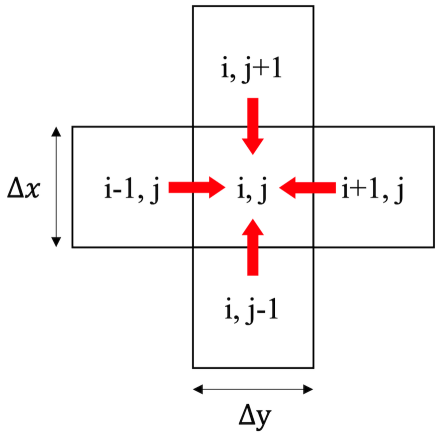

Figure 3.2: Square pixel mesh

$$\int_{\Delta x}\int_{\Delta y}\frac{\partial}{\partial x}\left(k\frac{\partial T}{\partial x}\right)dxdy+\int_{\Delta x}\int_{\Delta y}\frac{\partial}{\partial y}\left(k\frac{\partial T}{\partial y}\right)dxdy+\int_{\Delta x}\int_{\Delta y}\dot{q}dxdy=0 \tag{3.2}$$

$$\left[kA_{c,left}\left(\frac{\partial T}{\partial x}\right)_{left}+kA_{c,right}\left(\frac{\partial T}{\partial x}\right)_{right}\right]+ \tag{3.3}$$
$$\left[kA_{c,top}\left(\frac{\partial T}{\partial y}\right)_{top}+kA_{c,bottom}\left(\frac{\partial T}{\partial y}\right)_{bottom}\right]+\dot{q}\Delta V=0$$

where,

$$kA_{c,left}\left(\frac{\partial T}{\partial x}\right)_{left}=kA_{c,left}\frac{T_{i-1,j}-T_{i,j}}{\Delta x/2} \tag{3.3.a}$$

$$kA_{c,right}\left(\frac{\partial T}{\partial x}\right)_{right}=kA_{c,right}\frac{T_{i+1,j}-T_{i,j}}{\Delta x/2} \tag{3.3.b}$$

$$kA_{c,top}\left(\frac{\partial T}{\partial y}\right)_{top}=kA_{c,top}\frac{T_{i,j+1}-T_{i,j}}{\Delta y/2} \tag{3.3.c}$$

$$kA_{c,bottom}\left(\frac{\partial T}{\partial y}\right)_{bottom} = kA_{c,bottom}\frac{T_{i,j-1} - T_{i,j}}{\Delta y/2} \tag{3.3.d}$$

In Eq. (3.3), the subscripts *left*, *right*, *top* and *bottom* are with respect to the location of cell *i, j*. Thus, *left*, *right*, *top*, and *bottom* represent cells (*i-1,j*), (*i+1, j*), (*i, j+1*), and (*i, j-1*), respectively. The term A_c represents the cross-section area of the cell.

Expanding the concept, the pseudo overall heat transfer coefficient (U) is calculated using Eq. (3.4), where k_{nbr} represents the thermal conductivity of the neighboring cell.

$$\frac{1}{U} = \frac{\Delta s}{2k_{nbr}} + \frac{\Delta s}{2k} \tag{3.4}$$

At a boundary interface of tissue and air, the pseudo overall heat-transfer coefficient is calculated using Eq. (3.5)

$$\frac{1}{U_{skin-air}} = \frac{1}{h_{amb}} + \frac{\Delta s}{2k_{i,j}} \tag{3.5}$$

Using the energy conservation principle and Eq. (3.3),

$$\begin{aligned}(UA_c)_{left}(T_{i-1,j} - T_{i,j}) + (UA_c)_{right}(T_{i+1,j} - T_{i,j}) + \\ (UA_c)_{top}(T_{i,j+1} - T_{i,j}) + (UA_c)_{bottom}(T_{i,j-1} - T_{i,j}) + \dot{q}\Delta V = 0\end{aligned} \tag{3.6}$$

The discretized equation Eq. (3.6) allows the properties to vary from pixel to pixel and thus can be applied to highly inhomogenous structures such as the human body.

In the process of refining the mesh (shown in Fig. 3.2.b), it is observed that the curvature of the geometry is replaced with a perpendicular stair-step effect of the square pixels. This results in an error in the total surface area of the geometry, which cannot be avoided irrespective of mesh resolution. If the radius of the cylinder is defined to be "a" and a unit

thickness in the z-direction is assumed, the surface area of the cylinder (circumference of circle in 2D) is given by $2\pi a$. The pixel dimensions of the perfect square pixel represented by the blue square in Fig. 3.2 are $2a \times 2a$. The perimenter of a square is considered as the surface area and is given as $8a$. Regardless of pixel dimensions (fine mesh or course mesh), the total surface area of pixels representing a circular domain always remains $8a$ (Fig. 3.1.b), resulting in a constant surface-area error of $1.72a$. This error of $1.72a$ corresponding to an overestimate of 27 %. To demonstrate this error, a circle of radius 0.03 m generating heat at 1333 W m^{-3} was simulated exposed to air at 20 °C. The parameters used for this simulation are given in Table 3.1. Using Eq. (3.6), the temperatures at the circumference of the domain are shown in Fig. 3.3.

Table 3.1: Simulation parameter for pixel surface area error analysis

Parameter	Symbol	Value	Units
Ambient Temperature	T_{amb}	20	°C
Radius	r	0.03	m
Thermal conductivity	k	0.3	W m^{-1} °C^{-1}
Convective heat transfer coefficient	h_{amb}	3.0	W m^{-2} °C^{-1}
Internal heat generation	$\dot{q}$	1333	W m^{-3}

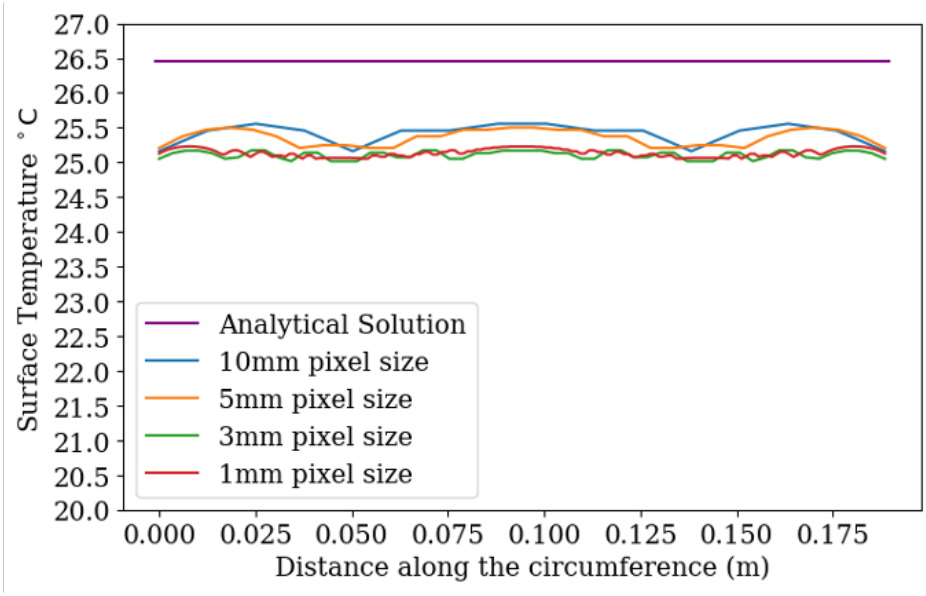

Figure 3.3: Intrinsic surface area error

In Fig. 3.3, the analytical solution for a perfect circle shows the circumference at a constant temperature of 26.5 °C. When different pixel sizes are used to construct the same circle, the circumference temperature is reduced to 25 °C to 25.45 °C. This is due to the stair-step effect of the square pixels. As the surface area of a pixelized circle is larger, more heat loss occurs to the environment, reducing the domain temperature.

3.1.1 Sub-Pixelization

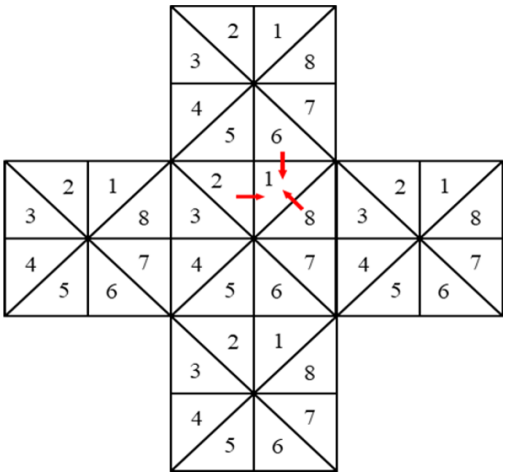

Figure 3.4: Triangle pixel mesh

One solution to reduce this error is to convert square pixels to triangular pixels as shown in Fig. 3.4. The triangular pixels are generated such that when grouped they comprise square pixels from which they were generated. This method is thus considered a sub-pixelization approach in 2D and a sub-voxelization approach in 3D.

In Fig. 3.4, red arrows show the heat exchange occuring around cell 1 with cells 2, 6, and 8. Cell 2 shares a non-hypotenuse side with cell 1. Similarly, cell 6 shares a non-hypotenuse side with cell 1. These non-hypotenuse sides will be referred to as "rectangular sides" for this dissertation. Cell 8 and cell 1 share a hypotenuse side of the triangular pixel. The pseudo-overall heat transfer coefficient at a rectangular side is calculated using Eq. (3.7).

$$\frac{1}{U} = \frac{\Delta s}{6k_{nbr,tri}} + \frac{\Delta s}{6k} \tag{3.7}$$

Triangular pixels have the advantage of using the hypotenuse to reduce the stair-step effect. The pseudo-overall heat transfer coefficient for a hypotenuse side is calculated using Eq. (3.8)

$$\frac{1}{U} = \frac{\Delta s}{6\sqrt{2}k_{nbr,tri}} + \frac{\Delta s}{6\sqrt{2}k} \tag{3.8}$$

In Eqs. (3.7) and (3.8), Δs represents Δx or Δy depending on the axis of heat transfer. Similarly, the pseudo overall heat transfer coefficient for a cell exposed to air is calculated using Eqs. (3.9) and (3.10) for rectangular side and hypotenuse side, respectively.

$$\frac{1}{U} = \frac{1}{h} + \frac{\Delta s}{6k} \tag{3.9}$$

$$\frac{1}{U} = \frac{1}{h} + \frac{\Delta s}{6\sqrt{2}k} \tag{3.10}$$

Once the pixels are converted into triangle sub-pixels, a smoothing method is needed to reduce the surface area. Two methods are proposed to smoothen the surface of a pixel mesh (2D) and voxel mesh (3D). These methods are termed as the removal method and the addition method, respectively.

3.1.2 Removal Method

After sub-pixelization, the triangular elements can be removed from the domain to smooth the outer surface without a significant effect on volume. Here, removal means the material of that specific pixel is changed to the material it is being exposed to. For this simple example, the domain is composed of only two materials: air and tissue. The process steps are shown below.

1. Each pixel is tagged with its number of sides exposed to a different material. If only one side is exposed to a material different than that of the pixel itself, then 1; if two sides are exposed then 2, and so on.

2. If zero or one side of the tissue pixel is exposed to air, no change is made to the sub-pixel.

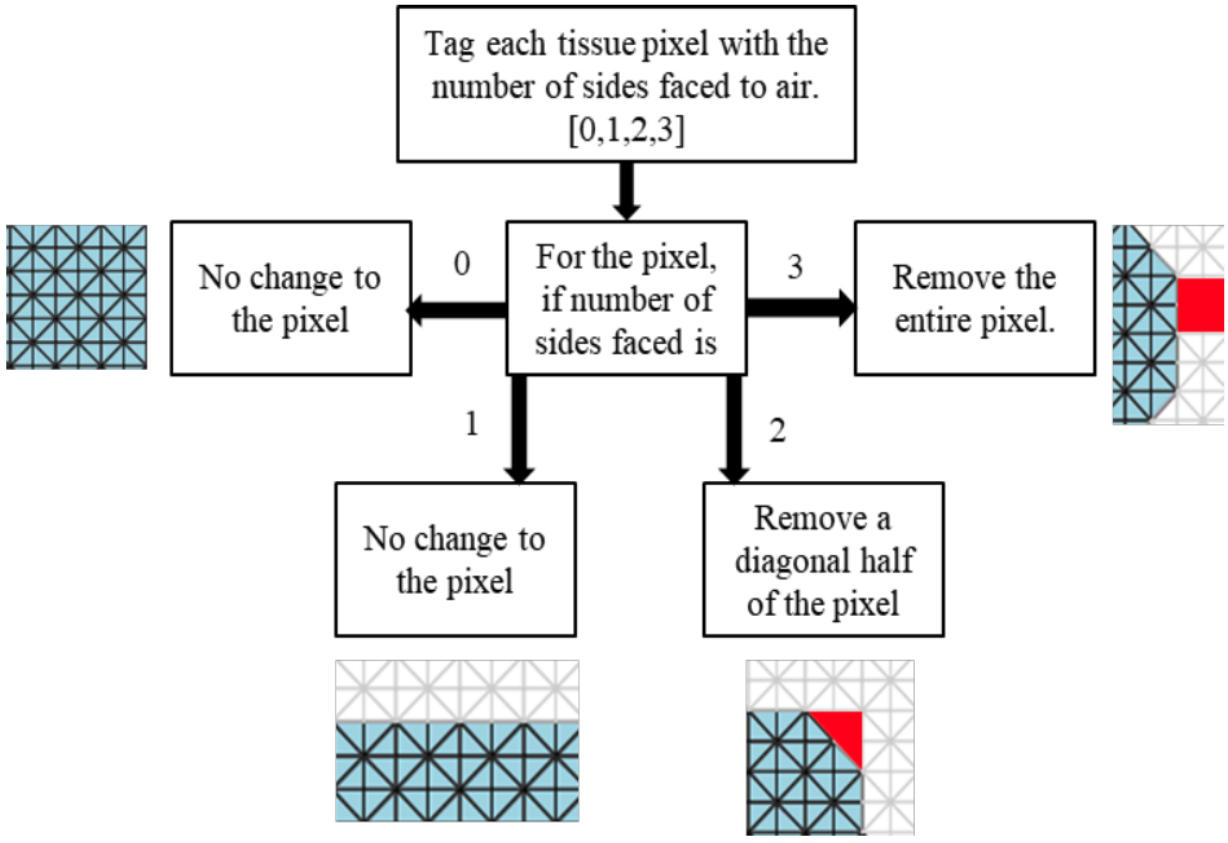

Figure 3.5: Removal method algorithm

3. If two sides of the tissue pixel are exposed to air, the tag of diagonal portion exposed to air is changed to air. This means half of the sub-pixel is converted to air, separated by the hypotenuse.

4. If three sides of tissue pixels are exposed to air, the entire pixel tag is changed air.

The results of applying the algorithm are shown in Fig. 3.6. The purple triangles represent the triangualar cells for which the material tag was changed from tissue to air.

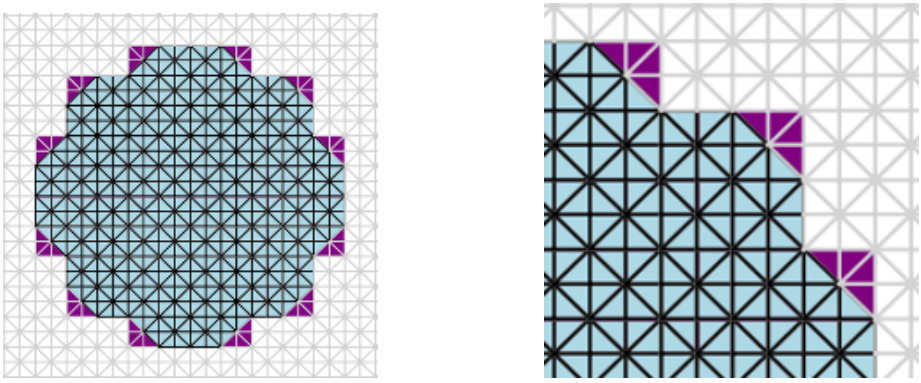

(a) (b)

Figure 3.6: Removal of material: (a) overall view of the effect of removal method (b) zoomed-in version of the surface

3.1.3 Addition Method

In this method, extra material is added to the object's periphery to mitigate the stair-step effect. In other words, if tissue is exposed to air, the triangular cells of air at the interface of tissue-air are converted to tissue. The algorithm is similar to the removal method, with the difference being that the non-object material pixels are altered. In the removal method, the tissue pixels were changed to air, whereas in the addition method, air pixels are changed to tissue.

Fig. 3.7.a shows the overall effect of the addition method on the domain. The blue pixels represent the domain under consideration. Fig. 3.7.b shows a zoomed-in version of the surface. The pink triangular pixels are the material being added to the domain.

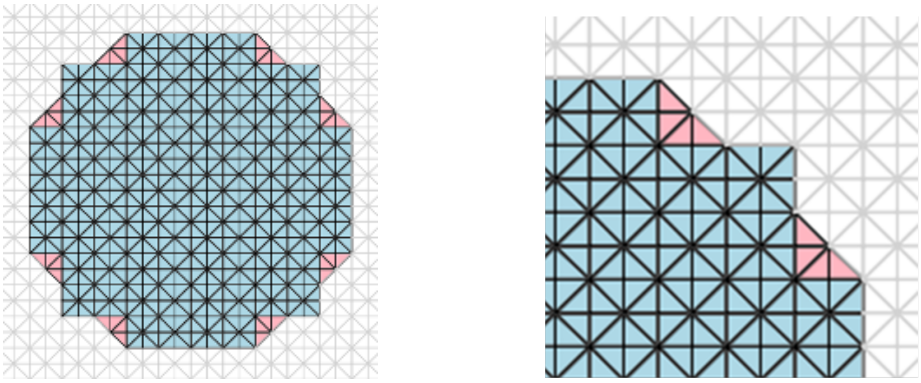

(a) (b)

Figure 3.7: Addition of material: (a) overall view of the effect of addition method (b) zoomed-in version of the surface

3.1.4 Analysis and Results

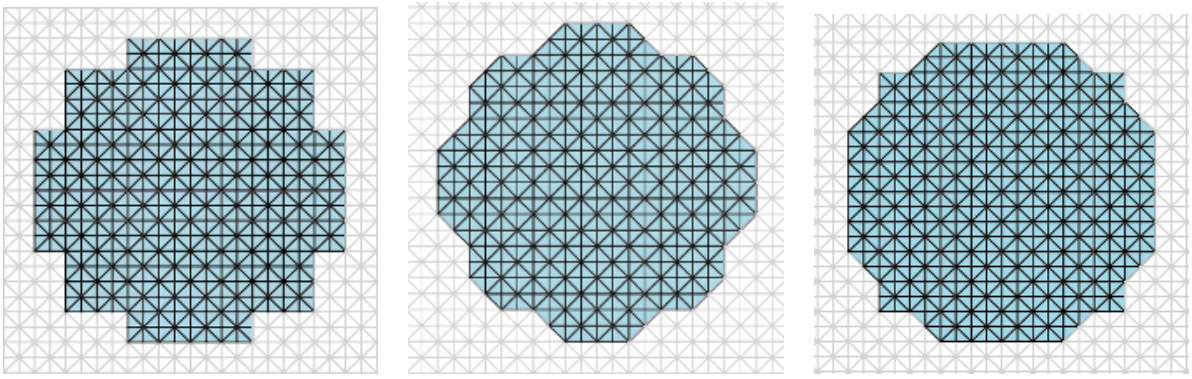

(a) (b) (c)

Figure 3.8: 2D smoothing (a) unsmoothed (b) removal method (c) addition method

An unsmoothed circle, smoothed circle using the removal method, and smoothed circle using the addition method, are shown in Fig. 3.8. When the removal method is applied, loss of volume occurs because the material tags are changed to surrounding material. Similarly, the addition method results in more volume than the original as the material is added to smoothen the surface. Neither of these options is perfect, as voxel meshes are expected to have correct volume representation and any variation in volume can introduce additional error due to differences in total heat generated by metabolic heat generation. Thus an analysis to understand the error in volume introuduced due to the use of the addition and

removal method, respectively, compared to reduction in the surface area error was conducted. The reduction in surface area error and the resultant volume error can be seen in Fig. 3.9. Fig. 3.9.a shows the ratio of mesh volume to actual reference volume for different pixel sizes. Fig. 3.9.b shows the surface area ovestimation for a mesh for different pixel sizes. For larger pixel sizes, there is greater volume error. As the pixel size is reduced, the error introduced due to the use of addition or removal methods converges to less than 1 % and the surface area error is reduced to less than 10 %. From Fig. 3.9, it can be seen that the removal and addition method have similar effect on the volume error and surface area error convergence. Thus, only the removal method was used for further analysis for simplicity.

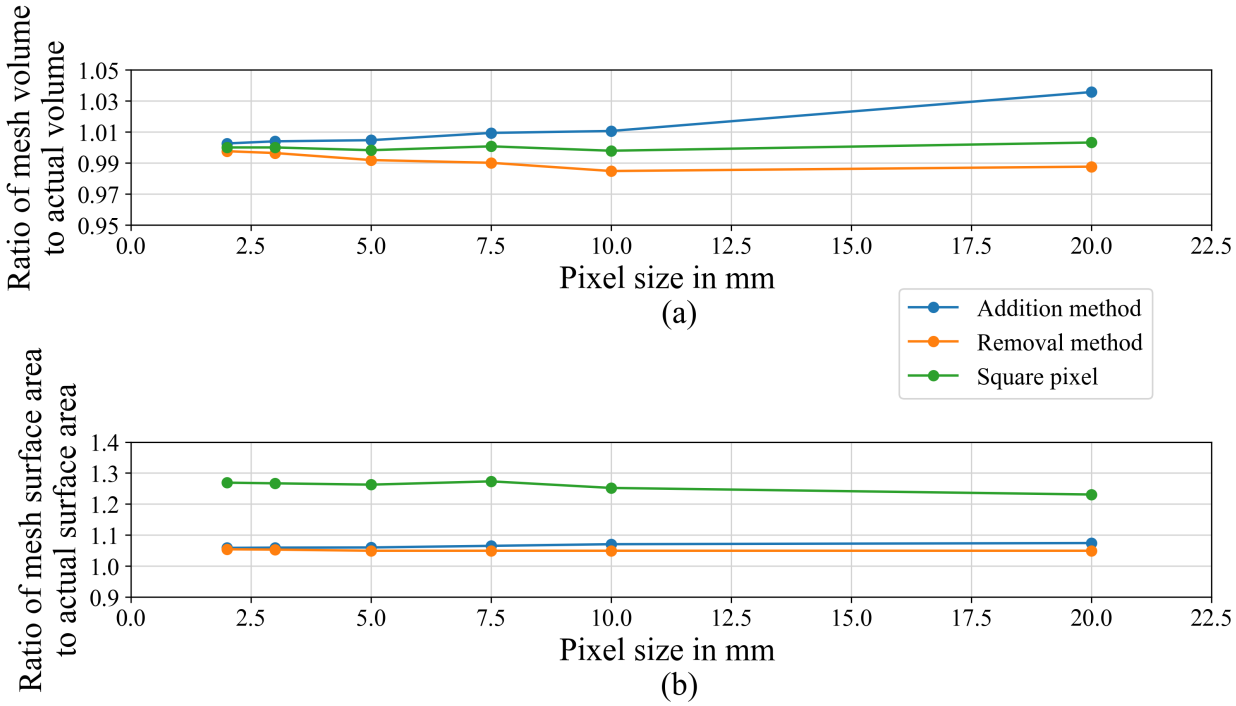

Figure 3.9: Surface area and volume convergence in 2D

To demonstrate the effectiveness of the removal method, an inhomogeneous domain was designed as shown in Fig. 3.10, with parameters given in Table 3.2. Fig. 3.11.a shows the temperature of triangularized pixels along the circumference of skin-air interface. The analytical solution results in a uniform circumferential temperature of 26.48 °C. As can be seen in Fig. 3.11.a and Fig. 3.11.b, there is an average error of 1.4 °C for square pixels and 0.39 °C for triangularized smoothened pixels.

Table 3.2: Simulation parameter for inhomogeneous domain

Parameter	Symbol	Value	Units
Ambient Temperature	T_{amb}	20	°C
Radius - bone	r_{bo}	6	mm
Radius - tissue	r_t	27	mm
Radius - skin	r_s	30	mm
Thermal conductivity of skin[130]	k_s	0.37	$\mathrm{W\,m^{-1}\,°C^{-1}}$
Thermal conductivity of tissue[130]	k_t	0.49	$\mathrm{W\,m^{-1}\,°C^{-1}}$
Thermal conductivity of bone[130]	k_{bo}	0.31	$\mathrm{W\,m^{-1}\,°C^{-1}}$
Convective heat transfer coefficient	$\mathrm{h_{amb}}$	3.1	$\mathrm{W\,m^{-2}\,°C^{-1}}$
Internal heat generation	$\dot{q}$	1333	$\mathrm{W\,m^{-3}}$

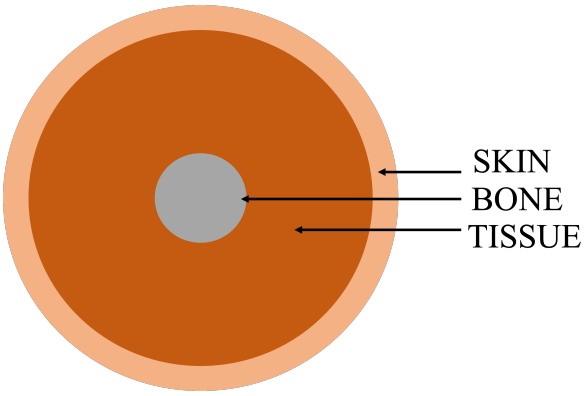

Figure 3.10: Inhomoegeneous domain

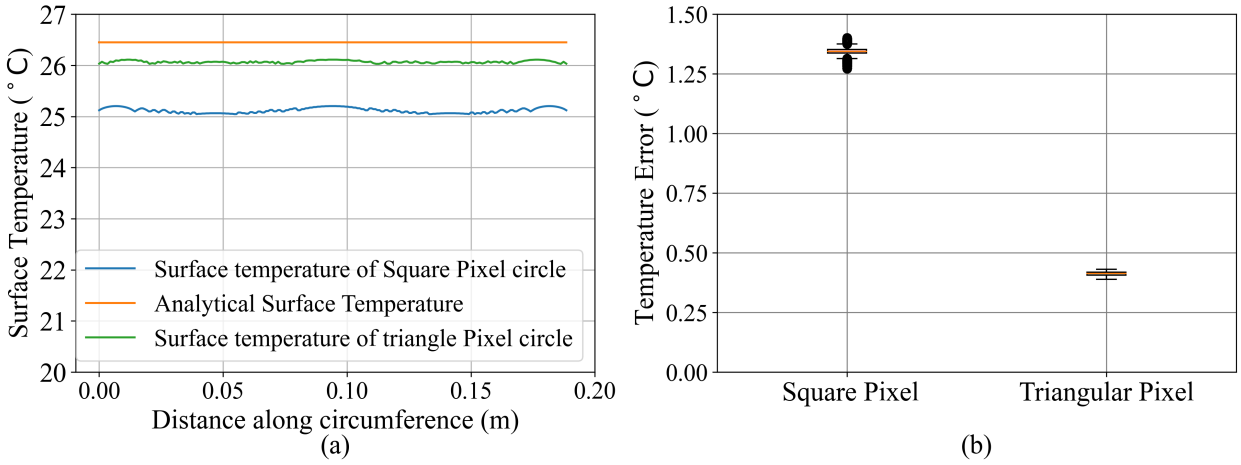

Figure 3.11: Inhomogeneous domain temperature analysis (a) Temperature along the circumference (b) Error distribution for pixel mesh and triangular-smoothed mesh

3.2 3D Analysis

In the previous section, the cleaving method for a 2D domain was discussed. This section illustrates the methodology for extending the cleaving method for 3D.

Step 1: Pre-processing to Determining interface voxels

Voxels in voxel phantoms are assigned different tags, which can represent the voxel material or different properties of the voxel. Along with these existing voxel tags, a new tag is created that will differentiate a voxel on the surface of the domain from a voxel on the interior. This tag will be called the "side-exposed tag" for this dissertation. The side-exposed tag stores information about which sides of the voxel are exposed to different materials, which will be used to smooth the surface in the following steps.

Step 2: Converting voxels to tetrahedrons

Consider a voxel shown in Fig. 3.12.a, which is cut along all the diagonals shown by AF, BE, EC, AG, BC, and AD on all sides. The cut along the diagonals results in 24 tetrahedrons that share a common vertex with the centroid of the voxel. Each side of voxel is now represented with four tetrahedrons. Fig. 3.12.b shows a cross-section of tetrahedrons in a voxel. The exploded view of Fig. 3.12.b, showing the tetrahedrons separated, is in Fig. 3.12.c, and all 24 tetrahedrons are shown in Fig. 3.12.d in an exploded view. Each of these tetrahedrons has the same material as that of the parent voxel.

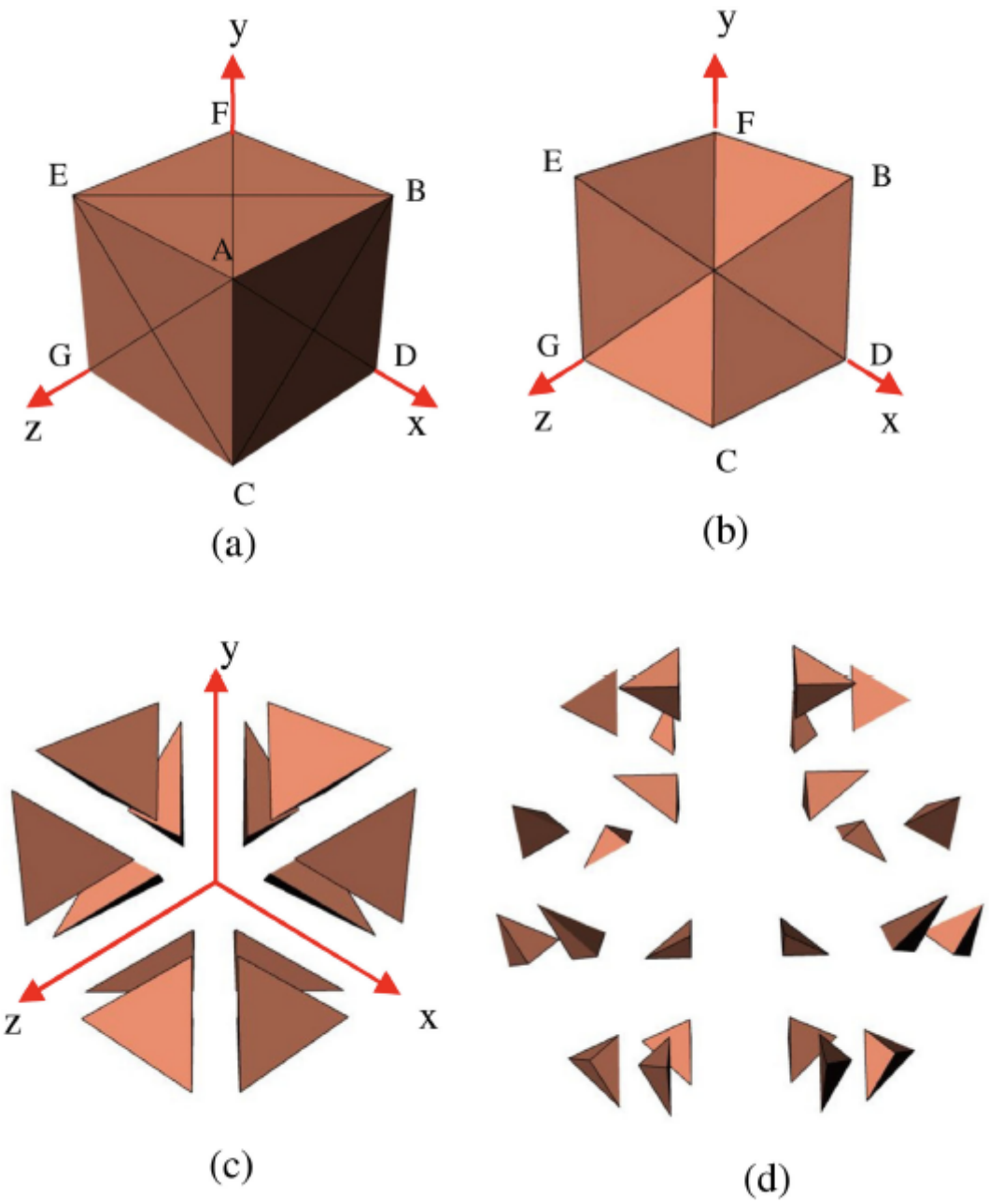

Figure 3.12: Voxel to tetrahedron

Step 3: Smoothing the surface

Converting the voxels to tetrahedrons does not alone solve the problem of the stair-step effect on the surface. A smoothing algorithm is needed to smooth the surface of the object after converting voxels to tetrahedrons, similar to the removal method used for 2D domain.

Consider the parent voxel shown in Fig. 3.13, surrounded by neighboring parent voxels. The red arrows show the six directions with reference to the voxel under consideration. Fig. 3.14 shows the possible modifications during the smoothing process, while Fig. 3.15 shows the methodology to smoothen a matrix of $3 \times 3 \times 3$ voxels. In Fig. 3.15.a an unsmoothed domain with one-side, two-sides, and three-sides exposed voxels marked in white, blue, and green outlines for reference, respectively, are exhibited. The entire domain is made up of the same material and is exposed to the surrounding, which is not shown. The smoothing procedure shown using Figs. 3.13, 3.14, and 3.15 is described in the following steps.

1. If the parent voxel has no side or only one side exposed to a different material, then the voxel does not undergo modification. In Fig. 3.15.a, the voxel marked with a white outline is an example of such a voxel with only one side exposed to different material. This voxel will not be changed.

2. If the parent voxel has more than one neighboring voxel of a different material, for example, north and front voxels, the material tags of the tetrahedrons, which are part of the side exposed to these voxels, will be changed from the parent material to the neighboring voxel material. The parent voxel after modification is shown in Fig. 3.14.a.

3. The side-exposed tag of neighboring tissue voxels will now be checked. From Fig. 3.14.a it can be seen when two sides are modified, a valley-like surface is formed. To avoid this, the neighboring tissue voxels need to be modified, as well. In the example considered, the north and front sides were exposed to a different-material, and the respective tetrahedrons material was changed in previous step. Now the east and west sides of tissue-voxel neighbors will be checked for their side-exposed tag. If the east-neighboring voxel has more than one side exposed to a different material, the neighboring voxel will be modified. This would result in the material tags of tetrahedrons that share the edge with east-north and east-front sides to change. The result is shown in Fig. 3.14.b.

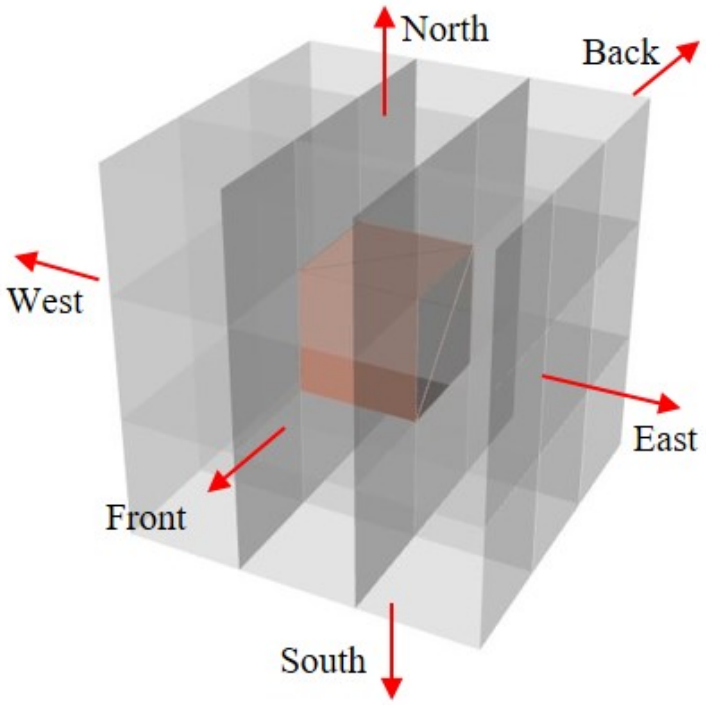

Figure 3.13: Voxel array

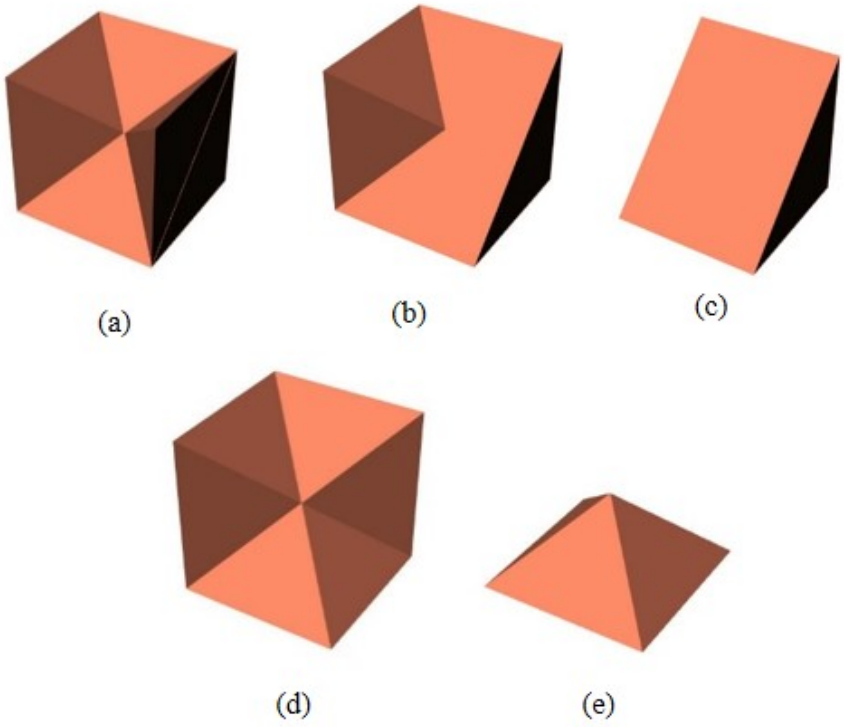

Figure 3.14: Modification of parent voxel

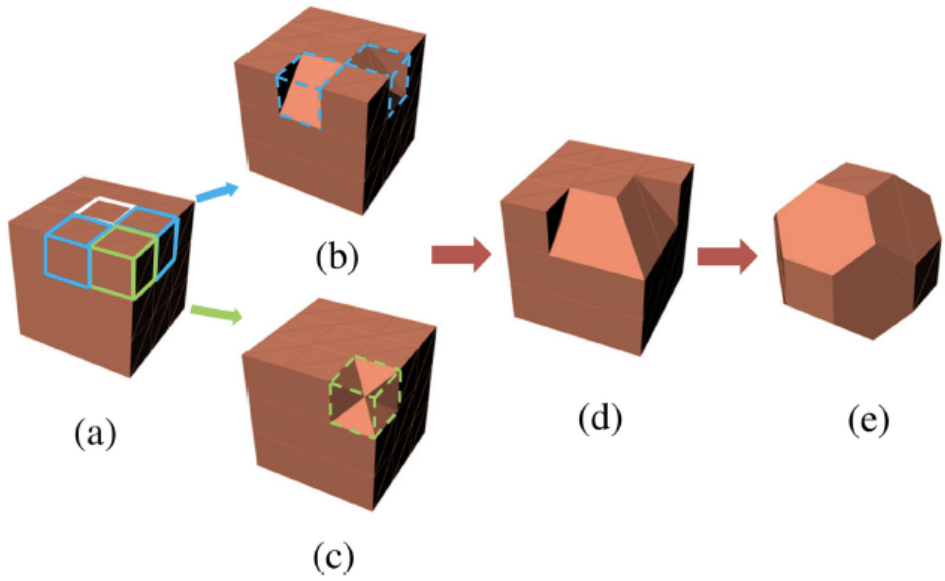

Figure 3.15: Methodology of smoothing

4. Similar to the east side, if the side-exposed tag of west-neighboring voxels has more than one side exposed to different material, the material tags of tetrahedrons that share the edge with the west-north and west-front sides will be changed. This modification is shown in Fig. 3.14.c, and would result in a smooth diagonal cut of the parent voxel under consideration. The final result of steps 2, 3 and 4 is shown in Fig. 3.15 as a transformation from Fig. 3.15.a to Fig. 3.15.b. The two-side exposed voxels marked in blue in Fig. 3.15.a result in the diagonal cut voxels as shown in Fig. 3.15.b

5. Consider a voxel with north, front, and east sides exposed to neighbors, i.e., three sides exposed. Similar to the two-sides-exposed condition, material tags of the tetrahedrons that are part of the voxel's three sides will be changed to the material of the neighboring voxels in the respective direction. In other words, the material of these tetrahedrons will be changed to that of the surrounding material to the domain. The resultant parent voxel structure is shown in Fig. 3.14.d. In Fig. 3.15.a, the three sides exposed voxel is shown on a vertex marked by a green outline. This voxel after undergoing the modification is transformed in a shape as shown in Fig. 3.15.c. When the steps 1, 2, 3 and 4 are repeated over a corner of the matrix, a partially smoothed domain similar

to one shown in Fig. 3.15.d. is achieved.

6. For a case where five sides are exposed to different materials, the resultant parent voxel is a pyramid with one side that is not exposed to a different material. This is shown in Fig. 3.14.e. A five-sides-exposed voxel will be completely converted to the neighboring material. This is done because the the pyramid like structure shown in Fig. 3.14.e has more surface area than the base of that pyramid. To reduce the surface area error further, the pyramid structure is avoided and hence a voxel with five sides exposed tag is removed completely.

7. The end result of applying the smoothing algorithm on the grid shown in Fig. 3.15.a. results in a domain shown in Fig. 3.15.e.

3.3 Structured Cleaving Mesh and Heat Transfer

MRI scans of four lab mice with tumors were obtained from the Biomedical Computing and Devices Laboratory at Kansas State University to demonstrate the methodology described. The tumors in these scans were manually segmented using 3DSlicer (version 4.8.1)[131]. The voxel size obtained from these scans was $0.117\,\text{mm} \times 0.117\,\text{mm} \times 1.5\,\text{mm}$. A 3D unstructured mesh of each tumor was generated using the 3DSlicer meshing feature. This mesh was converted to a NURBS surface using Rhinoceros (version 5)[132] to obtain a reference surface area and volume. The domain was re-voxelized with cuboidal voxels with the dimensions of $0.12\,\text{mm}$ in all three axes. This process is described in Fig. 3.16, which shows, using blue arrows, development from an MRI scan to the final, tetrahedral-smoothed tumor undertaken for this research. The golden arrow from Fig. 3.16.c to Fig. 3.16.f indicates that though a NURBS surface was generated to use as a reference, there is no need to generate a NURBS surface to apply the proposed method of smoothing a voxel mesh obtained from a medical imaging dataset. To show the effect of this method on simple geometric objects, a sphere and a cylinder were also considered. The volume and surface area convergence for a sphere with a radius of $1\,\text{cm}$ and a cylinder with a radius of $1\,\text{cm}$ and height $2\,\text{cm}$ are demonstrated.

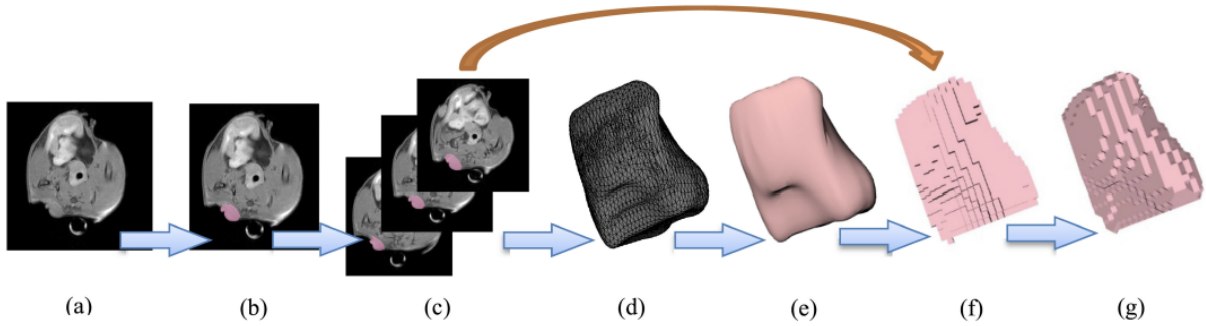

Figure 3.16: Example

The heat transfer equation for a 3D domain (Eq. (3.11)) is discretized as described previously. Using the discretization method, Eq. (3.11) can be written as Eq. (3.12a). Where UA is calculated using Eq. (3.12b) if the neighboring cell is tissue, and Eq. (3.12c) if the neighboring cell is air, respectively.

$$\nabla^2(k_t T) + \dot{q} = 0 \tag{3.11}$$

$$\sum_{i=1}^{n}(UA)_i(T_i - T_0) + \dot{q}\Delta V = 0 \tag{3.12a}$$

$$\frac{1}{(UA)_i} = \frac{1}{A_i}\left(\frac{\Delta s}{2k_i} + \frac{\Delta s}{2k_0}\right) \tag{3.12b}$$

$$\frac{1}{(UA)_i} = \frac{1}{A_i}\left(\frac{1}{h} + \frac{\Delta s}{2k_0}\right) \tag{3.12c}$$

The variable n represents the total number of sides of the mesh element. The value of n is 6 for a voxel (hexahedral mesh element) and 4 for a tetrahedron. The values taken by i

from 1 to n represent different directions to the mesh element and 0 is reserved for the mesh element under consideration. Thus, for a voxel mesh, 1 to 6 represent north, south, east, west, front, and back, while tetrahedron 1 to 4 represent the neighboring tetrahedra to its four sides. The term Δs is a generic representation of voxel dimensions, Δx, Δy, and Δz in the x, y, and z directions respectively. A represents the cross-sectional area of the side under consideration.

3.3.1 Benchmarking with Sphere

Benchmarking the heat transfer simulation is first completed by considering a spherical tissue domain since an analytical solution for a sphere is readily available. To study the effect of voxel representation and tetrahedral smoothing, the steady-state surface temperature is calculated and compared with the exact analytical solution. When using the removal technique for smoothing described previously, material is "lost". Thus, it is important to find a balance between the loss of material and accurate surface representation. The difference in the volume resulting from material loss will influence total heat generated, which will affect surface temperature. To handle the volume error introduced due to the removal method and its effect on domain temperature, an equation to determine the allowable tolerance in volume is derived from Newton's law of convection heat transfer. The convection heat-transfer in a domain with heat generation is shown in Eq. (3.13)).

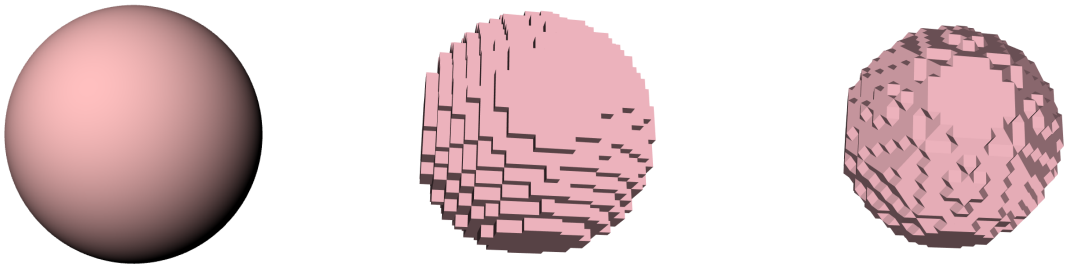

(a) Reference sphere (b) Voxel sphere (c) Tetra sphere

Figure 3.17: Sphere

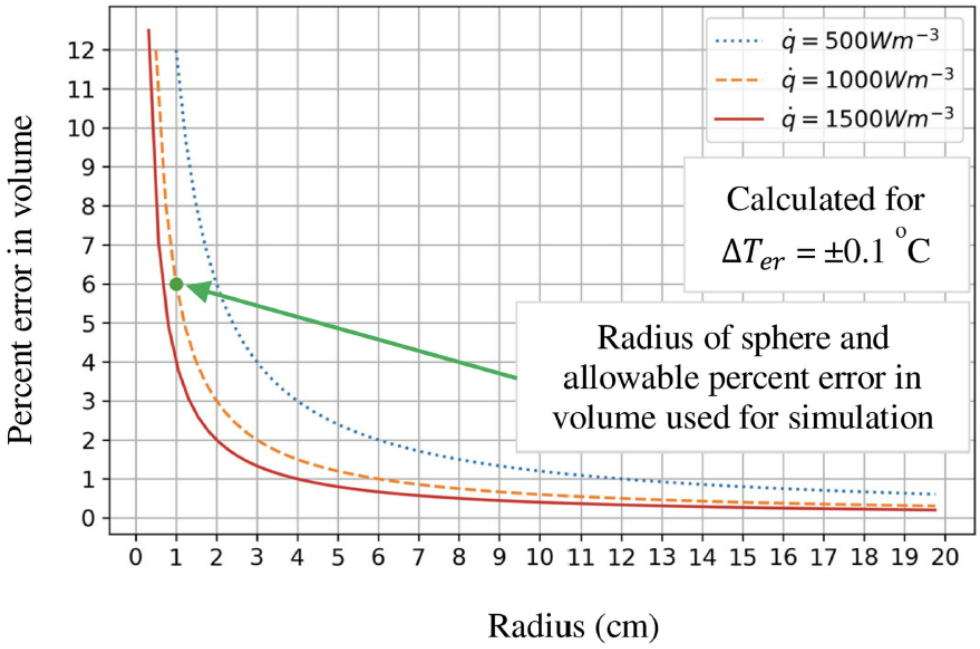

Figure 3.18: Allowable percentage volume error

$$\dot{q}V = hA_s(T_s - T_{amb}) \tag{3.13}$$

Rearranging Eq. (3.13) and dividing by the reference volume V results in an equation that can be used to determine the volume tolerance, which is given in Eq. (3.14)

$$\frac{\Delta V}{V} = \left(\Delta T_{er} \frac{h}{\dot{q}} \frac{A_s}{V}\right) \tag{3.14}$$

In Eq. (3.14), ΔT_{er} is the allowable temperature variation due to error in the volume ΔV for the same surface area. Smaller voxel resolution is needed for a smaller value of ΔT_{er}, which results in an increase in mesh elements and higher computational memory. Thus, an optimum value of acceptable ΔT_{er} is needed based on the available computational resources and domain size. This optimum value for the present study was considered as $\pm 0.1\,^{\circ}\mathrm{C}$. Using this value, the allowable error in the volume ΔV is calculated. In other words, for

the same surface area, the difference in volume should be within ΔV so that the variation of surface temperature due to volume difference would not be more than $\pm 0.1\,^{\circ}\mathrm{C}$. This allowable percent error in volume against the radius of sphere for different heat generation rates is shown in Fig. 3.18. Here, a convective heat transfer coefficient of $2\,\mathrm{W\,m^{-2}\,K^{-1}}$ was used. The plot shows for a given heat transfer rate, the allowable error in volume decreases as the size of the domain under consideration increases. In this case, as the radius of the sphere increases, the allowable tolerance in volume error decreases.

Using Eq. (3.14), the acceptable error in volume for a sphere with a radius of 1 cm and a heat-generation rate of $1000\,\mathrm{W\,m^{-3}}$ is 6 %. Given that volume tolerance is inversely proportional to the heat generation rate and size of the domain, as radius increases the volume tolerance decreases for a given heat generation rate. Thus, for a heat generation rate of $1000\,\mathrm{W\,m^{-3}}$ and 10 cm radius sphere, which is an average size of the human head when approximated as a sphere, the allowable volume error is 0.6 %. For research purpose, a sphere of 1 cm radius with thermal conductivity of $0.3\,\mathrm{W\,m^{-1}\,K^{-1}}$ was considered with a heat generation rate of $1000\,\mathrm{W\,m^{-3}}$, exposed to air at $20\,^{\circ}\mathrm{C}$, assuming a convective heat transfer coefficient $2\,\mathrm{W\,m^{-2}\,K^{-1}}$. This is shown in Fig. 3.18 as a green dot at radius 1 cm and 6 % volume error. The voxel size for the simulation used was 0.8 mm.

Heat Transfer Application With Medical Imaging Data

Once the code was benchmarked, heat transfer simulations for four different tumors generated from MRI scans were conducted. The MRI scans showed that these tumors were anatomically present at a subcutaneous level. A medical probe was seen in the MRI scans closer to the tumor with a small air gap between the mouse and the probe. For the simulation, the tumors were considered to be deep, meaning that they are surrounded on all sides with healthy tissue for simplicity. The resolution of the MRI scans resulted in an elongated, pin-like voxel with its length in the z-axis that represents slice thickness. To smooth the tumor, the geometry was re-voxelized to have a cuboidal voxel with dimensions of voxel the same in all three axes. The simulation on the tumors was performed for a voxel size of 0.12 mm x 0.12 mm

x 0.12 mm. This was done to maintain the dimension of the voxel similar to the x-axis and y-axis resolutions of the MRI scans. These tumors are shown in Fig. 3.19. Figs. 3.20 and 3.21 show the tumors in voxelized mesh and after the application of structured cleaving method, respectively.

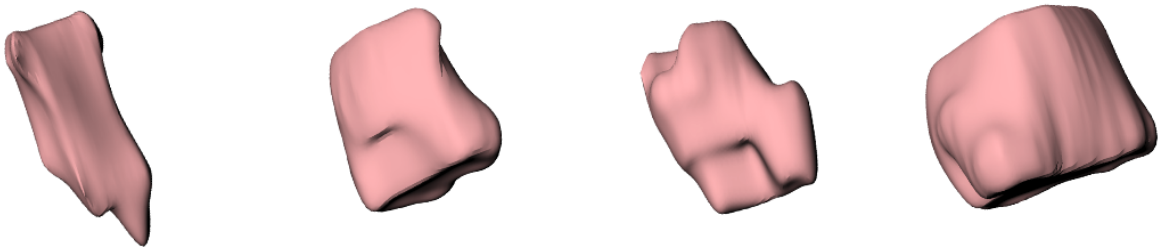

(a) Tumor 1 (b) Tumor 2 (c) Tumor 3 (d) Tumor 4

Figure 3.19: NURBS tumors

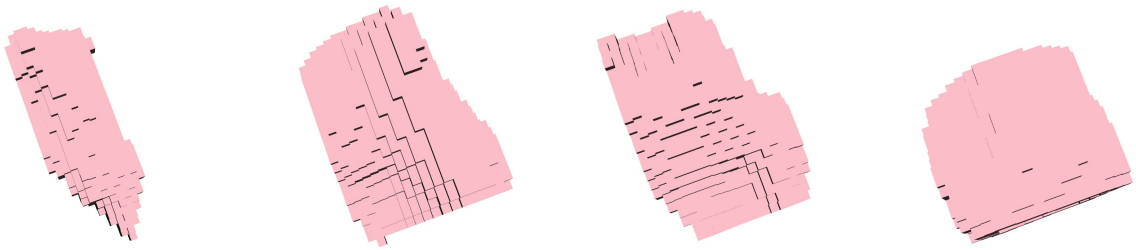

(a) Tumor 1 (b) Tumor 2 (c) Tumor 3 (d) Tumor 4

Figure 3.20: Voxel tumors

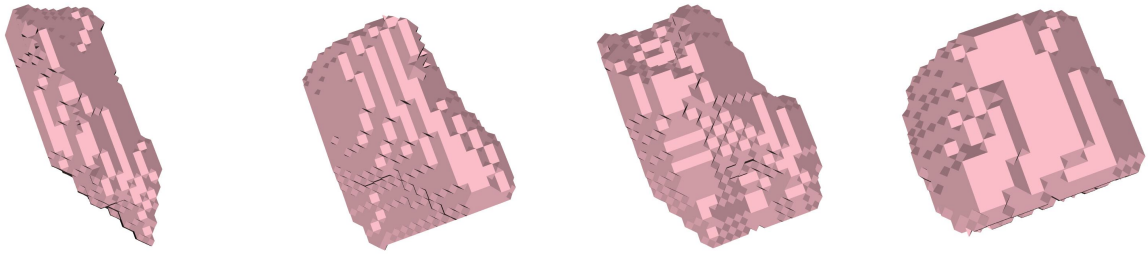

(a) Tumor 1 (b) Tumor 2 (c) Tumor 3 (d) Tumor 4

Figure 3.21: Tetrahedralized smoothed tumors

For the tumor, the metabolic heat-rate generation was considered to be $1.2\,\mathrm{mW\,mm^{-3}}$ based on the metabolic heat-production rate proposed by F. J. Gonzalez[133] for breast tumors using a non-invasive method and numerical simulation for humans. For the surrounding tissue, the metabolic heat-rate generation was considered as $0.001\,\mathrm{mW\,mm^{-3}}$ based on values obtained from the IT'IS Foundation database for muscle tissues[130]. The thermal conductivity for the tumor and surrounding tissue was considered to be $0.5\,\mathrm{mW\,mm^{-1}\,{}^{\circ}C^{-1}}$, representative of tissue[130]. A Dirichlet boundary condition of $30\,^{\circ}\mathrm{C}$ was imposed on the edge of the simulation domain in all directions.

Table 3.3: Parameters used for energy simulation of 3D tumors

Parameter	Symbols	Value	Units
Voxel size		0.12	mm
Thermal Conductivity[130]	k_t	0.5	$\mathrm{mW\,mm^{-1}\,{}^{\circ}C^{-1}}$
Tumor Metabolic heat gen. rate[133]	$\dot{q}_{m,tumor}$	1.2	$\mathrm{mW\,mm^{-3}}$
Healthy Tissue Metabolic heat gen. rate[130]	$\dot{q}_m$	0.001	$\mathrm{mW\,mm^{-3}}$
Ambient tissue temperature	T_∞	30	$^{\circ}\mathrm{C}$

3.3.2 Results and Analysis

A sphere represents the worst possible overestimate of surface area in 3D for a convex shape when voxelized. The voxel mesh overestimates surface area by 50 %, and the overestimate is reduced to around 16 % using the structured tetrahedral smoothing method proposed in this work. For the 2D circle (analogous to an infinite cylinder) the surface area overestimate dropped from 20 % to 4 % using the smoothing methodology. It is expected that other objects would demonstrate surface area overestimates between the cylinder and sphere. This is observed when investigating surface areas for the four tumors in Fig. 3.22.c and Fig. 3.22.d. Each of the tumors surface-area ratios show a steady drop from an average of 42.5 % to 15 %, roughly bounded by the overestimations for the cylinder and sphere.

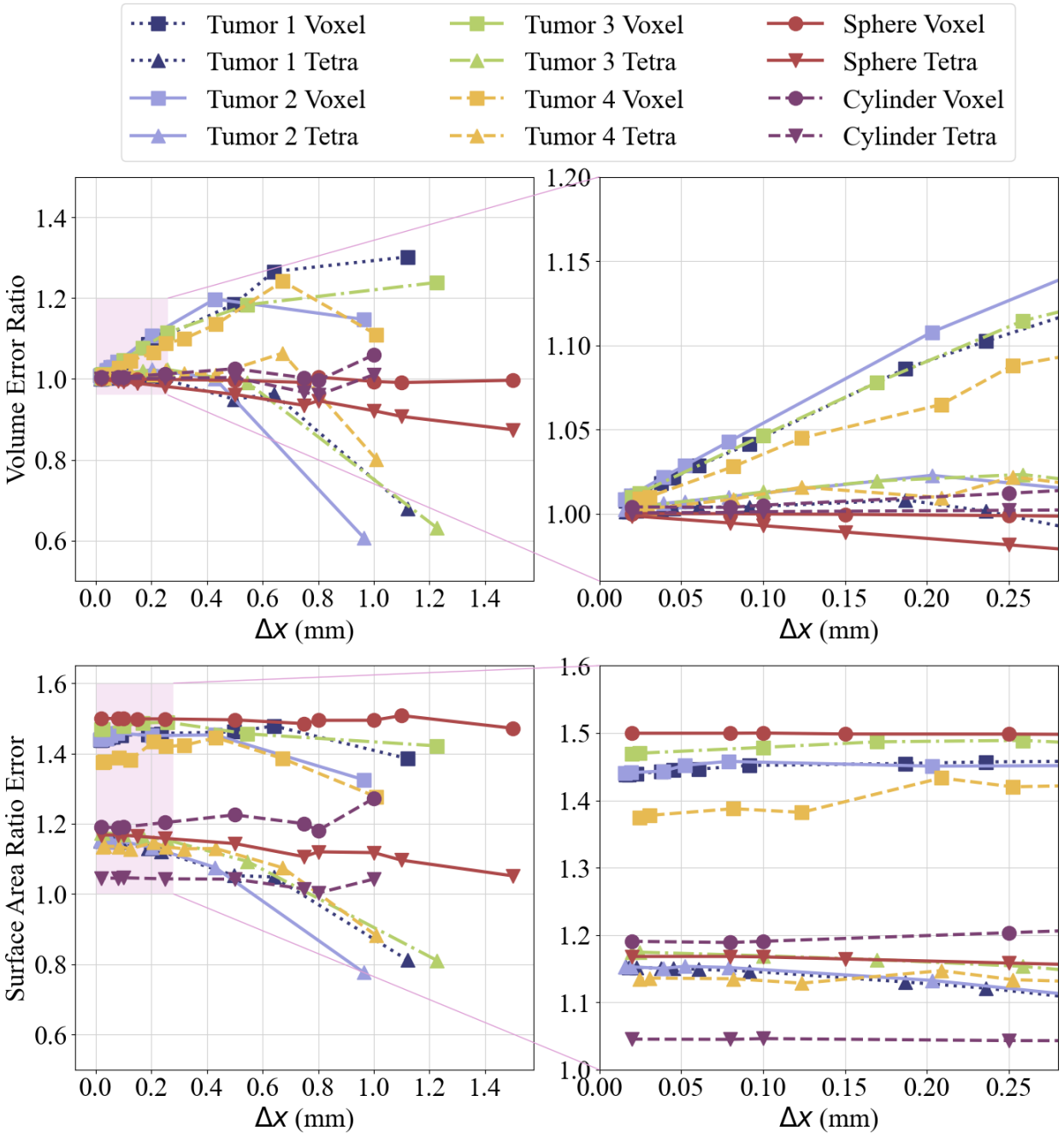

Figure 3.22: Convergence of volume and surface area

The effect of surface area overestimation for heat transfer simulation is shown with the example of a sphere. Fig. 3.23 shows the radial temperature plot for the sphere. The voxel mesh, having the highest overestimation of surface area, results in the most heat loss from the sphere and the lowest surface temperature. The tetrahedral smoothed domain reduces

this error by around 50 %. For the voxel sphere, the surface area is overestimated by about 50 %, and the temperature error obtained is 0.55 °C. This surface error is reduced to around 16 %, and the temperature error is 0.25 °C. Since the smoothing method does not affect a flat boundary or surface, no change would be observed in the area on two ends of a finite cylinder.

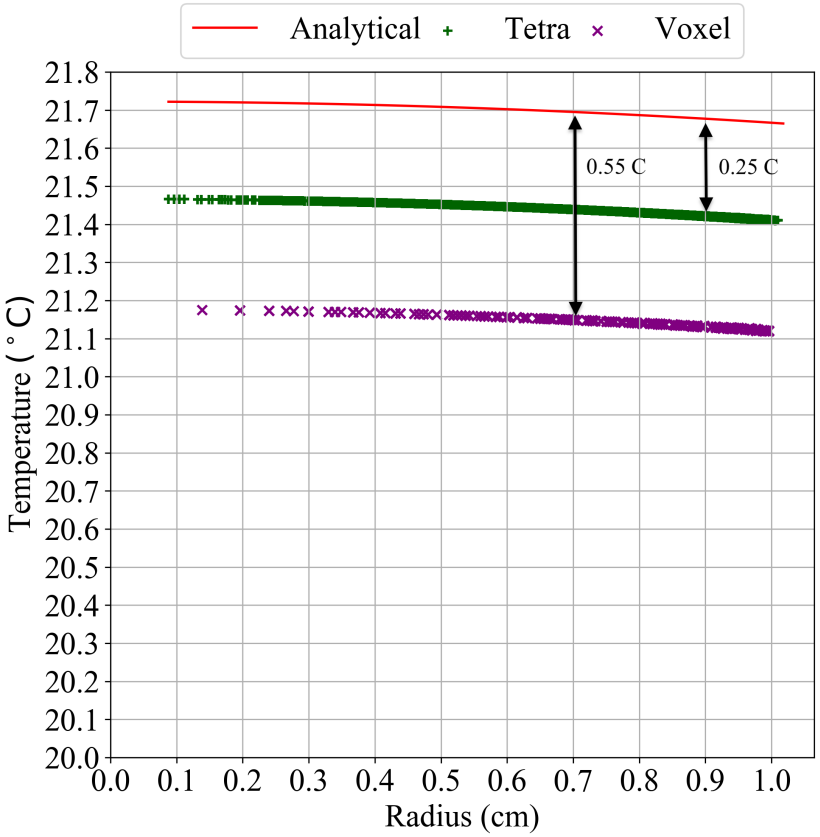

Figure 3.23: Radial temperature distribution in a sphere

The heat transfer simulation results for tumor 1 are shown in Fig. 3.24, which shows a comparison of the temperature map of a voxel and tetrahedral smoothed tumor at a cross-section taken at the midpoint of the z-axial length. Referencing Fig. 3.22, the volume of the voxel domain is more than the NURBS reference for the tumors due to the resolution of the MRI scan. A finer resolution would result in better volume convergence of the voxelized mesh to the actual domain. As the voxel resolution increases, the amount of volume lost during the removal method decreases, and the volume difference becomes negligible.

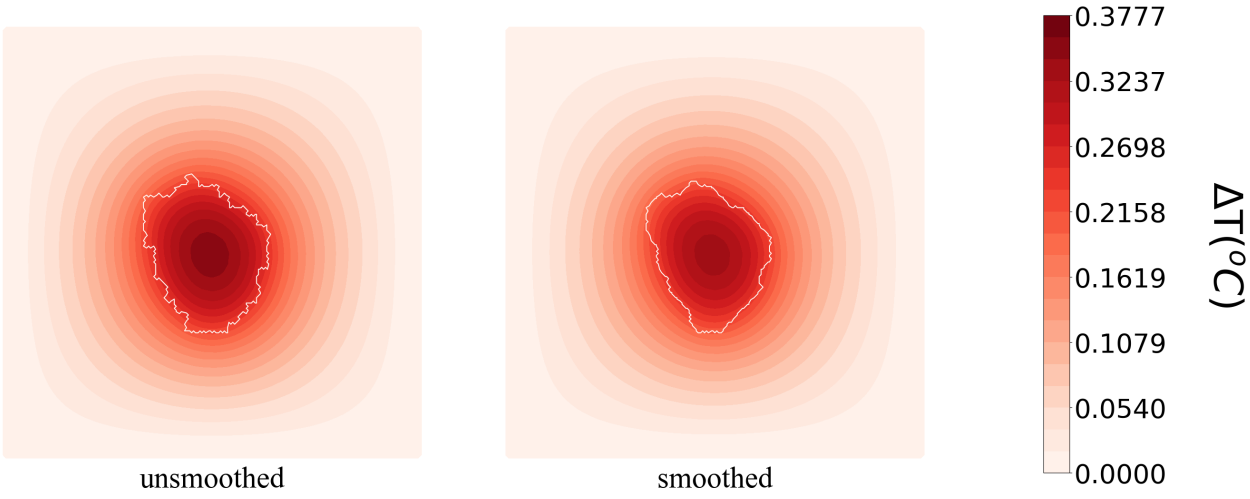

Figure 3.24: Cross-section of tumor 1 in x-y plane at the midpoint of z-axial length

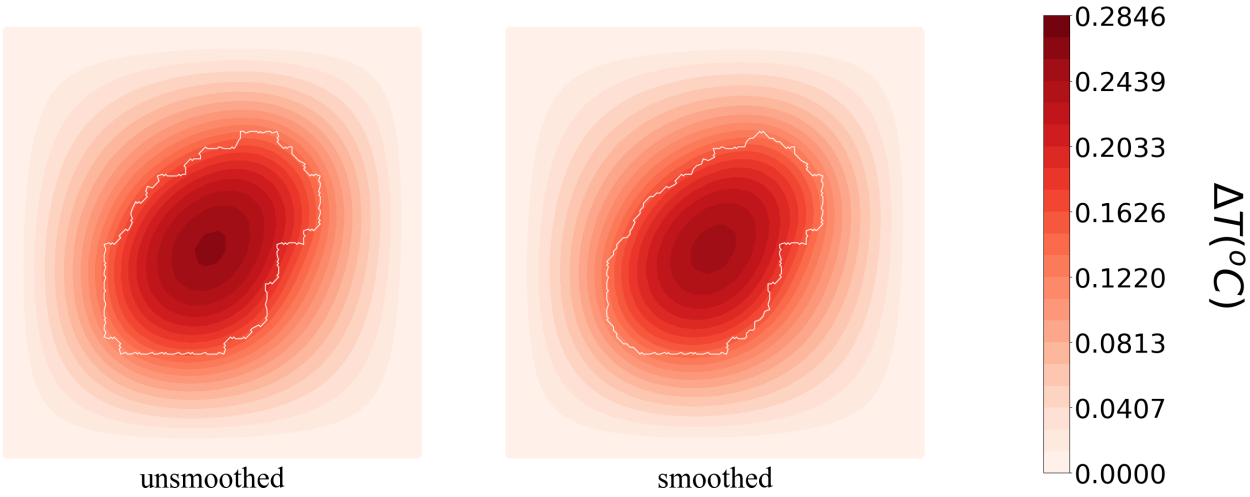

Figure 3.25: Cross-section of tumor 2 in x-y plane at the midpoint of z-axial length

At the voxel resolution used for the tumor simulations, there is a 4 % reduction in the volume of the tumors after the application of the removal method. Since the voxel tumor volumes were already greater than the reference NURBS tumor volumes, the reduction in volume results in a better accuracy of volume and surface area with respect to NURBS tumors. The voxelized tumors thus show a higher core temperature than the corresponding smoothed tumor due to the volume difference. This difference in maximum temperatures for all four tumors is within 0.5 °C for the simulations conducted. The thermal maps for the remaining three tumors studied are shown in Fig. 3.25, Fig. 3.26 and Fig. 3.27. These three tumors show a similar temperature profile to that observed in Fig. 3.24. As stated previously,

when voxel dimensions are decreased further, this difference in volume becomes negligible and only changes in surface area are observed. Execution of the smoothing method and heat transfer simulation for the tumors was used to demonstrate the applicability of the proposed methodology on a domain directly generated from MRI data. Thus, it can be applied to any animal or human using medical imaging data of the subject.

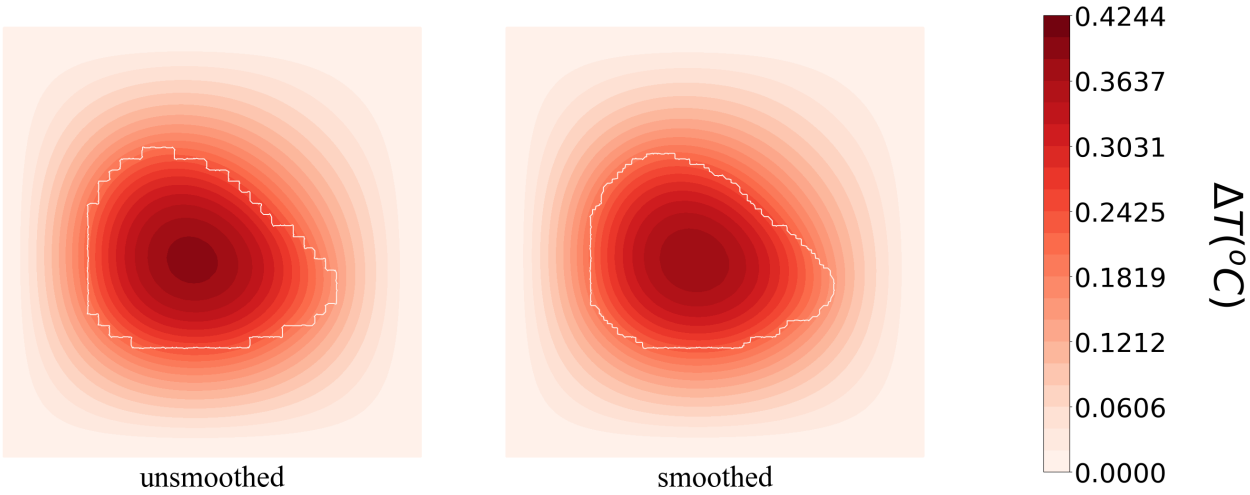

Figure 3.26: Cross-section of tumor 3 in x-y plane at the midpoint of z-axial length

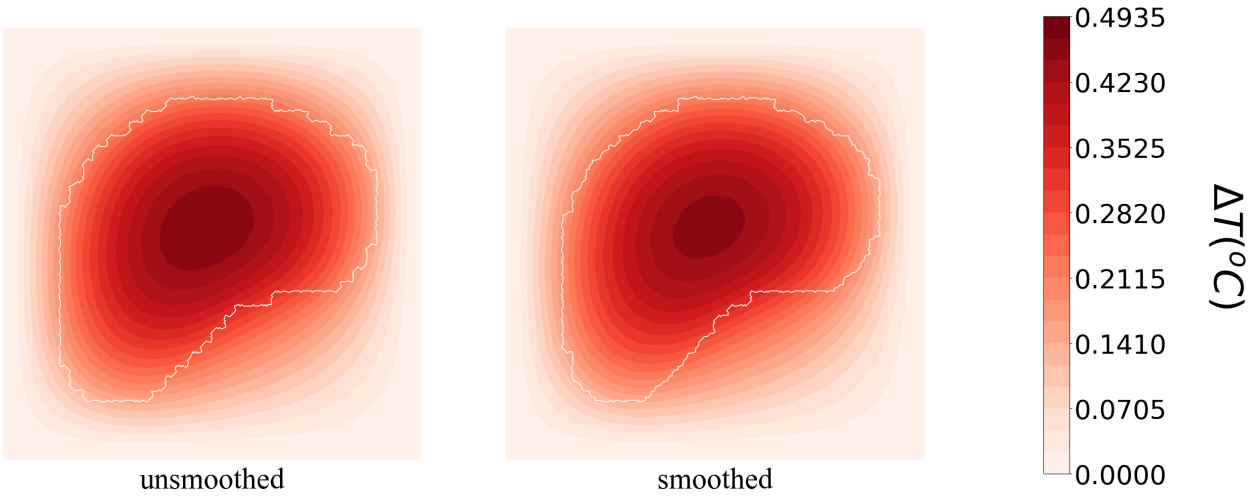

Figure 3.27: Cross-section of tumor 4 in x-y plane at the midpoint of z-axial length

To maintain the simplicity of this study, the perfusion rate of the blood flow was taken as zero, and other than metabolic generation of heat, no additional heat source is acting on the domain. In the Pennes BHE (Eq. (2.1)), the blood perfusion term (ω_{pennes}) is specified per

unit volume. The addition or removal method described earlier has been shown to change the volume of the domain (Fig. 3.22). The acceptable volume error for this simulation was considered without blood perfusion. This analysis of acceptable volume error needs to be conducted before simulating blood perfusion using the addition or removal method of smoothing.

As discussed in the previous chapter (2.1), skin temperature and core temperature act as input signals to the hypothalamus. Accuracy in these values is important when simulating the human thermoregulatory mechanism. Surface area error results in reduced accuracy for skin and core temperatures. Reduction of surface area error from 50 % to 16 % for the sphere and 42.5 % to 15 % for tumors is significant, but requires more work for to reduce the error further. The surface area error is much smaller when modeling the domain with a polygon mesh or unstructured mesh, since the techniques, such as lattice cleaving[83], can be used to represent curvature with greater accuracy. However, these techniques present other challenges in terms of modeling bioheat transfer, especially for the entire human body. Since the goal is to extend this work to such a domain, a direct technique to generate models from medical imaging data and maintain approximate representation is important. In a simple case such as the sphere, the actual surface area is known and thus surface area error due to voxel representation can be calculated. When the domain is generated from medical imaging data, actual surface area and volume are not known. The proposed methodology can be used to represent an individual's organ of any shape, or an entire human body, and perform heat transfer simulations with better surface area accuracy than can be achieved with voxels.

The structured cleaving method is not the most efficient method, as it divides a single voxel in 24 tetrahedrons. The mesh size increases by 24 times and still has an error in surface area of around 15 %. This increase in mesh size results in an increased computational time and memory resource requirements. This can be avoided by modifying the structured cleaving method.

One solution to avoid the increase in mesh density would be to calculate the area correction parameter for each voxel at an interface that needs correction rather than dividing the voxel in 24 tetrahedrons. This can be achieved by developing an algorithm that uses a

surface normal vector to calculate error rectification. Newell's algorithm is used in the computational graphic research field to calculate the normal vector of irregular surfaces[134]. This algorithm can calculate the normal at each voxel, and then a correcting factor to smoothen the region can be determined. This will avoid dividing a voxel into 24 sub-tetrahedrons and reduce the computational requirements. Such a method will not be limited to the angle of voxel slicing and is expected to reduce the surface area error further.

Another solution would be to use the cut-cell method of mesh modification[135]. In the cut-cell method, only the voxels at the interface requiring modification are divided into sub-voxels using quadtree or octree methods. In a quadtree, a voxel is divided into four sub-voxels; in an octree, a voxel is divided into eight sub-voxels. Once the voxels at the interfaces are subdivided, the structured cleaving method can be implemented only at the interface. This would reduce the number of mesh elements compared to dividing the entire voxel mesh into 24 tetrahedrons.

3.4 Chapter Summary

Voxel meshes overestimate the surface area by 27 % in 2D and 50 % in 3D. This surface area error results in inaccuracies in heat transfer simulation. The rectification methods found in the literature rely on an unstructured tetrahedral mesh. To avoid losing the structured aspect of a voxel mesh to reduce the surface area error, a structured cleaving method was developed tested.

The structured cleaving method divides a pixel into four triangles and a voxel into 24 tetrahedrons. This new triangular mesh for 2D and tetrahedral mesh for 3D is treated with either of the two smoothing algorithms: the removal method or the addition method. After the application of the removal method, the surface area error was demonstrated to reduce from 27 % to 4 % for a 2D mesh of circle, and from 50 % to 16 % for a 3D mesh of a sphere, respectively. The structured cleaving method and the removal method, when applied on four mice tumors obtained from MRI scans, reduced the surface area error from 42.5 % to 15 %.

Chapter 4

VoM-PhyS Framework

The literature review on bioheat equations in Chapter 2 elaborated on the limitations of various bioheat models. Simulation of bioheat transfer is challenging, and a simulation framework adaptable to different tissue domains to verify various other models is required. This chapter describes the development of a novel Voxelized Multiphysics Simulation (VoM-PhyS) Framework.

The VoM-PhyS framework is developed using the existing multidimensional coupled blood flow method solver found in the literature. In this chapter, this existing blood flow solver is explained briefly. The development of the novel VoM-PhyS framework using the blood flow solver is demonstrated by coupling heat transfer with blood flow then used along with frog tongue data found in the literature to demonstrate the framework's ability to consider different bioheat transfer assumptions.

4.1 Existing Blood Flow Model

Macro- and micro-scale blood flows are modeled in a coupled fashion for continuous blood flow. The macro-scale blood flow model employs the Hagen-Poiseuille equation in a 1D flow domain. The 3D micro-scale blood flow is modeled with the two-compartment model theory[104;136] and the Darcy equation for porous media.

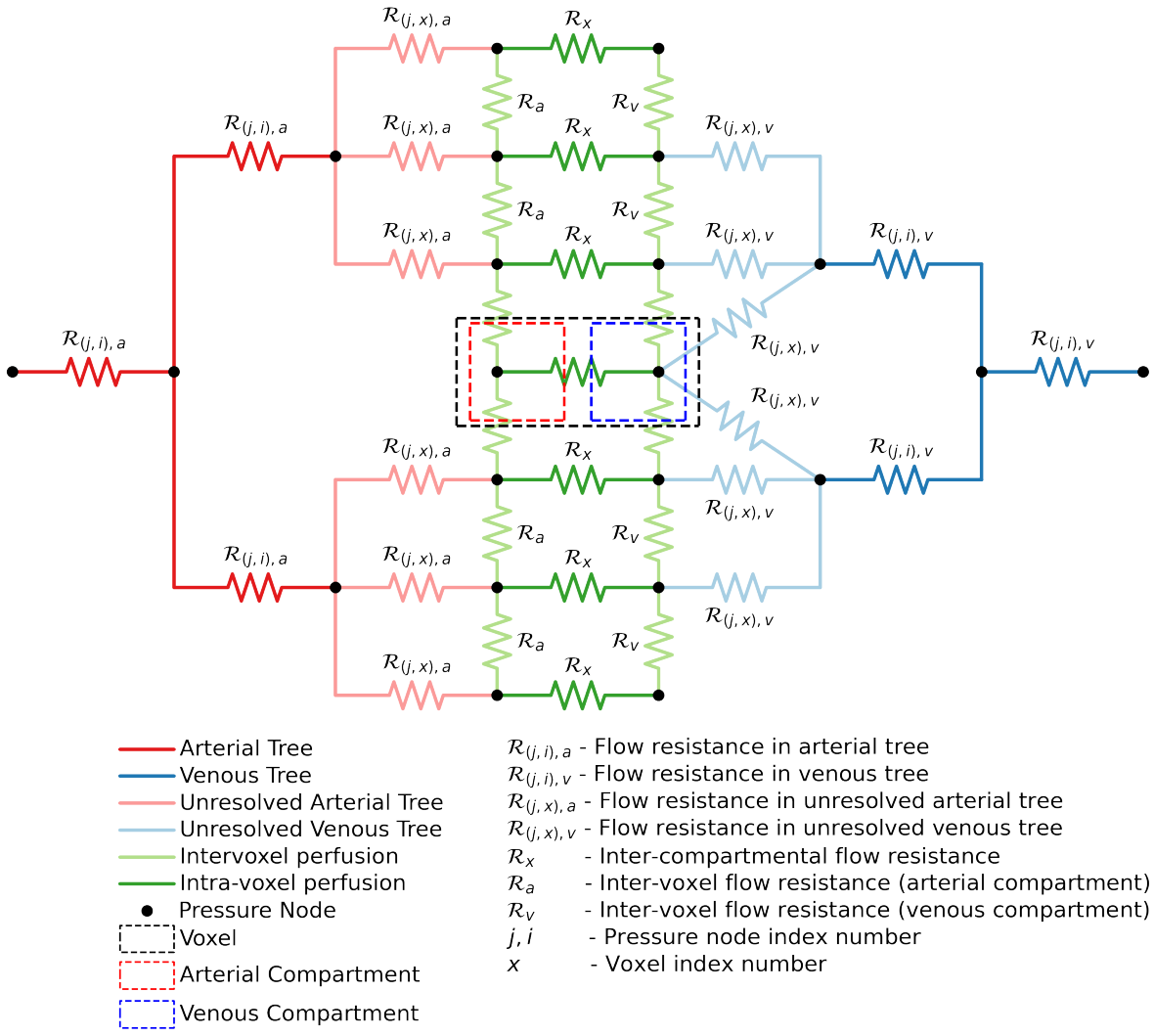

Figure 4.1: Resistance diagram of mixed-dimensional simulation framework

A resistance diagram of Hodneland's[101] mixed-dimensional blood flow framework is shown in Fig. 4.1 and a graphical representation is shown in Fig. 4.2. Blood vessels that can be recreated from imaging data are represented in red for arteries and blue for veins in Fig. 4.1 and Fig. 4.2. The flow resistance offered by each element of these blood vessels is represented by $\mathcal{R}_{ji}$ in Fig. 4.1. Blood vessels that cannot be segmented from imaging data are represented using dotted arrows in Fig. 4.2 and the flow resistance offered by them is shown using pink and light blue resistances in Fig. 4.1. The capillary bed and tissue are modelled as a two-compartment porous domain shown in Fig. 4.2. The inter-voxel permeability between

arterial and venous compartment is represented using light green arrows in Fig. 4.2 and the respective flow resistance using light green resistances in Fig. 4.1. Within the voxel, the arterial to venous compartment perfusion is represented using dark green arrow in Fig. 4.2, and the respective flow resistance using dark green resistor in Fig. 4.1.

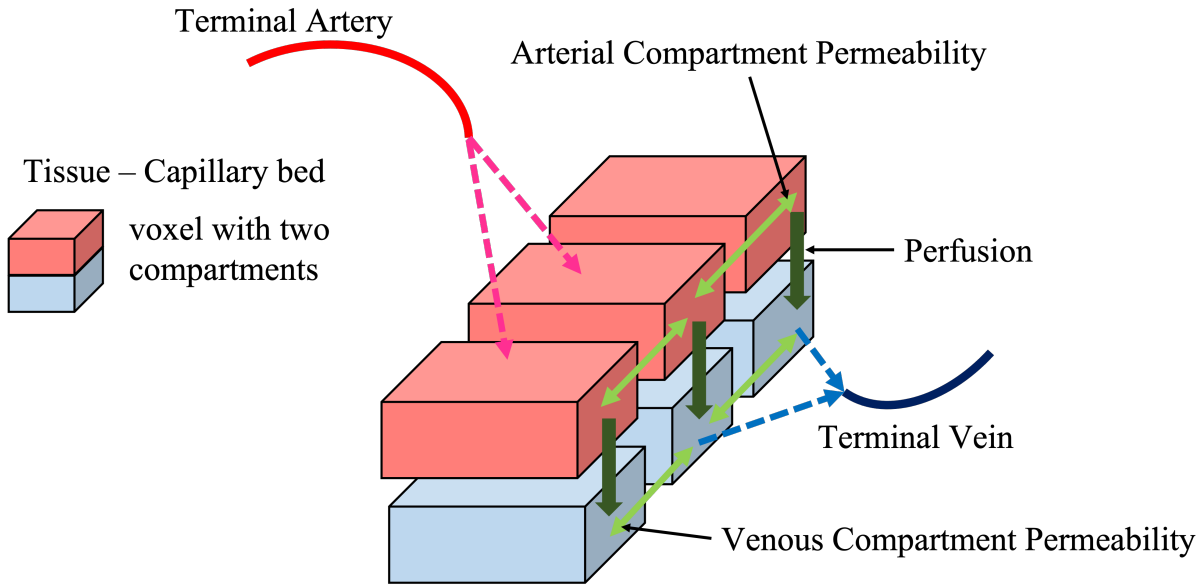

Figure 4.2: Graphical illustration of mixed-dimensional simulation framework

The segmented blood vessels were modelled as a 1D pipe network using the Hagen-Poiseuille equation (Eq. (4.1)). The blood was assumed to be laminar, at steady state, and the pulsatile behavior of blood was ignored.

$$q_{v,ji} = \kappa_{\mathrm{ji}} \Delta p_{ji} \tag{4.1}$$

where

$$\mathcal{R}_{ji}{}^{-1} = \kappa_{\mathrm{ji}} = \frac{\pi R_{ji}^4}{8 \mu L_{ji}} \tag{4.1a}$$

$$\Delta p_{ji} = p_j - p_i \tag{4.1b}$$

In Eq. (4.1), the flow conductivity offered by a blood vessel element is represented as

κ_{ji}, the net flow from an element is given by $q_{v,ji}$, and the radius and length of the specific element are represented by R and L, respectively. The nodes represented by j and i are the locations for which pressure is calculated and are represented as black dots (pressure nodes) in Fig. 4.1. The pressure drop parameter (γ_β) is used to calculate effective resistance ($\mathcal{R}_{(j,x),\beta}$) in the unresolved network extending from the resolvable blood vessels to tissue voxels[101].

The 3D voxel domain consists of tissue and a capillary bed. Each voxel has two compartments: one representing the arterial capillary bed and tissue (referred to as arterial compartment), and the other representing the venous capillary bed and tissue (referred to as venous compartment). Darcy's equation (Eq. (4.2)) provides the relationship between mass flux u and pressure drop across the porous domain.

$$u = -\frac{\mathrm{K}}{\mu}\nabla P \tag{4.2}$$

The viscosity μ is considered constant and K represents the permeability of the porous domain. The cross-voxel flow resistance ($\mathcal{R}_a, \mathcal{R}_v$), shown using the light green resistance network in Fig. 4.1, controls the distribution of blood across neighboring voxels. The subscripts a and v denote the arterial and venous compartment properties, respectively. The estimation of tissue permeability (K_a, K_v) was obtained from literature.[137].

Perfusion between the arterial compartment and the venous compartment represents the transition of blood from oxygenated to deoxygenated state. This perfusion is driven by the pressure difference and perfusion proportionality factor α as shown in Eq. (4.3).

$$u_{perf} = \alpha(P_a - P_v) \tag{4.3}$$

The perfusion parameter α controls the resistance offered to the flow between the compartments in a voxel of volume V.

The mass conservation equation for an incompressible fluid at steady state and constant density (Eq. (4.4)), when applied to a porous domain with two compartments, results in Eqs. (4.5a) and (4.5b).

$$\nabla \cdot u = \mathcal{G} \tag{4.4}$$

$$-\nabla \left(\frac{\mathrm{K}_a}{\mu} \nabla P_a \right) = -\alpha (P_a - P_v) + \sum_{i \in N_{a,j}^T} \mathcal{G}_{a,i} \tag{4.5a}$$

$$-\nabla \left(\frac{\mathrm{K}_v}{\mu} \nabla P_v \right) = \alpha (P_a - P_v) - \sum_{i \in N_{v,j}^T} \mathcal{G}_{v,i} \tag{4.5b}$$

In the arterial compartment, the oxygenated blood enters from the arteries and is represented as a mass source term $\mathcal{G}_a$. Similarly, in the venous compartment, the deoxygenated blood leaves the tissue and enters the veins. This is represented by a sink term $\mathcal{G}_v$ in the venous compartment. $\mathcal{G}_{a,i}$ represents the mass flow rate of blood arriving at the arterial compartment from an i-th arterial terminal. A voxel can receive blood from multiple arterial terminals ($N_{a,j}^T$). Similarly, $\mathcal{G}_{v,i}$ represents the mass flow rate of blood leaving the tissue to i-th venous vessels. A voxel can exchange blood with multiple venous terminals ($N_{v,j}^T$). The amount of blood flow exchange ($\mathcal{G}_{a,i}$, $\mathcal{G}_{v,i}$) that occurs between a tissue voxel and a blood vessel is determined using a Dirac function (Eq. (4.6a)).

$$\mathcal{G}^\epsilon(x) = \int_\Omega \mathcal{G}(y) \eta^\epsilon (x - y) ds \tag{4.6a}$$

$$\eta^{\epsilon}(x) = \frac{1}{\epsilon^n}\eta\left(\frac{x}{\epsilon}\right) \tag{4.6b}$$

$$\eta(x) = \begin{cases} C\exp\left(\frac{1}{|x|^2-1}\right), & \text{if } |x| < 1 \\ 0, & \text{if } |x| \geq 1 \end{cases} \tag{4.6c}$$

$$\int_{\Omega} \eta^{\epsilon}(x)dx = 0 \tag{4.6d}$$

Eq. (4.6a) is a distribution function of flow between the terminal points of the arterial or venous tree and the voxels in the neighborhood of the terminal. The distribution function is applied over the computational domain Ω. $Q(y)$ represents the flow in the terminal arterial and venous elements. Considering an arterial tree, $\mathcal{G}(y)$ represents flow in the terminal arterial element, and a voxel at location x receives $\mathcal{G}^{\epsilon}(x)$ amount of flow from the respective terminal arterial element. The amount of flow that a voxel receives from a specific arterial element depends on the distance between the voxel and the respective arterial terminal. For this work, the blood flow distrubution from a blood vessel terminal was considered to be normal distribution. This normal distribution given by the function $\eta^{\epsilon}(x)$ depends on the characteristic radius ϵ and constant C. The superscript n in Eq. (4.6b) is the number of dimensions of simulation domain. The characteristic radius, ϵ, is the radius of the sphere of influence (SoI). Any voxel that falls within the SoI of a terminal vessel, exchanges blood with that respective vessel. The value of constant C depends on characteristic radii and is calculated using Eq. (4.6d). Eq. (4.6d) conserves the mass in the virtual unresolved blood vessels. The finite volume two-point flux approximation (TPFA)[138] provides the discretized flow equation for the voxel domain given in Eq. (4.7) and Eq. (4.8) for the arterial and venous compartments, respectively[101].

$$\sum_{j\in N}\tau_{ij}(P_{a,i}-P_{a,j})+\alpha_i(P_{a,i}-P_{v,i})V_i- \sum_{k\in N^T_{a,i}} q_{a,k}\eta^{\epsilon}_{a,k}(x_i-x_k)V_i=0 \tag{4.7}$$

where

$$q_{a,k}=\kappa_{a,jk}(p_{a,j}-p_{a,k}) \qquad j\in\mathcal{N}(N^T_{a,k})$$

and

$$\sum_{j\in N}\tau_{ij}(P_{v,i}-P_{v,j})-\alpha_i(P_{a,i}-P_{v,i})V_i- \sum_{k\in N^T_{v}} q_{v,k}\eta^{\epsilon}_{v,k}(x_i-x_k)V_i=0 \tag{4.8}$$

where

$$q_{v,k}=\kappa_{v,jk}(p_{v,j}-p_{v,k}) \qquad j\in\mathcal{N}(N^T_{v,k})$$

In Eq. (4.7) and Eq. (4.8), N represents the number of neighboring voxels exchanging blood with voxel i and, N^T_a and N^T_v represent the set of terminal arterial and venous nodes exchanging blood with voxels, respectively. $\mathcal{N}$ represents the nodes that are neighboring the k-th blood vessel element. The sub-script j represents the node of a terminal blood vessel element, which is connected to node k. The last equation to complete the system is the pressure continuity equation (Eq. (4.9)).

$$q_{\beta,k}=\frac{\gamma_\beta}{\mu}(p_{\beta,k}-\sum_{j\in N^V_{\beta,k}}(\eta^{\epsilon}_{\beta,k}(x_j-x_k)P_{\beta,j}V_j) \qquad k\in N^T_\beta \tag{4.9}$$

$$\beta = \begin{cases} a : \text{artery} \\ v : \text{vein} \end{cases}$$

Eq. (4.9) represents the pressure continuity across the virtual blood vessels which are modeled using Eq. (4.6a). N_β^T represents all the terminal blood vessels and $N_{\beta,k}^V$ represents the set of tissue voxels that fall within the SoI of vessel terminal k.

Eqs. (4.1), (4.7), (4.8), and (4.9) provide a set of equations that can be solved to calculate pressure at each pressure node when applied to blood vessel elements and arterial and venous compartments of voxels. A more detailed description and derivation of these equations can be found in literature[101;138;139]. A detailed description of matrix generation using these equations is presented below.

4.1.1 Blood Flow Matrix Generation

Rearranging the mass balance equations (Eq. (4.7) and Eq. (4.8)) results in Eqs. (4.10) and (4.11) for blood flow in arterial and venous compartments of tissue voxels, respectively.

$$\begin{aligned} &\left[\sum_{j\in N} \tau_{ij} + \alpha_i V_i\right](P_{a,i}) - \sum_{j\in N} t_{ij}(P_{a,j}) - \alpha_i(P_{v,i})V_i \\ &- \sum_{\substack{j\in\mathcal{N}(N_{a,k}) \\ k\in N_a^T}} \kappa_{a,jk}\eta_{a,k}^{\epsilon}(x_i - x_k)V_i(p_{a,j}) - \sum_{\substack{j\in\mathcal{N}(N_{a,k}) \\ k\in N_a^T}} \kappa_{a,jk}\eta_{a,k}^{\epsilon}(x_i - x_k)V_i(p_{a,k}) = 0 \end{aligned} \tag{4.10}$$

$$\begin{aligned} &\left[\sum_{j\in N} \tau_{ij} + \alpha_i V_i\right](P_{v,i}) - \sum_{j\in N} t_{ij}(P_{v,j}) - \alpha_i(P_{a,i})V_i \\ &- \sum_{\substack{j\in\mathcal{N}(N_{v,k}) \\ k\in N_v^T}} \kappa_{v,jk}\eta_{v,k}^{\epsilon}(x_i - x_k)V_i(p_{v,j}) - \sum_{\substack{j\in\mathcal{N}(N_{v,k}) \\ k\in N_v^T}} \kappa_{v,jk}\eta_{v,k}^{\epsilon}(x_i - x_k)V_i(p_{v,k}) = 0 \end{aligned} \tag{4.11}$$

Applying Eqs. (4.10) and (4.11) over all the tissue voxels, a sub-matrix of size $(2N_t) \times (2N_t + N_a + N_v)$ is generated, where N_t, N_a and N_v represent number of tissue voxels,

number of arterial nodes and number of venous nodes, respectively. The column matrix $b_{2N_t \times 1}$ is a zero matrix.

Applying the mass conservation equation to every intermediate node in the arterial and venous tree, a set of $N_a^I + N_v^I$ equations is generated using Eq. (4.12) and Eq. (4.13). The superscripts T, I and R represent terminal, intermediate and root nodes of blood vessel tree, respectively. The root nodes are the ones where the Dirichlet boundary condition is applied. Terminal nodes are the last vascular nodes within the tissue. The intermediate nodes are all the nodes between root and terminals.

$$\sum_{j \in \mathcal{N}(N_{a,k})} (\kappa_{a,jk}(p_{a,j} - p_{a,k})) = 0 \tag{4.12}$$

$$\sum_{j \in \mathcal{N}(N_{v,k})} (\kappa_{v,jk}(p_{a,j} - p_{a,k})) = 0 \tag{4.13}$$

For the number of terminals nodes (N_a^T, N_v^T), rearranging the pressure continuity Eq. (4.9) results in Eq. (4.14) and Eq. (4.15) for arterial and venous tree, respectively.

$$\kappa_{a,k} p_{a,j} - \left[\kappa_{a,k} + \frac{\gamma_a}{\mu}\right] p_{a,k} + \frac{\gamma_a}{\mu} \sum_{i \in \mathcal{N}(N_{a,k}^v)} \eta_{a,k}^{\epsilon}(x_i - x_k) V_i P_{a,i} = 0 \tag{4.14}$$

$$\kappa_{v,k} p_{v,j} - \left[\kappa_{v,k} + \frac{\gamma_v}{\mu}\right] p_{v,k} + \frac{\gamma_v}{\mu} \sum_{i \in \mathcal{N}(N_{v,k}^v)} \eta_{v,k}^{\epsilon}(x_i - x_k) V_i P_{v,i} = 0 \tag{4.15}$$

Eq. (4.16) and Eq. (4.17) represent the Dirichlet boundary condition for pressure applied at the root nodes of arterial and venous tree

$$p_{a,k} = P_{in} \qquad k \in N_a^R \tag{4.16}$$

$$p_{v,k} = P_{out} \qquad k \in N_v^R \tag{4.17}$$

For the matrix equation $\mathcal{A}_n x = b$, $n = 2N_t + N_a + N_v$ and column matrix x is as shown below.

$$x^T = [\ P_{a,1}\ P_{a,2}\ \ldots\ P_{a,N_t}\ P_{v,1}\ P_{v,2}\ \ldots\ P_{v,N_t}\ p_{a,1}\ p_{a,2}\ \ldots\ p_{a,N_a}\ p_{v,1}\ p_{v,2}\ \ldots\ p_{v,N_v}\ ]$$

$x[1 : N_t]$ - Pressure in arterial compartment of tissue voxels ($P_{a,i}$)

$x[N_t + 1 : 2N_t]$ - Pressure in venous compartments of tissue voxels ($P_{v,i}$)

$x[2N_t + 1 : 2N_t + N_a]$ - Pressure in arterial tree nodes ($p_{a,i}$)

$x[2N_t + N_a + 1 : 2N_t + N_a + N_v]$ - Pressure in venous tree nodes ($p_{v,i}$)

The coefficient matrix $\mathcal{A}$ is generated using Eqs. (4.10) to Eqs. (4.17) on respective mesh elements. Column matrix b consists of the pressure boundary condition applied at the arterial and venous nodes.

$$b[k] = \begin{cases} P_{in} & \text{if } k \in N_a^R \\ P_{out} & \text{if } k \in N_v^R \\ 0 & \text{if } k \notin (N_a^R, N_v^R) \end{cases}$$

Simulation

The flow matrix generated above was simulated using a Python[140] script on the Beocat High-Performance Computing (HPC) cluster at Kansas State University. The developed Python script can be found at VoM-PhyS.

4.2 Modeling Heat Transfer Coupled with Blood Flow

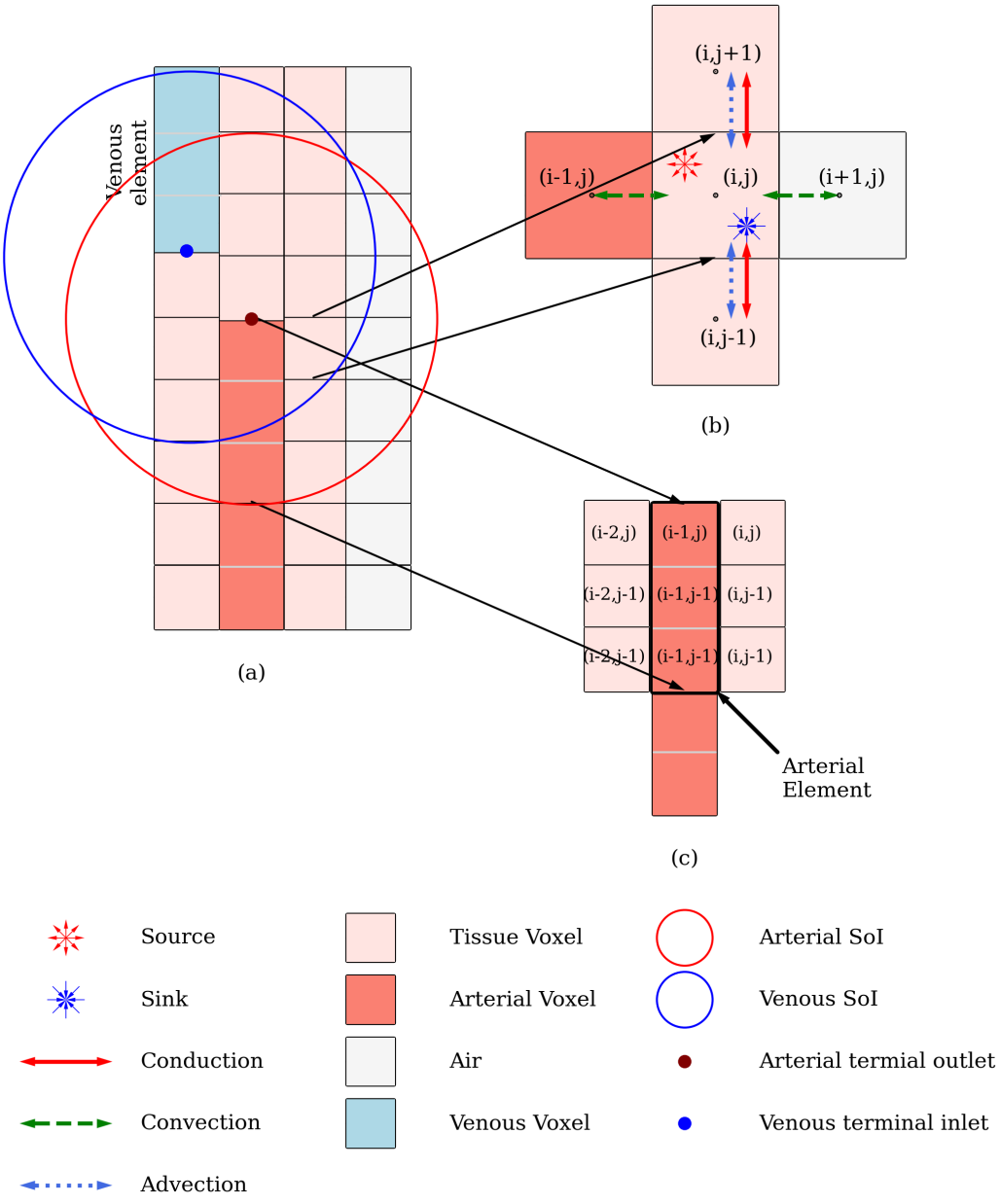

Figure 4.3: An illustrative description of the heat transfer model
(a) A small voxel domain representing artery, vein, and tissue, with SoI for an artery and vein (b) Zoomed in voxel (i, j) with its neighbor. (c) Multiscale mesh example for heat transfer between a blood vessel and tissue. The arterial element represented using a thick border consists of multiple arterial voxels.

Each voxel acts as a control volume (CV) exchanging heat with its surroundings. For flow simulation, the CV was defined as a compartment of the voxel. Thus, for flow simulation, each voxel contains two CVs, representing the arterial and venous compartments. The heat transfer simulation incorporates the Pennes bioheat model (PBM) assumption of instant thermal equilibrium once the blood enters the tissue voxel. Blood enters the tissue voxel in an arterial compartment and perfuses to venous compartment. An assumption of thermal equilibrium was made within a tissue voxel. Due to this assumption, the arterial compartment, the venous compartment, and blood within these compartments are at equal temperature, and blood perfusion occuring between the arterial and venous compartment has no effect on temperature. Hence, this perfusion was ignored for heat transfer analysis.

An illustration of the heat transfer model proposed in this study is shown in Fig. 4.3. Fig. 4.3.a shows a 2D voxel domain to represent an artery, vein, and tissue. For simplicity, only the terminal elements of arterial and venous tree are shown with the arterial terminal outlet and venous terminal inlets marked with dots. For a SoI of a given ϵ, the resultant 2D circles are shown in red for the arterial terminal and blue for the venous terminal, with their centers at the ends of the respective terminal elements. Fig. 4.3.b shows a zoomed in image of tissue voxel (i, j) with its four neighbors. The neighboring voxels $(i, j+1)$ and $(i, j-1)$ are tissues, voxel $(i-1, j)$ is part of the arterial terminal element, and $(i+1, j)$ is air.

If a tissue voxel falls within the SoI of any arterial terminal element, it receives blood from that element. In Fig 4.3.b, voxel (i, j) is one of the tissue voxels that falls within the SoI, and thus it receives a specific amount of blood from the respective arterial element. This source term of blood discussed in the previous section is shown in Fig 4.3.b for voxel (i, j). Similarly, if the tissue voxel falls within the SoI of a venous terminal element, a sink term that collects blood from the voxel and transports it to the venous terminal. This sink term is shown for voxel (i, j), as it falls in the SoI of a venous terminal element in Fig 4.3. The amount of blood flow related to a source or sink term depends on the distance of the voxel (i, j) from the arterial and venous terminal element, respectively, as calculated by Eq. (4.6a). If the voxel falls within the SoI of multiple arterial or venous terminal elements, multiple source and sink terms are applied to the voxel.

The blood flow model considers blood perfusion among tissue voxels. This perfusion of blood results in advection. In Fig 4.3.b, the inter-voxel perfusion and resulting advection among the tissue voxels is shown for $(i, j+1)$ and $(i, j-1)$ with (i, j). Blood cannot permeate through a blood vessel wall to a tissue, so there is no direct mass transfer between voxel $(i-1, j)$ and tissue voxel (i, j). This is one of foundational differences of VoM-PhyS with the VaPor model[73], in which blood perfusion occurs across the vessel walls. Heat is exchanged between a neighboring blood vessel and tissue via convection. Similarly, convective heat exchange takes place with the environment the boundary is exposed to as shown between (i, j) and $(i+1, j)$. The source term that appears in the tissue voxel brings blood from the respective arterial terminal element as shown in Fig 4.3. The mass source term that appears in an arterial compartment of voxel (Eq. (4.6a) and Eq. (4.7)) results in the addition of energy in the voxel due to advection. Each tissue voxel also has metabolic heat generation, represented by the term $\dot{q}_m$. Considering these possible heat exchanges across the CV and the thermal equilibrium of blood and tissue in a voxel, the problem is similar to a moving solid with heat generation. An energy equation for this problem is given in Eq. (1-36), (1-37), and (1-38) in Ozisik[141]. The combined form of these equations is Eq. (4.18)

$$\rho_t c_{p,t} \frac{\partial T_t}{\partial t} = \nabla(k_t \nabla T_t) - \rho c_{p,b} \nabla(T_t \vec{v}) + \dot{Q} \tag{4.18}$$

In Eq. (4.18), T_t represents the tissue temperature and V represents the voxel volume. Due to the assumption of thermal equilibrium between blood and tissue in a voxel, the temperature of blood in a voxel is the same as tissue temperature, T_t. Thermal conductivity and specific heat capacity of tissue are represented by k_t and $c_{p,t}$, respectively. The specific heat capacity of blood is represented by $c_{p,b}$ and the velocity of blood across voxels is represented by $\vec{v}$. Traditionally, the velocity vector $\vec{v}$ is assumed to be constant along the flow direction, as there is no mass source or sink term. However, in this framework, the CV consists of volumetric source and sink terms that need to be considered in the mass conservation and the resultant energy conservation. Here, blood is considered as the moving solid, and within

a tissue voxel, blood and tissue are at same temperature. The coupling of heat equations with flow equations occurs for blood flow, resulting in the addition of energy due to blood entering a tissue voxel via source terms. This is incorporated by using Eq. (4.19). The term $\dot{Q}$ in Eqs. (4.18) and (4.19) is a sum of metabolic heat generation rate ($\dot{q}_m$) and advection. Advection in Eq. (4.19) is a result of N_s source terms that appears in a tissue voxel (arterial compartment). These source terms supply blood directly from the respective N_s arteries. The temperature of blood received from these arterial elements by a voxel is given as T_i.

$$\dot{Q} = \dot{q}_m + \sum_{i}^{N_s} \frac{m_i c_{p,b} T_i}{V} \tag{4.19}$$

The convective heat loss from a voxel to a neighboring blood vessel is given by Eq. (4.20). T_t represents the temperature of the tissue voxel next to a blood vessel element denoted by subscript k. The blood vessel element can be an artery or vein represented by β. The surface area of the voxel in contact with the blood vessel is shown by A_s, and the convective heat transfer coefficient between blood and tissue is h_b.

$$\dot{Q}_\beta = \frac{h_b A_s}{V}(T_{\beta,k} - T_t) \tag{4.20}$$

where

$$\beta = \begin{cases} a : \text{artery} \\ v : \text{vein} \end{cases}$$

Similarly, the convective heat exchange between a voxel and air is given by $\dot{Q}_\infty$, calculated using Eq. (4.21). Here, T_∞ represents the ambient air temperature and h_∞ represents the convective heat transfer coefficient between air and tissue.

$$\dot{Q}_\infty = \frac{h_\infty A_s}{V}(T_\infty - T_t) \tag{4.21}$$

Combining Eqs. (4.18), (4.19), (4.20) and (4.21), leads to the differential Eq. (4.22)

$$\rho c_{p,t}\frac{\partial T_t}{\partial t} = k_t\nabla^2 T_t - \rho c_{p,b}\nabla\vec{v}T_t + \sum_i^{N_s}\frac{m_i c_{p,b}T_i}{V} + \dot{q}_m + \frac{h_\infty A_s}{V}(T_\infty - T_t) + \frac{h_b A_s}{V}(T_{\beta,k} - T_t) \tag{4.22}$$

and

$$\beta = \begin{cases} a : \text{artery} \\ v : \text{vein} \end{cases}$$

Eq. (4.22) is discretized using a first-order Finite Volume Method (FVM) to arrive at Eq. (4.23a).

$$\rho c_{p,t}V\frac{\Delta T_{t,j}}{\Delta t} = \sum_{i\in\mathrm{N}} UA(T_{\beta,i} - T_{t,j}) + \sum_{i\in\mathrm{N_n}} m_i c_{p,b}(T_{t,i} - T_{t,j}) + \sum_{k\in\mathrm{N_s}} m_{a,k}c_{p,b}(T_{a,k} - T_{t,j}) + \dot{q}_m V \tag{4.23a}$$

$$U = \left[\frac{\Delta s}{2k_t} + \frac{\Delta s}{2k_t}\right]^{-1} = \frac{k_t}{\Delta s} \tag{4.23b}$$

$$U = \left[\frac{\Delta s}{2k_t} + \frac{1}{h_\infty}\right]^{-1} \tag{4.23c}$$

$$U = \left[\frac{\Delta s}{2k_t} + \frac{1}{h_b}\right]^{-1} \tag{4.23d}$$

and

$$\beta = \begin{cases} a : \text{artery} \\ v : \text{vein} \\ t : \text{tissue} \end{cases}$$

Each voxel has six neighbors in 3D and four neighbors in 2D. The voxel neighbors can be any material, so the solution must accommodate the previously-described heat transfer mechanisms. The first term on the right-hand-side in Eq. (4.23a) addresses heat exchange between neighboring voxels. In this term, N is the total number of neighbors of a voxel. The overall heat transfer coefficient U varies based on the material of the neighboring voxel. If the neighboring voxel is tissue, then $U = k_t/\Delta s$ as shown in Eq. (4.23b). If the neighboring voxel is air or a blood vessel, the value of the overall heat transfer coefficient U is calculated using Eq. (4.23c) or Eq. (4.23d), respectively.

Some neighboring voxels may not supply blood to the voxel under consideration but rather may receive from it due to pressure differential. N_n in the second summation term in Eq. (4.23a), represents the number of neighbors from which blood is flowing into the current voxel. N_n may be less than or equal to N, depending on the pressure differentials. The third summation term in Eq. (4.23a) represents the energy delivered to the voxel via advection from N_s number of arterial sources that supply blood to the voxel. The fourth term in Eq. (4.23a) is the heat added to the voxel due to metabolic heat generation.

4.2.1 Multiscale Meshing

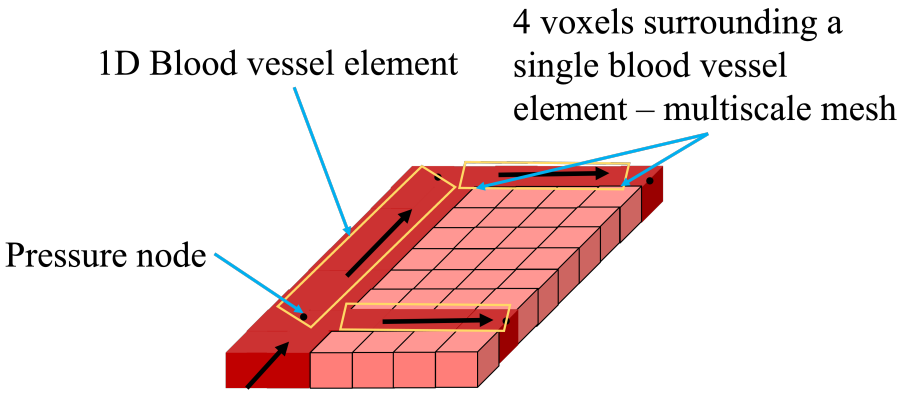

Figure 4.4: Multiscale mesh

A graphical illustration of a multiscale mesh is shown in Fig. 4.4. The major blood vessels that can be generated from imaging data are modeled as 1D pipe networks and are divided into elements only along the flow direction. The dimensional scale of elemental division may

not be the same as the voxel dimension, resulting in different mesh scales. Due to this scale difference, one blood vessel element can traverse multiple tissue voxels along its length. Each blood vessel element acts as a differential cell and the entire element is considered to be at the same temperature.

An illustration of this can also be seen in Fig 4.3.a and Fig 4.3.c. In Fig 4.3.a, the five voxels tagged as Arterial Voxel represent a section of an arterial tree. Fig 4.3.c shows the difference between an arterial element and arterial voxel. The three arterial voxels surrounded by thick black border create one arterial tree element. A similar venous tree element is shown in Fig 4.3.a. In Fig 4.3.c, voxels $(i-1, j)$, $(i-1, j-1)$, and $(i-1, j-2)$ will have a uniform temperature as they fall under the same arterial element. This one element of the blood vessel mesh is at a different scale than the tissue voxels, resulting in multiple tissue voxels surrounding a single blood vessel element. This is shown in Fig. 4.3 and Fig. 4.4. The surrounding tissue voxels are not isothermic and exchanges heat via convection governed by the convective heat transfer coefficient. The energy balance for the blood vessel tree is modeled using Eq. (4.24).

$$\rho_b c_{p,b} V_{\beta,e} \frac{\Delta T_j}{\Delta t} = \sum_{\beta,k \in N_k} m_k c_{p,b} (T_{\beta,k} - T_{\beta,j}) + \sum_{i \in N_i^V} h_b A_i (T_i - T_{\beta,j}) \tag{4.24}$$

In Eq. (4.24), the first term on the RHS represents the advection heat added to the blood vessel element under consideration at temperature $T_{\beta,j}$. This advection is the result of the mass flow of blood from one vessel element to another as it flows across the blood vessel network. In the arterial tree, following the direction of flow, the elements divide further, so each element receives blood only from one element. Conversely, in a venous tree, multiple blood vessel elements merge to form single element. Thus, one element may receive blood from multiple elements or from multiple voxels that fall within the SoI. The number of voxels or blood vessel elements that supply blood to the current vessel element is given by N_k. This blood vessel element is also exchanging heat with surrounding tissue given by the second term. N_i^V shows the tissue voxels that are in immediate contact with the blood vessel element

under consideration. These voxels will be at temperatures T_i and have different surface areas A_i in contact with the element.

4.2.2 Matrix Generation

Rearranging Eq. 4.23a for steady state results in Eq. (4.25). Eq. (4.25) represents energy conservation for a i-th tissue voxel. $\mathcal{N}_i$ is a set of voxels that surround tissue voxel i and $\mathcal{N}_n$ represents the neighboring tissue from which blood flows into voxel i. $\mathcal{N}_s$ is a set of arterial outlets which supply blood to voxel i. Eq. (4.25) when iterated over all the tissue voxels in the domain generates a coefficient matrix of size N_t x $(N_t + N_a + N_v)$, where N_t, N_a and N_v represent the total number of tissue voxels, arterial elements and venous elements respectively. The column matrix b_{N_t} is generated using RHS of Eq. (4.25)

$$\begin{aligned} &\sum_{j\in\mathcal{N}_i}(UA)_{(ij)}(T_{\beta,j}) + \sum_{j\in\mathcal{N}_n} m_{(ij)}c_{p,b}(T_{t,j}) + \sum_{k\in\mathcal{N}_s} m_{a,k}c_{p,b}(T_{a,k}) \\ &- \left[\sum_{j\in\mathcal{N}_i}(UA)_{(ij)} + \sum_{j\in\mathcal{N}_n} m_{(ij)}c_{p,b} + \sum_{k\in\mathcal{N}_s} m_{a,k}c_{p,b}\right](T_{t,i}) = -\dot{q}_m V_i \end{aligned} \tag{4.25}$$

$$\beta = \begin{cases} a : \text{artery} \\ v : \text{vein} \end{cases}$$

$\mathcal{N}_i$: Set of voxels neighboring tissue voxel i

$\mathcal{N}_n$: Set of tissue voxels supplying blood to tissue voxel i

$\mathcal{N}_s$: Set of arterial terminals supplying blood to tissue voxel i

Eq. (4.26) and Eq. (4.27) present a rearrangement of Eq. 4.25 and ensure energy conservation for a i-th blood vessel element of arterial and venous tree, respectively. $\mathcal{N}_k$ represents the set of blood vessel elements that supply blood to i-th element and, $\mathcal{N}_v$ is a set of tissue voxels that surround the i-th blood vessel element and exchange heat via convection with it. Eq. (4.26) is applicable to all the blood vessel elements except for the elements that are identified as inlets.

$$\sum_{k\in\mathcal{N}_k} m_k c_{p,b}(T_{a,k}) + \sum_{j\in\mathcal{N}_v} h_b A_j(T_j) - \left[\sum_{a,k\in\mathcal{N}_k} m_k c_{p,b} + \sum_{j\in\mathcal{N}_v} h_b A_j\right](T_{a,i}) = 0 \tag{4.26}$$

$$\sum_{k\in\mathcal{N}_k} m_k c_{p,b}(T_{v,k}) + \sum_{j\in\mathcal{N}_v} h_b A_j(T_j) - \left[\sum_{v,k\in\mathcal{N}_k} m_k c_{p,b} + \sum_{j\in\mathcal{N}_v} h_b A_j\right](T_{v,i}) = 0 \tag{4.27}$$

$\mathcal{N}_k$: Set of blood vessel elements supplying blood to vessel i

$\mathcal{N}_v$: Set of tissue voxels neighboring blood vessel element i

The last set of equations needed are the boundary conditions. Eq. (4.28) represents the Dirichlet boundary condition of inlet temperature applied to the arterial tree roots.

$$T_{a,k} = T_{in} \qquad k \in N_a^R \tag{4.28}$$

Considering the matrix equation $\mathcal{A}_m x = b$, $m = (N_t + N_a + N_v)$, and column matrix x is as shown below.

$$x^T = [\ T_{t,1}\ T_{t,2}\ ...\ T_{t,N_t}\ T_{a,1}\ T_{a,2}\ ...\ T_{a,N_a}\ T_{v,1}\ T_{v,2}\ ...\ T_{v,N_v}\ ]$$

$x^T[1 : N_t]$ - Temperature of tissue voxels

$x^T[N_t + 1 : N_t + N_a]$ - Temperature of arterial tree elements

$x^T[N_t + N_a + 1 : N_t + N_a + N_v]$ - Temperature of venous tree elements

The coefficient matrix $\mathcal{A}$ is generated using Eq. (4.25), (4.26), (4.27) and (4.28) on respective mesh elements.

4.2.3 Domain Modification

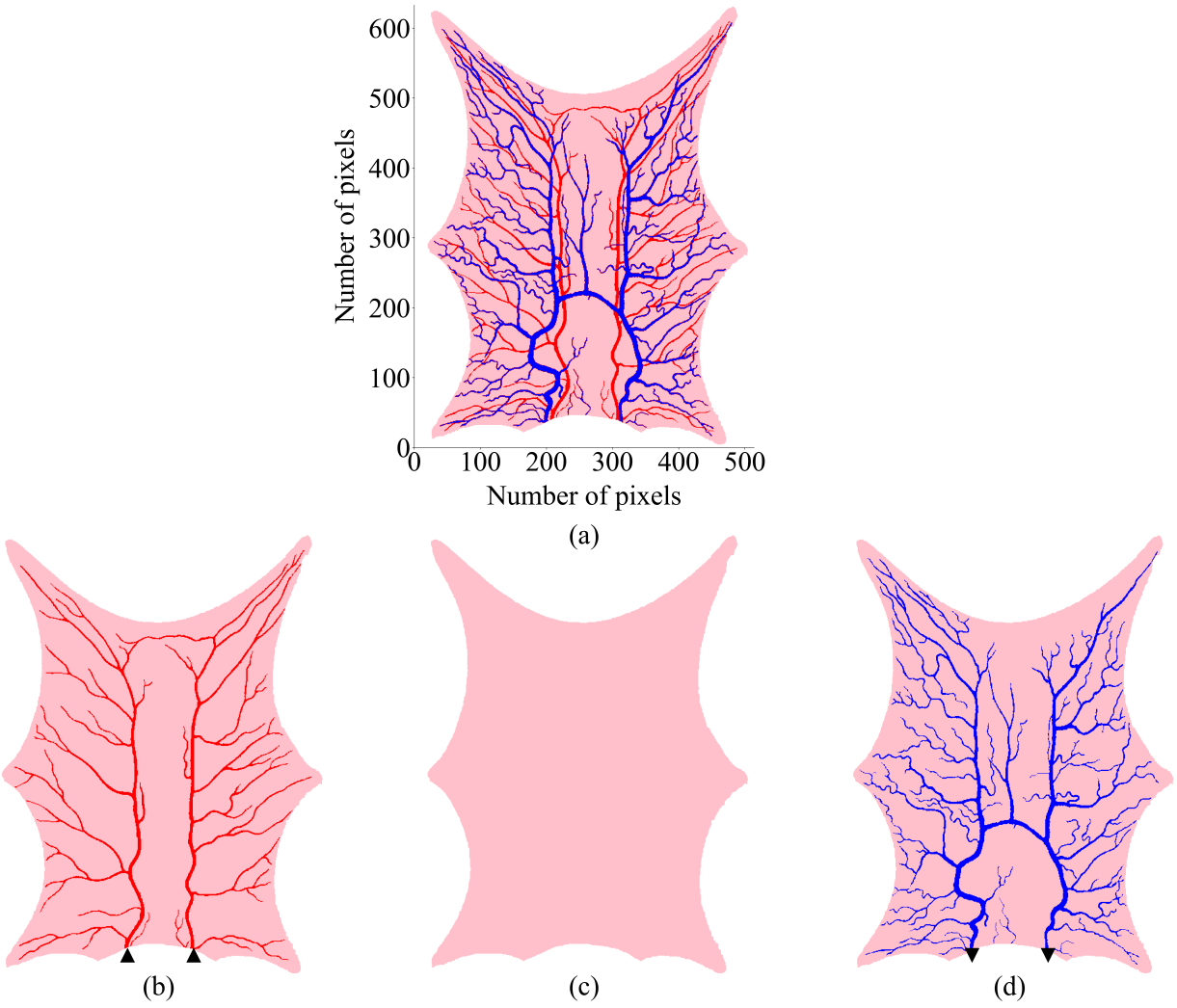

Figure 4.5: (a) Original frog tongue data with arteries in red and veins in blue. The number of pixels in original 2D data are 634 x 515, with pixel dimensions as 0.063 mm x 0.064 mm x 1 mm. The slice was modified for generating three slices each one-third the thickness as follows (a) Layer 1: Arterial tree and tissue (b) Layer 2: Tissue (c) Layer 3: Venous tree and tissue.

The original imaging data of the frog tongue obtained from literature[101] was 2D, as it consisted of only a single layer of voxels. Fig 4.5.a shows the original frog tongue data with the arterial tree in red and the venous tree in blue. The thickness of the original slice was 1 mm. When such a 2D slice is used for simulation, the source and sink terms generated by the terminals of arteries and veins in the domain are decoupled. This prevents blood perfusion between a tissue-blood interface. As a result, the blood vessels become a separator

between source and sink terms and the flow system is discontinuous. To address this, the blood vessels were completely separated from the domain and the entire system was assumed to be tissue[101]. To simulate convective heat exchange at the blood-tissue interface, blood vessel locations are required with reference to surrounding tissue. Hence, the 2D frog tongue domain was converted to 3D by dividing the single slice into three sub-slices across the depth. The top layer contains the main arterial tree, the middle layer consists only of tissue, and the bottom layer contains the venous tree. These layers will be addressed as Layer 1, Layer 2, and Layer 3, respectively, and are shown in Fig. 4.5. In Fig. 4.5 ▲ represents the arterial tree root nodes and ▼ represents the venous tree root nodes with Dirichlet boundary condition, respectively.

The order of these layers affects the blood perfusion across the domain. Since the arteries and veins are in the top and bottom layer separated by a tissue, blood entering the domain via source terms in the top layer (Layer 1) must perfuse across the tissue layer (Layer 2) to reach the venous sinks in the bottom layer (Layer 3). If the layers were to be otherwise ordered, the proximity of the source and the sink terms would reduce the perfusion of blood in the tissue layer (Layer 2).

4.2.4 Simulation

To demonstrate the VoM-PhyS framework, a steady state simulation on the frog tongue shown in Fig. 4.5 was conducted. Frogs are cold-blooded and have low metabolic heat generation rates[143]. For this study, the metabolic heat generation rate was taken to be zero, and other thermo-physiological parameters were obtained from literature[101;137;142]. These parameters are presented in Table 4.1. Here, $\epsilon = 10\,\text{mm}$ was used for flow simulation and heat transfer. This value ensures that each voxel has at least one direct source of blood from the arterial tree and at least one sink to the venous tree. No tissue voxel relies solely on cross-voxel permeability to receive blood from the arterial tree or deliver blood to the venous tree.

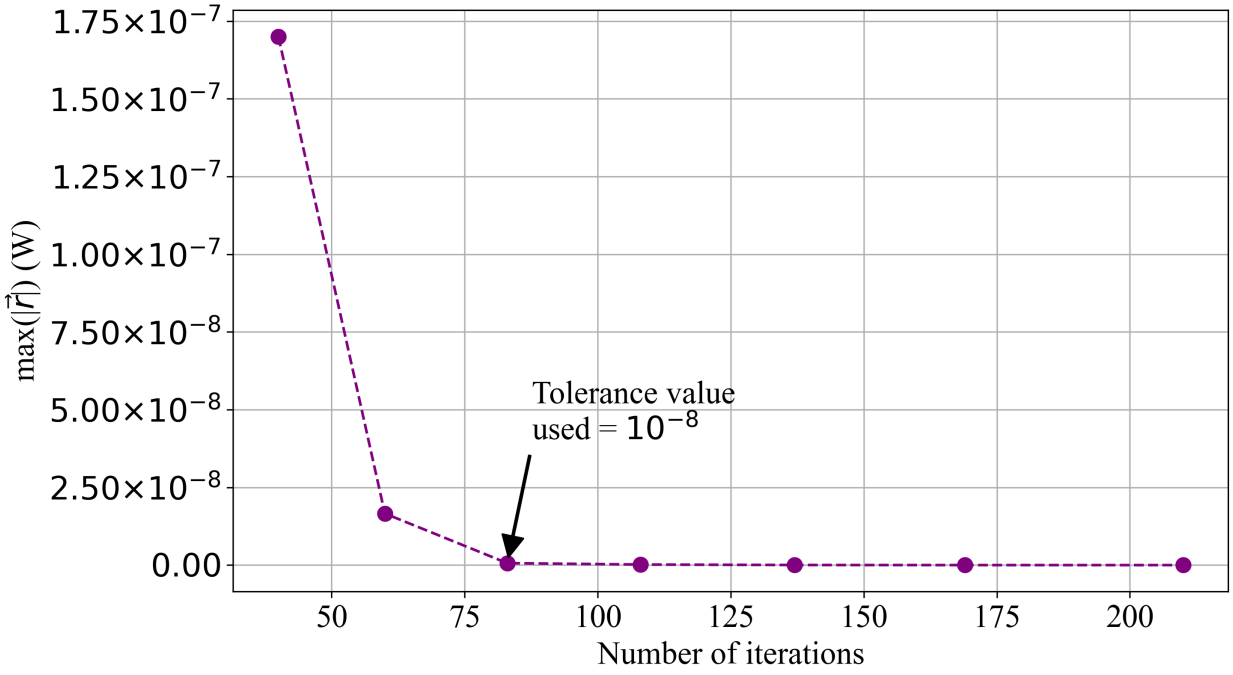

Figure 4.6: Convergence Analysis

Table 4.1: Parameters used for simulation

Domain	Parameter	Symbols	Value	Units
Tongue	Specific heat[142]	c_{pt}	3421	$\mathrm{J\,kg^{-1}\,{}^{\circ}C^{-1}}$
	Density[142]	ρ_t	1090	$\mathrm{kg\,m^{-3}}$
	Thermal conductivity[142]	k_t	0.49	$\mathrm{W\,m^{-1}\,{}^{\circ}C^{-1}}$
	Perfusion[142]	α	1×10^{-6}	$\mathrm{m\,s\,kg^{-1}}$
	Arterial permeability[101;137]	$\mathrm{K_a}$	1×10^{-12}	$\mathrm{m^2}$
	Venous permeability[101;137]	$\mathrm{K_v}$	5×10^{-10}	$\mathrm{m^2}$
	Metabolic heat gen. rate[143]	$\dot{q}_m$	0	$\mathrm{W\,m^{-3}\,s^{-1}}$
Blood	Specific heat[142]	c_{pb}	3617	$\mathrm{J\,kg^{-1}\,{}^{\circ}C^{-1}}$
	Viscosity[101]	μ	3×10^{-3}	Pa s
	Thermal conductivity[142]	k_b	0.52	$\mathrm{W\,m^{-1}\,{}^{\circ}C^{-1}}$
	Density[142]	ρ_b	1050	$\mathrm{kg\,m^{-3}}$
	Pressure drop parameter[101]	γ	1×10^{-14}	$\mathrm{m^3}$
	Arterial inlet pressure[101]	P_{in}	10.6	kPa
	Venous outlet pressure[101]	P_{out}	1.60	kPa
	Voxel dimensions[101]		64 x 64 x 333	$\mu\mathrm{m}^3$
	Ambient temperature	T_∞	20	°C
	Inlet blood temperature	T_{in}	35	°C

The blood flow matrix $\mathcal{A}_n$ was generated using Eqs. (4.10), (4.11), (4.12), (4.13), (4.14), (4.15), (4.16), and (4.17) on flow mesh elements. A heat transfer matrix $\mathcal{A}_m$ was generated using Eq. (4.25), (4.26), (4.27), and (4.28), on respective heat mesh elements. Both matrices $\mathcal{A}_n$ and $\mathcal{A}_m$ had a sparsity of 99.99 % and matrix size $n = 1\,111\,803$ and $m = 556\,078$, respectively. These matrices were solved using the Generalized Minimal Residual (GMRES) method[144;145]. To increase the solver speed, incomplete LU decomposition of the matrices was used as a preconditioner M. The convergence study conducted for this problem to determine the appropriate tolerance setting is shown in Fig. 4.6. The residual $\vec{r} = \mathcal{A}_m\vec{x} - \vec{b}$ was calculated and the maximum of $|\vec{r}|$ is plotted against number of iterations needed in Fig. 4.6. At a tolerance value of 1×10^{-8}, the maximum residual error is 6.35×10^{-10} W, and continues to reduce exponentially as the tolerance is decreased. Thus, a tolerance of 1×10^{-8} was used for GMRES function in Python[140]. The Python script can be found at VoM-PhyS.

4.2.5 Parameter Sensitivity Analysis

A numerical sensitivity analysis was conducted to determine how uncertainties in input parameter values propagate through the model and affect the output parameter. The primary aim of this study was to analyse propagation of error from an input parameter to the final result. A one-at-a-time (OAT) method[101] was used to calculate normalized sensitivity coefficient $\mathcal{X}_{i,w}$ using Eq. (4.29a)

$$\mathcal{X}_{i,x} = \frac{\partial\theta_i/\theta_i}{\partial x/x} \tag{4.29a}$$

$$\theta_i = \mathrm{T}_i - \mathrm{T}_\infty \tag{4.29b}$$

The relative sensitivity coefficient $\mathcal{X}_{i,x}$ was calculated for input variable x at location i. A temperature offset θ was used for the sensitivity analysis. The offset was calculated by

subtracting a reference temperature value throughout the entire domain. In Eq. (4.29a), subscript i represents every mesh element for which temperature is calculated as an output parameter. The relative sensitivity coefficient is represented using an average calculated across the entire domain $\bar{\mathcal{X}}_x$ using Eq. (4.30). In Eq. (4.30), $\mathcal{N}$ is the total number of unknowns for which temperature is calculated. Each input variable was increased by 1 % to calculate $\bar{\mathcal{X}}_x$.

$$\bar{\mathcal{X}}_x = \frac{\sum_{\mathrm{i}}^{\mathcal{N}} \mathcal{X}_{i,x}}{\mathcal{N}} \tag{4.30}$$

4.3 Results

4.3.1 Flow Simulation

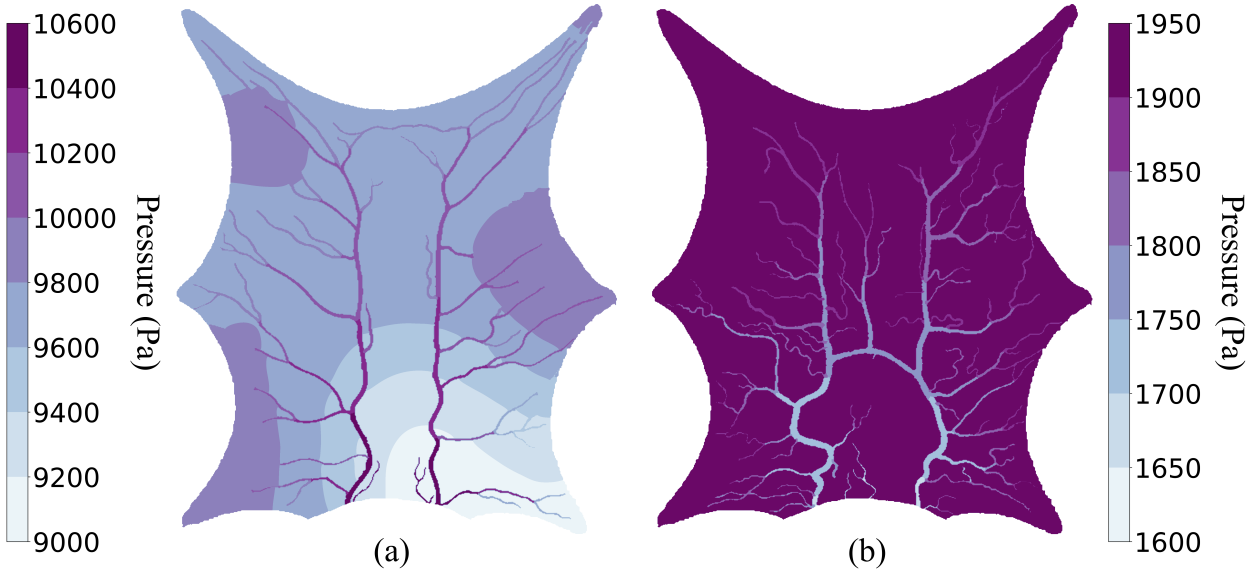

Figure 4.7: For $\epsilon = 10$mm (a) Arterial compartment pressure of Layer 1 (b) Venous compartment pressure of Layer 3

Fig. 4.7 shows the pressure map for flow simulation using a 10 mm SoI radius. Fig. 4.7.a, shows the pressure for the arterial compartment of Layer 1. The pressure is greatest (10.6 kPa) at the inlet and continues to drop along the blood flow in the arterial tree. The

minimum pressure observed in the arterial compartments of the entire domain is around 9 kPa. Fig. 4.7.b shows the pressure map of the venous compartment in Layer 3. The blood in the venous compartment side of the voxel is at approximately 1.95 kPa in the tissue. We observe a pressure drop of around 8 kPa across the capillary bed within the voxels. As the blood flows from the venous compartment of tissue towards the venous outlet through veins, it loses more pressure and the blood exits at 1.6 kPa, which is the defined boundary condition.

4.3.2 Pennes Bioheat Model Assumption

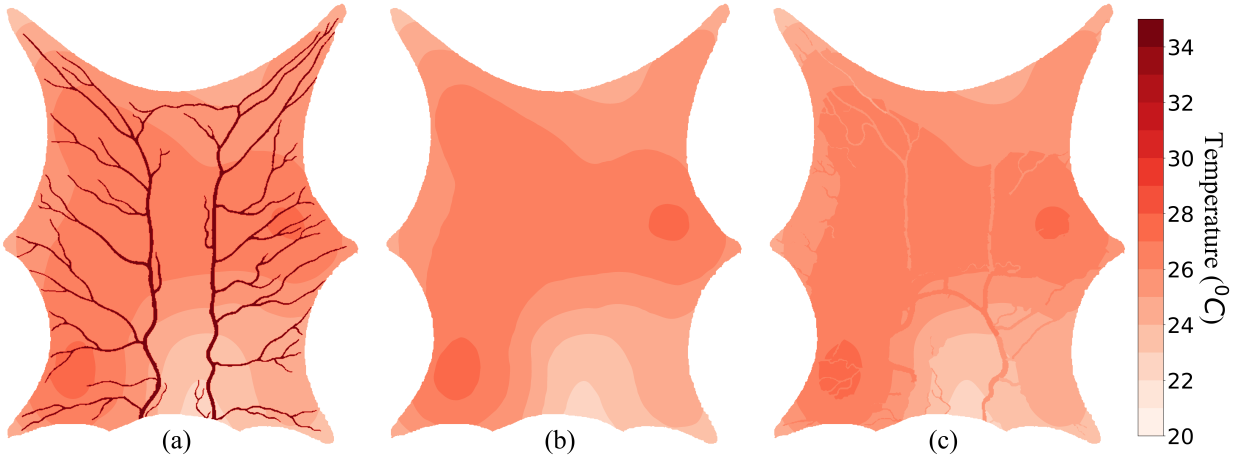

Figure 4.8: Thermal map using PBM Assumption $h_b = 0.001\,\mathrm{W\,m^{-2}\,{}^{\circ}C^{-1}}$ and $\epsilon = 10\,\mathrm{mm}$ (a) Layer 1 (b) Layer 2 (c) Layer 3

For this simulation, the convective heat transfer coefficient for blood vessels and ambient air were taken to be as $0.001\,\mathrm{W\,m^{-2}\,{}^{\circ}C^{-1}}$ and $20\,\mathrm{W\,m^{-2}\,{}^{\circ}C^{-1}}$, respectively. The SoI radius was again taken to be 10 mm. The blood temperature leaving the domain was 25.8 °C at a steady state. The minimum and maximum tissue temperatures observed were 22.5 °C and 27.3 °C, respectively. The temperature profiles for the three layers are shown in Fig. 4.8. The blood temperature remains constant at 35 °C from the entrance to the extremities in the arterial tree and enters tissue at the same temperature. Every voxel that directly receives blood from an artery receives it at 35 °C regardless of how far the voxel is from the inlet boundary condition. Once the blood has perfused across the tissue, it enters the venous

tree through various volumetric sink terms coupled to venous extremities. The temperatures at which blood enters through the extremities in a venous tree are different due to local temperature variations within the tissue domain.

4.3.3 Weinbaum and Jiji Model Assumption

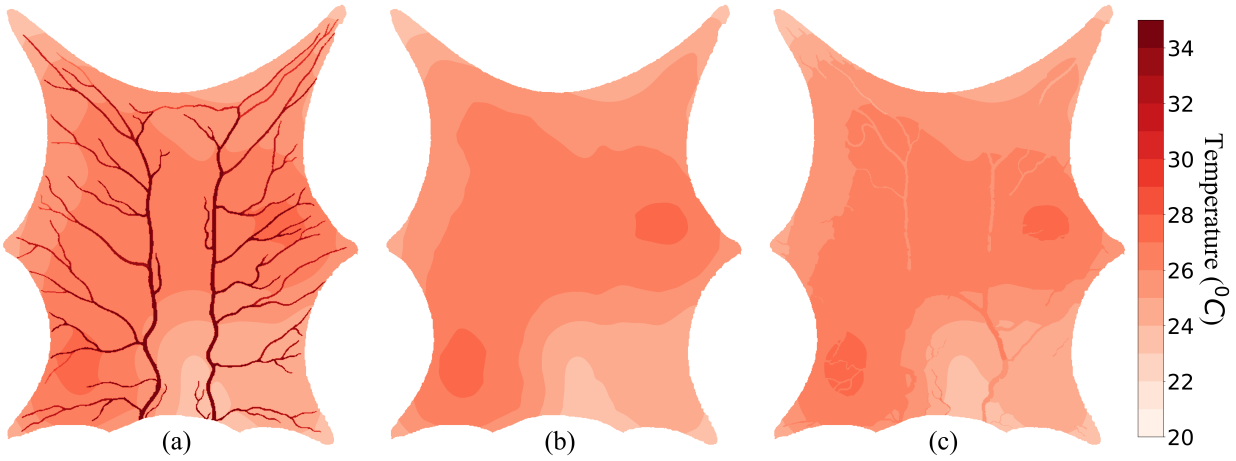

Figure 4.9: Thermal map using WJM Assumption $h_b = 10\,\mathrm{W\,m^{-2}\,^{\circ}C^{-1}}$ and $\epsilon = 10\,\mathrm{mm}$ (a) Layer 1 (b) Layer 2 (c) Layer 3

For this simulation, the convective heat transfer coefficient for blood vessels and ambient air were taken to be $10\,\mathrm{W\,m^{-2}\,^{\circ}C^{-1}}$ and $20\,\mathrm{W\,m^{-2}\,^{\circ}C^{-1}}$, respectively. The SoI radius was again taken to be 10 mm. The temperature of blood leaving the domain was 25.9 °C at a steady state. The minimum and maximum tissue temperatures observed were 23.1 °C and 27.4 °C. The temperature profiles for the three layers are shown in Fig 4.9.

Blood loses heat as it enters the arterial tree and flows towards the extremities to enter the tissue region. Each voxel receives blood at a temperature that depends on its distance from the inlet. The minimum temperature observed in the arterial tree was 27.7 °C at the extremity where blood enters the tissue. Similar to the PBM simulation shown in Fig. 4.8, blood enters the venous tree at different temperatures but gains heat from the tissue along the flow direction. This effect can be observed via the temperature difference at which the blood leaves the domain through the venous side. Blood leaves at 25.8 °C and 25.9 °C when the convective heat transfer coefficient between blood and tissue is used as $0.001\,\mathrm{W\,m^{-2}\,^{\circ}C^{-1}}$

and $10\,\mathrm{W\,m^{-2}\,^{\circ}C^{-1}}$, respectively.

4.4 Discussion

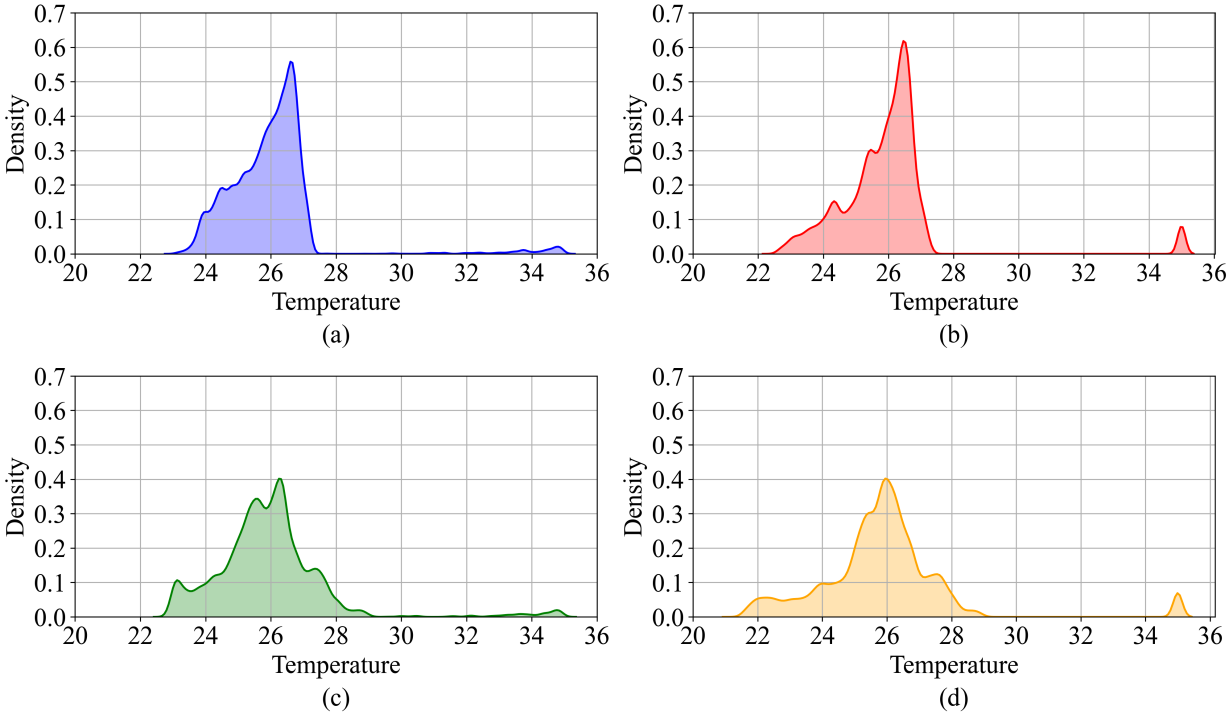

Figure 4.10: Distribution plots
(a) $\epsilon = 10\,\mathrm{mm}$ and $h_b = 10\,\mathrm{W\,m^{-2}\,^{\circ}C^{-1}}$ (b) $\epsilon = 10\,\mathrm{mm}$ and $h_b = 0.001\,\mathrm{W\,m^{-2}\,^{\circ}C^{-1}}$
(c) $\epsilon = 5\,\mathrm{mm}$ and $h_b = 10\,\mathrm{W\,m^{-2}\,^{\circ}C^{-1}}$ (d) $\epsilon = 5\,\mathrm{mm}$ and $h_b = 0.001\,\mathrm{W\,m^{-2}\,^{\circ}C^{-1}}$

To study the effect of SoI and convective heat transfer coefficient in VoM-PhyS model, the SoI radius was varied between 5 mm and 10 mm, and heat transfer coefficient between blood vessel and tissue was varied between $0.001\,\mathrm{W\,m^{-2}\,^{\circ}C^{-1}}$ and $10\,\mathrm{W\,m^{-2}\,^{\circ}C^{-1}}$. A distribution plot for the voxel temperature is shown in Fig. 4.10. The distributions are non-normal and skewed, and hence non-parametric statistical tests were considered to study the significance in the differences. Since the results are compared with each other for the respective reference voxel, the statistical test used was Wilcoxon signed Rank Test [146;147].

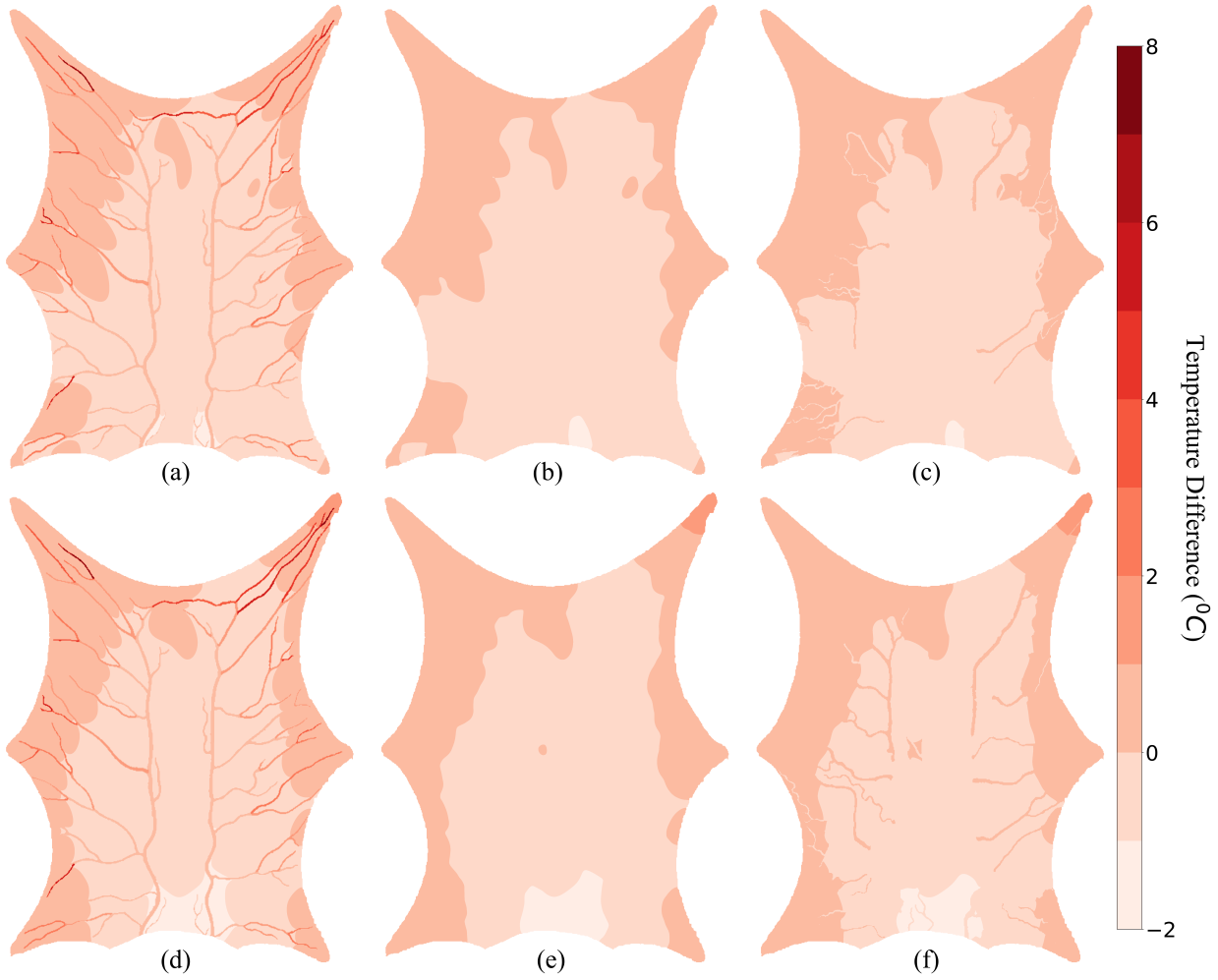

Figure 4.11: Effect of convective heat exchange between blood and tissue. The positive temperature difference shows the regions which are warmer when we use the PBM assumption and the negative temperature difference shows the region where the WJM assumption results in higher temperature.
$\epsilon = 5\,\text{mm}$ - (a) Layer 1 (b) Layer 2 (c) Layer 3
$\epsilon = 10\,\text{mm}$ - (d) layer 1 (e) Layer 2 (f) Layer 3

Table 4.2: Statistical significance of Fig. 4.11. Parameter $\mathcal{V}_+$ represents percentage of domain volume that has $\Delta T \geq 1\,^\circ\text{C}$. Parameter $\mathcal{V}_-$ represents percentage of domain volume that has $\Delta T \leq -1\,^\circ\text{C}$. Parameter $\mathcal{V}_0$ represents percentage of domain volume that has $-1\,^\circ\text{C} < \Delta T < 1\,^\circ\text{C}$.

ϵ (mm)	Wilcoxon statistic	p-value	$\mathcal{V}_+$ (%)	$\mathcal{V}_-$ (%)	$\mathcal{V}_0$ (%)
5	2.72×10^9	0.0	6.13	16.82	77.04
10	5.4×10^8	0.0	2.14	9.04	88.8

Fig 4.11 shows the effect of convective heat transfer coefficient between blood vessel and tissue for different SoI radius. A characteristic thermal pattern can be seen in Fig. 4.11. There is a difference of a maximum of 1 °C throughout the tissue domain. The extremities are warmer by 1 °C when $h_b = 0.001\,\mathrm{W\,m^{-2}\,°C^{-1}}$ and the region farther away from arterial terminal elements is warmer by 1 °C when $h_b = 10\,\mathrm{W\,m^{-2}\,°C^{-1}}$. This difference shows the regions that are dominantly dependent on convective heat exchange between the blood vessel and tissue. The tissue regions further from the arterial outlets primarily rely on inter-tissue blood perfusion. When $h_b = 10\,\mathrm{W\,m^{-2}\,°C^{-1}}$, the convective heat exchange warms this region and the extremities receive cooler blood. Blood is at a maximum temperature at the inlet for this domain. Under the PBM assumption ($h_b = 0.001\,\mathrm{W\,m^{-2}\,°C^{-1}}$), blood reaches the entire arterial tree at the same temperature. For the WJM assumption, the blood loses heat along its flow. The highest tissue temperature difference is observed in the region closest to the inlet boundary condition. This is where blood is warmest and, if the convective coefficient is significant, it will exchange heat and raise the temperature of the tissue. This warmer tissue, in return, heats the venous return blood, and thus a warmer blood at the outlet is obtained compared to $h_b = 0.001\,\mathrm{W\,m^{-2}\,°C^{-1}}$ as shown in Table 4.3. This is the system described by Weinbaum in the literature[58]. The work of Coccarelli[99] shows that inner convection plays a crucial role in organ temperatures when there exists a major artery in proximity, and so the results obtained from this simulation support the work of Coccarelli for a micro-scale domain.

Table 4.3: Temperature for different simulation conditions

Parameters	units	$\epsilon = 10\,\mathrm{mm}$		$\epsilon = 5\,\mathrm{mm}$		$\epsilon = 2\,\mathrm{mm}$	
Convective coefficient	$\mathrm{W\,m^{-2}\,°C^{-1}}$	10	0.001	10	0.001	10	0.001
Inlet temperature	°C	35.0	35.0	35.0	35.0	35.0	35.0
Outlet temperature	°C	25.9	25.8	25.9	25.8	26.1	26.0
Min arterial temperature	°C	27.7	35.0	27.4	35.0	27.4	35.0
Min venous temperature	°C	24.1	23.7	23.5	22.9	23.1	22.3
Max venous temperature	°C	26.8	26.6	27.6	27.5	29.0	29.1
Min tissue temperature	°C	23.1	22.5	22.8	21.5	22.6	21.3
Max tissue temperature	°C	27.4	27.3	29.0	28.9	31.6	31.8

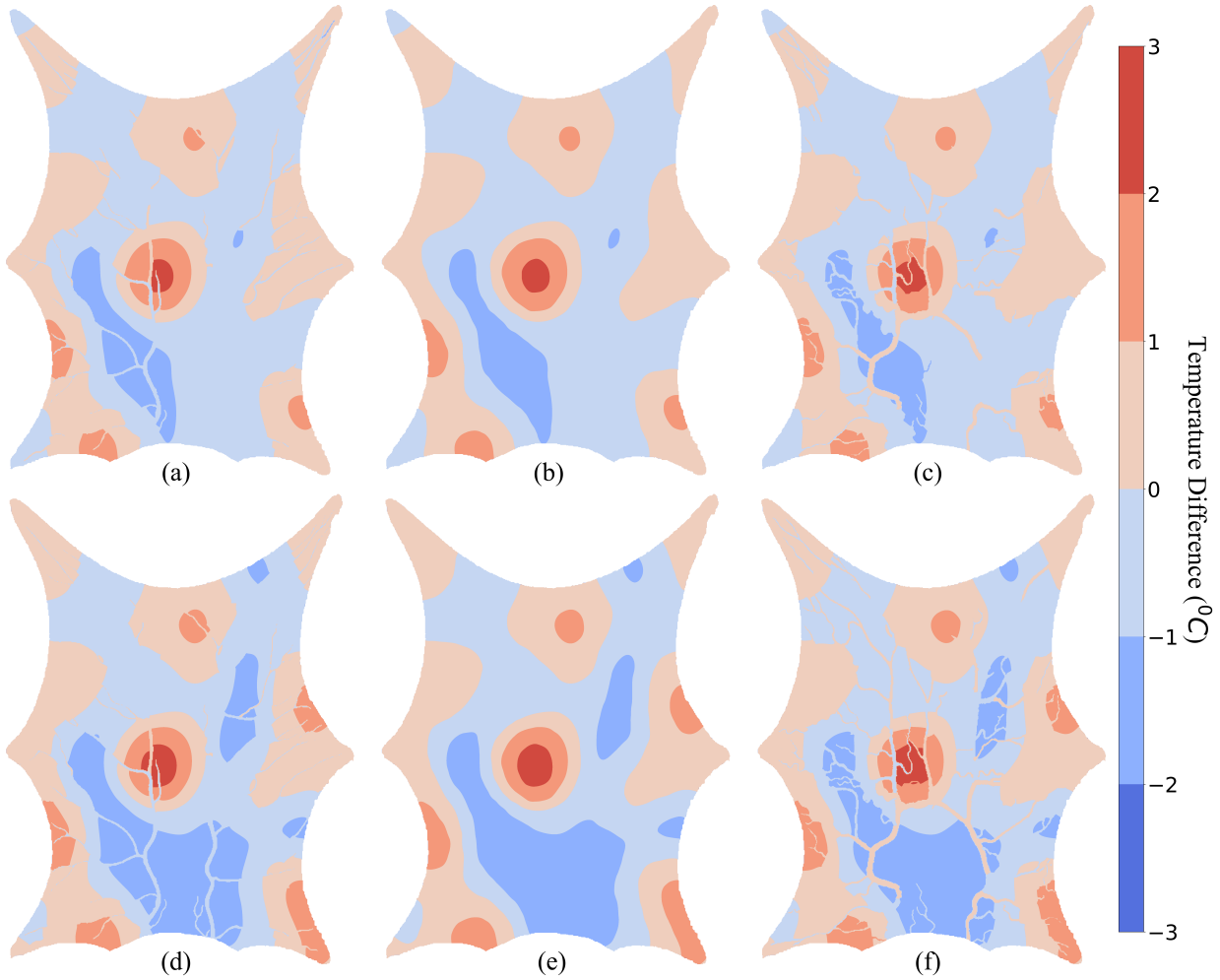

Figure 4.12: Temperature difference between $\epsilon = 5\,\text{mm}$ and $\epsilon = 10\,\text{mm}$. The positive temperature difference shows the region which is warmer when ϵ is smaller.
$h_b = 0.001\,\text{W m}^{-2}\,^\circ\text{C}^{-1}$ - (a) Layer 1 (b) Layer 2 (c) Layer 3
$h_b = 10\,\text{W m}^{-2}\,^\circ\text{C}^{-1}$ - (d) Layer 1 (e) Layer 2 (f) Layer 3

Table 4.4: Statistical significance of Fig. 4.12. Parameter $\mathcal{V}_+$ represents percentage of domain volume that has $\Delta T \geq 1\,^\circ\text{C}$. Parameter $\mathcal{V}_-$ represents percentage of domain volume that has $\Delta T \leq -1\,^\circ\text{C}$. Parameter $\mathcal{V}_0$ represents percentage of domain volume that has $-1\,^\circ\text{C} < \Delta T < 1\,^\circ\text{C}$.

$h_b(\text{W m}^{-2}\,^\circ\text{C}^{-1})$	Wilcoxon statistics	p-value	$\mathcal{V}_+$ (%)	$\mathcal{V}_-$ (%)	$\mathcal{V}_0$ (%)
0.001	25.9×10^9	0.0	25.11	32.4	42.48
10	17.3×10^9	0.0	19.5	28.33	52.16

The Wilcoxon signed-rank test was performed to study the significance of temperature difference observed in Fig. 4.11 and the data are shown in Table 4.2. The test resulted in minimum of sum of the ranks of differences above or below zero as 5.4×10^8 and 2.7×10^9 for SoI radius as 5 mm and 10 mm, respectively. For both, the p-value of test was very small, which gives the confidence that the results compared are different. Three new parameters $\mathcal{V}_+$, $\mathcal{V}_-$, and $\mathcal{V}_0$ were calculated. $\mathcal{V}_+$ represents the percentage of volume that has temperature difference higher than 1 °C. Similarly, $\mathcal{V}_-$ represents the percentage of volume that has temperature difference lower than −1 °C, and $\mathcal{V}_0$ represents percentage of volume that has temperature difference between ±1 °C. As shown in Table 4.2, 88.8 % of total voxels in the domain do not have a temperature difference of ±1 °C for $\epsilon = 10$ mm. Thus, the effect of convective heat transfer between tissue and voxel is not significantly seen in majority of the domain for a larger ϵ.

Fig. 4.12 shows the effect of varying ϵ when the convective heat transfer coefficient between blood and tissue is constant. The positive temperature difference shows a higher temperature when ϵ is smaller. The SoI controls the volume over which the flow is distributed in the tissue. A larger volume in the SoI results in a lesser of flow to each tissue voxel. Thus, higher temperatures for tissues in close proximity to arterial outlets are observed when SoI is smaller. The negative temperature differences are observed away from arterial outlets. These regions rely on a larger SoI to receive blood from arteries and, thus, higher temperatures are observed with $\epsilon = 10$ mm compared to those observed with $\epsilon = 5$ mm.

Table 4.4 shows the Wilcoxon signed-rank test results for Fig. 4.12. Similar to Table 4.2, a temperature difference of minimum ±1 °C is considered. The minimum of sum of the ranks of differences above or below zero and their respective p-value are given in Table 4.4. Unlike the results observed in Table 4.2, more than 50 % of total voxels have a temperature difference more than ±1 °C between $\epsilon = 5$ mm and 10 mm for h_b =0.001 W m^{-2} °C^{-1} and only 52.16 % of total voxels have a temperature difference less than ±1 °C between $\epsilon = 5$ mm and 10 mm for h_b =10 W m^{-2} °C^{-1}. This shows a significant difference in the thermal maps can be observed based on the SoI radius. Thus, the SoI radius and the corresponding Dirac distribution method used in this work and in literature[137] play a crucial role in the analysis.

The RRT method[98] used in the VaPor model[73] generates additional levels of blood vessels that cannot be segmented from medical imaging data. Blowers[73] demonstrated this on a brain by generating additional blood vessels to simulate hyperthermia. Wang et al.[96] use the same VaPor model and RRT method for thermal analysis of the skin and foot. In both of these simulations, blood perfusion happens across the terminal vessels - tissue interface. This modeled perfusion is uniform across the entire length of the terminal vessel and every voxel that intersects the vessel receives equal amount of flow. This is very efficient when a single organ is under consideration and the density of the blood vessels can be modeled to the level where such perfusion physically takes place. However, such detailed micro-vasculature at the level of the skin over the entire human is likely to incur a very large computational cost. In the research area of human thermoregulation and human thermal modeling[74;148;149], accurate localized skin temperature over the entire human body is important. This skin temperature is regulated by blood flow across the skin and acts as a feedback signal to the hypothalamus for thermal regulation. Recently developed thermoregulation models[4] are designed to be able to couple with thermal manikins. These models require an accurate, local skin temperature, and thus a blood vessel network that can provide accurate results. If the blood vessels generated using the RRT algorithm do not reach the capillary level, where the assumption of blood perfusion across the vessel wall is valid, it would result in pressure drop error. VoM-PhyS provides the solution to find the optimum level to generate additional branches using the RRT method and later use SoI technique to supply blood to a volume of region from the terminal vessels.

In the VoM-PhyS framework, the SoI radius ensures that each voxel has at least one source and one sink term. This guarantees that no voxel is left unperfused when the pressure drop across the domain is applied. Many levels of vasculature would be required to achieve this using RRT method, which is tantamount to recreating the entire capillary blood network as obtained from literature[87;88;150]. A model that can simulate blood flow and heat transfer needs to map pressure boundary conditions across the vascular network. This becomes more challenging as the relative domain size increases when compared to the size of capillary network. Using the porous media approximation is one way to represent these capillaries.

The coupling between discretized blood vessels and this porous media domain plays a key role on addressing the issue of pressure and blood flow. Such a framework can be used to simulate a tracer distribution as shown in literature[101]. The VoM-Phys framework provides the ability to model the pressure distribution, blood flow, and heat transfer, irrespective of the domain size relative to the capillary bed.

The VoM-PhyS framework relies on the Dirac distribution method (Eq. (4.6a)) and the pressure drop parameter to simulate pre-capillary vessels. These two parameters are analysed and discussed in the next chapter. Determining the correct value of the SoI radius (ϵ) remains a challenge that requires further research. The present study considers laminar flow throughout the blood vessel network and porous media. This assumption has its limitations which are not covered here. As blood enters a capillary bed, it behaves as a non-Newtonian fluid[151–153]. The effect of non-Newtonian blood in the VoM-PhyS framework is beyond the scope of this dissertation but needs to be studied in future work. The domain generated from imaging data relies on the accuracy on image and segmentation process involved to create the domain. The diameters of blood vessels obtained during segmentation are dependent on the state of vasodilation or vasoconstriction at the moment when the image was taken. These parameters are expected to affect the blood flow. The future work for present study would require to consider transient analysis of blood flow and spatial and transient variations due to thermal response.

4.4.1 Propagation of Error

In Fig. 4.13, the relative sensitivity coefficient averaged over the domain ($\bar{\mathcal{X}}_x$) is plotted for various input parameters. $\bar{\mathcal{X}}_x$ represents an average percent change in temperature offset for a 1 % change in a given input parameter value. The reference inlet temperature offset θ_{in} is 15 °C. When the inlet temperature is specified as 35.15 °C to simulate for 1 % increase in θ_{in}, an average increase of 1.023 % is observed. Since metabolic generation is defined to be zero for the simulation, the temperature variation in the domain shows a linear relationship with inlet temperature. When the convective heat transfer coefficient of ambient air (h_∞) is

increased by 1 %, the average temperature offset reduces by 0.65 %. This is due to more heat being convected out of the domain reducing the overall domain temperature. For a percent increase of arterial to venous compartmental perfusion (α), an average of 0.4 % increase in temperature was observed. Other flow resistance parameters used in VoM-PhyS (K_a, K_v, γ_a and γ_v) exhibited an average change of less than $\pm$ 0.1 % in temperature.

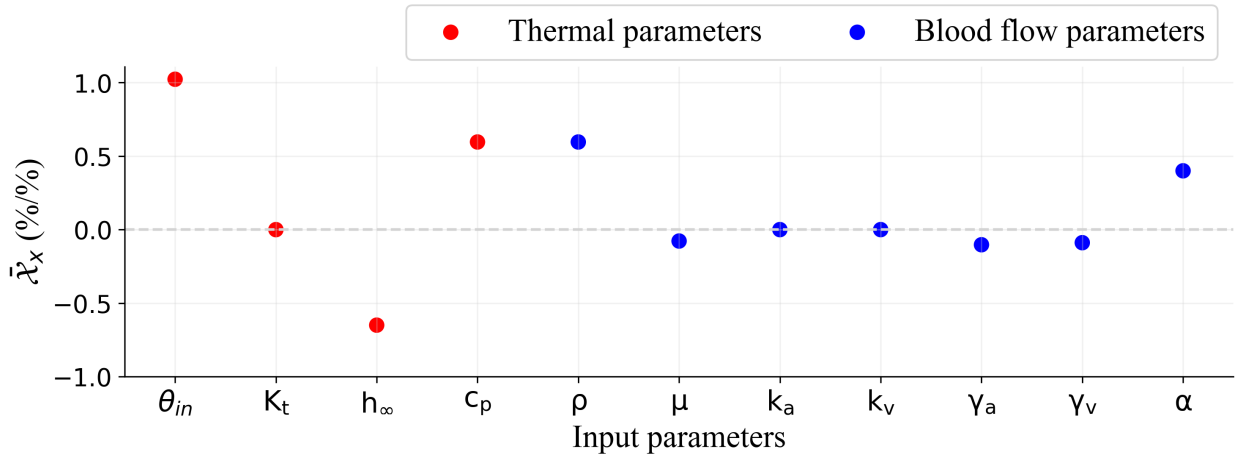

Figure 4.13: Parameter sensitivity analysis

4.5 Chapter Summary

In this chapter, the existing blood flow model[137] was described, which was used to develop the novel VoM-PhyS framework. This simulation framework was developed to simulate heat exchange coupled with blood flow for a voxel mesh obtained from medical imaging data. The VoM-PhyS framework was demonstrated on frog tongue data obtained from the literature.

The VoM-PhyS framework was designed to accommodate different assumptions of bioheat transfer. Classification of thermally significant vessels has been a topic of debate in the literature. The VoM-PhyS framework allows the flexibility to vary thermally significant vessels. This adaptability of the VoM-PhyS framework was demonstrated by varying the heat transfer coefficient of segmented vessels to simulate the Weinbaum and Jiji[58;60] BHM and the Pennes[23] BHM.

The SoI is a spherical tissue volume within which a segmented terminal vessel exchanges

blood with tissue voxels. The SoI couples the 1D vessel mesh with 3D tissue mesh. The value of SoI radius ϵ remains empirical with no *in vivo* data available for benchmarking. The effect of different values of ϵ in the VoM-PhyS was studied. Use of smaller values of ϵ demonstrated locally warmer regions compared to the more uniform temperature distribution observed when using larger ϵ. The Wilcoxon statistical test was used to analyze the significance of the difference due to different ϵ values and heat exchange between the segmented vessels and tissue. The statistical analysis revealed that ϵ had a more significant effect on the simulation results than convective heat exchange between blood vessels and tissue.

Chapter 5

Mixed-Dimensional Coupling

In the VoM-PhyS Framework (described in Chapter 4), the multi-dimensional coupling is achieved using the SoI radius (ϵ) and the pressure drop parameter (γ). The SoI controls the number of tissue voxels exchanging blood with the segmented blood vessels. The pressure drop parameter dictates the flow resistance offered by the mathematical blood vessels within the SoI. The availability of segmented blood vessels is primarily limited by image resolution. However, in addition to image resolution, memory requirements can also restrict segmentation of blood vessels. An example of this is the mesh-based liver vasculature model developed by Correa-Alfonso et al.[86]. In this liver model, the blood vessels are generated using the Constrained Constructive Optimization (CCO) algorithm. The smallest diameter of the blood vessel modeled is 100 µm. A voxel mesh of this liver model with a voxel size of 500 µm results in 13.6×10^6 voxels and 71.4 % of hepatic arteries are lost as their diameter is less than 500 µm. The memory required for a voxel mesh of this size is in the range in terabytes. Unsegmented blood vessels are modeled using the SoI and the pressure drop parameter in the VoM-PhyS Framework. Hence, understanding these parameters and their effect on the simulation is crucial.

This chapter focuses on the effect of the SoI and the pressure drop parameter on simulation accuracy. Using a 2D domain, a set of two equations to calculate the pressure drop parameter for arterial and venous networks is presented. A reference domain of vascular

networks is used to demonstrate the application of derived pressure drop equations. The effect of replacing segmented vasculature with the pressure drop parameter on heat transfer simulation is presented, and two methods to reduce the resulting temperature errors are proposed and analyzed.

5.1 Methodology

To study the effect of SoI and pressure drop parameter γ_β ($\beta = a$ for arterial and $\beta = v$ for venous), a simulation domain shown in Fig. 5.1 was created. A thin tissue slice of thickness 0.001 m and 0.09 m x 0.09 m was connected to a vasculature. The arterial and venous networks consist of bifurcations at every level. The daughter vessels have a bifurcation angle of 30° between them[151]. The radii of parent and daughter vessels are restricted using the Murray's Principle of Bifurcation[154], shown in Eq. (5.1).

$$r_p^\lambda = r_{d1}^\lambda + r_{d2}^\lambda \tag{5.1}$$

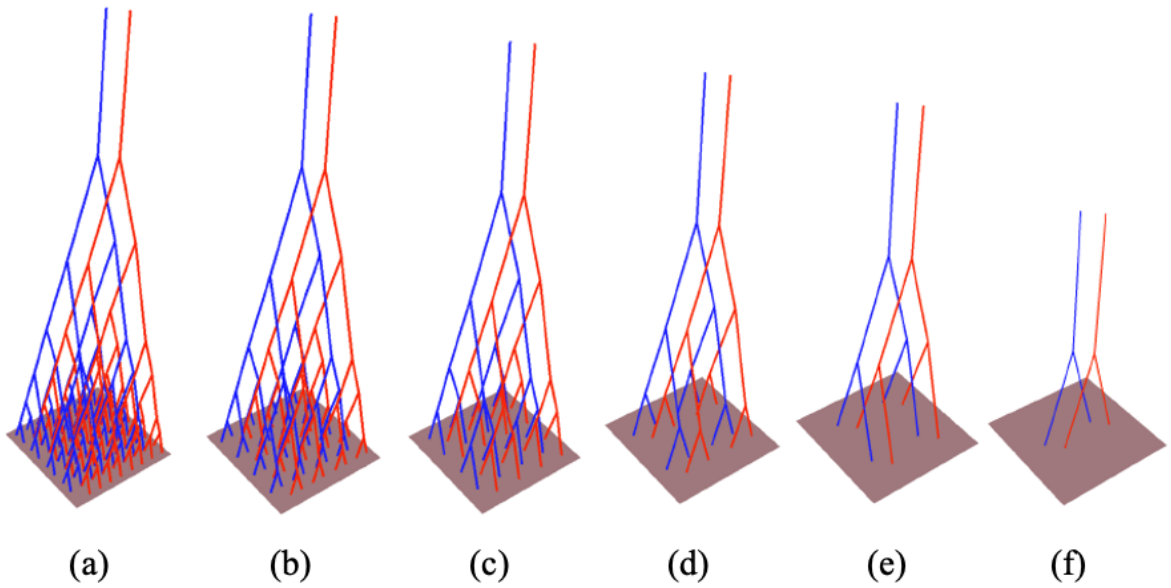

Figure 5.1: Simulation Domain (a) Nt64 (b) Nt32 (c) Nt16 (d) Nt8 (e) Nt4 (f) Nt2

In Eq. (5.1), subscripts $d1$ and $d2$ represent daughter-1 and daughter-2 of parent vessel, respectively. The value of λ has been researched extensively. In literature, $\lambda = 3$ is shown to provide uniform wall shear stress throughout the vasculature[86;125;126;154;155], while, $\lambda = 2$ minimizes the total cross-sectional area available for blood flow[155]. The blood vessel model developed for this research was only for preliminary study to understand the pressure drop parameter and SoI. Variation in the λ value is not expected to affect the correlation of the pressure drop parameter and SoI with the available vasculature. Thus, a value of $\lambda = 2.5$ was used for this work.

The arterial and venous networks will be addressed in this dissertation based on the number of terminal vessels (Nt). The arterial and venous networks bifurcate at each generation resulting in 2^n terminals, where n represents the branch generation level. The 6 generation tree consists of 64 terminals and was assumed to be the most detailed model for simulation purposes, and will be referred to as Nt64.

To generate the vasculature, the radii of terminal arterial vessels for Nt64 were equated to one voxel dimension. Similarly, the radii of terminal venous vessels for Nt64 were equated to 1.5 voxel dimension since veins are larger than arteries in general[156;157]. Using the bifurcation angle and Eq. 5.1, the radii and length of the vascular network were calculated. The dimensions of the blood vessels in the arterial and the venous networks at every branching level are shown in Table 5.1, where branch level 0 is the root branch of the arterial and the venous networks. Nt64 is shown in Fig. 5.1.a. To simulate the lack of detailed vasculature data, the terminal vessels of the networks were removed keeping the radii and length of the

Table 5.1: Dimensions of simulation domain

	Arterial Tree		**Venous Tree**	
Branch Level	radius (mm)	length (mm)	radius (mm)	length (mm)
0	5.27	100.00	7.91	100.00
1	4.00	77.88	6.00	77.80
2	3.03	77.62	4.54	77.62
3	2.29	38.32	3.44	38.32
4	1.74	38.32	2.61	38.32
5	1.32	19.65	1.98	19.65
6	1.00	18.68	1.50	18.68

rest of the branches same. Following this procedure, Nt32, Nt16, Nt8, Nt4 and Nt2 networks were generated as shown in Fig. 5.1.

Table 5.2: Parameters used for 2D flow simulation

Parameter	Symbol	Value	Units
Perfusion	α	0.5	$\mathrm{m\,s\,kg^{-1}}$
Arterial permeability[137]	$\mathrm{K_a}$	1×10^{-5}	$\mathrm{m^2}$
Venous permeability[137]	$\mathrm{K_v}$	1×10^{-5}	$\mathrm{m^2}$
Viscosity[130]	μ	3×10^{-3}	Pa s
Arterial inlet pressure	P_{in}	100	Pa
Venous outlet pressure	P_{out}	0	Pa
Voxel dimensions		1 x 1 x 1	$\mathrm{mm^3}$

The importance of the SoI radius is discussed in Chapter 4. A schematic to illustrate the same is shown in Fig. 5.2. In Fig. 5.2.a, four vascular terminals are shown each having a SoI of radius ϵ. The spread of the SoI from the four terminals does not cover the entire cell array. Thus, some cell voxels rely on inter-voxel perfusion to receive and exchange blood. In such a system, these cells could be oxygen deprived. To ensure that no cell-voxel is deprived of oxygenated blood, the ϵ of SoI was selected such that each cell-voxel lies within the spread of at least one arterial and one venous terminal, respectively. A 100 % coverage of tissue volume within SoI is shown in Fig. 5.2.b. As the number of vascular terminals reduces, the ϵ required to achieve a 100 % coverage of tissue volume within SoI increases. This is shown in Fig. 5.2.c and Fig. 5.2.d. For the simulation domains shown in Fig. 5.1, the percentage of volume coverage achieved for different values of ϵ is shown in Fig. 5.3.

The parameters used for simulation are given in Table 5.2. The value of the perfusion parameter (α) was limited by the total flow resistance offered by the arterial and venous networks. This was done because if the flow resistance between the arterial and venous compartments is larger than the flow resistance of the segmented vascular network, an unphysical condition of a negative flow rate results. Since the simulation domain was generated and not obtained from any medical imaging data or literature, the value of α was varied to avoid this condition.

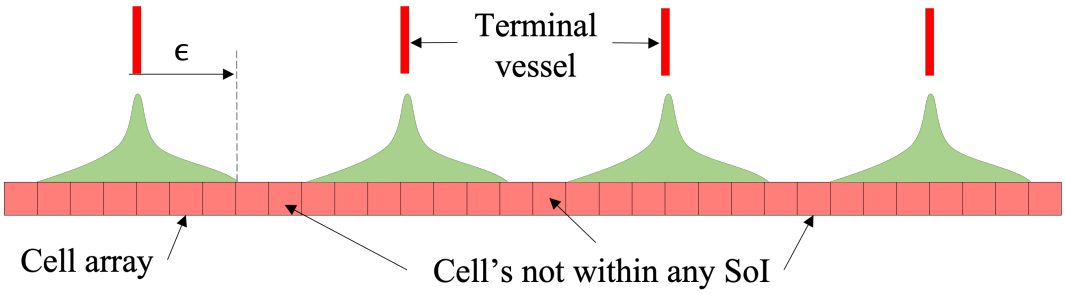

(a)

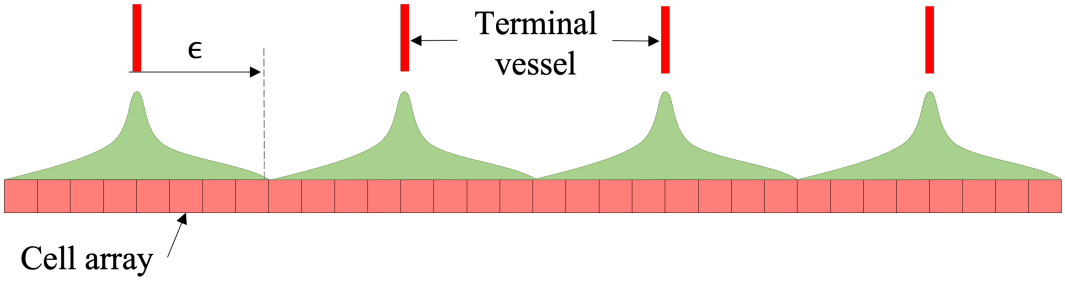

(b)

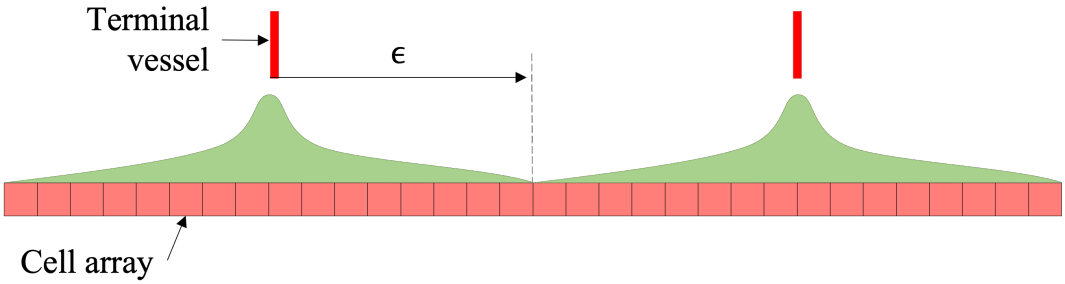

(c)

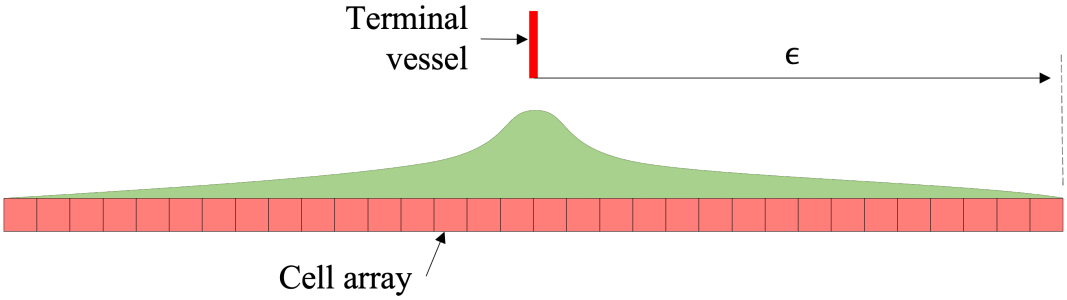

(d)

Figure 5.2: Representation of tissue volume coverage for different values of ϵ

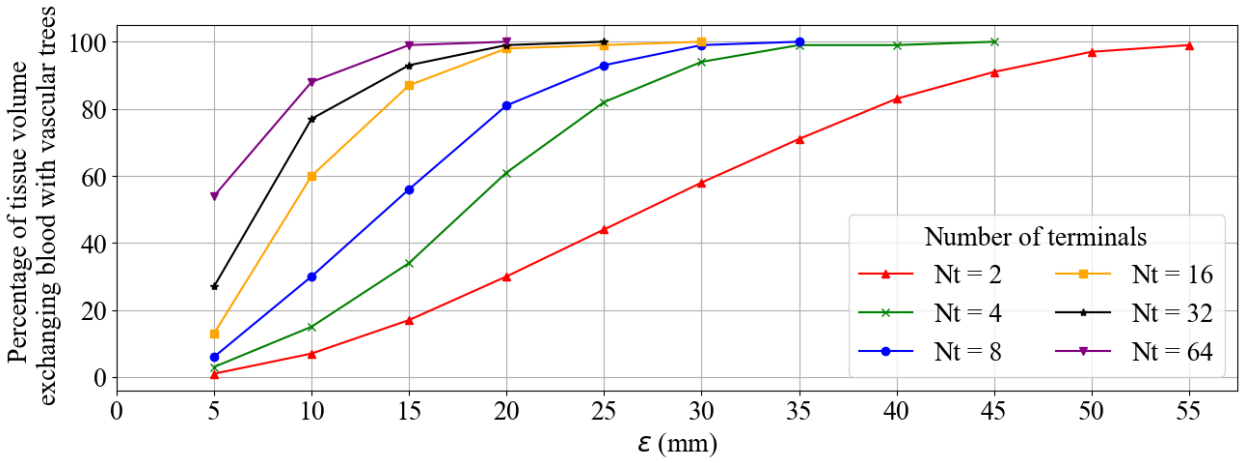

Figure 5.3: Effect of Nt and SoI on the fraction of tissue volume receiving direct blood from the arterial tree.

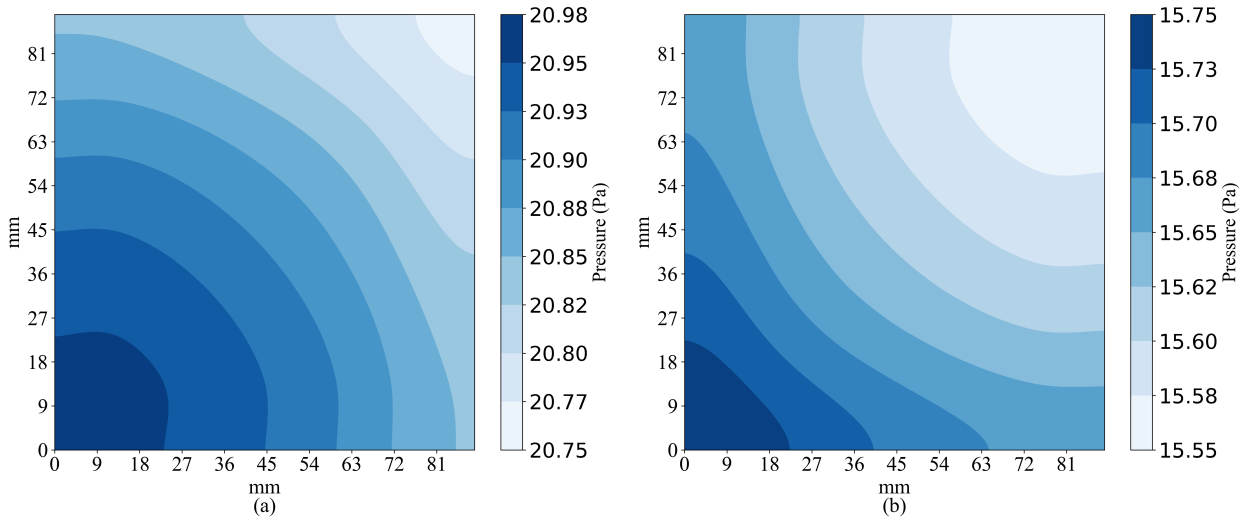

Figure 5.4: Pressure map for 64 terminals, $\epsilon = 20\,\text{mm}$ and $\gamma = 1 \times 10^{-5}\,\text{m}^3$ (a) Arterial compartment in tissue (b) Venous compartment in tissue

Using the simulation parameters given in Table 5.2 and Eqs. (4.10), (4.11), (4.12), (4.13), (4.14), (4.15), (4.16), and (4.17), the blood flow matrix was solved and the resulting total flow rate flowing through domain Nt64 was calculated. For this simulation, the pressure drop parameter for arterial and venous networks was taken to be $1 \times 10^{-5}\,\text{m}^3$. The pressure drop parameter represents the flow conductivity of the unsegmented, mathematically modeled blood vessels. A value of $\gamma = 1 \times 10^{-5}\,\text{m}^3$ was selected because it offered the flow conductivity of unsegmented vessels higher than the conductivity of segmented vascular tree. In other

words, for a value of $\gamma = 1 \times 10^{-5}\,\mathrm{m}^3$, the flow resistance of segmented vasculature dominates the flow in Nt64. This results in a total flow rate $\mathcal{Q}$ that is dependent on the physical blood vessels in Nt64, ensuring that Nt64 represents the most detailed network for this study. Once the total flow rate was obtained, the equivalent flow resistance ($\mathcal{R}_{eq}$) offered by Nt64 was calculated using Eq. (5.2).

$$\mathcal{R}_{eq} = \frac{P_{in} - P_{out}}{\mathcal{Q}} \tag{5.2}$$

As discussed earlier, ϵ determines the volume fraction covered by the SoIs of terminal vessels. As shown in Fig. 5.3, $\epsilon = 20\,\mathrm{mm}$ for Nt64 results in 99.9 % coverage. The pressure maps for the arterial and venous compartments for Nt64 and $\epsilon = 20\,\mathrm{mm}$ are shown in Fig. 5.4. This solution of Nt64 with $\epsilon = 20\,\mathrm{mm}$ is considered as the reference to which other simulation cases are compared.

5.1.1 Effect of the SoI Radius

The value of ϵ determines how much of tissue volume directly exchanges blood with the segmented vasculature. To study any variation that could occur in the results due to ϵ, different values of ϵ were simulated, and the results were compared.

Fig. 5.5 shows the pressure drop along the flow direction from the inlet of the arterial tree (0) to the outlet of the venous network (17). The pressure plots are shown for Nt64 for $\epsilon = 20\,\mathrm{mm}$ and $\epsilon = 10\,\mathrm{mm}$. In Fig. 5.5 nodes 8 and 9 represent the average pressure in the arterial and venous compartments of tissue voxels, respectively. Nodes 7 and 10 represent the terminal nodes of the arterial and venous vascular network for Nt64, respectively. Since the vascular networks are symmetric, the pressure gradient in daughter vessels is identical to each other.

It can be seen from Fig. 5.5 that the pressure slopes are identical. The value of ϵ does not affect the pressure drop across the vascular tree. The contour pressure maps in the arterial

and venous compartment of tissue voxel for $\epsilon = 10\,\text{mm}$ (Nt64) are shown in Fig. 5.6.a and Fig. 5.6.b, respectively. The pressure error for $\epsilon = 20\,\text{mm}$ and $\epsilon = 10\,\text{mm}$ is shown in Fig. 5.6.c and Fig. 5.6.d for arterial and venous compartment, respectively.

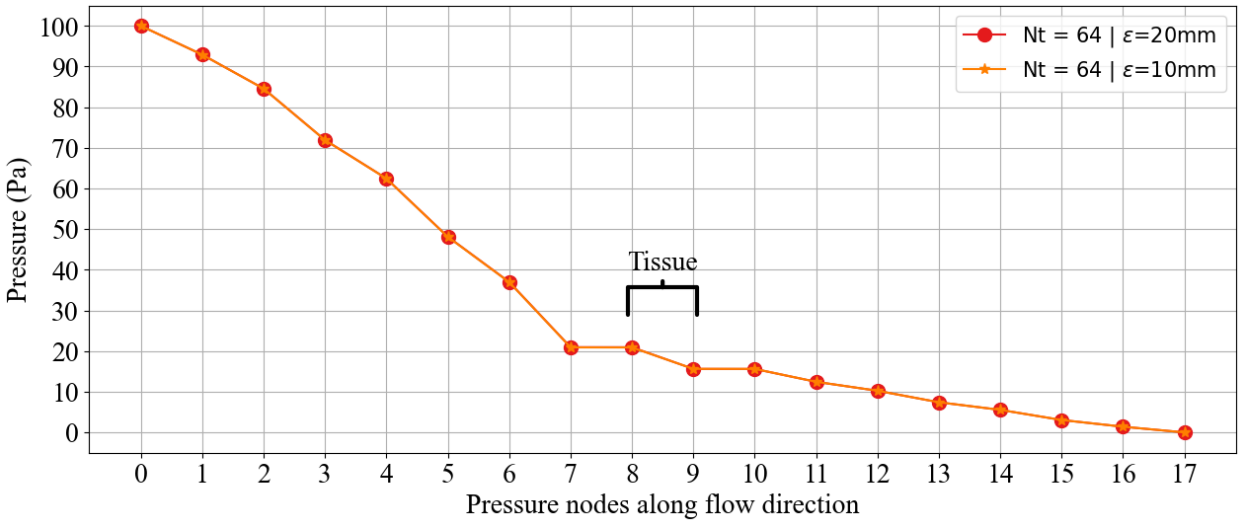

Figure 5.5: Effect of Nt and SoI on the fraction of tissue volume receiving direct blood from the arterial network.

The maximum error observed due to different ϵ is 0.019 Pa. Compared to a pressure drop of 100 Pa imposed as a boundary condition, the maximum error is less than 0.1 %. Thus, it can be concluded that ϵ does not affect flow simulation and the resulting pressure maps.

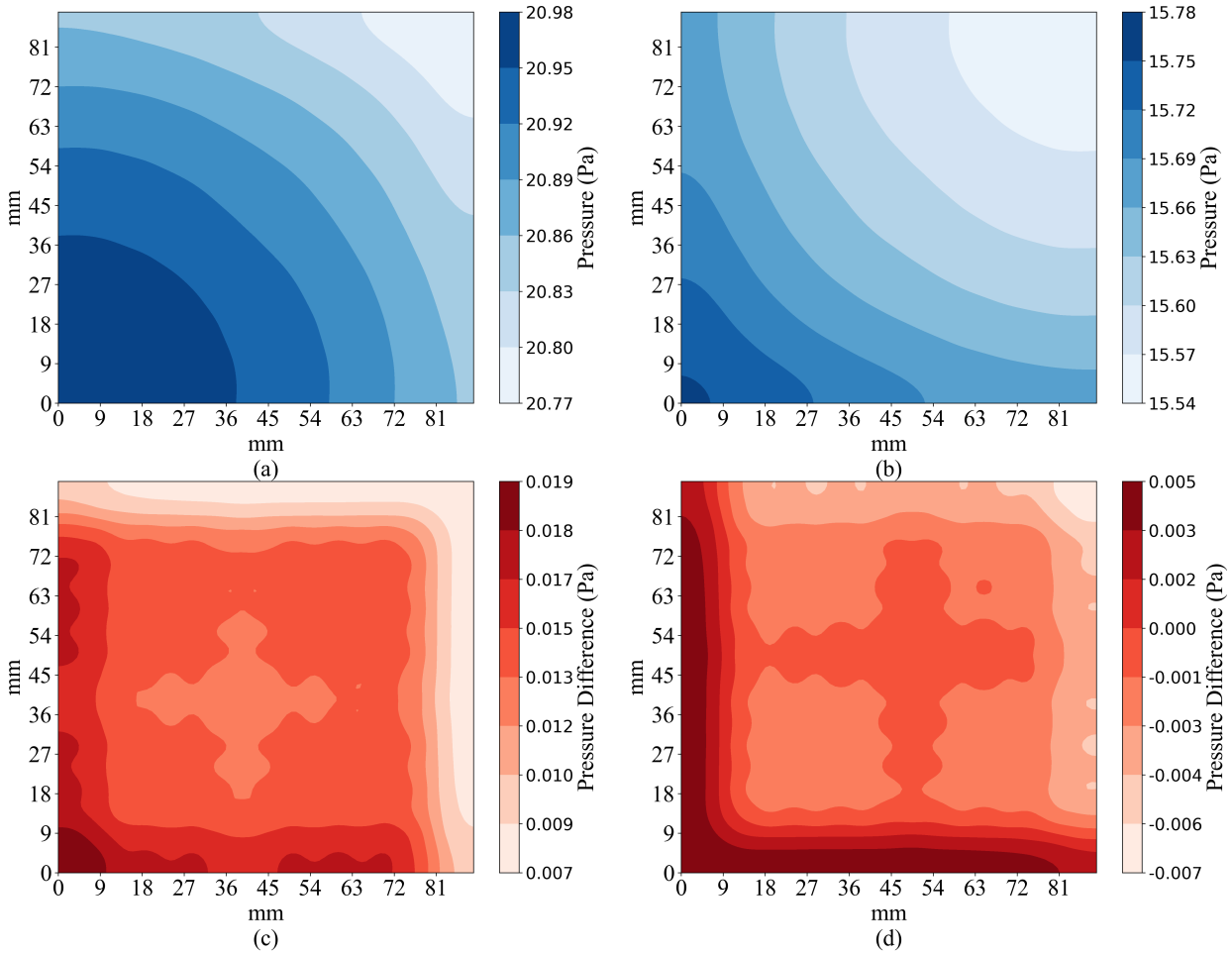

Figure 5.6: Pressure map for 64 terminals, $\epsilon = 10\,\text{mm}$ and $\gamma = 1 \times 10^{-5}\,\text{m}^3$
(a) Arterial compartment in tissue (b) Venous compartment in tissue
Pressure difference between $\epsilon = 20\,\text{mm}$ and $10\,\text{mm}$ (c) Arterial compartment (d) Venous compartment

5.1.2 Effect of the Pressure Drop Parameter

The pressure drop parameter represents the effective conductivity of the vasculature that could not be represented from medical imaging data due to lack of spatial resolution or computational memory limitations. The effect of lack of segmentation data on pressure gradient is shown in Fig. 5.7. As the available segmented vasculature decreases, the pressure gradient becomes more negative, i.e., the total flow rate flowing in the domain increases.

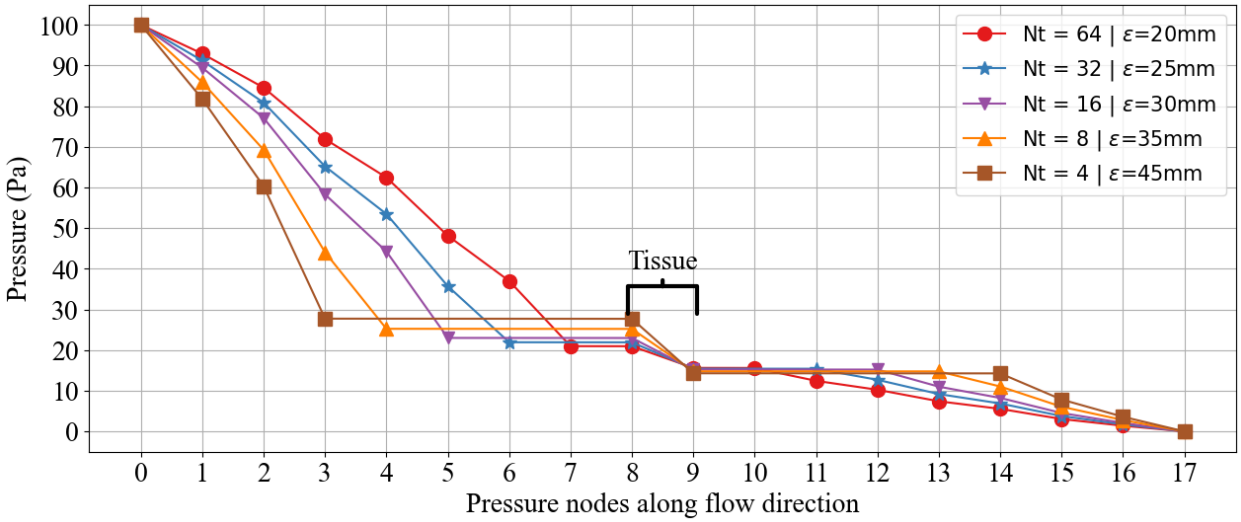

Figure 5.7: Effect of number of branch generations on $\mathcal{R}_{eq}$

As the number of branch generations are reduced, the $\mathcal{R}_{eq}$ offered by the network decreases, and the resultant flow rate $\mathcal{Q}$ increases for a constant pressure drop. In Fig. 5.7, a change in the $\mathcal{R}_{eq}$ is seen in the steepness of pressure gradient.

When the pressure drop parameter is adjusted as shown in Fig. 5.8, the $\mathcal{R}_{eq}$ of the network can be recovered. This demonstrates the importance of determining the correct pressure drop parameter when simulating blood flow network using the VoM-PhyS framework. In Fig. 5.8, when the pressure drop parameter is varied from $1 \times 10^{-5}\,\mathrm{m}^3$ to $8 \times 10^{-11}\,\mathrm{m}^3$ for Nt32, the pressure drop slopes shift closer to the reference solution, thus indicating that the correct pressure drop parameter can rectify the flow error.

Fig. 5.9.a, Fig. 5.9.b, Fig. 5.9.c and Fig. 5.9.d show the variation of flow rate $\mathcal{Q}$ for different values of γ for Nt32, Nt16, Nt8 and Nt4, respectively. The solution obtained for

Nt = 64, $\epsilon = 20\,\text{mm}$ and $\gamma_a = \gamma_v = 1 \times 10^{-5}\,\text{m}^3$ is used as a reference. The resulting flow rate in Nt64 for these parameters was $21.7\,\text{cm}^3\,\text{s}^{-1}$.

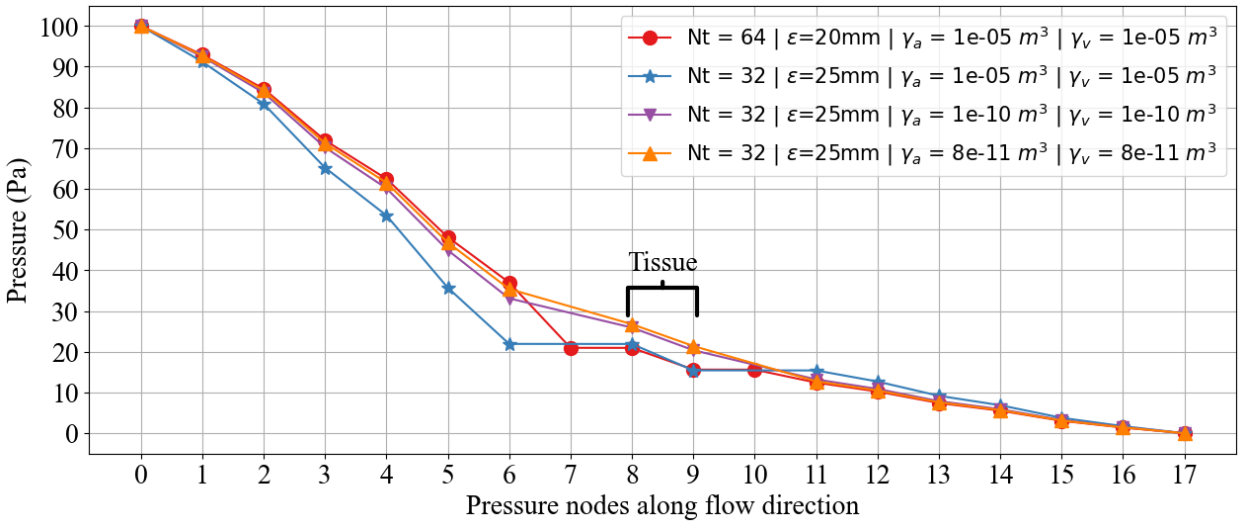

Figure 5.8: Effect of γ on $\mathcal{R}_{eq}$

For all the vascular networks shown (Nt32, Nt16, Nt8, and Nt4), the flow rate remains nearly constant up to a threshold value, and then it starts to decrease. This threshold value corresponds to the value where flow conductance (γ_a and γ_v) of virtual vessels equals the overall flow conductance offered by the physical vasculature. Before the threshold, the values of γ_a and γ_v offer higher flow conductance than the physical vessels, and the resistance of segmented blood vessels limits the flow rate. This is demonstrated by the plateaus observed in Fig. 5.9.

Once the values of γ_a for a given γ_v are lowered beyond the threshold, the flow resistance offered by the mathematical vessels is dominant and controls the overall flow rate. This behavior is observed by the sudden drop from plateau converging towards zero in Fig. 5.9. Conducting a graphical analysis, the value of γ_a can be extracted for a reference flow rate of $21.7\,\text{cm}^3\,\text{s}^{-1}$ for a given γ_v. This combination of γ_a and γ_v where the net flow rate of $21.7\,\text{cm}^3\,\text{s}^{-1}$ represents the optimum values of pressure drop parameter to be used in the simulation. The γ_a tends to lie between $1 \times 10^{-9}\,\text{m}^3$ and $1 \times 10^{-10}\,\text{m}^3$ for Nt32 (Fig. 5.9.a), Nt16 (Fig. 5.9.b), Nt8 (Fig. 5.9.c), and Nt4 (Fig. 5.9.d).

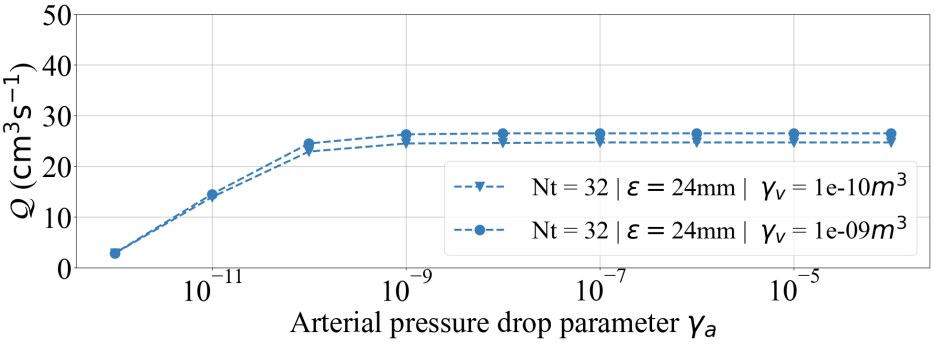

(a)

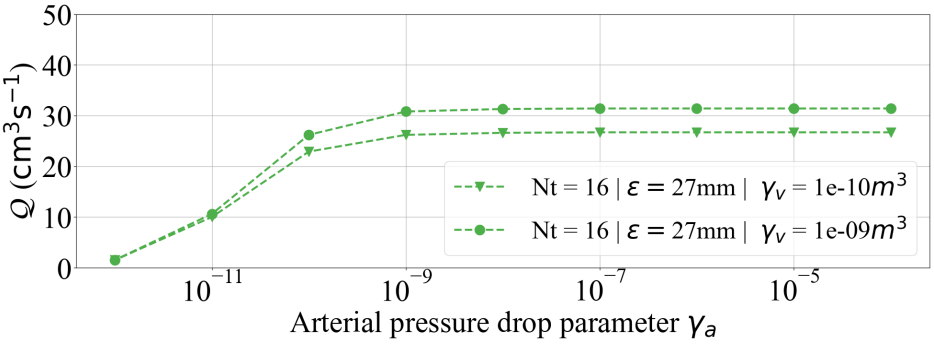

(b)

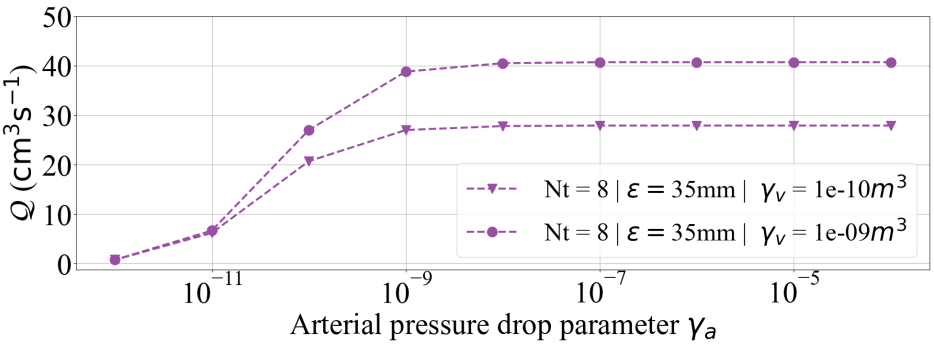

(c)

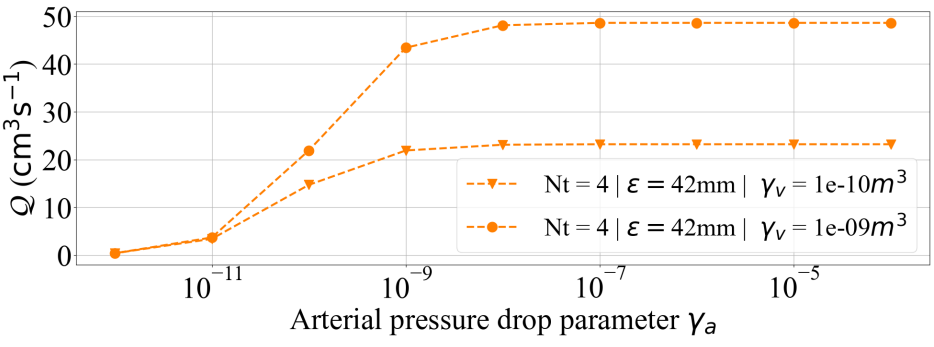

(d)

Figure 5.9: Variation in total flow rate with γ for (a) Nt32 (b) Nt16 (c) Nt8 (d) Nt4

5.2 Pressure Drop Parameter Equation

From the observations discussed in the previous section, it is evident that the pressure drop parameter is the key to simulating the correct pressure map in VoM-PhyS Framework. The previous section elaborates calculating the pressure drop parameter using graphical analysis. In this subsection, a mathematical equation to calculate the pressure drop parameter is derived.

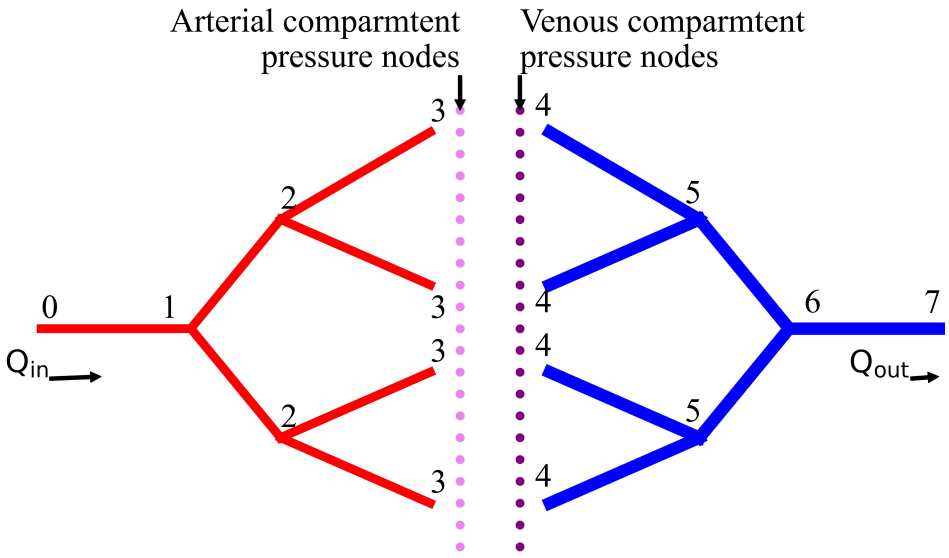

Figure 5.10: Example domain illustration

Fig. 5.10 illustrates an example domain with arterial and venous vasculature shown in the red and blue networks, respectively. The porous tissue region is represented using the pressure nodes for the arterial compartment and venous compartment. The net blood flow rate flowing in the volume is $\mathcal{Q}_{in}$ from the arterial side, and the net flow rate leaving the domain is $\mathcal{Q}_{out}$, respectively. Since mass is conserved, $\mathcal{Q}_{in}$ is equal to $\mathcal{Q}_{out}$ as shown in Eq. (5.3)

$$\mathcal{Q} = \mathcal{Q}_{in} = \mathcal{Q}_{out} \tag{5.3}$$

The flow entering the tissue domain is considered to be uniformly distributed[85;86;124;125].

Thus, the flow rate leaving the arterial terminals (nodes: 3) is considered to be equal. With the equal distribution assumption, the blood flow rate in the terminal vessels is calculated using Eq. (5.4) where n represents the number of bifurcation generations. In the illustrated example, n is equal to 2.

$$\mathcal{Q}_{term} = \frac{\mathcal{Q}}{2^n} \tag{5.4}$$

In Fig. 5.10, the arteries and veins are considered to be the segmented vasculature for which the length and diameter can be calculated from imaging data. Using the dimensions of the vasculature, the equivalent flow resistance offered by each arterial and venous vascular tree can be calculated using parallel and series resistance methods. The equivalent resistance of arterial and venous trees are represented as $\mathcal{R}_A$ and $\mathcal{R}_V$, respectively, and shown in Fig. 5.11. The blood flow equation for the arterial and venous trees is shown in Eq. (5.5) and Eq. (5.6), respectively.

$$(P_{in} - P_{A,term}) = \mathcal{Q}\mathcal{R}_A \tag{5.5}$$

$$(P_{V,term} - P_{out}) = \mathcal{Q}\mathcal{R}_V \tag{5.6}$$

In Eq. (5.5) and Eq. (5.6), The terminal pressure for arterial tree and venous tree is represented as $P_{A,term}$ and $P_{V,term}$, respectively. Rearranging Eq. (5.5) and Eq. (5.6), Eq. (5.7) and Eq. (5.8) are obtained.

$$P_{A,term} = P_{in} - \mathcal{Q}\mathcal{R}_A \tag{5.7}$$

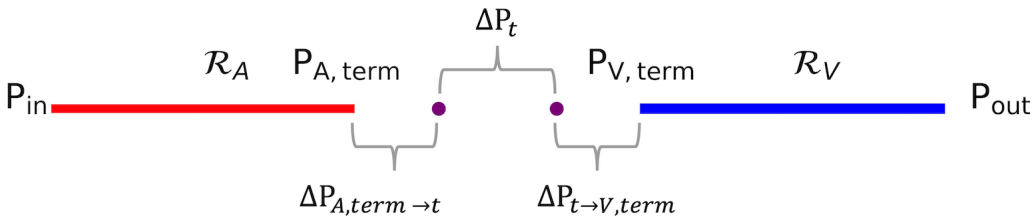

Figure 5.11: Simplified domain

$$P_{V,term} = P_{out} + \mathcal{Q}\mathcal{R}_V \tag{5.8}$$

The total pressure drop between terminal arteries and terminal veins can be calculated using Eq. (5.9), where $\Delta P_{A,term\rightarrow t}$ and $\Delta P_{t\rightarrow V,term}$ represent the pressure drop between the terminal artery and arterial compartment, and, venous compartment and terminal vein, respectively. ΔP_t represents the pressure drop across arterial and venous compartments within the tissue and is calculated using the perfusion coefficient (α) as shown in Eq. (5.10).

$$P_{A,term} - P_{V,term} = \Delta P_{term} = \Delta P_{A,term\rightarrow t} + \Delta P_t + \Delta P_{t\rightarrow V,term} \tag{5.9}$$

$$\Delta P_t = \frac{\mathcal{Q}}{\alpha V} \tag{5.10}$$

In the previous section, a correlation between the flow resistance of arterial and venous trees and the pressure drop between terminal vessels and tissue was observed. Thus, a hypothesis is proposed between the flow resistance and pressure drop between terminal vessels

and tissue as shown in Eq. (5.11)

$$\frac{\Delta P_{A,term\rightarrow t}}{\Delta P_{t\rightarrow V,term}} = \left[\frac{\mathcal{R}_A}{\mathcal{R}_V}\right] = \psi \tag{5.11}$$

$$\Delta P_{A,term\rightarrow t} = \psi \Delta P_{t\rightarrow V,term} \tag{5.12}$$

Using Eq.(5.12) and substituting in Eq. (5.9), equations for $\Delta P_{A,term\rightarrow t}$ and $\Delta P_{t\rightarrow V,term}$ are derived, shown in Eq. (5.13) and Eq. (5.14), respectively

$$\Delta P_{A,term\rightarrow t} = \frac{\psi(\Delta P_{term} - \Delta P_t)}{(\psi + 1)} \tag{5.13}$$

$$\Delta P_{t\rightarrow V,term} = \frac{(\Delta P_{term} - \Delta P_t)}{(\psi + 1)} \tag{5.14}$$

The resistance equation for flow in virtual vessels can be written as Eq. (5.15) and (5.16) where the resistance offered by virtual arterial and venous networks is represented using blood viscoity μ and pressure drop parameter γ_β

$$\Delta P_{A,term\rightarrow t} = \mathcal{Q}_{A,term}\frac{\mu}{\gamma_a} \tag{5.15}$$

$$\Delta P_{t\rightarrow V,term} = \mathcal{Q}_{V,term}\frac{\mu}{\gamma_v} \tag{5.16}$$

Using Eq. (5.13), (5.14) and Eq. (5.15), (5.15), the equations to determine pressure drop parameter for the arterial and venous tree is derived as shown in Eq. (5.17) and Eq. (5.18), respectively.

$$\gamma_a = \frac{\mathcal{Q}\mu}{2^n \Delta P_{A,term \to t}} \tag{5.17}$$

$$\gamma_v = \frac{\mathcal{Q}\mu}{2^n \Delta P_{t \to V,term}} \tag{5.18}$$

The Equations can be further modified by substituting Eq. (5.13) and Eq. (5.14) to obtain Eq. (5.19) and Eq. (5.20).

$$\gamma_a = \frac{\mathcal{Q}\mu}{2^n} \frac{(\psi + 1)}{\psi \left[\Delta P_{term} - \frac{\mathcal{Q}}{\alpha V}\right]} \tag{5.19}$$

$$\gamma_v = \frac{\mathcal{Q}\mu}{2^n} \frac{(\psi + 1)}{\left[\Delta \mathrm{P}_{\mathrm{term}} - \frac{\mathcal{Q}}{\alpha V}\right]} \tag{5.20}$$

Eq. (5.17) and Eq. (5.18) are further modified as Eq. (5.21) and Eq. (5.22)

$$\gamma_a = \frac{\mu \mathcal{Q}}{2^n} \frac{(\frac{\mathcal{R}_A}{\mathcal{R}_V} + 1)}{\frac{\mathcal{R}_A}{\mathcal{R}_V} \left[\Delta P - \mathcal{Q}\left[\mathcal{R}_A + \mathcal{R}_V + (\alpha V)^{-1}\right]\right]} \tag{5.21}$$

$$\gamma_v = \frac{\mu \mathcal{Q}}{2^n} \frac{(\frac{\mathcal{R}_A}{\mathcal{R}_V} + 1)}{\left[\Delta P - \mathcal{Q}\left[\mathcal{R}_A + \mathcal{R}_V + (\alpha V)^{-1}\right]\right]} \tag{5.22}$$

Eq. (5.21) and Eq. (5.22) are the final forms of equations to calculate the pressure drop parameter for arterial and venous trees. It can be seen from these equations that the pressure drop parameters can be calculated using total blood flow rate in the simulation domain, pressure drop across the simulation domain and the equivalent resistance of arterial and venous trees calculated from the segmented vasculature.

5.3 Application of the Pressure Drop Parameter Equation

5.3.1 2D Domain

The domain in Fig. 5.12 is similar to Fig. 5.1, the only difference being, two extra generations of bifurcation have been modeled to create Nt256. To get a reference flow rate for Nt256, the γ_a and γ_v were considered as $1 \times 10^{-5}\,\mathrm{m}^3$. This was done to provide a very high flow conductivity in the mathematically modeled vessels for Nt256. The resultant flow rate from this simulation was considered as the reference flow rate for analysis. The pressure drop parameter value for Nt256 are shown in Table 5.3. The pressure drop parameter for arterial and venous trees is calculated using Eq. (5.21) and Eq. (5.22). The pressure drop parameter for Nt256 shown in Table 5.3 represents the minimum value for which reference flow rate will be affected only by the resistance of physical vasculature.

Table 5.3: Pressure drop parameters obtained from Eq. (5.21) and Eq. (5.22) for 2D domain

Nt	γ_a (m^3)	γ_v (m^3)	% error in $\mathcal{Q}$
256	1.54×10^{-7}	1.45×10^{-6}	0.00
128	1.05×10^{-10}	9.83×10^{-10}	0.01
64	1.26×10^{-10}	1.19×10^{-9}	0.04
32	1.49×10^{-10}	1.4×10^{-9}	0.08
16	2.35×10^{-10}	2.21×10^{-9}	0.05
8	3.70×10^{-10}	3.47×10^{-9}	0.01
4	6.47×10^{-10}	6.07×10^{-9}	0.06
2	1.10×10^{-9}	1.03×10^{-8}	0.36

Fig. 5.13 and Fig. 5.14 show the pressure maps for (a) arterial compartment, (b) venous compartment, and error in the pressure maps with reference to Nt256 in (c) arterial compartment and (d) venous compartment, respectively. The pressure maps and error maps for Nt64, Nt32, Nt16, Nt8, and Nt4 are shown in the Appendix as Fig. A.1, Fig. A.2, Fig. A.3, Fig. A.4, and Fig. A.5, respectively.

From Table 5.3 and Figs. 5.13 and 5.14, it is confirmed that the equations for pressure drop parameters (Eq. (5.21) and Eq. (5.22)) derived in previous section are accurate and can

determine the flow resistance of unsegmented vessels.

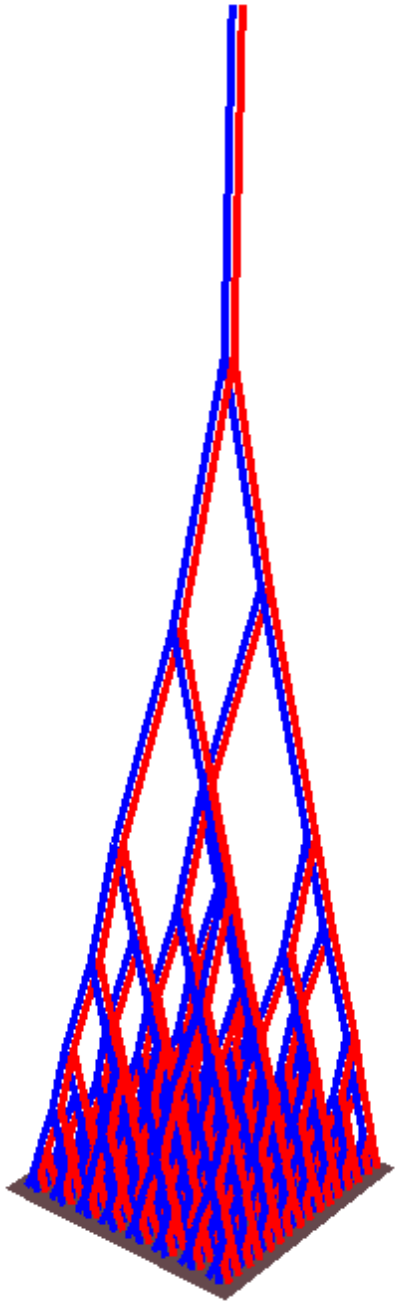

Figure 5.12: Simulation domain Nt256

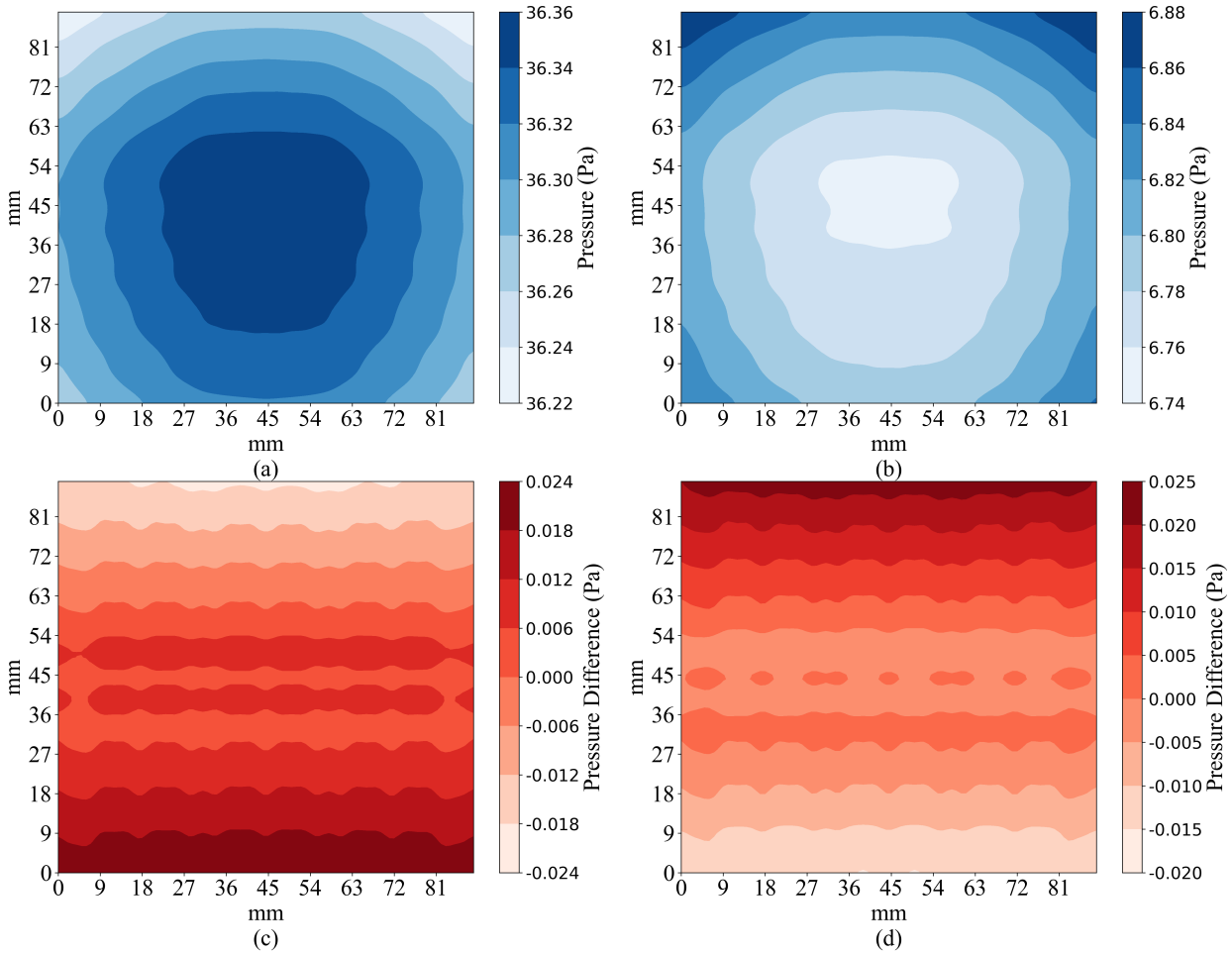

Figure 5.13: Nt128
(a) Arterial compartment pressure map (b) Venous compartment pressure map (c) Error in arterial compartmental pressure compared to Nt256 (d) Error in venous compartmental pressure compared to Nt256

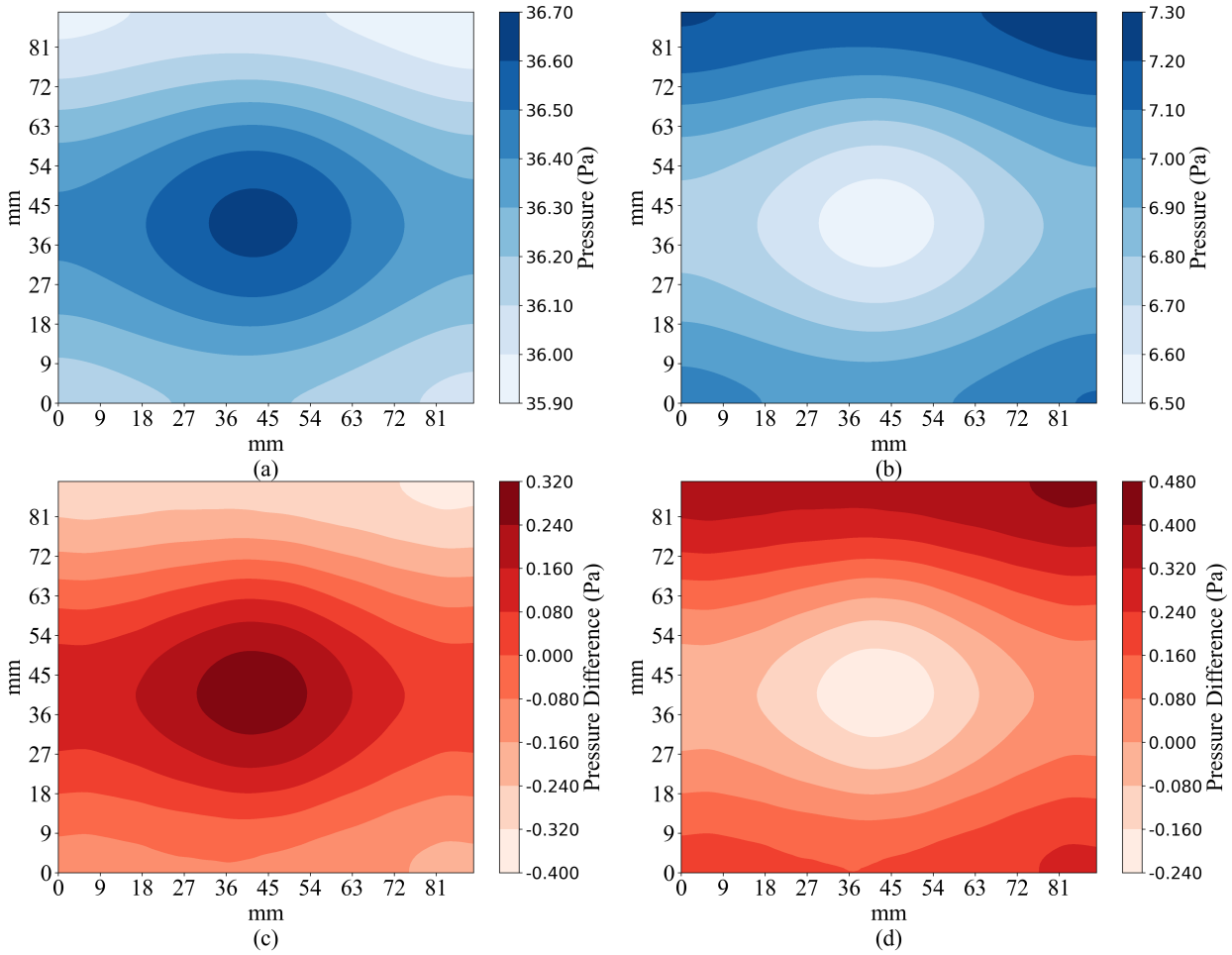

Figure 5.14: Nt2
(a) Arterial compartment pressure map (b) Venous compartment pressure map (c) Error in arterial compartmental pressure compared to Nt256 (d) Error in Venous compartmental pressure compared to Nt256

5.3.2 3D Domain analysis

To verify the applicability of the Eq. (5.21) and Eq. (5.22) on a 3D domain, a test case shown in Fig. 5.15 was generated using Rhinoceros[132]. The domain modeled had 32 terminals for arterial and venous trees, and the cuboidal tissue size encasing the vasculature was 20 cm x 20 cm x 20 cm. The voxel dimensions were 2.5 mm x 2.5 mm x 2.5 mm. The 32 terminal domain was considered as a reference solution for comparison and will be referred to as Case 1 henceforth. Similar to the 2D domain, the number of terminals was reduced gradually to create different simulation domains which are shown in Fig. 5.16. The resultant domains are termed Case 2, Case 3, Case 4, and Case 5 for 16, 8, 4, and 2 terminals, respectively (Fig. 5.16).

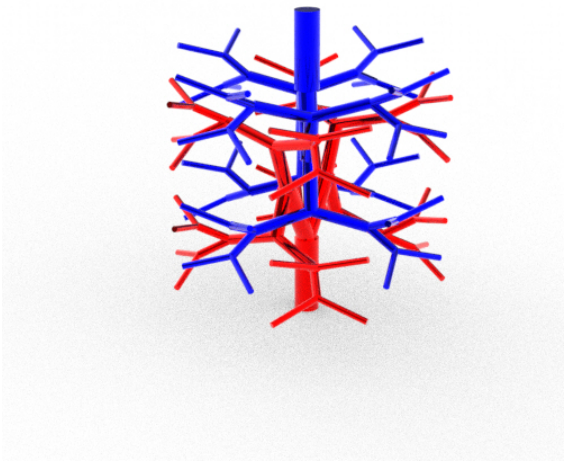

Figure 5.15: 3D simulation domain

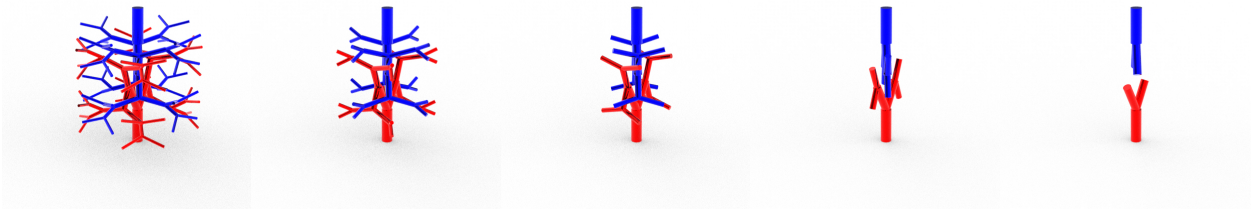

(a) Case 1 (b) Case 2 (c) Case 3 (d) Case 4 (e) Case 5

Figure 5.16: 3D simulation domain cases

The dimensions of arterial and venous tree were considered same for this simulation for simplicity and are given in Table 5.4

Table 5.4: Dimensions of vasculature in 3D Domain

Branch level	radius (mm)	length (mm)
0	8.00	50.00
1	6.06	44.70
2	4.60	31.60
3	3.48	36.70
4	2.64	23.50
5	2.00	33.10

An inlet pressure of 1000 Pa was applied at the arterial inlet node and an exit pressure of 1 Pa at the venous outlet node. To calculate the reference flow rate, the pressure drop parameter for arterial and venous trees were taken as $1\,m^3$. Similar to 2D analysis, this was done to ensure that the resultant flow rate is limited by physical vasculature and not mathematical pressure drop parameter. Using the calculated net flow equivalent flow rate, the pressure drop parameter for various case were calculated using Eq. (5.21) and Eq. (5.22), and are given in Table 5.5.

Table 5.5: Pressure drop parameters calculated using Eq. (5.21) and Eq. (5.22) for 3D domain

case	Nt	γ_a (m^3)	γ_v (m^3)
1	32	8.29×10^{-7}	8.29×10^{-7}
2	16	3.78×10^{-10}	3.78×10^{-10}
3	8	5.16×10^{-10}	5.16×10^{-10}
4	4	7.76×10^{-10}	7.76×10^{-10}
5	2	1.36×10^{-9}	1.36×10^{-9}

The pressure maps for the arterial compartment and venous compartment at $z = 40$ are shown in Fig. 5.18 and Fig. 5.19, respectively. The location of slice z = 40 is shown in Fig. 5.17. The pressure maps are fairly consistent as seen in Fig. 5.20 with errors less than $\pm$ 0.7 Pa. The pressure maps for other z locations are given in Appendix B.

Similar to the 2D analysis, the pressured drop parameter equations (Eqs. (5.21) and (5.22)) are accurate in simulating flow and pressure maps for domains where segmented vasculature is limited, as can be seen from the pressure maps.

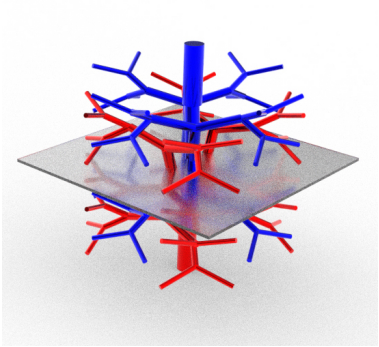

Figure 5.17: Location of $z = 40$

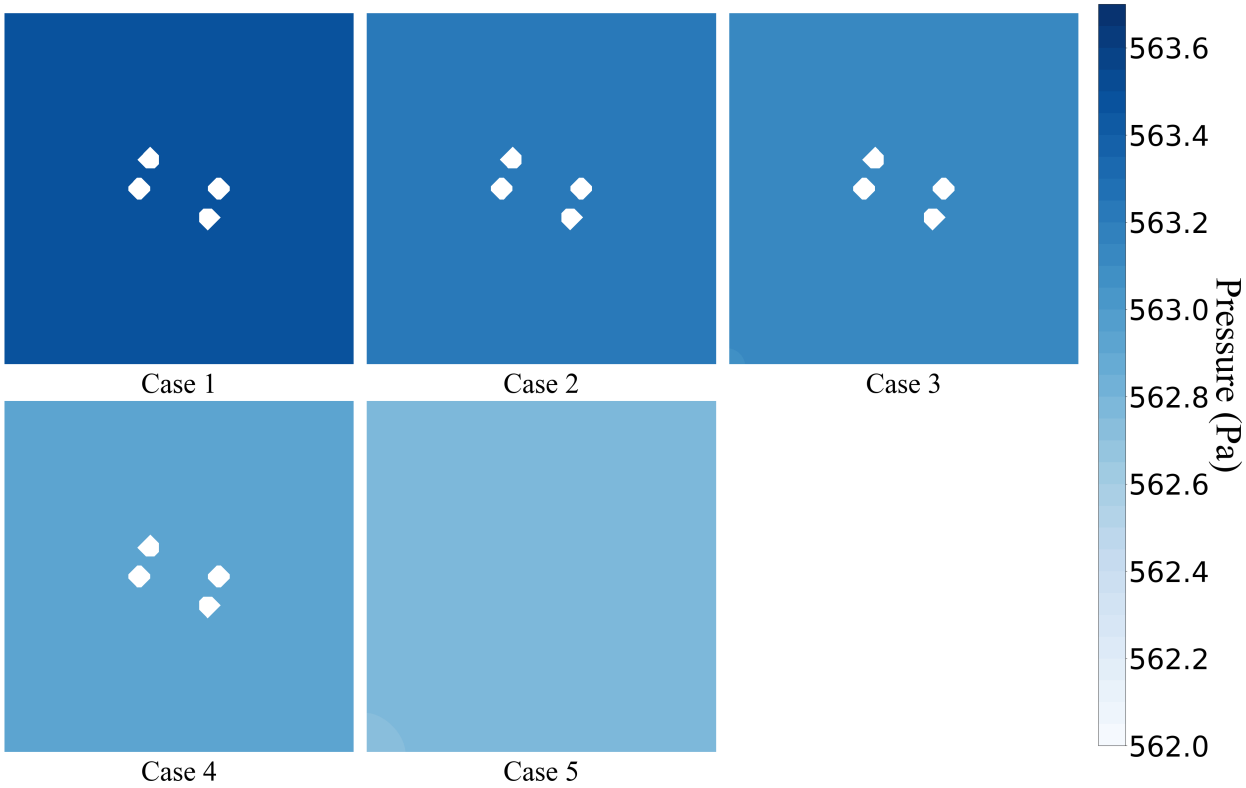

Figure 5.18: Arterial compartment pressure map of five simulation cases at $z = 40$

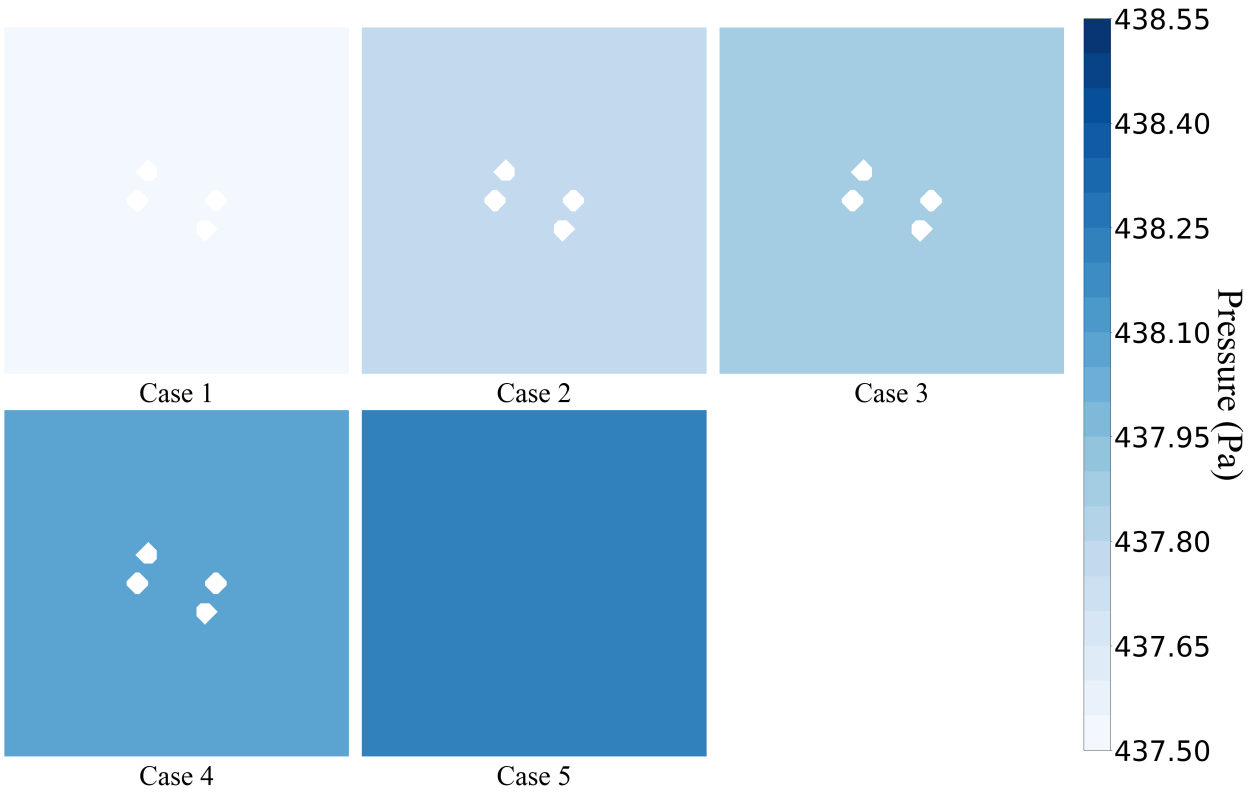

Figure 5.19: Venous compartment pressure map of five simulation cases at $z = 40$

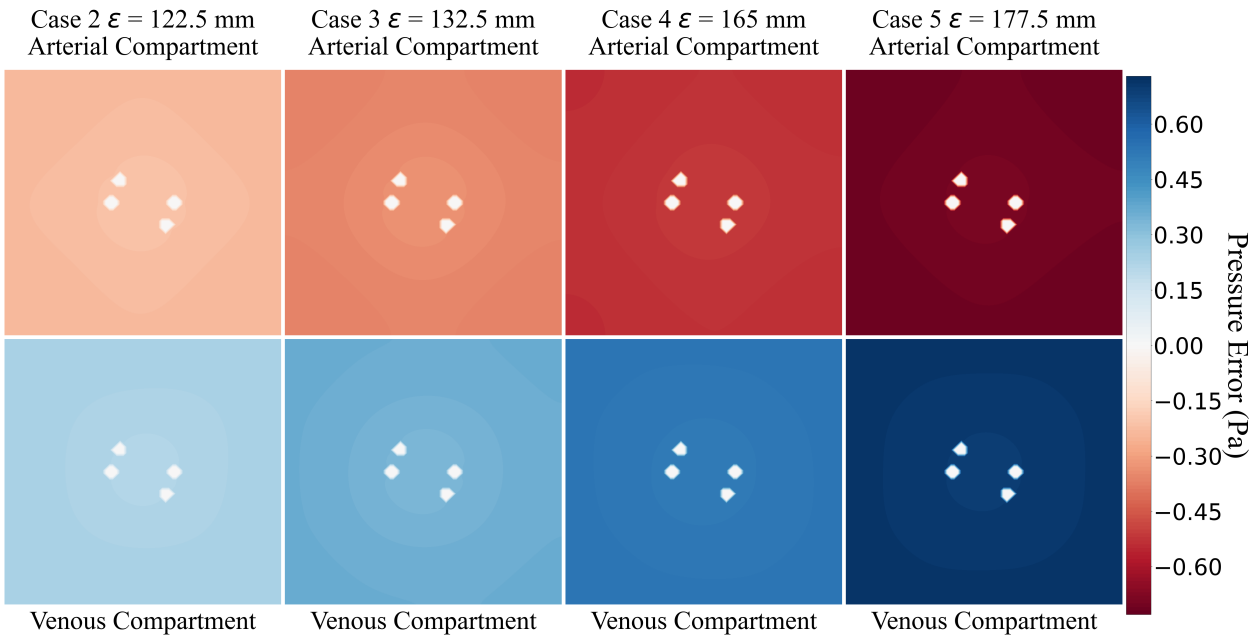

Figure 5.20: Pressure error at $z = 40$

5.4 Energy Analysis

Once the pressure maps across the simulation domain were examined, analysis to determine the changes in heat exchange due to lack of segmentation data was conducted. The goal was to observe the error introduced in the simulation due to the lack of segmentation data. The parameters used for energy analysis are given in Table 5.6.

Table 5.6: Parameters used for 3D energy simulation

Parameter	Symbols	Value	Units
Specific heat	c_{pt}	1000	$\mathrm{J\,kg^{-1}\,{}^{\circ}C^{-1}}$
Density	ρ_t	1000	$\mathrm{kg\,m^{-3}}$
Thermal conductivity[130]	k_t	0.5	$\mathrm{W\,m^{-1}\,{}^{\circ}C^{-1}}$
Perfusion	α	1×10^{-3}	$\mathrm{m\,s\,kg^{-1}}$
Arterial permeability[137]	$\mathrm{K_a}$	1×10^{-5}	$\mathrm{m^2}$
Venous permeability[137]	$\mathrm{K_v}$	1×10^{-5}	$\mathrm{m^2}$
Metabolic heat gen. rate	$\dot{q}_m$	1000	$\mathrm{W\,m^{-3}\,s^{-1}}$
Viscosity[130]	μ	3×10^{-3}	Pa s
Ambient temperature	T_∞	20	$^{\circ}$C
Inlet blood temperature	T_{in}	35	$^{\circ}$C
Ambient convective heat transfer coefficient	h_{amb}	10	$\mathrm{W\,m^{-2}\,{}^{\circ}C^{-1}}$
Blood convective heat transfer coefficient	h_b	10	$\mathrm{W\,m^{-2}\,{}^{\circ}C^{-1}}$

The temperature contours at $z = 40$ for Case 1, Case 2, Case 3, Case 4 and Case 5 are shown in Fig. 5.21. The temperature plots for other z locations are given in the Appendix (Fig. C.1, Fig. C.2, Fig. C.3, Fig. C.4). The thermal map of Case 1 (32 vascular terminals) was considered as the reference solution. The temperature maps of Case 2 (16 terminals), Case 3 (8 terminals), Case 4 (4 terminals), and Case 5 (2 terminals) are compared with the reference solution of Case 1. To analyze the error, the dimensionless temperature error θ_i is calculated using Eq. (5.23).

$$\theta_i = \frac{T_{c,i} - T_{ref,i}}{T_{in} - T_{amb}} \tag{5.23}$$

In Eq. (5.23), subscript i represents the voxel index, c represents the case number 2,3,4, and 5, and *ref* represents Case 1.

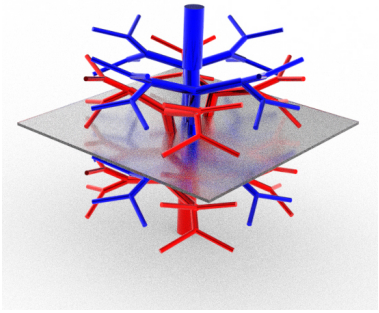

(a)

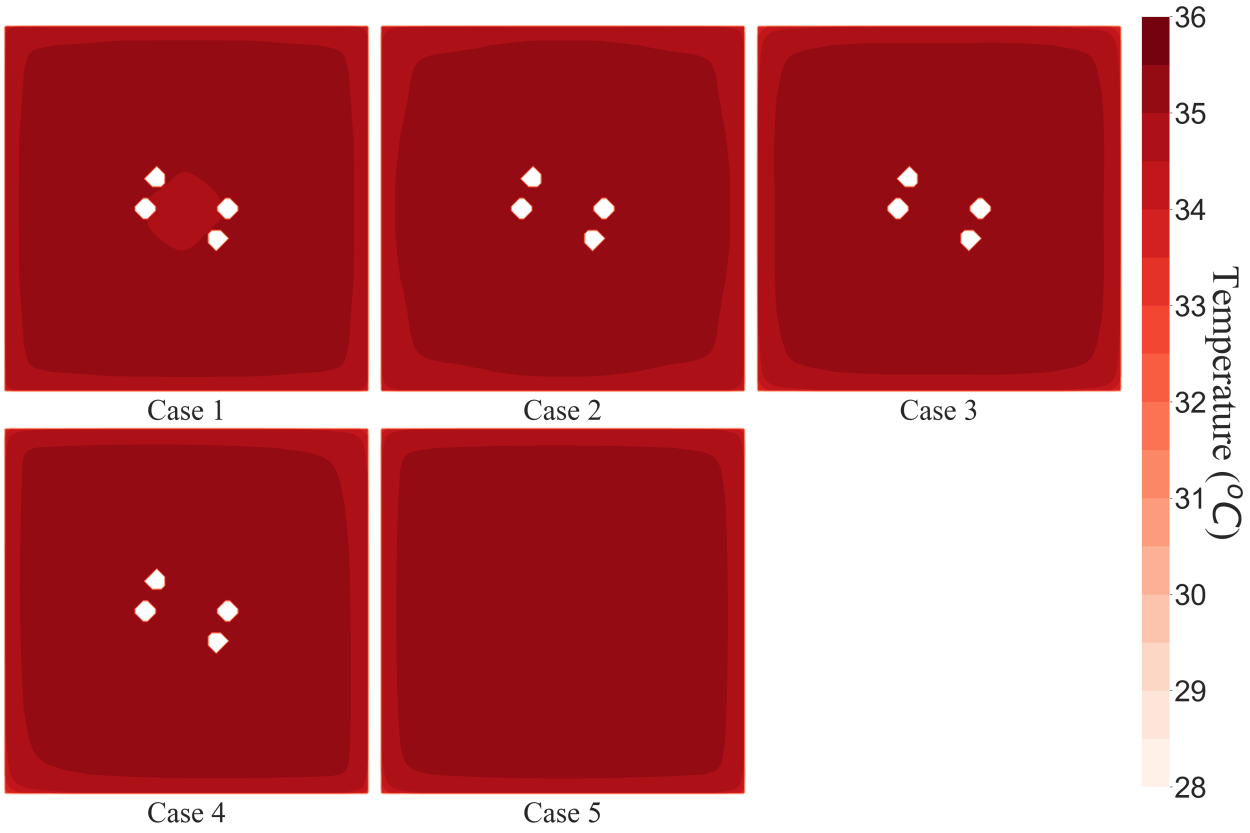

(b)

Figure 5.21: Temperature at z = 1

The observed maximum dimensionless temperature error and maximum temperature error are given in Table 5.7. The temperature error for various cases at $z = 40$ are shown in Fig. 5.22, Fig. 5.23, Fig. 5.24, and Fig. 5.25. The temperature error plot at other z locations is given in the Appendix D. Fig. 5.26 and Fig. 5.27 show the error plots at $z = 1$ and $z = 80$ for all the cases.

Table 5.7: Maximum temperature error observed in various simulation cases

Case	θ	ΔT (°C)
Case 2	$\pm$ 0.09	$\pm$ 1.37
Case 3	$\pm$ 0.10	$\pm$ 1.50
Case 4	$\pm$ 0.13	$\pm$ 2.05
Case 5	$\pm$ 0.18	$\pm$ 2.74

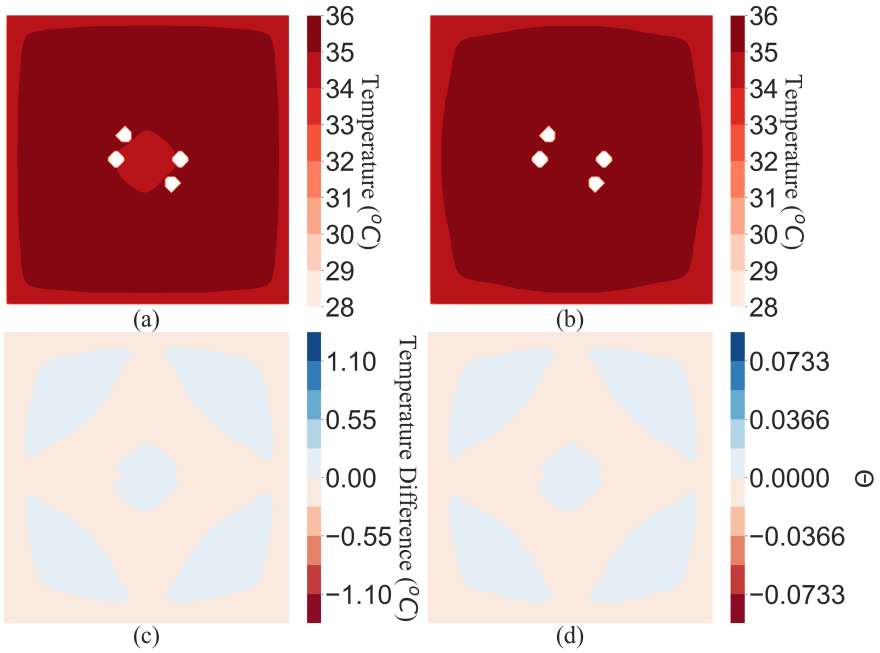

Figure 5.22: Temperature error in Case 2 at z = 40 (a) Temperature map of Case 1 (b) Temperature map of Case 2 (c) Temperature difference between Case 2 and Case 1 (d) Non-dimensional temperature error between Case 2 and Case 1

As can be seen from Fig. 5.22 to Fig. 5.27, the maximum error is observed at the four edges of the cuboidal tissue domain. It is important to note that such sharp edges are not typically observed in biological tissues and organs. An important observation from the above simulation is that the maximum error in Case 5 is $-1.26\,^{\circ}$C in the region away from the extremities of tissue. Similarly, the maximum errors for Case 2, Case 3, and Case 4 in the region away from eight corners of the tissue were $-0.3\,^{\circ}$C, $-0.93\,^{\circ}$C, and $-1.17\,^{\circ}$C, respectively. The negative temperature error shows that lack of segmented vascular data results in lower temperatures than the reference domain.

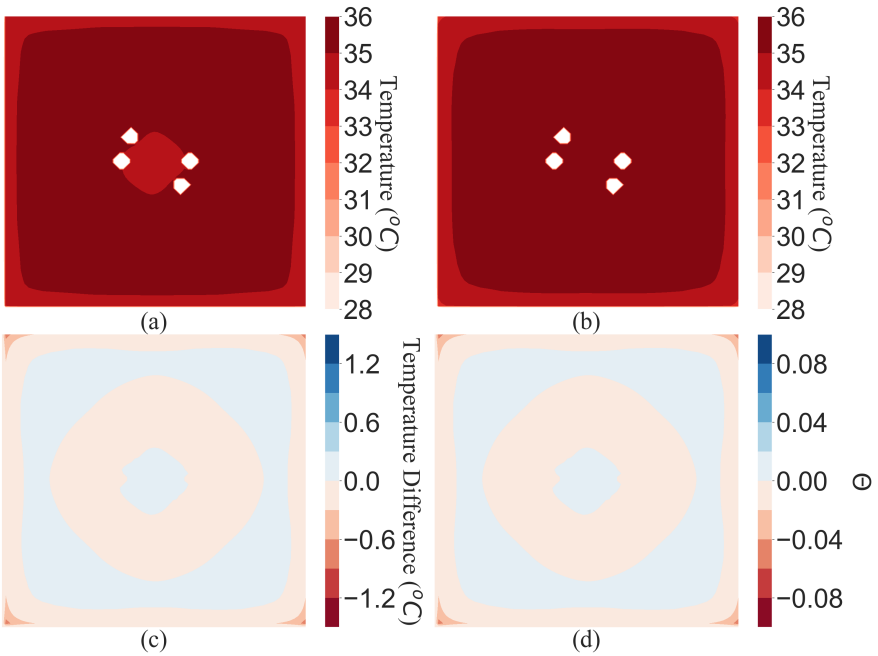

Figure 5.23: Temperature error in Case 3 at z = 40 (a) Temperature map of Case 1 (b) Temperature map of Case 3 (c) Temperature difference between Case 3 and Case 1 (d) Non-dimensional temperature error between Case 3 and Case 1

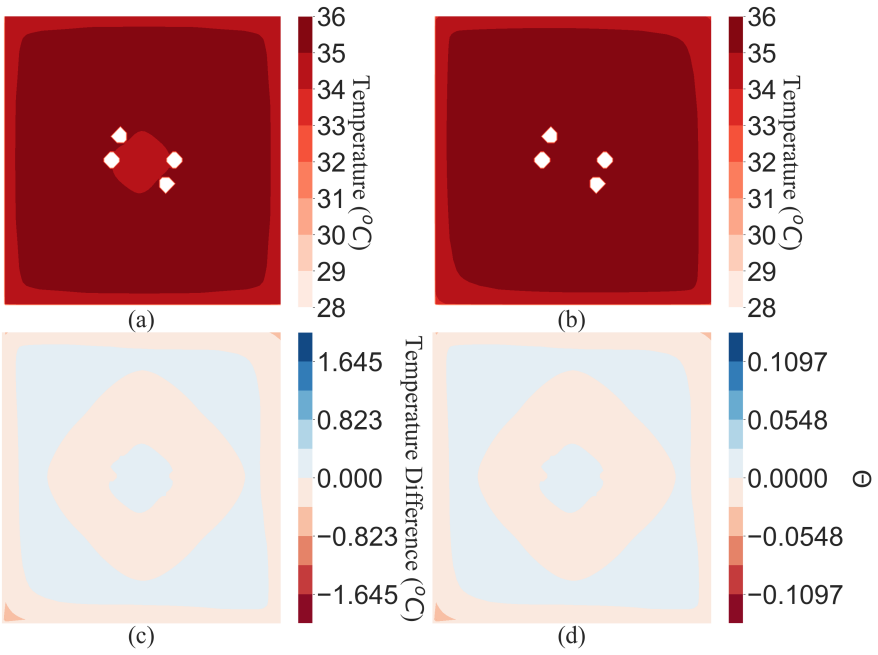

Figure 5.24: Temperature error in Case 4 at z = 40 (a) Temperature map of Case 1 (b) Temperature map of Case 4 (c) Temperature difference between Case 4 and Case 1 (d) Non-dimensional temperature error between Case 4 and Case 1

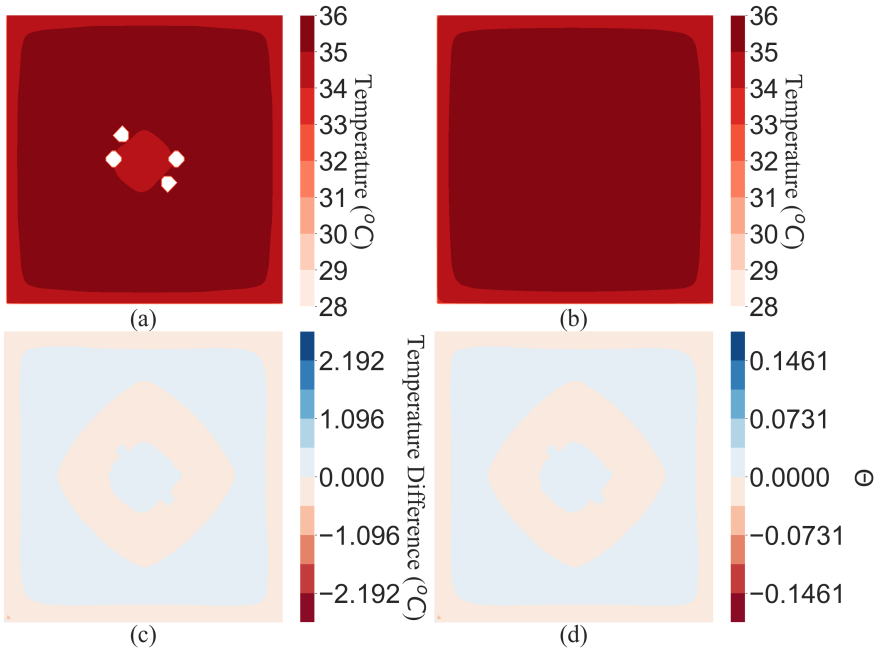

Figure 5.25: Temperature error in Case 5 at z = 40 (a) Temperature map of Case 1 (b) Temperature map of Case 5 (c) Temperature difference between Case 5 and Case 1 (d) Non-dimensional temperature error between Case 5 and Case 1

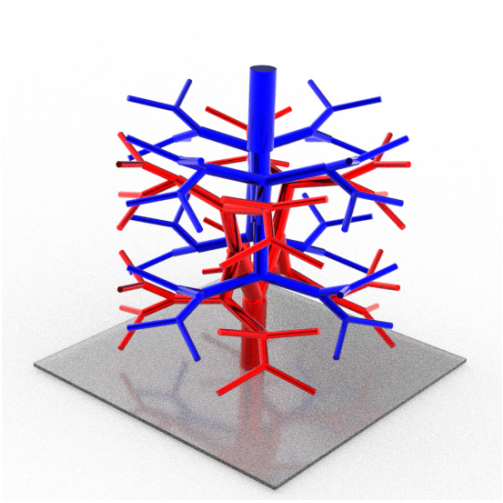

(a)

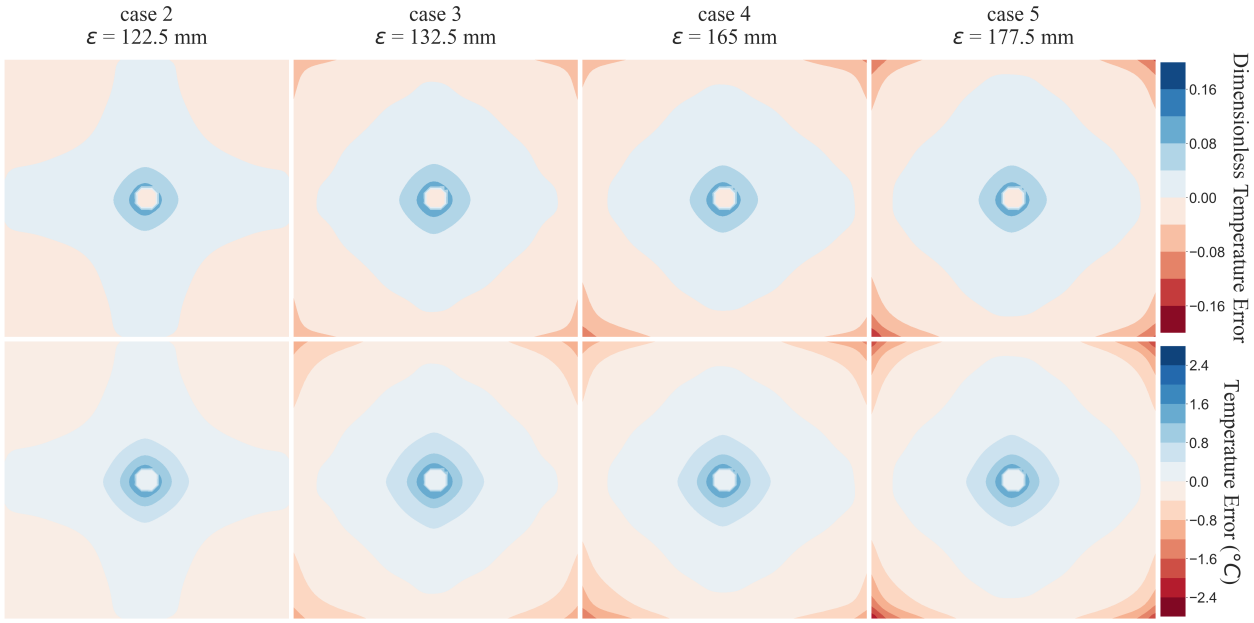

(b)

Figure 5.26: Temperature error at z = 1

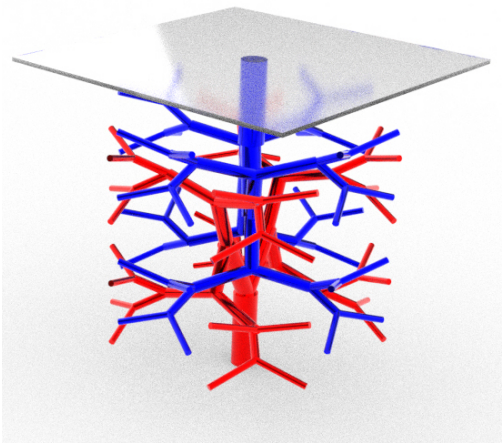

(a)

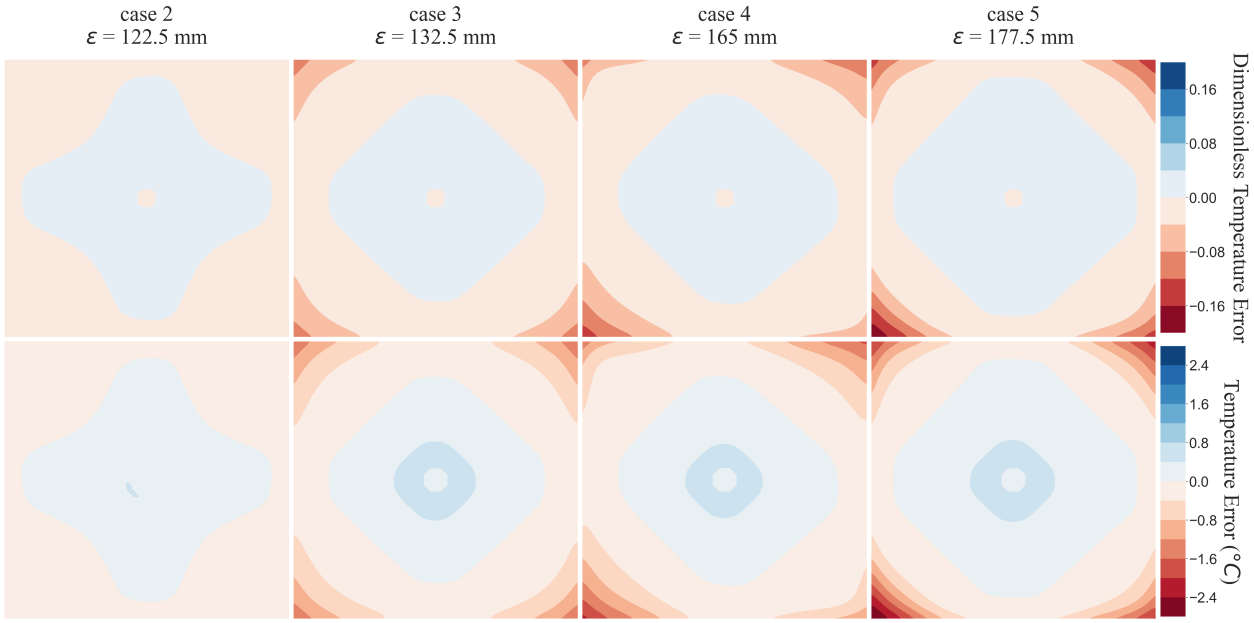

(b)

Figure 5.27: Temperature error at z = 80

5.4.1 Error Analysis in Different Modes of Bioheat Transfer

A further analysis was conducted by examining the energy exchange error at the individual tissue voxel level. Three different modes of bioheat transfer occur at a tissue voxel level - (1) advection-conduction with neighboring tissue voxels (2) advection from arterial terminals; and (3) convection with a neighboring vessels. The energy exchanges (W) are calculated for each tissue voxel in these three processes and compared with those from reference Case 1. The equations used to calculate the error are given in Eq. (5.24), Eq. (5.25), and Eq. (5.26).

$$\Delta E_{term,art,k} = \sum_{i \in \mathcal{N}_{A,term,ci}} \dot{m}_{art,i,ci} \rho_b c_p T_{art,i,ci} - \sum_{j \in \mathcal{N}_{A,term,c1}} \dot{m}_{art,j,c1} \rho_b c_p T_{art,j,c1} \tag{5.24}$$

$$\Delta E_{ves,conv,k} = \sum_{i \in \mathcal{N}} \left(\frac{1}{h_b} + \frac{k_t}{2\Delta s} \right) A_s T_{i,ci} - \sum_{j \in \mathcal{N}} \left(\frac{1}{h_b} + \frac{k_t}{2\Delta s} \right) A_s T_{j,c1} \tag{5.25}$$

$$\Delta E_{tis,k} = \sum_{i \in \mathcal{N}} \left(\dot{m}_{b,i} c_p \rho_b + \frac{k_t}{ds} A \right) T_i - \sum_{j \in \mathcal{N}} \left(\dot{m}_{b,j} c_p, \rho_b + \frac{k_t}{\Delta s} A \right) T_j \tag{5.26}$$

Eq. 5.24 represents the difference in energy a voxel recieves via advection from terminal arteries. This difference is calculated for a simulation case with respect to Case 1. The first term on right hand side (RHS) of Eq. (5.24), represents the total energy a tissue voxel k recieves via advection from arterial terminals in set $\mathcal{N}_{A,term}$ for a specific simulation case. The second term on RHS of Eq. (5.24) represents the total energy a tissue voxel k recieves via advection from arterial terminals in set $\mathcal{N}_{A,term}$ for Case 1.

Eq. (5.25) represents the difference in energy a voxel receives via convection with a neighboring vessel. The first term on RHS of Eq. (5.25) represents the total energy a tissue voxel k receives via convection if it is next to a blood vessel of temperature $T_{i,ci}$ for a specific simulation case represented by subscript ci. The second term on RHS of Eq. (5.25)

represents the total energy a tissue voxel k receives via convection if it is next to a blood vessel of temperature $T_{j,c1}$ for Case 1.

Eq. (5.26) represents the difference in energy a voxel receives via conduction-advection with a neighboring tissue voxel. The first term on RHS of Eq. (5.26) represents the sum of energy a tissue voxel k receives via advection and conduction from tissue voxels surrounding it for a specific simulation case. The second term on RHS of Eq. (5.26) represents the sum of energy a tissue voxel k receives via advection and conduction from neighboring tissue voxels for Case 1.

The energy exchange error plots are shown in Fig. 5.28 and Fig. 5.29 for all the cases at $z = 1$ and $z = 80$. The energy exchange error plots at other z locations are given in Appendix D. The maximum and minimum energy errors observed in the domain are given in Table 5.8. Fig. 5.28 and Fig. 5.29 represent the bottom and top cross-section layers in the simulation domain. There isn't any blood vessel physically present in these slices, thus there is no error observed in convective heat exchange from a vessel. Due to their location being farther away from the supply artery, as the branch generations are reduced, we observe less energy being transmitted via advection from supply arterial terminals. Since the tissue receives less energy from the supply artery, it results in less energy exchange between neighboring tissues compared to Case 1, and thus prominent error contours in the corners as observed in Fig. 5.26 and Fig. 5.27, when compared to Fig. D.17, Fig. D.18, and Fig. D.19.

Table 5.8: Energy error observed in various simulation cases

Case	ΔE_{tis} (W)		$\Delta E_{ves,conv}$ (W)		$\Delta E_{term,art}$ (W)	
	min	max	min	max	min	max
2	1.43	−3.48	9.51×10^{-7}	−0.0064	−0.17	0.575
3	2.39	−3.48	7.9×10^{-7}	−0.0064	−0.23	0.67
4	1.76	−3.76	3.97×10^{-7}	−0.0085	−0.2	0.45
5	1.11	−4.11	1.43×10^{-7}	−0.0085	−0.17	0.39

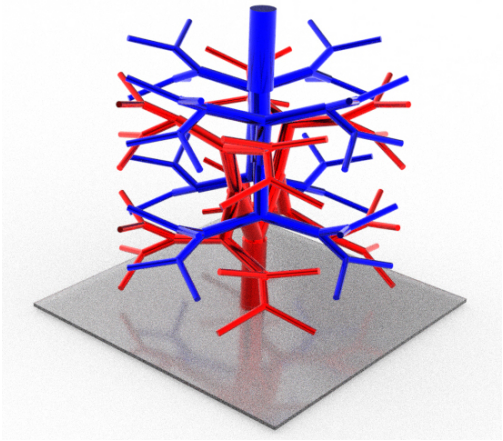

(a)

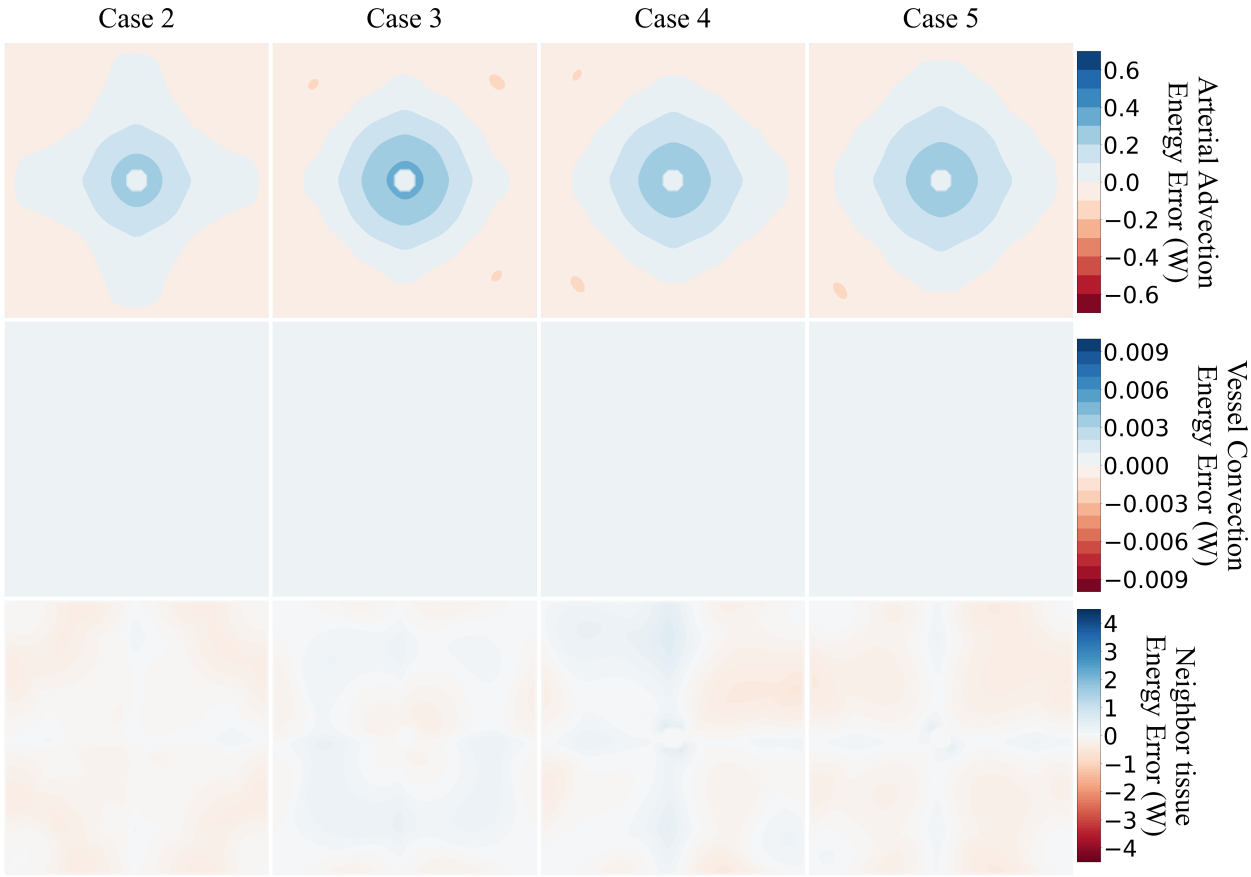

(b)

Figure 5.28: Energy error analysis at z = 1

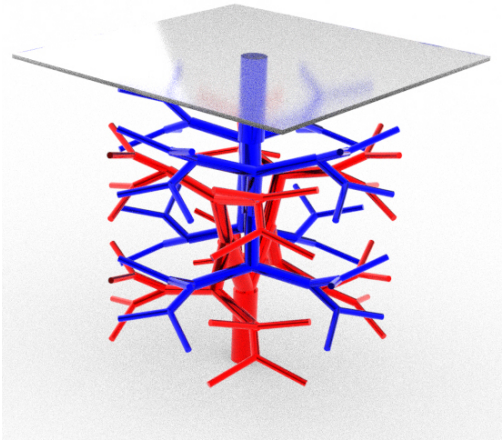

(a)

(b)

Figure 5.29: Energy error analysis at z = 80

5.5 Methods to Reduce Energy Error

An important observation in Figs. 5.28, 5.29, D.20, D.21, and D.22 is that the maximum energy exchange error is observed within advection - conduction between neighboring tissue voxels compared to other forms of energy exchange. Due to this a correction factor in the thermal conductivity of tissue could be a potential solution. The Weinbaum group[60;158] studied the effect of counter-current heat exchange in capillary beds. To model the effect of this heat transfer process, they introduced an effective tissue conductivity in their proposed new bioheat equation[60]. A similar approach could be undertaken to determine the variation in the thermal conductivity of tissue due to the lack of segmentation data.

The other alternative to reduce the energy error is varying the SoI radius. In section 4.4, it was shown that SoI plays a critical role in heat transfer. Earlier in this chapter, SoI radius was shown to not affect the pressure map; however, its effect on heat transfer could prove advantageous to reduce the energy error.

5.5.1 Modified Tissue Thermal Conductivity

As less blood vessels are segmented, they lie hidden within the tissue. The tissue now consists of larger blood vessel (un-segmented) than the reference domain. In the energy error analysis conducted, it can be seen that more error is observed in the advection - conduction heat exchange between neighboring tissues. Advection between two neighboring tissues is dictated by the pressure difference and resistance between the two voxels. From the flow analysis, the pressure map is shown to be consistent and the flow resistance between voxels is not varied. Hence, conduction between the tissue voxels is a key phenomenon. In literature, effective thermal conductivity is used to consider the effect of unsegmented blood vessels and counter-current heat exchange as described in Section 2.3. The same concept of effective thermal conductivity is used to compensate for the effect of cross-flow heat exchange between unsegmented blood vessels.

For this analysis, only Case 5 is considered as it represents the worst-case scenario in this study. As observed earlier, the maximum temperature error observed is $-2.74\,^{\circ}\mathrm{C}$ between

Case 5 and Case 1. The maximum temperature error and non-dimensional temperature error observed for different values of thermal conductivity are given in Table 5.9. The contour maps of temperature errors for different values of thermal conductivity are given in Fig. 5.30 and Fig. 5.31, for z = 1 and 80, respectively.

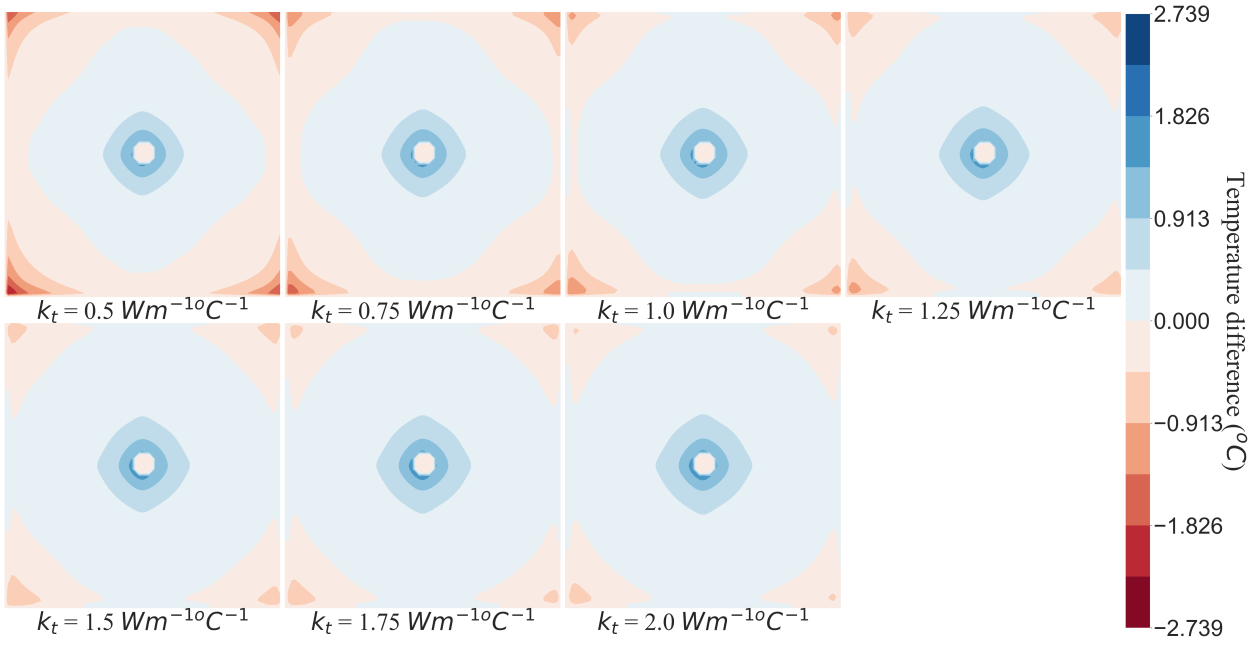

Figure 5.30: Effect of thermal conductivity at z = 1 for $\epsilon = 177.5\,\text{mm}$

Table 5.9: Effect of tissue thermal conductivity on temperature error

k_t ($\text{W m}^{-1}\,^{\circ}\text{C}^{-1}$)	max ΔT (°C)	max abs(ΔT) (°C)	max abs(θ)
0.50	-2.74	2.74	0.183
0.75	-2.03	2.03	0.135
1.00	-1.67	1.67	0.112
1.25	1.45	1.45	0.097
1.50	1.46	1.46	0.098
1.75	1.47	1.47	0.098
2.00	1.48	1.48	0.099

The minimum error is observed when k_t is $1.25\,\text{W m}^{-1}\,^{\circ}\text{C}^{-1}$. From Table 5.9 and Table 5.7, it can be seen that the maximum error when thermal conductivity was $1.25\,\text{W m}^{-1}\,^{\circ}\text{C}^{-1}$ for Case 5 is less than the maximum error for Case 3 ($k_t = 0.5\,\text{W m}^{-1}\,^{\circ}\text{C}^{-1}$). The Case 3 has more segmented bood vessels than Case 5. This reduction of error is substantial. The behavior observed for the temperature error in Table 5.9 shows there exists a minima. This

value of tissue thermal conductivity where the temperature error was minimum for Case 5 is termed as "optimum thermal conductivity". What factors affect this value and how it can be calculated is beyond the scope of this dissertation.

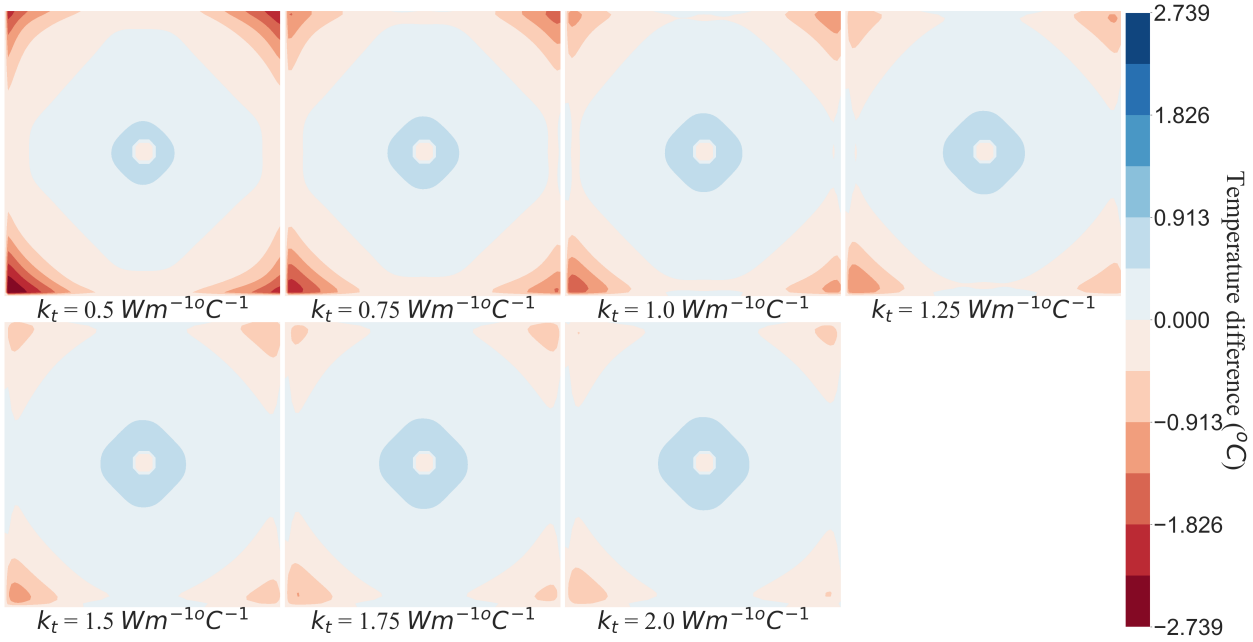

Figure 5.31: Effect of thermal conductivity at z = 80 for $\epsilon = 177.5\,\text{mm}$

5.5.2 Larger Sphere of Influence Radius

The top (z = 80) and bottom (z = 1) layers of the domain do not have any physical blood vessels. As the number of segmented blood vessels is reduced, these layers fall closer to the extremities of the SoI due to their distance from the terminal arteries and veins. For the simulation so far, the SoI radius was considered to be the minimum radius at which 100 % volume coverage is achieved to ensure no voxel is starved of oxygen due to its distance from the supply artery. However, as the number of terminals decreases, the average distance between tissue voxels and terminal vessel increases. This results in lower flow rates between terminal vessels and distant tissue voxels. This behavior though not observed in pressure maps it can be seen in the error introduced in energy analysis. Thus, the other solution to reduce the energy error could be to have larger SoI. When the ϵ is not restricted to minimum value at which 100 % coverage is achieved, more blood can be supplied to the tissue voxels

farther away from arterial terminals.

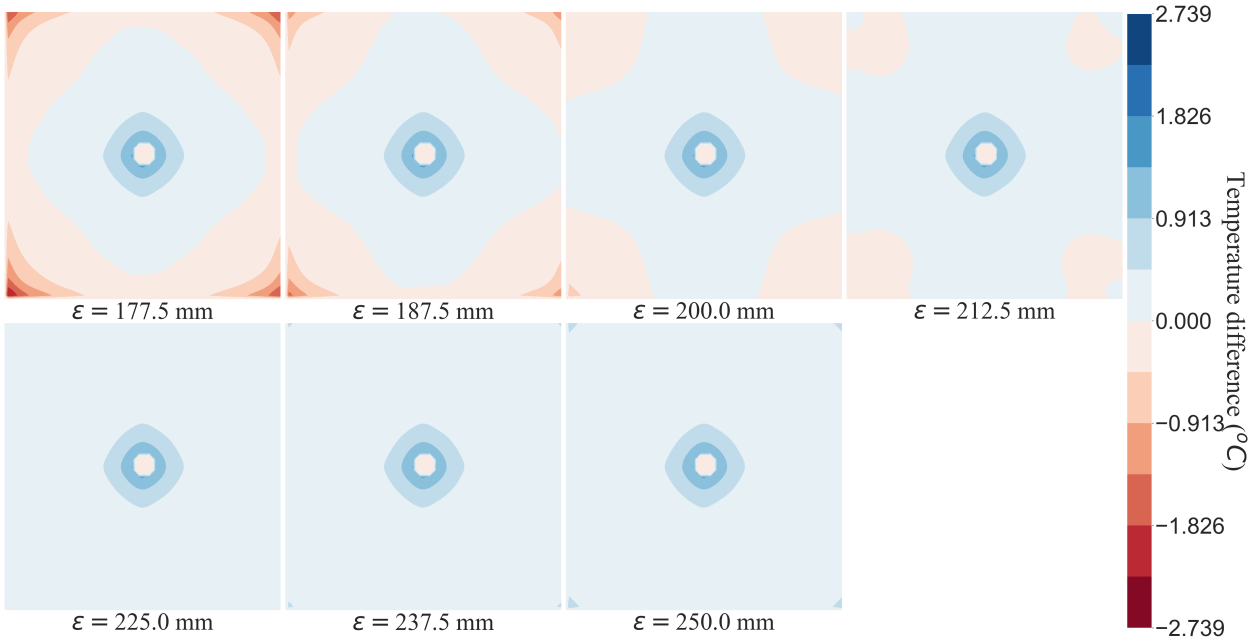

Figure 5.32: Effect of larger SoI at z = 1 for $k_t = 0.5\,\mathrm{W\,m^{-1}\,{}^{\circ}C^{-1}}$

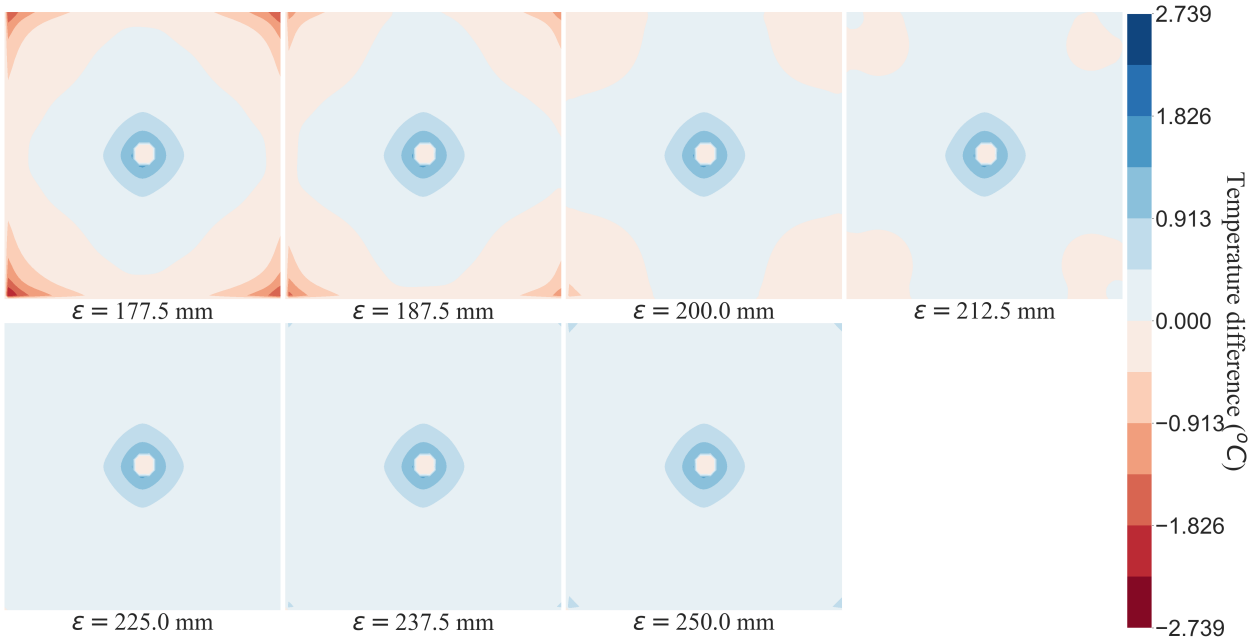

Figure 5.33: Effect of larger SoI at z = 80 for $k_t = 0.5\,\mathrm{W\,m^{-1}\,{}^{\circ}C^{-1}}$

The contour plots for temperature error for $k_t = 0.5\,\mathrm{W\,m^{-1}\,{}^{\circ}C^{-1}}$ at $z = 1$ and $z = 80$ (case 5) are shown in Fig. 5.32 and Fig. 5.33, respectively. In Appendix E Table E.1 and

Table E.2 show the maximum temperature error observed for different values of ϵ and tissue thermal conductivity, and the minimum error observed is marked with "$*$".

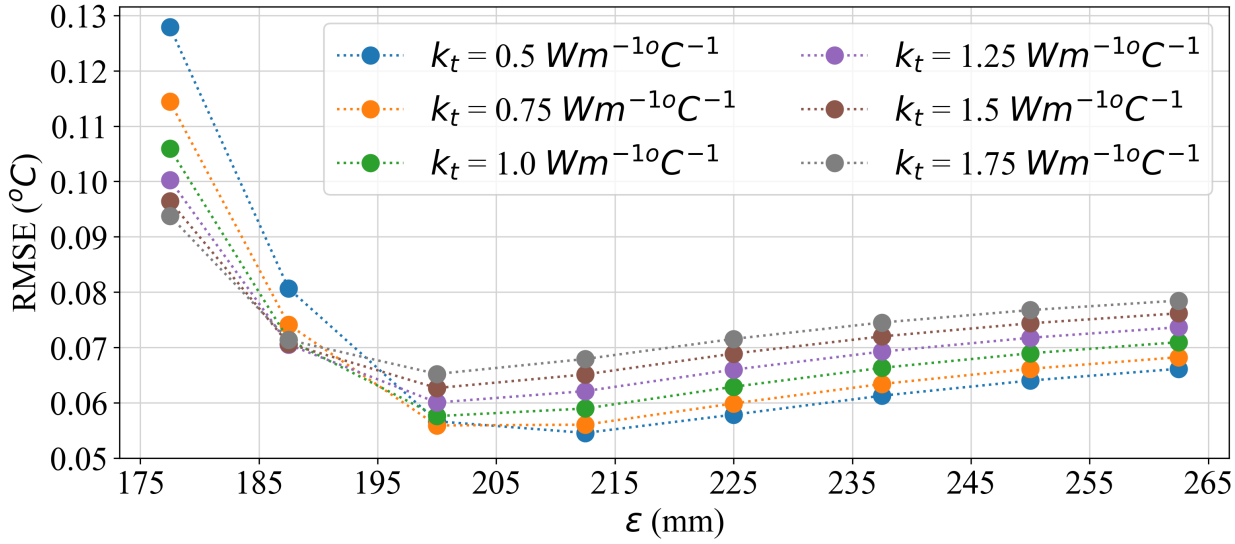

Figure 5.34: RMSE plot for comparing the effect of effective thermal conductivity and larger SoI on temperature error

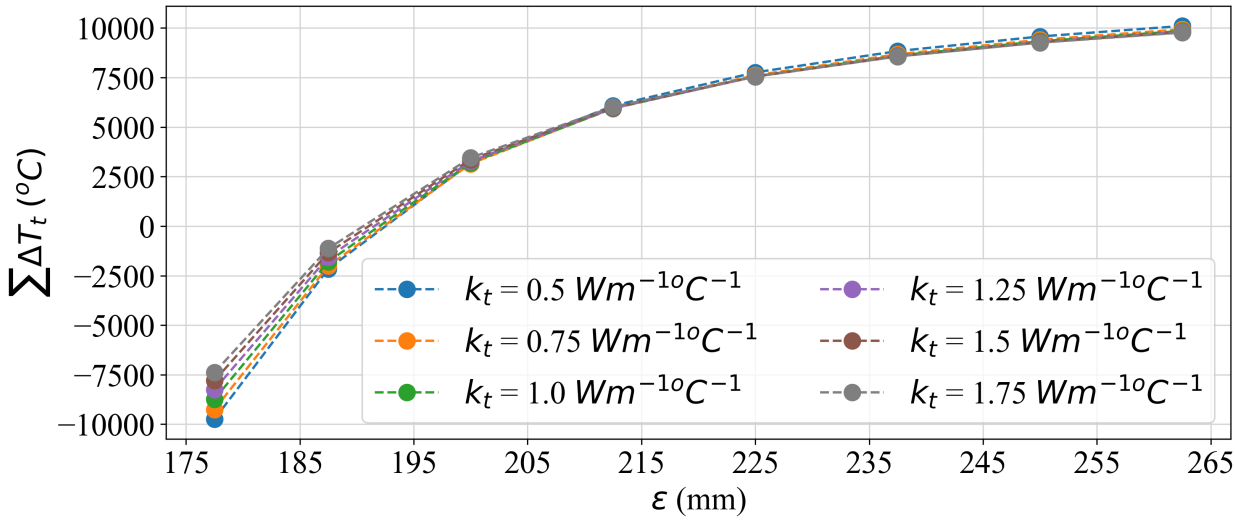

Figure 5.35: Summation error plot for comparing the effect of effective thermal conductivity and larger SoI on temperature error

From Table E.1 and Table E.2, it can be seen that the minimum temperature error observed for larger SoI is 1.38 °C, and is lower than the temperature error observed when tissue thermal conductivity is varied. Root mean square error (RMSE) and the sum of

temperature error (STE) in the entire domain ($\sum \Delta T_t$) were calculated. The data is shown in Table E.1 and Table E.2 and a graphical plot of RMSE and $\sum \Delta T_t$ for the different values of k_t and ϵ is shown in Fig. 5.34 and Fig. 5.35, respectively.

Table 5.10: Threshold value of ϵ and the corresponding summation of temperature error for Case 5

k_t (W m^{-1} °C^{-1})	RMSE (°C)	ϵ (mm)	$\sum \Delta T_t$ °C
0.50	0.053	209.00	5489.66
0.75	0.054	206.50	4865.98
1.00	0.057	204.75	4497.26
1.25	0.059	203.25	4158.20
1.50	0.062	201.75	3892.51
1.75	0.065	201.00	3770.50

Table 5.11: Value of ϵ where summation of temperature error in Case 5 equals to zero and the resultant RMSE

k_t (W m^{-1} °C^{-1})	ϵ (mm)	RMSE (°C)
0.50	191.73	0.069
0.75	191.60	0.065
1.00	191.22	0.065
1.25	190.90	0.066
1.50	190.41	0.068
1.75	190.02	0.069

In Fig. 5.34, it can be seen that as k_t increases, the RMSE decreases for ϵ till a threshold value. Beyond the threshold, the RMSE increases with an increase in k_t. Using polynomial regression, six polynomial functions of the fourth order were fitted for RMSE for each value of k_t, respectively. Similarly, six polynomial functions of the fourth order were fitted for STE for each value of k_t. Using the RMSE function, the threshold where minimum RMSE occurs is calculated, along with the corresponding STE. These values are given in Table 5.10. It is noteworthy that the STE is positive for all k_t at the threshold ϵ of minimum RMSE. This denotes that the VoM-PhyS framework would result in higher temperatures than the reference for a less segmented vascular domain.

Similarly, the ϵ where STE equals zero was calculated along with the corresponding RMSE. These values are given in Table 5.11. The values of ϵ where STE is zero are not the

same where minimum RMSE occurs, as can be seen. A further detailed statistical analysis of these values could lead to greater insight into the performance of the proposed energy error reduction methods. A further analysis is needed to determine what parameters affect the value of ϵ for any given vascular data.

The other noteworthy observation is that the minimum temperature for larger SoI is for $k_t = 0.5\,\mathrm{W\,m^{-1}\,{}^{\circ}C^{-1}}$, and this error increases for the same SoI when tissue thermal conductivity is varied. A SoI larger than the minimum required for 100 % coverage ensures the tissue domain lies closer to the source than the periphery of the SoI. This provides more blood flow to the entire tissue domain than the simulation case when SoI is restricted to minimum ϵ for 100 % coverage. As the SoI is increased, it is expected to achieve equal distribution in the entire tissue domain. This is illustrated in Fig. 5.37. This is expected when the SoI is considerably larger than the domain dimensions. This behavior ensures that we reach a plateau beyond which the temperature error cannot be decreased even if the SoI is increased. In Fig. 5.37 as the ϵ is increased, the distribution reaches near normal distribution as shown in Fig. 5.37.d. This behavior can also be seen in Table E.1 and Table E.2, the temperature error for a given tissue thermal conductivity reaches a minimum beyond which it does not reduce when SoI is increased.

Increasing the thermal conductivity of tissue reduced the temperature error for Case 5 ($k_t = 1.25\,\mathrm{W\,m^{-1}\,{}^{\circ}C^{-1}}$) to lower than the maximum temperature error observed for Case 3 ($k_t = 0.5\,\mathrm{W\,m^{-1}\,{}^{\circ}C^{-1}}$). In comparison, increasing the SoI reduced the temperature error for Case 5 to that of Case 2. This can be seen in the temperature error contour plots shown in Fig. 5.36. This is a substantial reduction in error as Case 2 represents a 16 terminal domain compared to Case 5 of 2 terminals. The variation of SoI did not affect the pressure map and reduced the temperature error. This is promising to further this research to minimize the temperature error in simulations due to the lack of segmented vasculature.

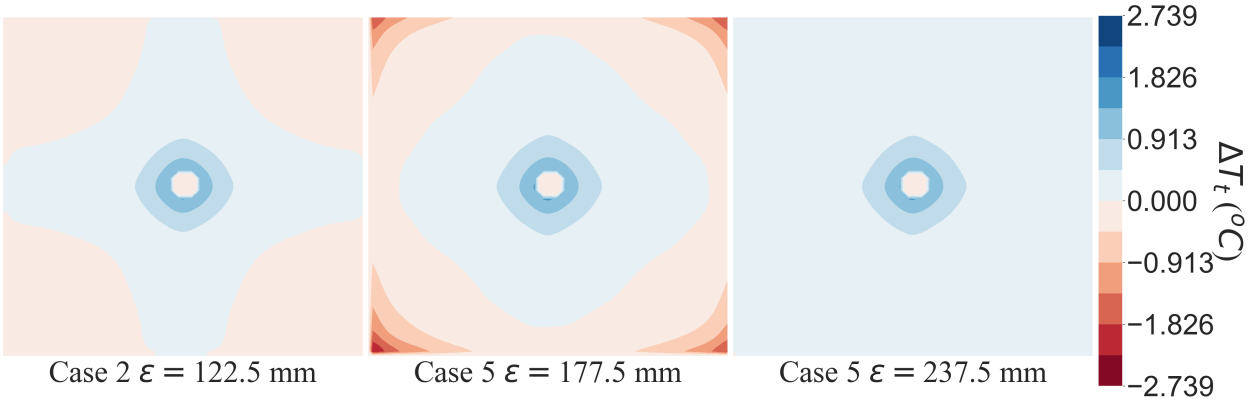

(a)

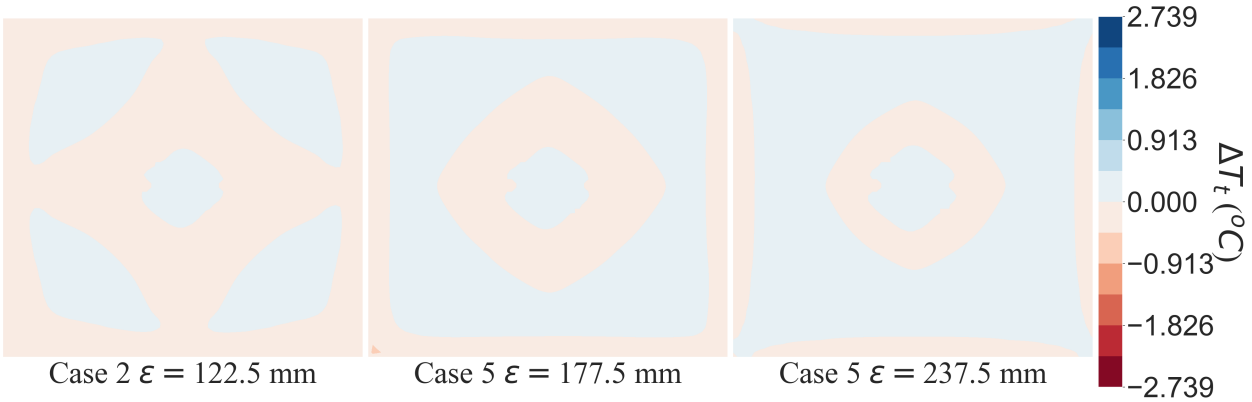

(b)

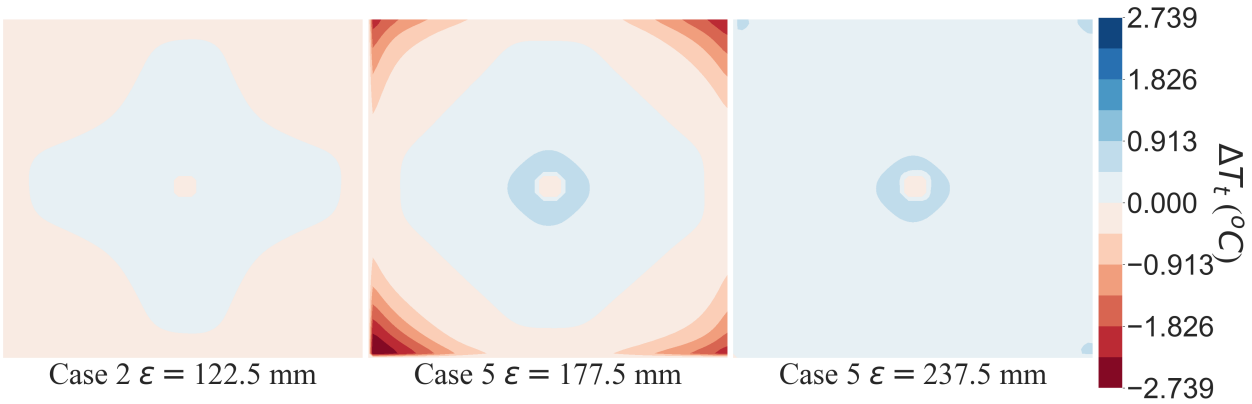

(c)

Figure 5.36: Effect of larger SoI for $k_t = 0.5\,\mathrm{W\,m^{-1}\,°C^{-1}}$ at (a) $x = 1$ (b) $x = 40$ (c) $x = 1$

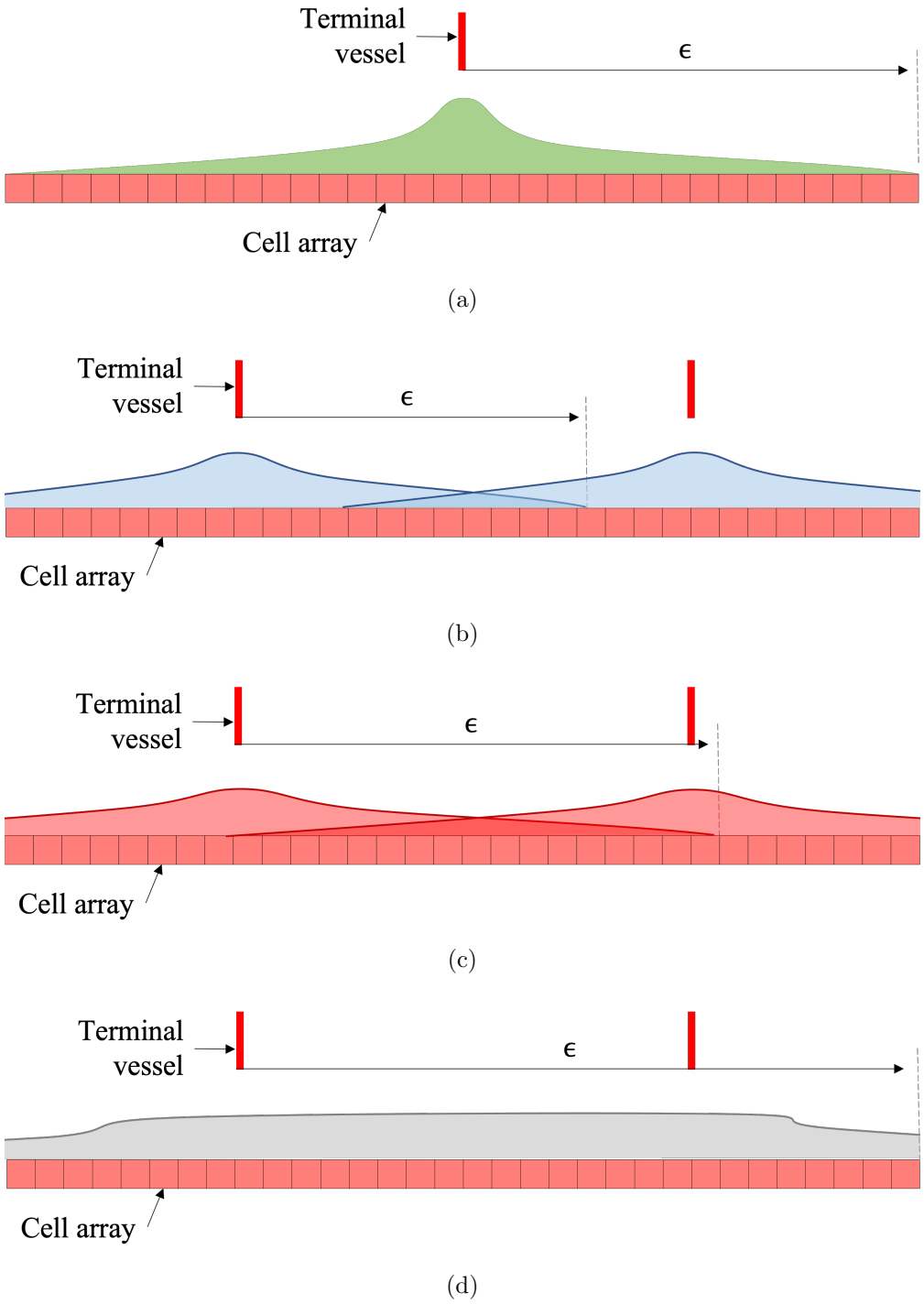

Figure 5.37: Effect of larger ϵ resulting in near normal distribution

5.6 Chapter Summary

This chapter provided a detailed analysis of the effect of SoI and the pressure drop parameter on flow and heat transfer simulation. The SoI radius did not affect the pressure map in flow simulation. In contrast, the pressure drop parameter showed to have a considerable effect. Since the pressure drop parameter represents the flow conductivity of virtual blood vessels, determining its value helps to recover the flow resistance of blood vessels that could not be segmented. No data was available in the literature to determine the correct pressure drop parameter for a given vasculature. This chapter derived the mathematical equation to calculate the pressure drop parameter for arterial and venous trees for a given vasculature, provided the total pressure drop across the simulation domain and a steady-state flow rate are known. This pressure drop parameter was used to simulate the lack of segmentation data on an example 3D domain and demonstrated very accurate flow simulation results.

The lack of segmentation data and varying the SoI radius affected energy analysis. Two methods were proposed to reduce this error. One method is to calculate an effective thermal conductivity for a domain with few segmented vasculatures. The other method is increasing the SoI radius until a near-equal distribution throughout the domain is achieved. Both these methods showed a reduction in energy error. Increasing the SoI radius provided better accuracy with less segmented data than varying the thermal conductivity of tissue for bioheat transfer.

Chapter 6

Summary and Conclusion

Multiphysical biological processes are complex, and simulating them remains a challenge. One needs to understand and model each of the processes involved and the relation of one process with another. This dissertation provides insight into using a voxel phantom for simulating thermoregulation using a novel Voxelized Multi-Physics Simulation (VoM-PhyS) Framework.

Chapter 2 provides a literature review of various thermophysiological models found in the literature and their limitations. An introduction to the computational human phantoms (CHPs) is provided to build the case for the requirement of a framework to simulate thermoregulation using a voxel phantom. Modeling the simulation domain directly from the imaging data provides the closest approximation to the actual research subject. Hence, voxel phantoms were used for simulation. However, the cuboidal nature of voxel phantoms results in stair-step effect, which causes an overestimation of surface area. These imaging data require post-processing that involves surface fitting to rectify the error introduced due to the image resolution and pixel/voxel structure. Such a reference surface area or curve fitting might not be available. Thus, an algorithm to reduce the surface area error independent of the overall shape of the domain was developed. The algorithm was tested for the worst-case scenario - a circle in 2D and a sphere in 3D. The overestimation of surface area was demonstrated to reduce from 27 % to 4 % in 2D and 50 % to 16 % in 3D. The stair-step

effect of voxel phantoms and the structured cleaving method to reduce the surface area error are elaborated in Chapter 3.

The novel VoM-PhyS framework provides one of its kind multiphysics platform for simulating multiscale and multidimensional problems. The development of the VoM-PhyS framework is elaborated in Chapter 4. The VoM-PhyS framework was demonstrated on frog tongue data obtained from the literature. The SoI is used as a Dirac function to couple 1D and 3D mesh in VoM-PhyS. The effect of SoI on heat transfer and the ability of VoM-PhyS to simulate competing hypotheses regarding the location of thermally significant vessels was studied on the frog tongue data. The SoI was found to have a more comparable effect than a small variation in convective heat exchange between vessel and tissue.

The SoI and the pressure drop parameter are the two mathematical parameters used in the VoM-PhyS Framework to couple 1D mesh with 3D mesh. The SoI controls the distribution spread with maxima centered at the location of the terminal vessel. In contrast, the pressure drop parameter controls the flow resistance offered by the virtual vessels within the SoI. No data is available in the literature to determine the pressure drop parameter for a given vasculature. Chapter 5 extensively analyzes the SoI and the pressure drop parameter and provides two equations to calculate the pressure drop parameter for any given vasculature, provided the total pressure drop across the domain and the steady state flow rate is known. To study the accuracy of these equations, a 3D vascular domain of 32 arterial and venous terminals, respectively, was generated using Rhinoceros[132], and each bifurcation level was gradually removed to simulate the lack of segmentation data. The vessels removed were substituted using the pressure drop parameter calculated from the developed equations, and the results were compared with the 32 terminal reference 3D domain. The analysis demonstrated less than 1 % error in flow simulations for lack of segmentations. The ability to calculate the flow resistances of pre-capillary vasculature that cannot be segmented due to image resolution opens new research areas. The pressure drop parameter equations are one of the major contributions of this dissertation to science, as they can simulate blood flow coupled with heat transfer with very high accuracy, even with fewer segmented vessels.

The error in heat transfer due to lack of segmentation data was studied, and two methods

to reduce this error were elaborated. The effective tissue thermal conductivity to compensate for unsegmented pre-capillary vessels in tissue was studied for temperature error reduction. Another method of increasing the SoI radius to achieve a near-equal distribution was proposed and studied for temperature error reduction. A larger SoI was shown to have a comparably greater reduction in energy error than effective thermal conductivity.

This dissertation addresses three challenges associated with simulating thermoregulation using a voxel phantom. The major contributions of this dissertation to science are as follows:

- An algorithm that smoothens the voxel mesh to reduce surface area error and maintain a structured mesh nature of a voxel phantom. The method demonstrated to reduce the surface area error from 50 % to 25 % in a worse-case-scenario in 3D.

- The VoM-PhyS framework is a state-of-the-art simulation framework for multiphysics. This framework can be easily extended to add more bio-physical processes like mass transfer, radiation dosimetry, and thermoregulatory response like vasomotion, coupled with the existing ones with ease.

- The pressure drop equations derived in this dissertation are not found in the literature. These equations provide an advantage to the VoM-PhyS framework to be applicable to any domain size and provide a way to recover the flow resistance data lost in image resolution.

- This dissertation's findings are a strong foundation to create a full-body thermoregulation simulation with highly advanced capabilities absent from current models.

This research provides foundational pieces to build a complete human thermoregulation simulation. One major challenge in using CHPs for thermoregulation is the mesh size and resulting computational requirements. Due to this, small domains like 3D tumors obtained from MRI scans and frog tongue were used to conduct the preliminary analysis. A human body was not used to demonstrate the VoM-PhyS framework; however, the VoM-PhyS framework is designed to be easily applicable to any domain and organ. Thus, the VoM-PhyS framework can be used for a complete human thermoregulation simulation.

This research has established the groundwork for exploring a multidisciplinary area in computational simulation. The goal of this dissertation was limited to Human Thermoregulation, and thus the domain used for simulation consisted of biological tissue and blood vessels obtained from medical imaging data or medical textbooks. But VoM-PhyS by no means is limited to only biomedical applications. The VoM-PhyS framework has the potential to be used for simulation in various other research areas like fracking, geothermal and microbiological processes involving interstitial fluids. These areas are not studied in this dissertation, but due to the similarities in the domain structures, the possibility can be suggested for exploration. The recommendations for furthering this study are as follows:

1. Developing an algorithm that uses a surface normal vector to calculate error rectification without further dividing the mesh. Newell's algorithm is used in the computational graphic research field to calculate the normal of irregular surfaces[134]. This algorithm can be used to calculate the normal at each voxel, and a correction factor to smoothen the region can be determined. This will avoid dividing a voxel into 24 sub-tetrahedrons and reduce the computational requirements.

2. Experimental studies to determine equations to calculate Sphere of Influence (SoI) for various applications. An experimental setup with a porous domain and 3D pipe network exchanging fluid can be used to derive equations for determining SoI for a domain. Such an experimental setup will require the ability to have a detailed 3D vasculature with the ability to remove terminals to simulate a lack of segmentation data.

3. Further analysis to understand the effect of elasticity of blood vessels on pressure drop parameter. The pressure drop parameter equations developed in this dissertation are limited to a Newtonian and laminar flow assumption of blood. *In vivo* the blood vessels are elastic and provide a damping effect for pulsatile flow, and blood is non-Newtonian. These physical properties of blood vessels and blood must be studied to determine a pressure drop equation applicable to non-Newtonian blood flow and elastic blood vessels.

4. Determining the time constant for blood distribution within the SoI for transient simulations. The simulations conducted in this dissertation were for steady state. Within a SoI, the tissue farther away from the terminal will receive blood later than the tissue closer to the terminal. This introduces a temporal distribution function within the SoI. A detailed analysis is required to determine this temporal function for different values of SoI radius.

5. Adding a feedback loop that simulates vasomotion by varying the resistances of blood vessels. Thermoregulation consists of a feedback signal to the hypothalamus and a regulatory signal controlling vasomotion, shivering, and sweating. These regulatory mechanisms are locally controlled by the chemical reaction within tissue cells and globally by the hypothalamus. Equations to vary the resistance of blood vessels as a response to temperature will provide a regulatory loop to the VoM-PhyS Framework.

6. The regulatory feedback signal will require determining which blood vessel and where vasomotion would occur for a specific feedback signal, followed by blood redirection within the domain for volume conservation. Blood volume within the human body remains constant, and vasomotion redirects the blood flow to maintain blood pressure and regulate temperature. Thus understanding blood redistribution is very important to simulate successful vasomotion.

7. Further analysis to derive a mathematical equation to calculate the changes in tissue thermal parameters as fewer blood vessels are segmented is required. Since non-segmented blood vessels will lie within the tissue domain, these blood vessels of larger dimensions than the capillary bed will vary the porosity of tissue. A preliminary analysis of the effect of effective thermal conductivity is given in this dissertation. The other parameter that needs to be considered is the permeability of tissue. As larger blood vessels are part of the 3D tissue domain, the permeability of tissue is expected to change. An equation to determine the correct permeability of tissue for a given vasculature is needed.

8. Sweating and drug delivery are the mass transport phenomena that occur within the human body. Adding the set of mass transport equations to VoM-PhyS will be highly useful.

9. Considering the computational requirements for thermoregulation using a CHP, performing a comparison study between thermoregulation simulation using stylized phantom and voxel phantom will be highly beneficial. This study could provide additional insights, various research questions, and avenues for advancing this work.

Bibliography

[1] A. Jamin, W. Bosschaerts, I. Nastase, and B. Janssens. Review of the existing state of the art regarding the use of CFD and human thermophysiological models for the vehicular comfort assessment. *IOP Conference Series: Earth and Environmental Science*, 664(1), 2021. ISSN 17551315. doi: 10.1088/1755-1315/664/1/012012.

[2] Laura H. Namisnak, Shahab Haghayegh, Sepideh Khoshnevis, and Kenneth R. Diller. Bioheat Transfer Basis of Human Thermoregulation: Principles and Applications. *Journal of Heat Transfer*, 144(3), 2022. ISSN 15288943. doi: 10.1115/1.4053195.

[3] Elizabeth A. McCullough, Steve Eckels, and Craig Harms. Determining temperature ratings for children's cold weather clothing. *Applied Ergonomics*, 40(5):870–877, 2009. ISSN 00036870. doi: 10.1016/j.apergo.2008.12.004. URL http://dx.doi.org/10.1016/j.apergo.2008.12.004.

[4] Agnes Psikuta, Jonas Allegrini, Barbara Koelblen, Anna Bogdan, Simon Annaheim, Natividad Martínez, Dominique Derome, Jan Carmeliet, and René M. Rossi. Thermal manikins controlled by human thermoregulation models for energy efficiency and thermal comfort research – A review. *Renewable and Sustainable Energy Reviews*, 78(April):1315–1330, 2017. ISSN 18790690. doi: 10.1016/j.rser.2017.04.115. URL http://dx.doi.org/10.1016/j.rser.2017.04.115.

[5] Barbara Koelblen, Agnes Psikuta, Anna Bogdan, Simon Annaheim, and René M. Rossi. Thermal sensation models: Validation and sensitivity towards thermophysiological parameters. *Building and Environment*, 130(December 2017):200–211, 2018. ISSN 03601323. doi: 10.1016/j.buildenv.2017.12.020. URL https://doi.org/10.1016/j.buildenv.2017.12.020.

[6] Naiping Gao, Jianlei Niu, and Hui Zhang. Coupling CFD and human body thermoregulation model for the assessment of personalized ventilation. *HVAC and R Research*, 12(3):497–518, 2006. ISSN 10789669. doi: 10.1080/10789669.2006.10391191.

[7] Kristijan Skok, Maja Duh, Andraž Stožer, Andrej Markota, and Marko Gosak. Thermoregulation: A journey from physiology to computational models and the intensive care unit. *Wiley Interdisciplinary Reviews: Systems Biology and Medicine*, (October 2020):1–20, 2020. ISSN 1939005X. doi: 10.1002/wsbm.1513.

[8] Ken Parsons. *Human thermal environments: the effects of hot, moderate, and cold environments on human health, comfort, and performance*. CRC Press, 2014.

[9] Paul C. Cropper, Tong Yang, Malcolm Cook, Dusan Fiala, and Rehan Yousaf. Coupling a model of human thermoregulation with computational fluid dynamics for predicting human-environment interaction. *Journal of Building Performance Simulation*, 3(3):233–243, 2010. ISSN 19401493. doi: 10.1080/19401491003615669.

[10] Adolf P Gagge. An effective Temperature Scale Based on a simple model of human Physiological Regulatory Response. *ASHRAE Transactions*, 77:247–262, 1971.

[11] Katarina Katić, Rongling Li, and Wim Zeiler. Thermophysiological models and their applications: A review. *Building and Environment*, 106:286–300, 2016. ISSN 03601323. doi: 10.1016/j.buildenv.2016.06.031.

[12] Liang Yu, Nan Jia, Ruomei Wang, Qingzhen Xu, Jiao Jiao, Qingzhen Xu, Ruomei Wang, Nan Jia, and Liang Yu. An improved human physiological simulation model for healthcare applications. *International Journal of Embedded Systems*, 11(3):251, 2019. ISSN 1741-1068. doi: 10.1504/ijes.2019.10020753.

[13] B W Jones and Y Ogawa. Transient Interaction Between The Human And The Thermal Environment. *ASHRAE Transactions*, 98(1):189–195, 1992.

[14] J A Stolwijk. A mathematical model of physiological temperature regulation in man.

Book, (August):83, 1971. ISSN 0031-6768. doi: NASACR-1855. URL http://hdl.handle.net/2060/19710023925.

[15] Dusan Fiala, Kevin J. Lomas, and Martin Stohrer. A computer model of human thermoregulation for a wide range of environmental conditions: the passive system. *Journal of Applied Physiology*, 87:1957–1972, 1999. ISSN 8750-7587. doi: 10.1152/jappl.1999.87.5.1957.

[16] Dusan Fiala, George Havenith, Peter Bröde, Bernhard Kampmann, and Gerd Jendritzky. UTCI-Fiala multi-node model of human heat transfer and temperature regulation. *International Journal of Biometeorology*, 56(3):429–441, 2012. ISSN 00207128. doi: 10.1007/s00484-011-0424-7.

[17] Dusan Fiala, Kevin J. Lomas, and Martin Stohrer. Computer Prediction of human Thermoregulation and temperature responses to a wide range of environmental conditions. *International Journal of Biometeorology*, 45:143–159, 2001. ISSN 0020-7128. doi: 10.1007/s004840100099.

[18] Shin Ichi Tanabe, Kozo Kobayashi, Junta Nakano, Yoshiichi Ozeki, and Masaaki Konishi. Evaluation of thermal comfort using combined multi-node thermoregulation (65MN) and radiation models and computational fluid dynamics (CFD). *Energy and Buildings*, 34(6):637–646, 2002. ISSN 03787788. doi: 10.1016/S0378-7788(02)00014-2.

[19] M. Salloum, H. Ghaddar, and K. Ghali. A new transient bio-heat model of the human body. *Proceedings of the ASME Summer Heat Transfer Conference*, 4:927–937, 2005. doi: 10.1115/HT2005-72303.

[20] M. Salloum, N. Ghaddar, and K. Ghali. A new transient bioheat model of the human body and its integration to clothing models. *International Journal of Thermal Sciences*, 46(4):371–384, 2007. ISSN 12900729. doi: 10.1016/j.ijthermalsci.2006.06.017.

[21] Dayi Lai and Qingyan Chen. A two-dimensional model for calculating heat transfer in the human body in a transient and non-uniform thermal environment. *Energy and*

Buildings, 118:114–122, 2016. ISSN 03787788. doi: 10.1016/j.enbuild.2016.02.051. URL http://dx.doi.org/10.1016/j.enbuild.2016.02.051.

[22] Eugene H. Wissler. Whole-body human thermal modeling, an alternative to immersion in cold water and other unpleasant endeavors. *Journal of Heat Transfer*, 134(3): 031019, 2012. ISSN 00221481. doi: 10.1115/1.4005155. URL http://heattransfer.asmedigitalcollection.asme.org/article.aspx?articleid=1450442.

[23] Harry H. Pennes. Analysis of Tissue and Arterial Blood Temperatures in the Resting Human Forearm. *Journal of Applied Physiology*, 1(2):93–122, 1948. URL www.physiology.org/journal/jappl.

[24] Carol Elaine Smith. *A transient, three-dimensional model of the human thermal system*. PhD thesis, 1991.

[25] Xiaoyang Sun, Steve Eckels, and Zhongquan Charlie Zheng. An improved thermal model of the human body. *HVAC and R Research*, 18(3):323–338, 2012. ISSN 10789669. doi: 10.1080/10789669.2011.617231.

[26] D. A. Nelson, S. Charbonnel, A. R. Curran, E. A. Marttila, D. Fiala, P. A. Mason, and J. M. Ziriax. A High-Resolution Voxel Model for Predicting Local Tissue Temperatures in Humans Subjected to Warm and Hot Environments. *Journal of Biomechanical Engineering*, 131(4):041003, 2009. ISSN 01480731. doi: 10.1115/1.3002765. URL http://biomechanical.asmedigitalcollection.asme.org/article.aspx?articleid=1475663.

[27] Tushar Gulati, Rajeev Hatwar, Ginu Unnikrishnan, Jose E. Rubio, and Jaques Reifman. A 3-D virtual human model for simulating heat and cold stress. *Journal of Applied Physiology*, 133(2):288–310, 2022. ISSN 15221601. doi: 10.1152/japplphysiol.00089.2022.

[28] Ginu Unnikrishnan, Rajeev Hatwar, Samantha Hornby, Srinivas Laxminarayan, Tushar Gulati, Luke N. Belval, Gabrielle E.W. Giersch, Josh B. Kazman, Douglas J. Casa,

and Jaques Reifman. A 3-D virtual human thermoregulatory model to predict whole-body and organ-specific heat-stress responses. *European Journal of Applied Physiology*, 121(9):2543–2562, 2021. ISSN 14396327. doi: 10.1007/s00421-021-04698-1. URL https://doi.org/10.1007/s00421-021-04698-1.

[29] Michael P. Castellani, Timothy P. Rioux, John W. Castellani, Adam W. Potter, Sean R. Notley, and Xiaojiang Xu. Finite element model of female thermoregulation with geometry based on medical images. *Journal of Thermal Biology*, page 103477, 2023. ISSN 03064565. doi: 10.1016/j.jtherbio.2023.103477. URL https://doi.org/10.1016/j.jtherbio.2023.103477.

[30] Xiaojiang Xu, Timothy P. Rioux, and Michael P. Castellani. Three dimensional models of human thermoregulation: A review. *Journal of Thermal Biology*, 112(January): 103491, 2023. ISSN 18790992. doi: 10.1016/j.jtherbio.2023.103491. URL https://doi.org/10.1016/j.jtherbio.2023.103491.

[31] Ming Fu, Wenguo Weng, Weiwang Chen, and Na Luo. Review on modeling heat transfer and thermoregulatory responses in human body. *Journal of Thermal Biology*, 62:189–200, 2016. ISSN 18790992. doi: 10.1016/j.jtherbio.2016.06.018. URL http://dx.doi.org/10.1016/j.jtherbio.2016.06.018.

[32] Wolfgang Kainz, Esra Neufeld, Wesley E. Bolch, Christian G. Graff, Chan Hyeong Kim, Niels Kuster, Bryn Lloyd, Tina Morrison, Paul Segars, Yeon Soo Yeom, Maria Zankl, X. George Xu, and Benjamin M. W. Tsui. Advances in Computational Human Phantoms and Their Applications in Biomedical Engineering—A Topical Review. *IEEE Transactions on Radiation and Plasma Medical Sciences*, 3(1):1–23, 2019. ISSN 2469-7311. doi: 10.1109/trpms.2018.2883437.

[33] Amir A. Bahadori, Mary Van Baalen, Mark R. Shavers, Edward J. Semones, and Wesley E. Bolch. Dosimetric impacts of microgravity: An analysis of 5th, 50th and 95th percentile male and female astronauts. *Physics in Medicine and Biology*, 57(4): 1047–1070, 2012. ISSN 00319155. doi: 10.1088/0031-9155/57/4/1047.

[34] Amir A. Bahadori, Mary Van Baalen, Mark R. Shavers, Charles Dodge, Edward J. Semones, and Wesley E. Bolch. The effect of anatomical modeling on space radiation dose estimates: A comparison of doses for NASA phantoms and the 5th, 50th, and 95th percentile male and female astronauts. *Physics in Medicine and Biology*, 56(6): 1671–1694, 2011. ISSN 00319155. doi: 10.1088/0031-9155/56/6/010.

[35] Amir A. Bahadori, Tatsuhiko Sato, Tony C. Slaba, Mark R. Shavers, Edward J. Semones, Mary Van Baalen, and Wesley E. Bolch. A comparative study of space radiation organ doses and associated cancer risks using PHITS and HZETRN. *Physics in Medicine and Biology*, 58(20):7183–7207, 2013. ISSN 00319155. doi: 10.1088/0031-9155/58/20/7183.

[36] X. George Xu. An exponential growth of computational phantom research in radiation protection, imaging, and radiotherapy: A review of the fifty-year history. *Physics in Medicine and Biology*, 59(18), 2014. ISSN 13616560. doi: 10.1088/0031-9155/59/18/R233.

[37] Amir Bahadori, Diana Miglioretti, Randell Kruger, Michael Flynn, Sheila Weinmann, Rebecca Smith-Bindman, and Choonsik Lee. Calculation of organ doses for a large number of patients undergoing CT examinations. *American Journal of Roentgenology*, 205(4):827–833, 2015. ISSN 15463141. doi: 10.2214/AJR.14.14135.

[38] Young Han Eun, Wesley E. Bolch, and Keith F. Eckerman. Revisions to the ornl series of adult and pediatric computational phantoms for use with the mird schema. *Health Physics*, 90(4):337–356, 2006. ISSN 00179078. doi: 10.1097/01.HP.0000192318.13190.c4.

[39] D. Coleman, K. T. Griffin, and S. A. Dewji. Stylized versus voxel phantoms: quantification of internal organ chord length distances. *Physics in Medicine and Biology*, 68 (5), 2023. ISSN 13616560. doi: 10.1088/1361-6560/acbbb6.

[40] Martin Caon. Voxel-based computational models of real human anatomy: A review.

Radiation and Environmental Biophysics, 42(4):229–235, 2004. ISSN 0301634X. doi: 10.1007/s00411-003-0221-8.

[41] M. J. Large, A. Malaroda, M. Petasecca, A. B. Rosenfeld, and S. Guatelli. Modelling ICRP110 Adult Reference Voxel Phantoms for dosimetric applications: Development of a new Geant4 Advanced Example. *Journal of Physics: Conference Series*, 1662(1), 2020. ISSN 17426596. doi: 10.1088/1742-6596/1662/1/012021.

[42] C. H. Kim, Y. S. Yeom, T. T. Nguyen, Z. J. Wang, H. S. Kim, M. C. Han, J. K. Lee, M. Zankl, N. Petoussi-Henss, W. E. Bolch, C. Lee, and B. S. Chung. The reference phantoms: voxel vs polygon. *Annals of the ICRP*, 45:188–201, 2015. ISSN 1872969X. doi: 10.1177/0146645315626036.

[43] Peter F. Caracappa, Ashley Rhodes, and Derek Fiedler. Multi-resolution voxel phantom modeling: A high-resolution eye model for computational dosimetry. *Physics in Medicine and Biology*, 59(18):5261–5275, 2014. ISSN 13616560. doi: 10.1088/0031-9155/59/18/5261.

[44] Keith T. Griffin, Thomas A. Cuthbert, Shaheen A. Dewji, and Choonsik Lee. Stylized versus voxel phantoms: A juxtaposition of organ depth distributions. *Physics in Medicine and Biology*, 65(6), 2020. ISSN 13616560. doi: 10.1088/1361-6560/ab7686.

[45] Pasquale A. Lombardo, Filip Vanhavere, Anne L. Lebacq, Lara Struelens, and Ria Bogaerts. Development and Validation of the Realistic Anthropomorphic Flexible (RAF) Phantom. *Health Physics*, 114(5):489–499, 2018. ISSN 15385159. doi: 10.1097/HP.0000000000000805.

[46] Choonsik Lee, Daniel Lodwick, Jorge Hurtado, Deanna Pafundi, Jonathan L Williams, and Wesley E. Bolch. the Uf Family of Reference Hybrid Phantoms for. *Phys. Med. Biol.*, 55(2):339–363, 2010. doi: 10.1088/0031-9155/55/2/002.THE.

[47] Juying Zhang, Yong Hum Na, Peter F. Caracappa, and George Xu. NIH Public Access.

Physics in Medicine and Biology, 54(19):5885–5908, 2010. doi: 10.1088/0031-9155/54/19/015.RPI-AM.

[48] Yeon Soo Yeom, Jong Hwi Jeong, Min Cheol Han, and Chan Hyeong Kim. Tetrahedral-mesh-based computational human phantom for fast Monte Carlo dose calculations. *Physics in Medicine and Biology*, 59(12):3173–3185, 2014. ISSN 13616560. doi: 10.1088/0031-9155/59/12/3173.

[49] Haegin Han, Yeon Soo Yeom, Chansoo Choi, Sungho Moon, Bangho Shin, Sangseok Ha, and Chan Hyeong Kim. POLY2TET: A computer program for conversion of computational human phantoms from polygonal mesh to tetrahedral mesh. *Journal of Radiological Protection*, 40(4):962–979, 2020. ISSN 13616498. doi: 10.1088/1361-6498/abb360.

[50] Zahra Shomali, Róbert Kovács, Péter Ván, Igor Vasilievich Kudinov, and Jafar Ghazanfarian. Lagging heat models in thermodynamics and bioheat transfer: a critical review. *Continuum Mechanics and Thermodynamics*, 34(3):637–679, 2022. ISSN 14320959. doi: 10.1007/s00161-022-01096-6.

[51] James P. Hartnett, Thomas F. Irvine, and Young I. Cho. *Advances in Heat Transfer: Bioengineering Heat Transfer*. Academic Press, 1992.

[52] W. Wulff. The Energy Conservation Equation for Living Tissue. *IEEE Transactions on Biomedical Engineering*, BME-21(6):494–495, 1974. ISSN 15582531. doi: 10.1109/TBME.1974.324342.

[53] M. Etehadtavakol and E. Y.K. Ng. Survey of numerical bioheat transfer modelling for accurate skin surface measurements. *Thermal Science and Engineering Progress*, 20 (June), 2020. ISSN 24519049. doi: 10.1016/j.tsep.2020.100681.

[54] Arka Bhowmik, Rupesh Singh, Ramjee Repaka, and Subhash C. Mishra. Conventional and newly developed bioheat transport models in vascularized tissues: A review. *Jour-*

nal of Thermal Biology, 38(3):107–125, 4 2013. ISSN 03064565. doi: 10.1016/j.jtherbio.2012.12.003. URL http://dx.doi.org/10.1016/j.jtherbio.2012.12.003.

[55] Michael M. Chen and Kenneth R. Holmes. Microvascular Contributions in Tissue Heat Transfer. *Annals of the New York Academy of Sciences*, 335(1):137–150, 1980. ISSN 17496632. doi: 10.1111/j.1749-6632.1980.tb50742.x.

[56] John W. Mitchell and Glen E. Myers. An Analytical Model of the Counter-Current Heat Exchange Phenomena. *Biophysical Journal*, 8(8):897–911, 1968. ISSN 00063495. doi: 10.1016/S0006-3495(68)86527-0.

[57] K. H. Keller and L. Seiler. An analysis of peripheral heat transfer in man. *Journal of applied physiology*, 30(5):779–786, 1971. ISSN 00218987. doi: 10.1152/jappl.1971.30.5.779.

[58] S. Weinbaum, L.M. M. Jiji, D.E. E. Lemons, S. Weinbaum, and D.E. E. Lemons. Theory and Experiment for the effect of Vascular Microstructure on Surface Tissue Heat Transfer-Part 1: Anatomical Foundation and Model Conceptualization.pdf. *Journal of Biomechanical Engineering*, 106(4):321–330, 1984. ISSN 15288951. doi: 10.1115/1.3138502.

[59] L.M. M. Jiji, S. Weinbaum, and D.E. E. Lemons. Theory and Experiment for the Effect of Vascular Microstructure on Surface Tissue Heat Transfer-Part 2: Model Formulation and solution.pdf. *Journal of Biomechanical Engineering*, 106(4):331–341, 1984. ISSN 15288951. doi: 10.1115/1.3138502.

[60] S. Weinbaum and L.M. M. M. Jiji. A New Simplified Bioheat Euqation for the effect of Blood Flow on Local Average Tissue Temperature.pdf. *Journal of Biomechanical Engineering*, 107(2):131–139, 1985. ISSN 15288951. doi: 10.1115/1.3138533.

[61] Yimin Xuan and W Roetzel. Bioheat Equation of the Human Thermal System. Technical report, 1997.

[62] A. Nakayama and F. Kuwahara. A general bioheat transfer model based on the theory of porous media. *International Journal of Heat and Mass Transfer*, 51(11-12):3190–3199, 6 2008. ISSN 00179310. doi: 10.1016/j.ijheatmasstransfer.2007.05.030.

[63] Assunta Andreozzi, Luca Brunese, Marcello Iasiello, Claudio Tucci, and Giuseppe Peter Vanoli. Modeling Heat Transfer in Tumors: A Review of Thermal Therapies. *Annals of Biomedical Engineering*, 47(3):676–693, 2019. ISSN 15739686. doi: 10.1007/s10439-018-02177-x.

[64] Isabelle Viviane Batista de Lacerda, José Wilson Vieira, Mércia Liane Oliveira, and Fernando Roberto de Andrade Lima. Comparative analysis of the conversion coefficient for internal dosimetry using different phantoms. *Radiation Physics and Chemistry*, 167 (May 2019):108351, 2020. ISSN 18790895. doi: 10.1016/j.radphyschem.2019.108351. URL https://doi.org/10.1016/j.radphyschem.2019.108351.

[65] Gennaro G. Bellizzi, Kemal Sumser, Iva VilasBoas-Ribeiro, Sergio Curto, Tomas Drizdal, Gerard C. van Rhoon, Martine Franckena, and Margarethus M. Paulides. Standardization of patient modeling in hyperthermia simulation studies: introducing the Erasmus Virtual Patient Repository. *International Journal of Hyperthermia*, 37(1):608–616, 2020. ISSN 14645157. doi: 10.1080/02656736.2020.1772996. URL https://doi.org/10.1080/02656736.2020.1772996.

[66] Andreas Christ, Wolfgang Kainz, Eckhart G. Hahn, Katharina Honegger, Marcel Zefferer, Esra Neufeld, Wolfgang Rascher, Rolf Janka, Werner Bautz, Ji Chen, Berthold Kiefer, Peter Schmitt, Hans Peter Hollenbach, Jianxiang Shen, Michael Oberle, Dominik Szczerba, Anthony Kam, Joshua W. Guag, and Niels Kuster. The Virtual Family - Development of surface-based anatomical models of two adults and two children for dosimetric simulations. *Physics in Medicine and Biology*, 55(2), 2010. ISSN 00319155. doi: 10.1088/0031-9155/55/2/N01.

[67] Jörg Peter, Martin P. Tornai, and Ronald J. Jaszczak. Analytical versus voxelized phantom representation for Monte Carlo simulation in radiological imaging. *IEEE*

Transactions on Medical Imaging, 19(5):556–564, 2000. ISSN 02780062. doi: 10.1109/42.870266.

[68] Hans Johansen and Phillip Colella. A Cartesian Grid Embedded Boundary Method for Poisson's Equation on Irregular Domains 1. *Journal of Computational Physics*, 147:60–85, 1998. URL http://ac.els-cdn.com/S0021999198959654/1-s2.0-S0021999198959654-main.pdf?_tid=ff9d8b54-124b-11e7-8676-00000aab0f6c&acdnat=1490550507_03b64e57e8537b315b90b6b6dae2e71d.

[69] Z. L. Wang, J. C.M. Teo, C. K. Chui, S. H. Ong, C. H. Yan, S. C. Wang, H. K. Wong, and S. H. Teoh. Computational biomechanical modelling of the lumbar spine using marching-cubes surface smoothened finite element voxel meshing. *Computer Methods and Programs in Biomedicine*, 80(1):25–35, 2005. ISSN 01692607. doi: 10.1016/j.cmpb.2005.06.006.

[70] M. C. Kolios, M. D. Sherar, and J. W. Hunt. Large blood vessel cooling in heated tissues: A numerical study. *Physics in Medicine and Biology*, 40(4):477–494, 1995. ISSN 00319155. doi: 10.1088/0031-9155/40/4/001.

[71] James N. Hayward and M. A. Baker. Role of cerebral arterial blood in the regulation of brain temperature in the monkey. *The American journal of physiology*, 215(2):389–403, 1968. ISSN 00029513. doi: 10.1152/ajplegacy.1968.215.2.389. URL www.physiology.org/journal/ajplegacy.

[72] V. M.M. M Flyckt, B. W. Raaymakers, and J. J.W. W Lagendijk. Modelling the impact of blood flow on the temperature distribution in the human eye and the orbit: Fixed heat transfer coefficients versus the Pennes bioheat model versus discrete blood vessels. *Physics in Medicine and Biology*, 51(19):5007–5021, 10 2006. ISSN 00319155. doi: 10.1088/0031-9155/51/19/018.

[73] Stephen Blowers, Ian Marshall, Michael Thrippleton, Peter Andrews, Bridget Harris,

Iain Bethune, and Prashant Valluri. How does blood regulate cerebral temperatures during hypothermia? *Scientific Reports*, 8(1):1–10, 2018. ISSN 20452322. doi: 10.1038/s41598-018-26063-7.

[74] José González-Alonso. Human thermoregulation and the cardiovascular system. *Experimental Physiology*, 97(3):340–346, 2012. ISSN 09580670. doi: 10.1113/expphysiol.2011.058701.

[75] V. Shanthoshini Deviha, P. Rengarajan, and R. Jahir Hussain. Modeling blood flow in the blood vessels of the cardiovascular system using fractals. *Applied Mathematical Sciences*, 7(9-12):527–537, 2013. ISSN 1312885X. doi: 10.12988/ams.2013.13044.

[76] M. Zankl, J. Becker, C. Lee, W. E. Bolch, Y. S. Yeom, and C. H. Kim. Computational phantoms, ICRP/ICRU, and further developments. *Annals of the ICRP*, 47(3-4):35–44, 2018. ISSN 1872969X. doi: 10.1177/0146645318756229.

[77] Valentin Alekseev, Maria Vasilyeva, and Vasily Vasiliev. Multiscale simulation of the heat and mass transfer with Brinkman model. *Journal of Physics: Conference Series*, 1392(1), 12 2019. ISSN 17426596. doi: 10.1088/1742-6596/1392/1/012063.

[78] Matthew R. Maynard, Natalia B. Shagina, Evgenia I. Tolstykh, Marina O. Degteva, Tim P. Fell, and Wesley E. Bolch. Fetal organ dosimetry for the Techa River and Ozyorsk offspring cohorts, part 1: a Urals-based series of fetal computational phantoms. *Radiation and Environmental Biophysics*, 54(1):37–46, 2015. ISSN 0301634X. doi: 10.1007/s00411-014-0571-4.

[79] T. Samaras, A. Christ, and N. Kuster. Effects of geometry discretization aspects on the numerical solution of the bioheat transfer equation with the FDTD technique. *Physics in Medicine and Biology*, 51(11), 2006. ISSN 00319155. doi: 10.1088/0031-9155/51/11/N02.

[80] Seth I. Dillard, John A. Mousel, Liza Shrestha, Madhavan L. Raghavan, and Sarah C. Vigmostad. From medical images to flow computations without user- generated meshes.

International journal for numerical methods in biomedical engineering, 30(10):1057–1083, 2014. doi: 10.1002/cnm.2644.From.

[81] Timothy S. Newman and Hong Yi. A survey of the marching cubes algorithm. *Computers and Graphics (Pergamon)*, 30(5):854–879, 2006. ISSN 00978493. doi: 10.1016/j.cag.2006.07.021.

[82] R. K. Crockett, P. Colella, and D. T. Graves. A Cartesian grid embedded boundary method for solving the Poisson and heat equations with discontinuous coefficients in three dimensions. *Journal of Computational Physics*, 230(7):2451–2469, 2011. ISSN 00219991. doi: 10.1016/j.jcp.2010.12.017. URL http://dx.doi.org/10.1016/j.jcp.2010.12.017.

[83] Jonathan Bronson, Joshua A. Levine, and Ross Whitaker. Lattice cleaving: A multimaterial tetrahedral meshing algorithm with guarantees. *IEEE Transactions on Visualization and Computer Graphics*, 20(2):223–237, 2014. ISSN 10772626. doi: 10.1109/TVCG.2013.115.

[84] Dorothea Kasiteropoulou, Anastasia Topalidou, and Soo Downe. A computational fluid dynamics modelling of maternal-fetal heat exchange and blood flow in the umbilical cord. *PLoS ONE*, 15(7 July):5–7, 2020. ISSN 19326203. doi: 10.1371/journal.pone.0231997. URL http://dx.doi.org/10.1371/journal.pone.0231997.

[85] Shu Xing, Jungwook Shin, Jennifer Pursley, Camilo M. Correa-Alfonso, Nicolas Depauw, Sean Domal, Julia Withrow, Wesley Bolch, Clemens Grassberger, and Harald Paganetti. A dynamic blood flow model to compute absorbed dose to circulating blood and lymphocytes in liver external beam radiotherapy. *Physics in Medicine and Biology*, 67(4):45010, 2022. ISSN 13616560. doi: 10.1088/1361-6560/ac4da4. URL http://dx.doi.org/10.1088/1361-6560/ac4da4.

[86] Camilo M. Correa-Alfonso, Julia D. Withrow, Sean J. Domal, Shu Xing, Jungwook Shin, Clemens Grassberger, Harald Paganetti, and Wesley E. Bolch. A mesh-

based model of liver vasculature: implications for improved radiation dosimetry to liver parenchyma for radiopharmaceuticals. *EJNMMI Physics*, 9(1), 2022. ISSN 21977364. doi: 10.1186/s40658-022-00456-0. URL https://doi.org/10.1186/s40658-022-00456-0.

[87] Mihail Ivilinov Todorov, Johannes Christian Paetzold, Oliver Schoppe, Giles Tetteh, Suprosanna Shit, Velizar Efremov, Katalin Todorov-Völgyi, Marco Düring, Martin Dichgans, Marie Piraud, Bjoern Menze, and Ali Ertürk. Machine learning analysis of whole mouse brain vasculature. *Nature Methods*, 17(4):442–449, 4 2020. ISSN 15487105. doi: 10.1038/s41592-020-0792-1.

[88] L. Silvestri, M. C. Müllenbroich, I. Costantini, A. P. Di Giovanna, G. Mazzamuto, A. Franceschini, D. Kutra, A. Kreshuk, C. Checcucci, L. O. Toresano, P. Frasconi, L. Sacconi, and F. S. Pavone. Universal autofocus for quantitative volumetric microscopy of whole mouse brains. *Nature Methods*, 18(8):953–958, 2021. ISSN 15487105. doi: 10.1038/s41592-021-01208-1. URL http://dx.doi.org/10.1038/s41592-021-01208-1.

[89] Claudio Tucci, Macarena Trujillo, Enrique Berjano, Marcello Iasiello, Assunta Andreozzi, and Giuseppe Peter Vanoli. Pennes' bioheat equation vs. porous media approach in computer modeling of radiofrequency tumor ablation. *Scientific Reports*, 11(1):1–13, 2021. ISSN 20452322. doi: 10.1038/s41598-021-84546-6. URL https://doi.org/10.1038/s41598-021-84546-6.

[90] Yuanliang Tang, Lizhong Mu, and Ying He. Numerical simulation of fluid and heat transfer in a biological tissue using an immersed boundary method mimicking the exact structure of the microvascular network. *Fluid Dynamics and Materials Processing*, 16 (2):281–296, 2020. ISSN 15552578. doi: 10.32604/fdmp.2020.06760.

[91] Jahrul M. Alam. A multiscale modeling study for the convective mass transfer in a subsurface aquifer. *Heat and Mass Transfer/Waerme- und Stoffuebertragung*, 51(9):

1247–1261, 8 2015. ISSN 14321181. doi: 10.1007/s00231-014-1490-2. URL http://arxiv.org/abs/1308.0308http://dx.doi.org/10.1007/s00231-014-1490-2.

[92] Luca Formaggia, Daniele Lamponi, and Alfio Quarteroni. One-dimensional models for blood flow in arteries. *Journal of Engineering Mathematics*, 47(3-4):251–276, 2003. ISSN 00220833. doi: 10.1023/B:ENGI.0000007980.01347.29.

[93] Ahmed Tamkin Butt, Yousif Abdalla Abakr, K B Mustapha, A T Butt, and Y A Abakr. Blood Flow Modelling to Improve Cardiovascular Diagnostics: A Preliminary Review of 1-D Modelling Numerical Modelling of the Human Arterial Network In Conjunction with the GTF Technique to improve Cardiovascular Diagnostics View project The investigation of microalgae biodiversity of temporary water habitats in Johor National Park as source of renewable novel bioactive compounds View project Blood Flow Modelling to Improve Cardiovascular Diagnostics: a Preliminary Review of 1-D Modelling. Technical report, 2018. URL https://www.researchgate.net/publication/335023049.

[94] Mariana Silva, Bruno Freitas, Renato Andrade, João Espregueira-Mendes, Filipe Silva, Óscar Carvalho, and Paulo Flores. Computational Modelling of the Bioheat Transfer Process in Human Skin Subjected to Direct Heating and/or Cooling Sources: A Systematic Review. *Annals of Biomedical Engineering*, 48(6):1616–1639, 2020. ISSN 15739686. doi: 10.1007/s10439-020-02515-y.

[95] A. T. Butt, Y. A. Abakr, and K. B. Mustapha. Blood flow modelling to improve cardiovascular diagnostics: A preliminary review of 1-D modelling. *International Journal of Engineering and Technology(UAE)*, 7(4):25–34, 2018. ISSN 2227524X. doi: 10.14419/ijet.v7i4.3.19547.

[96] Yue Ping Wang, Yuan Liang Tang, and Ying He. Numerical analysis of the influence of RBCs on oxygen transport within a tissue with an embedded capillary network. *Proceedings of the Institution of Mechanical Engineers, Part C: Jour-*

nal of Mechanical Engineering Science, 235(2):412–427, 2021. ISSN 20412983. doi: 10.1177/0954406220954482.

[97] Yue Ping Wang, Rui Hao Cheng, Ying He, and Li Zhong Mu. Thermal Analysis of Blood Flow Alterations in Human Hand and Foot Based on Vascular-Porous Media Model. *Frontiers in Bioengineering and Biotechnology*, 9(January):1–17, 2022. ISSN 22964185. doi: 10.3389/fbioe.2021.786615.

[98] Steven M. LaValle and James J Kuffner. Randomized Kinodynamic Planning. *The International Journal of Robotics Research*, 20(5):378–400, 5 2001. ISSN 0278-3649. doi: 10.1177/02783640122067453. URL http://journals.sagepub.com/doi/10.1177/02783640122067453.

[99] Alberto Coccarelli, Etienne Boileau, Dimitris Parthimos, and Perumal Nithiarasu. An advanced computational bioheat transfer model for a human body with an embedded systemic circulation. *Biomechanics and Modeling in Mechanobiology*, 15(5):1173–1190, 10 2016. ISSN 16177940. doi: 10.1007/s10237-015-0751-4.

[100] Yuanda Cheng, Jianlei Niu, and Naiping Gao. Thermal comfort models: A review and numerical investigation. *Building and Environment*, 47(1):13–22, 2012. ISSN 03601323. doi: 10.1016/j.buildenv.2011.05.011. URL http://dx.doi.org/10.1016/j.buildenv.2011.05.011.

[101] Erlend Hodneland, Erik Hanson, Ove Sævareid, Geir Nævdal, Arvid Lundervold, Veronika Šoltészová, Antonella Z. Munthe-Kaas, Andreas Deistung, Jürgen R. Reichenbach, and Jan M. Nordbotten. A new framework for assessing subject-specific whole brain circulation and perfusion using mri-based measurements and a multi-scale continuous flow model. *PLoS Computational Biology*, 15(6):1–31, 6 2019. ISSN 15537358. doi: 10.1371/journal.pcbi.1007073.

[102] E. Y.K. Ng and L. T. Chua. Prediction of skin burn injury. Part 1: Numerical modelling; Part 2: Parametric and sensitivity analysis. *Proceedings of the Institution of*

Mechanical Engineers, Part H: Journal of Engineering in Medicine, 216(6):426–427, 2002. ISSN 20413033. doi: 10.1243/095441102321032229.

[103] E. Y.K. Ng and L. T. Chua. Prediction of skin burn injury. Part 2: Parametric and sensitivity analysis. *Proceedings of the Institution of Mechanical Engineers, Part H: Journal of Engineering in Medicine*, 216(3):171–183, 2002. ISSN 09544119. doi: 10.1243/0954411021536388.

[104] A. N. Cookson, J. Lee, C. Michler, R. Chabiniok, E. Hyde, D. A. Nordsletten, M. Sinclair, M. Siebes, and N. P. Smith. A novel porous mechanical framework for modelling the interaction between coronary perfusion and myocardial mechanics. *Journal of Biomechanics*, 45(5):850–855, 2012. ISSN 00219290. doi: 10.1016/j.jbiomech.2011.11.026. URL http://dx.doi.org/10.1016/j.jbiomech.2011.11.026.

[105] D. E. Lemons, S. Chien, L. I. Crawshaw, S. Weinbaum, and L. M. Jiji. Significance of vessel size and type in vascular heat transfer. *American Journal of Physiology-Regulatory, Integrative and Comparative Physiology*, 253(1):R128–R135, 1987. ISSN 0363-6119. doi: 10.1152/ajpregu.1987.253.1.r128. URL www.physiology.org/journal/ajpregu.

[106] Kiet A. Tran, Abigail Baldwin-Leclair, Brandon J. DeOre, Morgan Antisell, and Peter A. Galie. Oxygen gradients dictate angiogenesis but not barriergenesis in a 3D brain microvascular model. *Journal of Cellular Physiology*, 237(10):3872–3882, 2022. ISSN 10974652. doi: 10.1002/jcp.30840.

[107] Marianne O. Stefanini, Amina A. Qutub, Feilim Mac Gabhann, and Aleksander S. Popel. Computational models of VEGF-associated angiogenic processes in cancer. *Mathematical Medicine and Biology*, 29(1):85–94, 2012. ISSN 14778602. doi: 10.1093/imammb/dqq025.

[108] Monica Corada, Marco Francesco Morini, and Elisabetta Dejana. Signaling pathways

in the specification of arteries and veins. *Arteriosclerosis, Thrombosis, and Vascular Biology*, 34(11):2372–2377, 2014. ISSN 15244636. doi: 10.1161/ATVBAHA.114.303218.

[109] John C. Chappell, Jordan Darden, Laura Beth Payne, Kathryn Fink, and Victoria L. Bautch. Blood Vessel Patterning on Retinal Astrocytes Requires Endothelial Flt-1 (VEGFR-1). *Journal of Developmental Biology*, 7(3):1–13, 2019. ISSN 22213759. doi: 10.3390/jdb7030018.

[110] Lei Tang, Anne L. Van De Ven, Dongmin Guo, Vivi Andasari, Vittorio Cristini, King C. Li, and Xiaobo Zhou. Computational modeling of 3D tumor growth and angiogenesis for chemotherapy evaluation. *PLoS ONE*, 9(1):1–12, 2014. ISSN 19326203. doi: 10.1371/journal.pone.0083962.

[111] Hisako Takigawa-imamura, Saito Hirano, Chisato Watanabe, and Chiaki Ohtaka-maruyama. Computational Model Exploring Characteristic Pattern Regulation in Periventricular Vessels. 2022.

[112] Eugene Kim, Spyros Stamatelos, Jana Cebulla, Zaver M. Bhujwalla, Aleksander S. Popel, and Arvind P. Pathak. Multiscale imaging and computational modeling of blood flow in the tumor vasculature. *Annals of Biomedical Engineering*, 40(11):2425–2441, 2012. ISSN 00906964. doi: 10.1007/s10439-012-0585-5.

[113] T. A.M. Heck, M. M. Vaeyens, and H. Van Oosterwyck. Computational models of sprouting angiogenesis and cell migration: Towards multiscale mechanochemical models of angiogenesis. *Mathematical Modelling of Natural Phenomena*, 10(1):108–141, 2015. ISSN 17606101. doi: 10.1051/mmnp/201510106.

[114] Yu Zhang, Hanwen Wang, Rebeca Hannah M. Oliveira, Chen Zhao, and Aleksander S. Popel. Systems biology of angiogenesis signaling: Computational models and omics. *WIREs Mechanisms of Disease*, 14(4):1–37, 2022. ISSN 2692-9368. doi: 10.1002/wsbm.1550.

[115] R. M H Merks and James A. Glazier. Dynamic mechanisms of blood vessel growth. *Nonlinearity*, 2006. ISSN 09517715. doi: 10.1088/0951-7715/19/1/000.

[116] Sheng Tong and Fan Yuan. Numerical simulations of angiogenesis in the cornea. *Microvascular Research*, 2001. ISSN 00262862. doi: 10.1006/mvre.2000.2282.

[117] James D. Murray. *Mathematical Biology II. Spatial Models and Biomedical Applications*, volume 18. 2003. ISBN 4420767936. doi: 10.1016/j.camwa.2013.03.019. URL http://link.springer.com/10.1140/epjb/e2013-40570-8%5Cnhttp://arxiv.org/abs/1406.6401%5Cnhttp://arxiv.org/abs/1204.1475%5Cnhttp://link.aps.org/doi/10.1103/PhysRevLett.91.058302%5Cnhttp://arxiv.org/abs/nlin/0111059%5Cnhttp://link.aps.org/doi/10.1103/PhysRe.

[118] James D. Murray. On the mechanochemical theory of biological pattern formation with application to vasculogenesis, 2003. ISSN 16310691.

[119] Sylvie Lorthois and Francis Cassot. Fractal analysis of vascular networks: Insights from morphogenesis. *Journal of Theoretical Biology*, 262(4):614–633, 2010. ISSN 00225193. doi: 10.1016/j.jtbi.2009.10.037. URL http://dx.doi.org/10.1016/j.jtbi.2009.10.037.

[120] L. Niemeyer, L. Pietronero, and H. J. Wiesmann. Fractal dimension of dielectric breakdown. *Physical Review Letters*, 52(12):1033–1036, 1984. ISSN 00319007. doi: 10.1103/PhysRevLett.52.1033.

[121] Vincent Fleury and Laurent Schwartz. Diffusion limited aggregation from shear stress as a simple model of vasculogenesis. *Fractals*, 7(1):33–39, 1999. ISSN 0218348X. doi: 10.1142/S0218348X99000050.

[122] Vincent Fleury and Laurent Schwartz. Modelisation of 3-D microvasculature by interlaced diffusion limited aggregation. *Fractals*, 8(3):255–259, 2000. ISSN 0218348X. doi: 10.1142/S0218348X00000317.

[123] T. A. Witten and L. M. Sander. Diffusion-Limited Aggregation, a Kinetic Critical Phenomenon. *Physical Review Letters*, 47(19):1400–1403, 11 1981. ISSN 0031-9007. doi: 10.1103/PhysRevLett.47.1400. URL https://link.aps.org/doi/10.1103/PhysRevLett.47.1400.

[124] W Schreiner. Computer generation of complex arterial tree models. *Journal of Biomedical Engineering*, 15(2):148–150, 3 1993. ISSN 01415425. doi: 10.1016/0141-5425(93)90046-2. URL https://linkinghub.elsevier.com/retrieve/pii/0141542593900462.

[125] Wolfgang Schreiner, Friederike Neumann, Martin Neumann, Adelheid End, Susanne M. Roedler, and Seyedhossein Aharinejad. The influence of optimization target selection on the structure of arterial tree models generated by constrained constructive optimization. *Journal of General Physiology*, 106(4):583–599, 1995. ISSN 15407748. doi: 10.1085/jgp.106.4.583.

[126] Wolfgang Schreiner, Rudolf Karch, Martin Neumann, Friederike Neumann, Paul Szawlowski, and Susanne Roedler. Optimized arterial trees supplying hollow organs. *Medical Engineering and Physics*, 28(5):416–429, 2006. ISSN 13504533. doi: 10.1016/j.medengphy.2005.07.019.

[127] L. F. M. Cury, G. D. Maso Talou, M. Younes-Ibrahim, and P. J. Blanco. Parallel generation of extensive vascular networks with application to an archetypal human kidney model. *Royal Society Open Science*, 8(12), 2021. doi: 10.1098/rsos.210973.

[128] Gonzalo Daniel Maso Talou, Soroush Safaei, Peter John Hunter, and Pablo Javier Blanco. Adaptive constrained constructive optimisation for complex vascularisation processes. *Scientific Reports*, 11(1):1–22, 2021. ISSN 20452322. doi: 10.1038/s41598-021-85434-9. URL https://doi.org/10.1038/s41598-021-85434-9.

[129] Junhong Shen, Abdul Hannan Faruqi, Yifan Jiang, and Nima Maftoon. Mathematical Reconstruction of Patient-Specific Vascular Networks Based on Clinical Images and

Global Optimization. *IEEE Access*, 9:20648–20661, 2021. ISSN 21693536. doi: 10.1109/ACCESS.2021.3052501.

[130] P A Hasgall, F Di Gennaro, C Baumgartner, E Neufeld, B Lloyd, MC Gosselin, D Payne, A Klingenböck, and N Kuster. IT'IS Database for thermal and electromagnetic parameters of biological tissues, 2018. URL http://www.itis.ethz.ch/virtual-population/tissue-properties/overview%0Ahttp://www.itis.ethz.ch/virtual-population/tissue-properties/overview.

[131] Steve Pieper, Michael Halle, and Ron Kikinis. 3D Slicer. *2004 2nd IEEE International Symposium on Biomedical Imaging: Macro to Nano*, 1:632–635, 2004. doi: 10.1109/isbi.2004.1398617.

[132] Robert McNeel et al. Rhinoceros 3d, version 6.0. *Robert McNeel & Associates, Seattle, WA*, 2010.

[133] Francisco Javier González. Non-invasive estimation of the metabolic heat production of breast tumors using digital infrared imaging. *Quantitative InfraRed Thermography Journal*, 8(2):139–148, 2011. ISSN 17686733. doi: 10.3166/qirt.8.139-148.

[134] Daniel Sunday. Fast Polygon Area and Newell Normal Computation. *Journal of Graphics Tools*, 7(2):9–13, 2002. ISSN 1086-7651. doi: 10.1080/10867651.2002.10487556.

[135] M. Berger. *Cut Cells: Meshes and Solvers*, volume 18. Elsevier B.V., 1 edition, 2017. doi: 10.1016/bs.hna.2016.10.008. URL http://dx.doi.org/10.1016/bs.hna.2016.10.008.

[136] Eduard Rohan, Vladimír Lukeš, and Alena Jonášová. Modeling of the contrast-enhanced perfusion test in liver based on the multi-compartment flow in porous media. *Journal of Mathematical Biology*, 77(2):421–454, 2018. ISSN 14321416. doi: 10.1007/s00285-018-1209-y.

[137] Erlend Hodneland, Erik Hanson, Antonella Z. Munthe-Kaas, Arvid Lundervold, and Jan M. Nordbotten. Physical Models for Simulation and Reconstruction of Human

Tissue Deformation Fields in Dynamic MRI. *IEEE Transactions on Biomedical Engineering*, 63(10):2200–2210, 2016. ISSN 15582531. doi: 10.1109/TBME.2015.2514262.

[138] Jørg E. Aarnes, Tore Gimse, and Knut-Andreas Lie. An Introduction to the Numerics of Flow in Porous Media using Matlab. In *Geometric Modelling, Numerical Simulation, and Optimization*, pages 265–306. Springer Berlin Heidelberg, Berlin, Heidelberg, 2007. ISBN 9783540687825. doi: 10.1007/978-3-540-68783-2{_}9. URL http://link.springer.com/10.1007/978-3-540-68783-2_9.

[139] Erlend Hodneland, Xiaozhe Hu, and Jan M. Nordbotten. Well-posedness and discretization for a class of models for mixed-dimensional problems with high-dimensional gap. *SIAM Journal on Applied Mathematics*, 81(5):2218–2245, 2021. ISSN 00361399. doi: 10.1137/20M1362541.

[140] Guido Van Rossum and Fred L. Drake. *Python 3 Reference Manual*. CreateSpace, Scotts Valley, CA, 2009. ISBN 1441412697.

[141] David W. Hahn and M. Necati Özişik. Heat Conduction Fundamentals. In *Heat Conduction*, pages 1–39. John Wiley & Sons, Inc., Hoboken, NJ, USA, 3 edition, 8 2012. ISBN 978-0470902936. doi: 10.1002/9781118411285.ch1. URL https://onlinelibrary.wiley.com/doi/10.1002/9781118411285.ch1.

[142] PA Hasgall, F Di Gennaro, C Baumgartner, E Neufeld, B Lloyd, MC Gosselin, D Payne, A Klingenböck, and N Kuster. Database of Tissue Properties, 2018. URL http://www.itis.ethz.ch/virtual-population/tissue-properties/overview%0Ahttp://www.itis.ethz.ch/virtual-population/tissue-properties/overview.

[143] KENNETH MELLANBY. The Body Temperature of the Frog. *Journal of Experimental Biology*, 18(1):55–61, 3 1941. ISSN 1477-9145. doi: 10.1242/jeb.18.1.55. URL https://journals.biologists.com/jeb/article/18/1/55/4661/The-Body-Temperature-of-the-Frog.

[144] Youcef Saad and Martin H. Schultz. GMRES: A Generalized Minimal Residual Algorithm for Solving Nonsymmetric Linear Systems. *SIAM Journal on Scientific and Statistical Computing*, 7(3):856–869, 1986. ISSN 0196-5204. doi: 10.1137/0907058.

[145] Yousef Saad. *Iterative Methods for Sparse Linear Systems, Second Edition*. 2003. ISBN 0898715342. URL http://www.amazon.ca/exec/obidos/redirect?tag=citeulike09-20&amp.

[146] Frank Wilcoxon. Individual Comparisons by Ranking Methods. In *Breakthroughs in statistics*, volume 1, pages 196–202. 1992. doi: 10.1007/978-1-4612-4380-9{_}16. URL http://link.springer.com/10.1007/978-1-4612-4380-9_16.

[147] Stephen W. Scheff. Nonparametric Statistics. In *Fundamental Statistical Principles for the Neurobiologist*, pages 157–182. Elsevier, 2016. ISBN 9789813148963. doi: 10.1016/B978-0-12-804753-8.00008-7. URL https://linkinghub.elsevier.com/retrieve/pii/B9780128047538000087.

[148] Etain A. Tansey and Christopher D. Johnson. Recent advances in thermoregulation. *Advances in Physiology Education*, 39(1):139–148, 2015. ISSN 15221229. doi: 10.1152/advan.00126.2014.

[149] Yutaka Kobayashi and Shin Ichi Tanabe. Development of JOS-2 human thermoregulation model with detailed vascular system. *Building and Environment*, 66:1–10, 2013. ISSN 03601323. doi: 10.1016/j.buildenv.2013.04.013. URL http://dx.doi.org/10.1016/j.buildenv.2013.04.013.

[150] Alexis Kotte, Gerard Van Leeuwen, Jacob De Bree, John Van Der Koijk, Hans Crezee, and Jan Lagendijk. A description of discrete vessel segments in thermal modelling of tissues. *Physics in Medicine and Biology*, 41(5):865–884, 5 1996. ISSN 00319155. doi: 10.1088/0031-9155/41/5/004.

[151] Jiho Yang, Y. Eugene Pak, and Tae Rin Lee. Predicting bifurcation angle effect on blood flow in the microvasculature. *Microvascular Research*, 108:22–28, 2016. ISSN

10959319. doi: 10.1016/j.mvr.2016.07.001. URL http://dx.doi.org/10.1016/j.mvr.2016.07.001.

[152] Hernán G. Morales, Ignacio Larrabide, Arjan J. Geers, Martha L. Aguilar, and Alejandro F. Frangi. Newtonian and non-Newtonian blood flow in coiled cerebral aneurysms. *Journal of Biomechanics*, 46(13):2158–2164, 2013. ISSN 00219290. doi: 10.1016/j.jbiomech.2013.06.034. URL http://dx.doi.org/10.1016/j.jbiomech.2013.06.034.

[153] Loke Kok Foong, Nima Shirani, Davood Toghraie, Majid Zarringhalam, and Masoud Afrand. Numerical simulation of blood flow inside an artery under applying constant heat flux using Newtonian and non-Newtonian approaches for biomedical engineering. *Computer Methods and Programs in Biomedicine*, 190:105375, 2020. ISSN 18727565. doi: 10.1016/j.cmpb.2020.105375. URL https://doi.org/10.1016/j.cmpb.2020.105375.

[154] Cecil D. Murray. The physiological principle of minimum work applied to the angle of branching of arteries. *Journal of General Physiology*, 9(6):835–841, 1926. ISSN 15407748. doi: 10.1085/jgp.9.6.835.

[155] Jian Yang and Yongtian Wang. Design of vascular networks: A mathematical model approach. *International Journal for Numerical Methods in Biomedical Engineering*, 29(4):515–529, 4 2013. ISSN 20407939. doi: 10.1002/cnm.2534. URL http://knowledgebase.terrafrica.org/fileadmin/user_upload/terrafrica/docs/Final_Rockefeller_Report4April08.pdfhttps://onlinelibrary.wiley.com/doi/10.1002/cnm.2534.

[156] M. P. WIEDEMAN. Dimensions of blood vessels from distributing artery to collecting vein. *Circulation research*, 12:375–378, 1963. ISSN 00097330. doi: 10.1161/01.RES.12.4.375.

[157] B. Rajagopalan, C. D. Bertram, T. Stallard, and G. De J. Lee. Blood flow in pulmonary

veins: III simultaneous measurements of their dimensions, intravascular pressure and flow. *Cardiovascular Research*, 13(12):684–692, 1979. ISSN 00086363. doi: 10.1093/cvr/13.12.684.

[158] Liang Zhu, Lisa X. Xu, Qinghong He, and Sheldon Weinbaum. A new fundamental bioheat equation for muscle tissue - Part II: Temperature of SAV vessels. *Journal of Biomechanical Engineering*, 124(1):121–132, 2002. ISSN 01480731. doi: 10.1115/1.1431263.

Appendix A

Pressure Maps for 2D Analysis

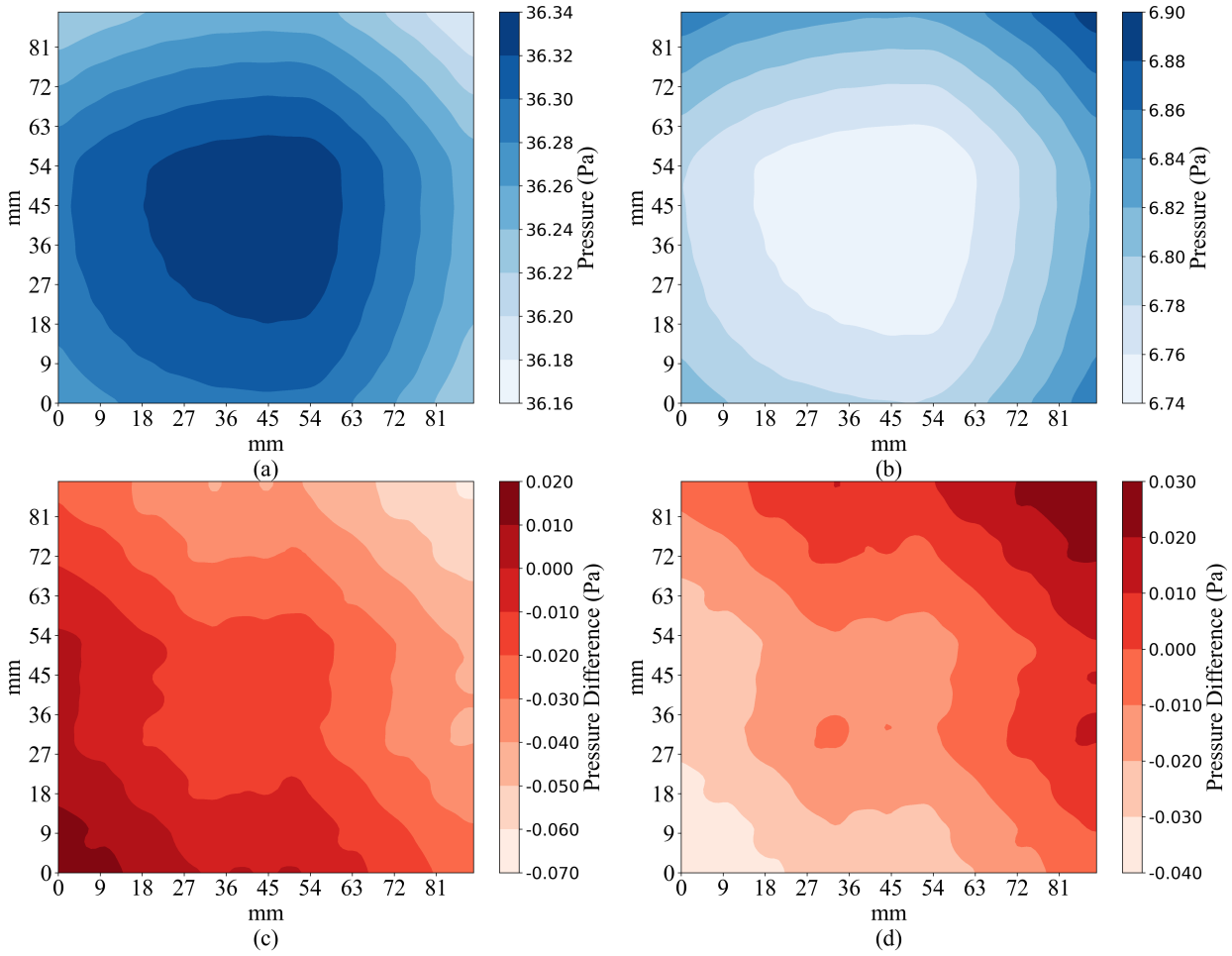

Figure A.1: Pressure map of ref. Nt256 compared with Nt64

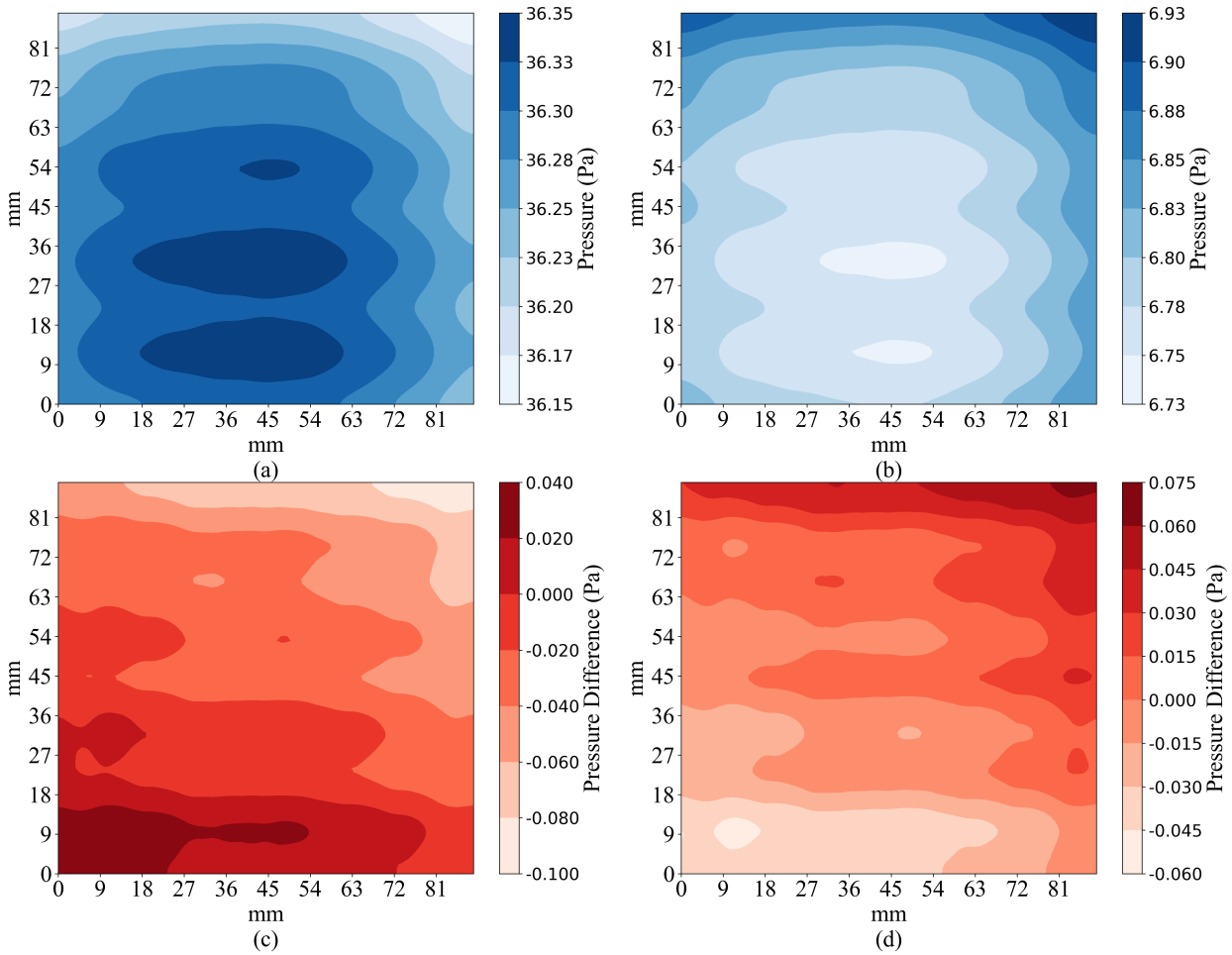

Figure A.2: Pressure map of ref. Nt256 compared with Nt32

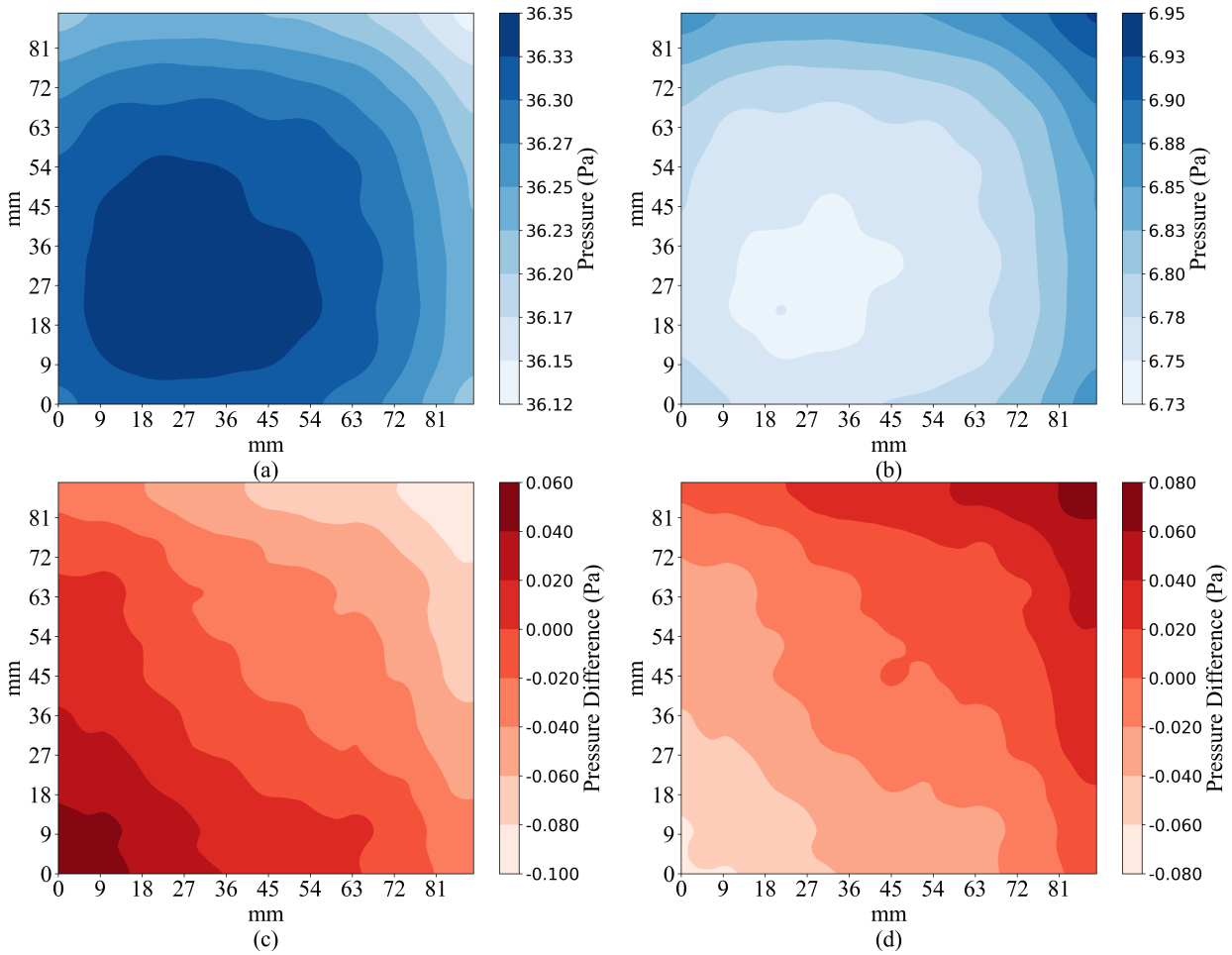

Figure A.3: Pressure map of ref. Nt256 compared with Nt16

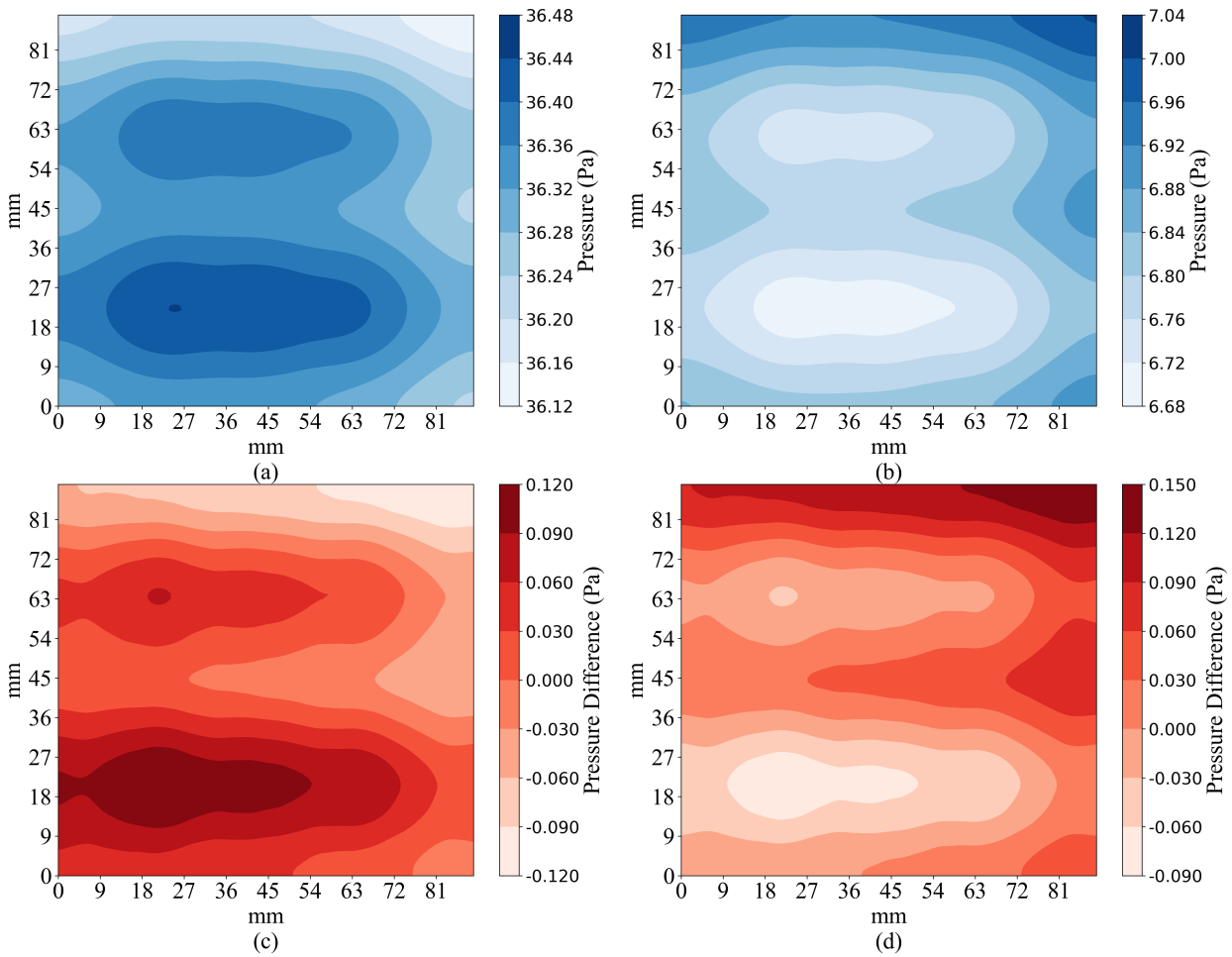

Figure A.4: Pressure map of ref. Nt256 compared with Nt8

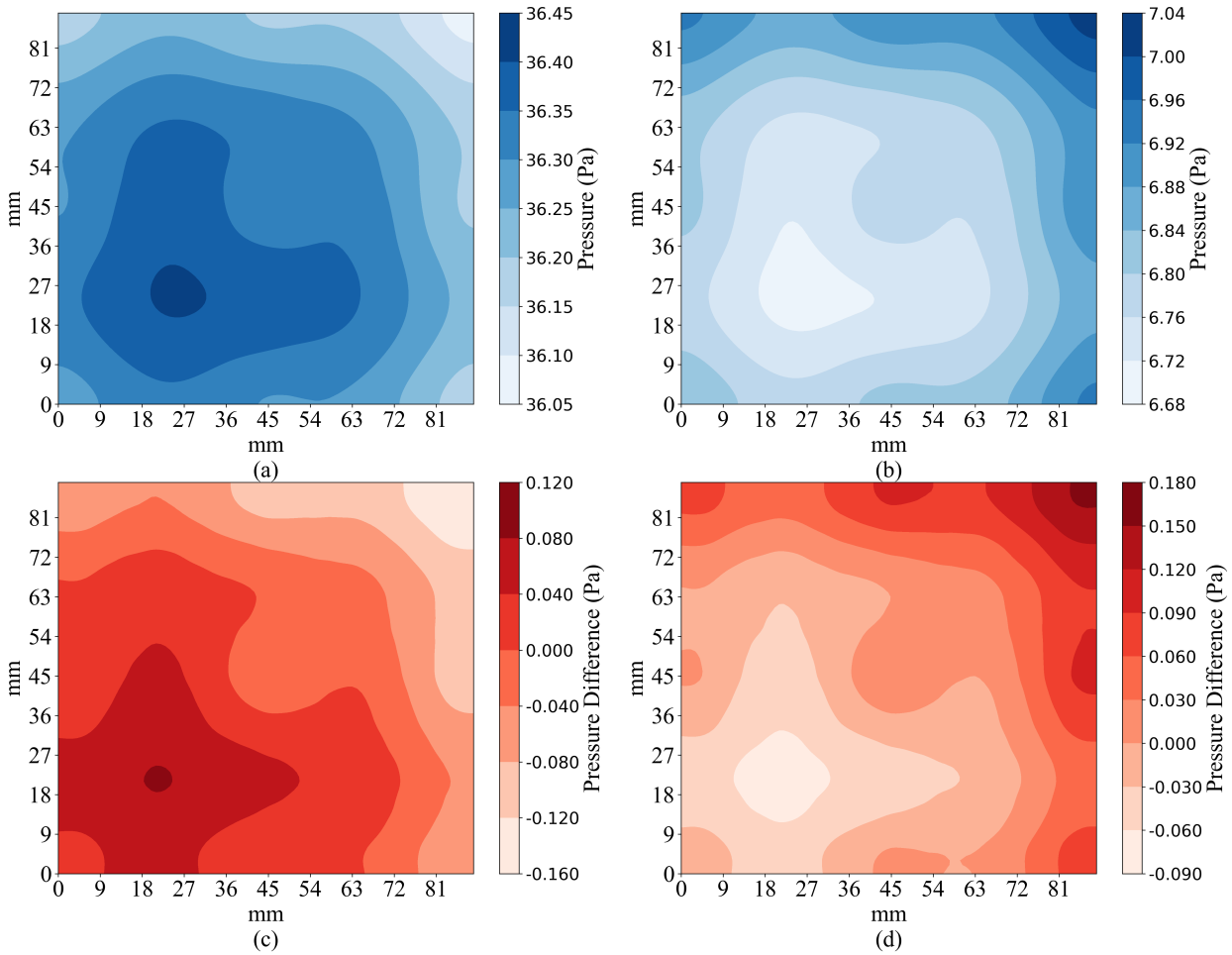

Figure A.5: Pressure map of ref. Nt256 compared with Nt4

Appendix B

Pressure Maps for 3D Analysis

B.1 Pressure Analysis at $z = 1$

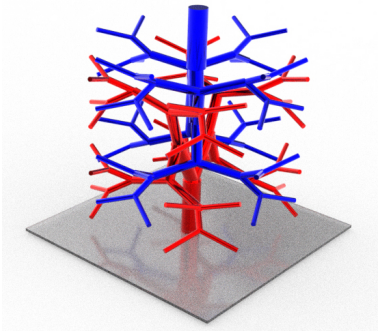

Figure B.1: Location of $z = 1$

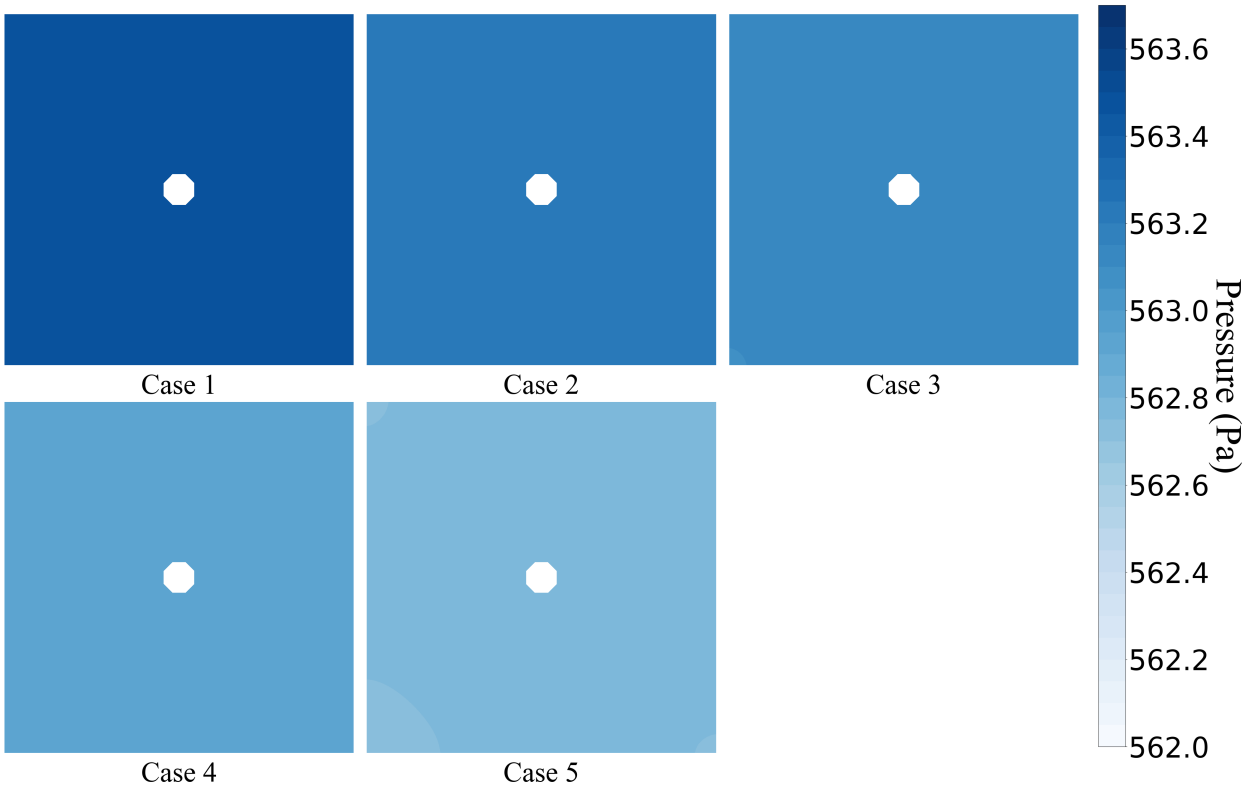

Figure B.2: Arterial compartment pressure map of five simulation cases at $z = 1$

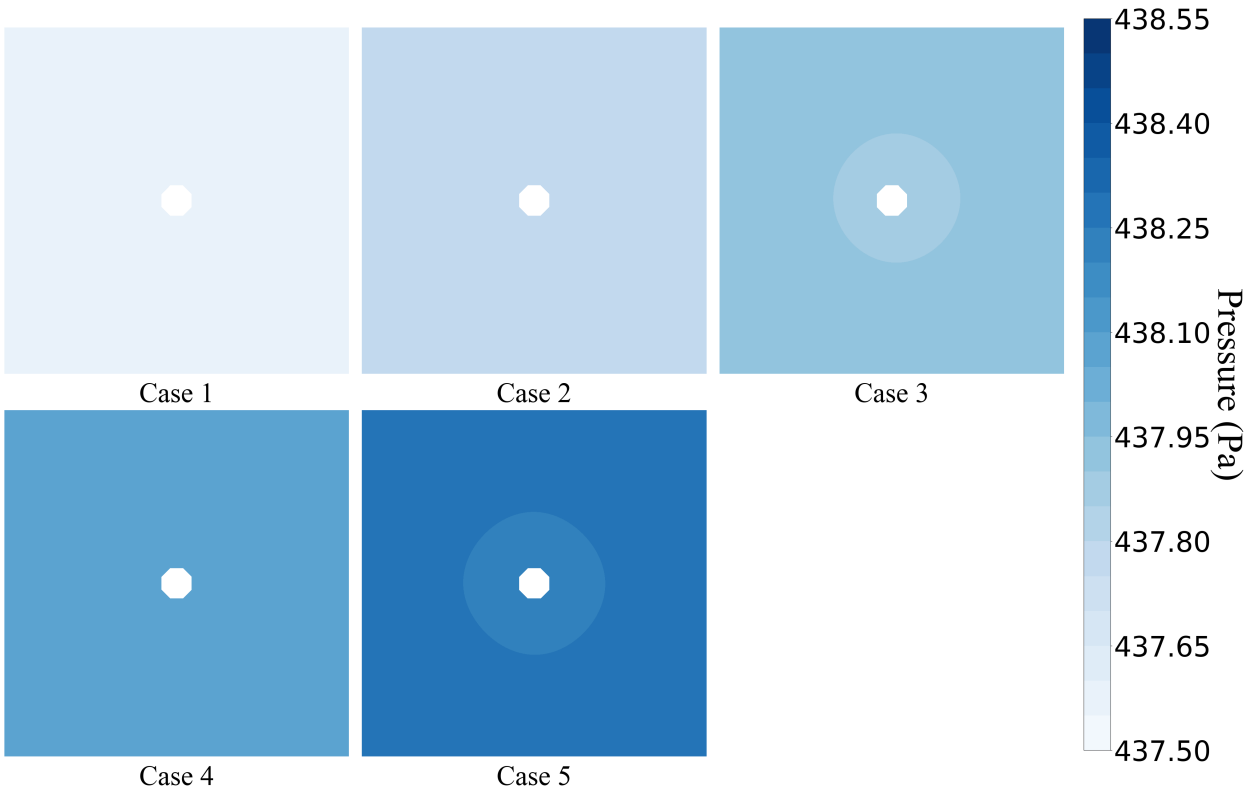

Figure B.3: Venous Compartment pressure map of five simulation cases at $z = 1$

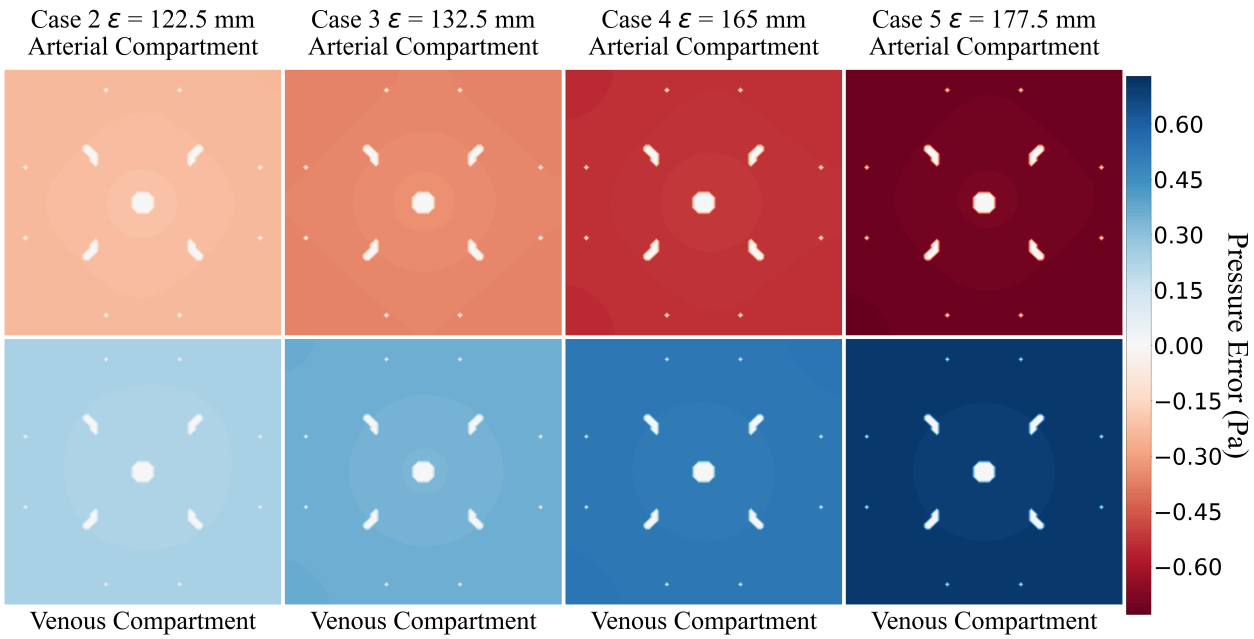

Figure B.4: Pressure error at $z = 1$

B.2 Pressure Analysis at $z = 20$

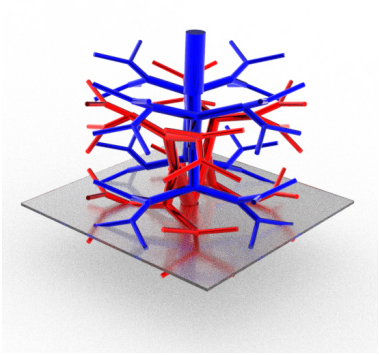

Figure B.5: Location of $z = 20$

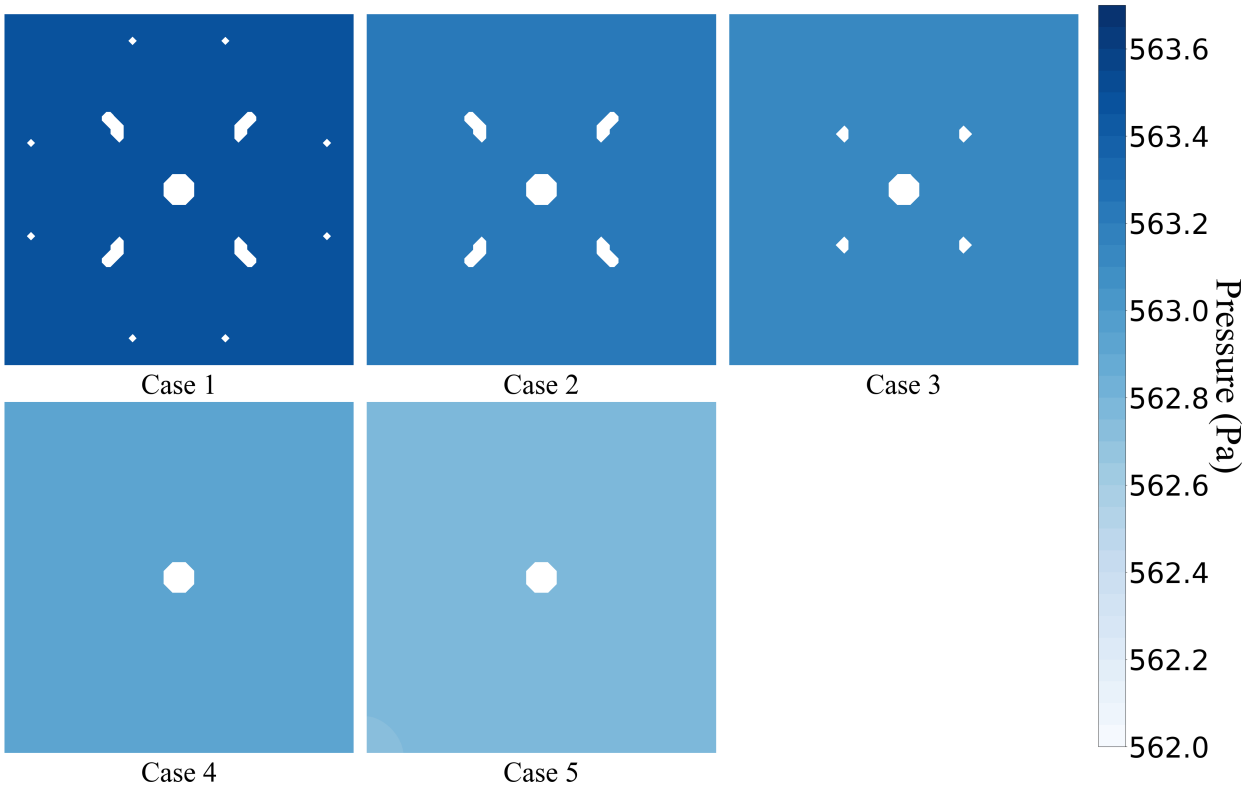

Figure B.6: Arterial compartment pressure map of five simulation cases at $z = 20$

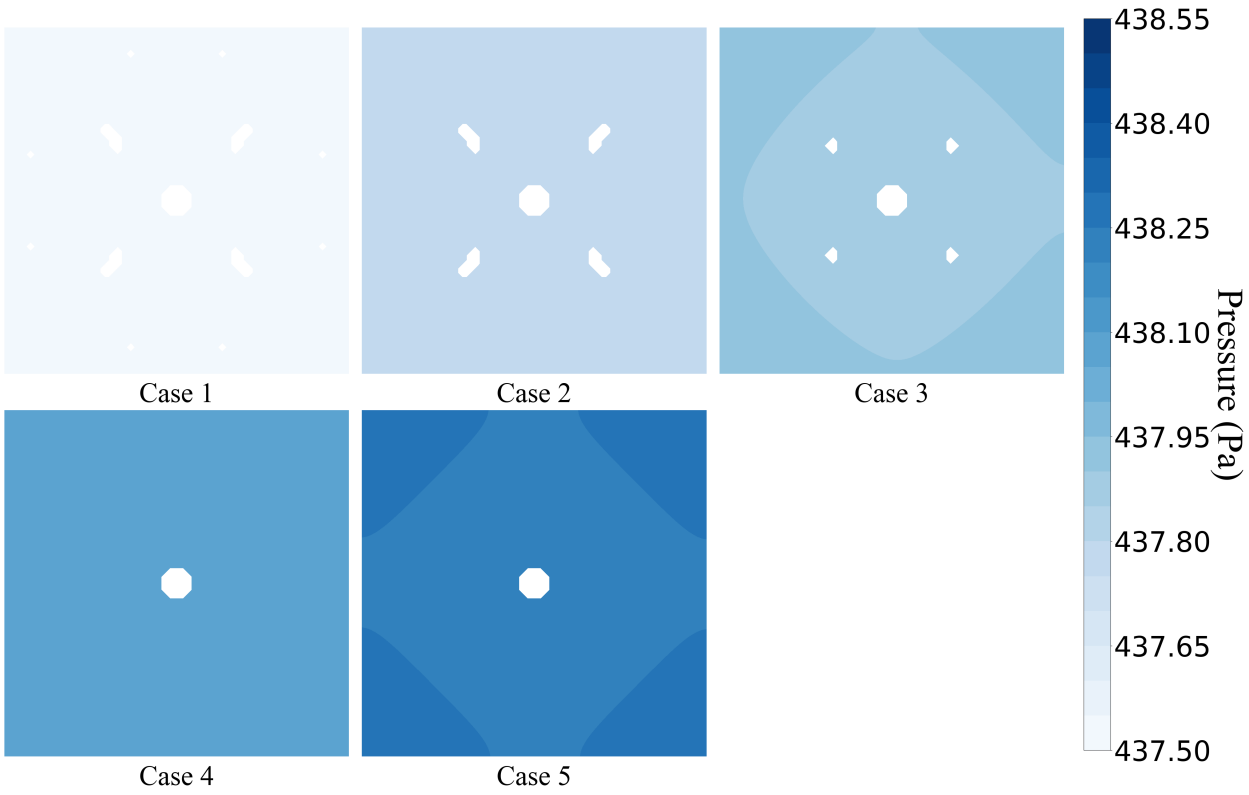

Figure B.7: Venous Compartment pressure map of five simulation cases at $z = 20$

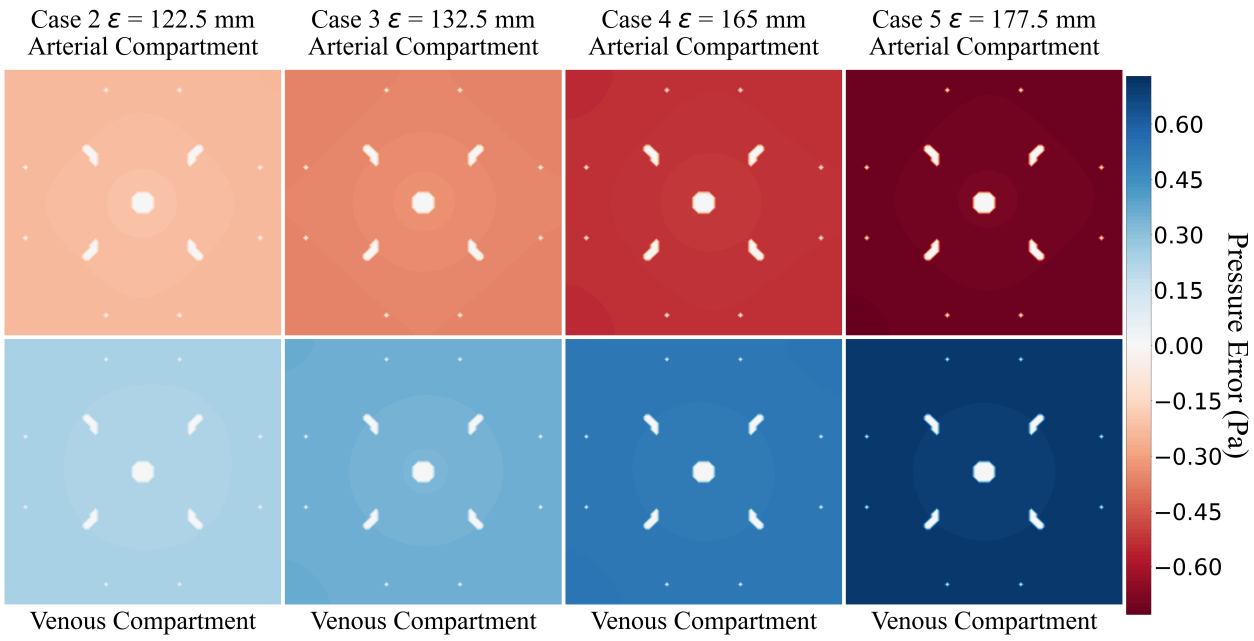

Figure B.8: Pressure error at $z = 20$

B.3 Pressure Analysis at $z = 60$

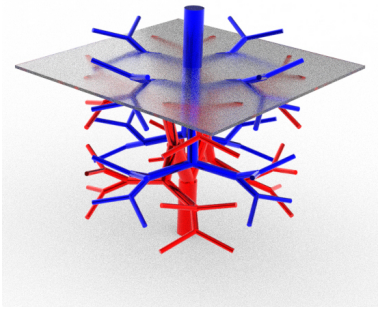

Figure B.9: Location of $z = 60$

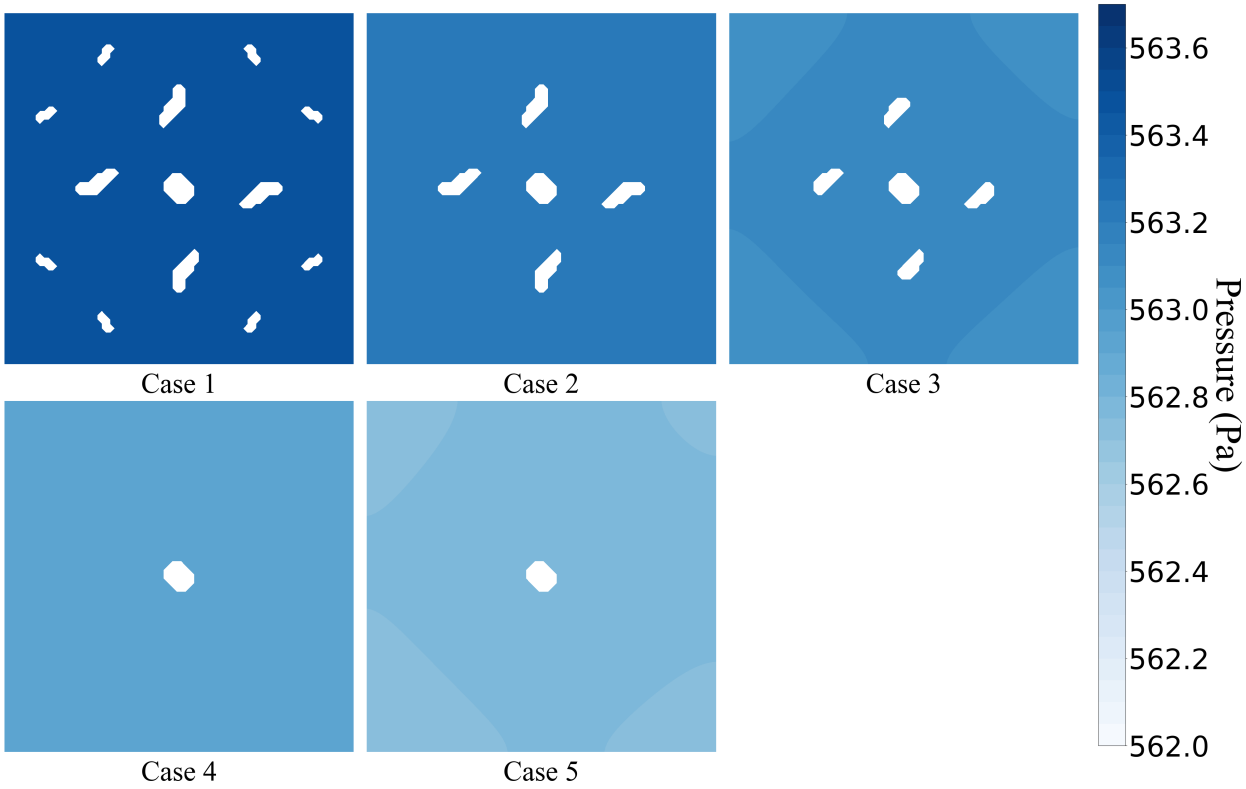

Figure B.10: Arterial compartment pressure map of five simulation cases at $z = 60$

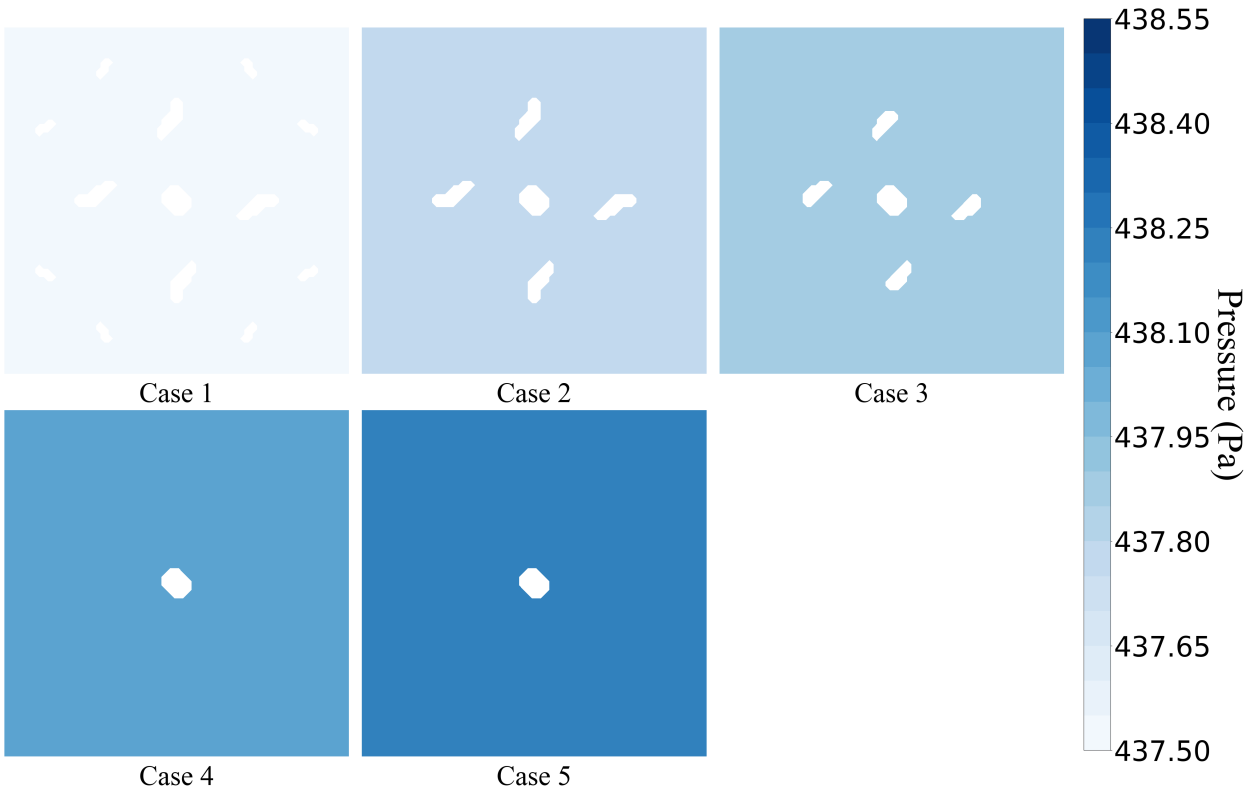

Figure B.11: Venous Compartment pressure map of five simulation cases at $z = 60$

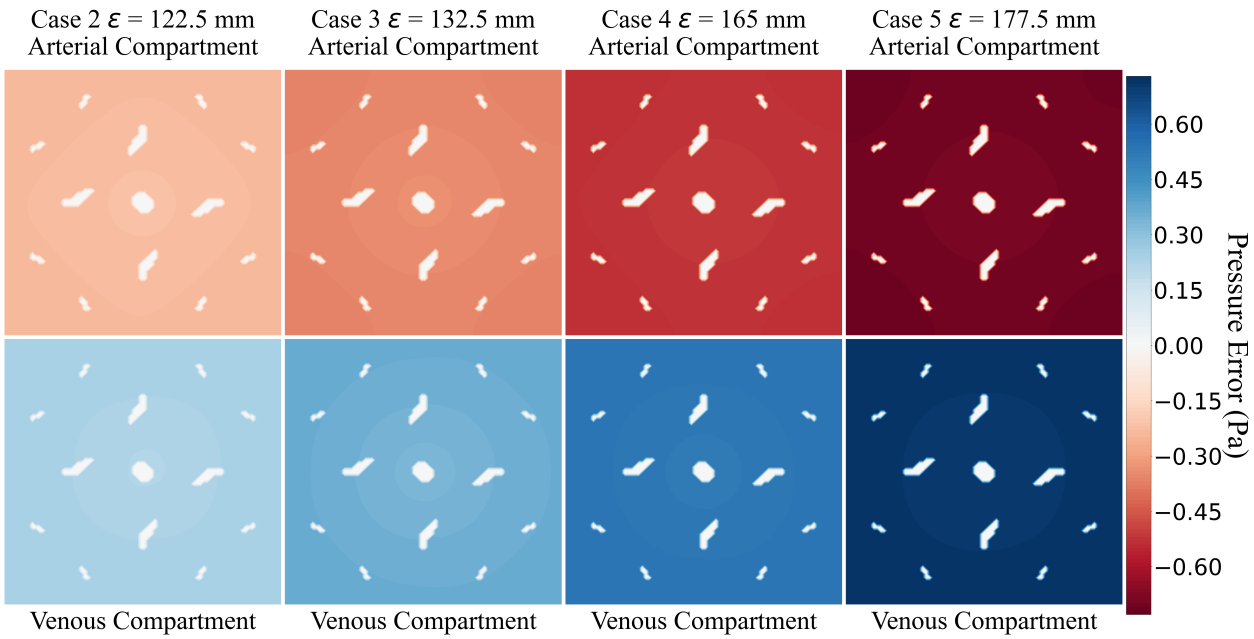

Figure B.12: Pressure error at $z = 60$

B.4 Pressure Analysis at $z = 80$

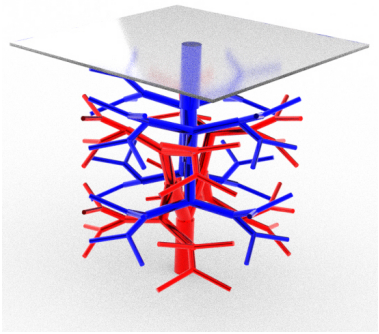

Figure B.13: Location of $z = 80$

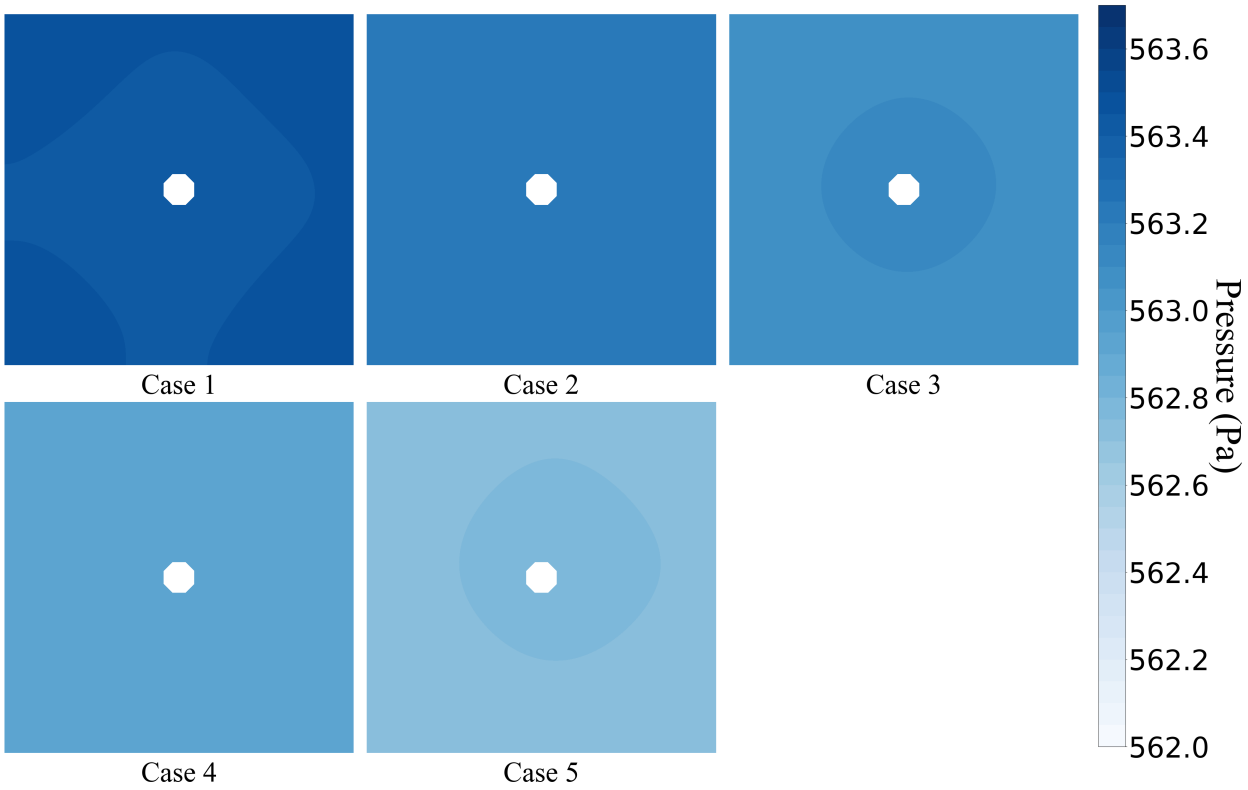

Figure B.14: Arterial compartment pressure map of five simulation cases at $z = 80$

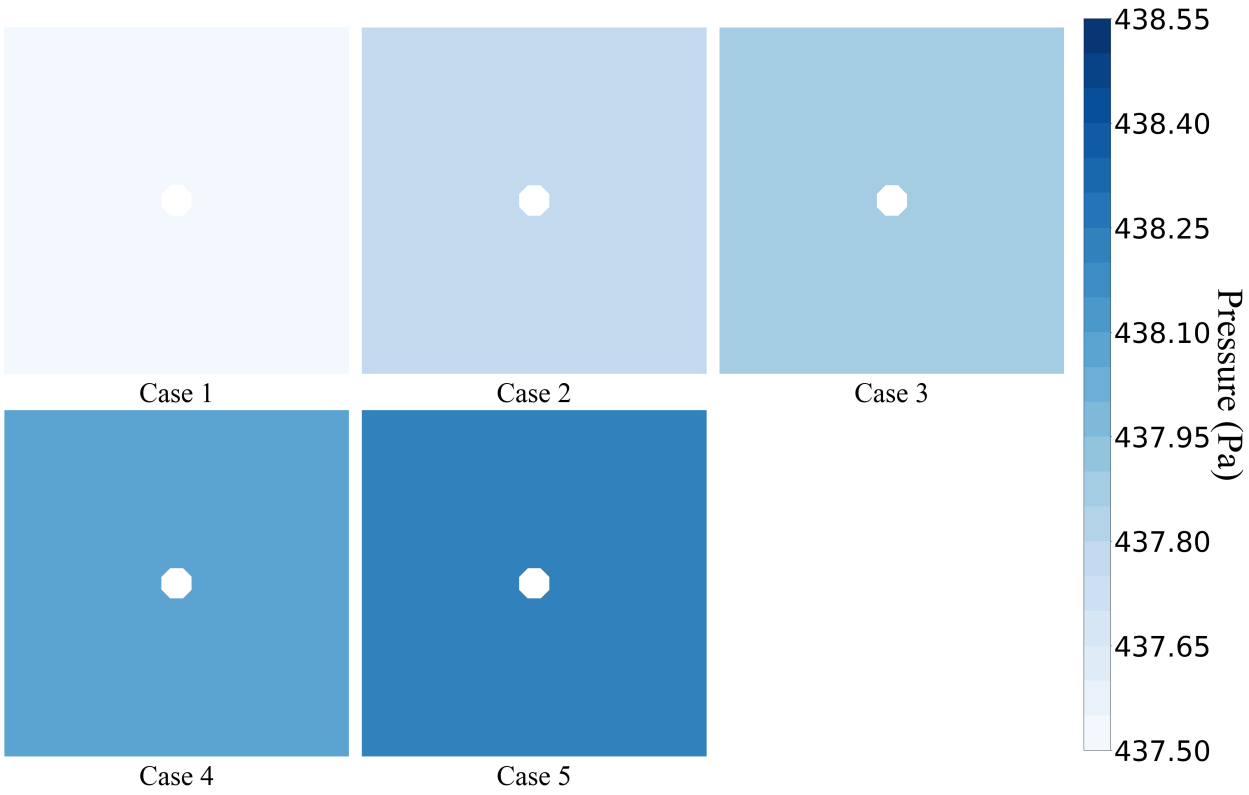

Figure B.15: Venous Compartment pressure map of five simulation cases at $z = 80$

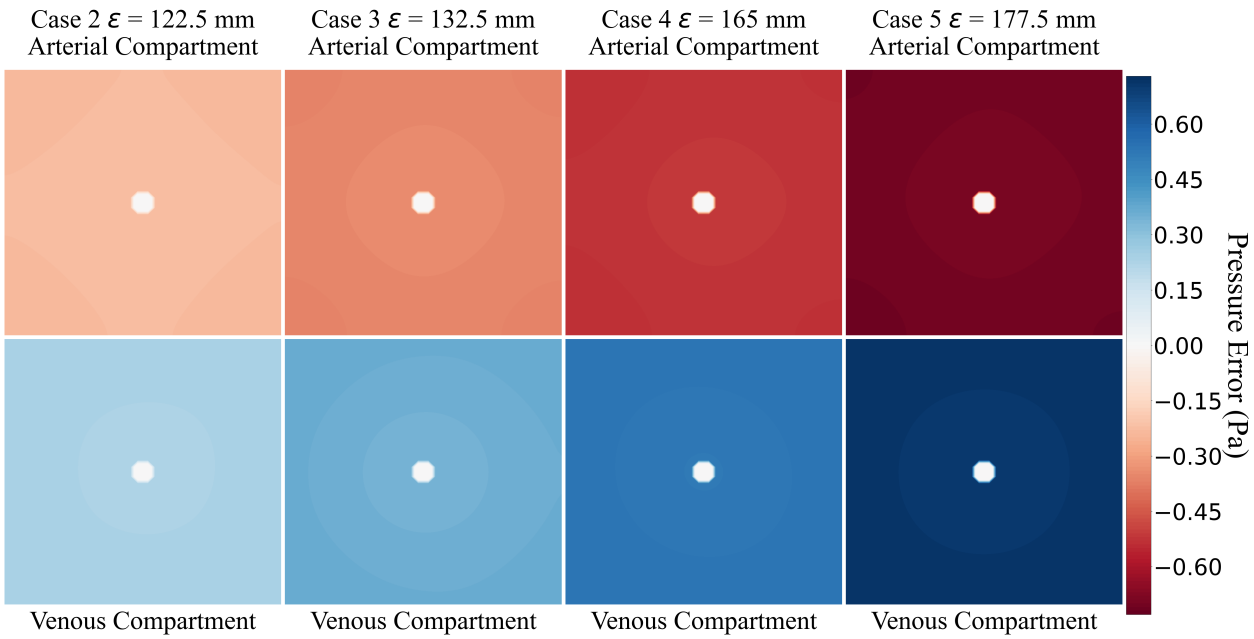

Figure B.16: Pressure error at $z = 80$

Appendix C

Temperature Plots for 3D Energy Analysis

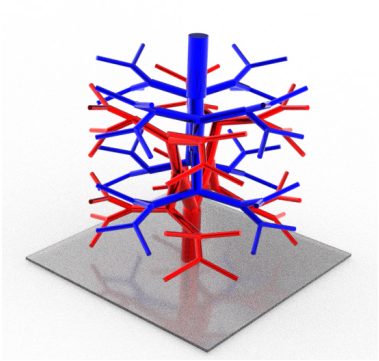

(a)

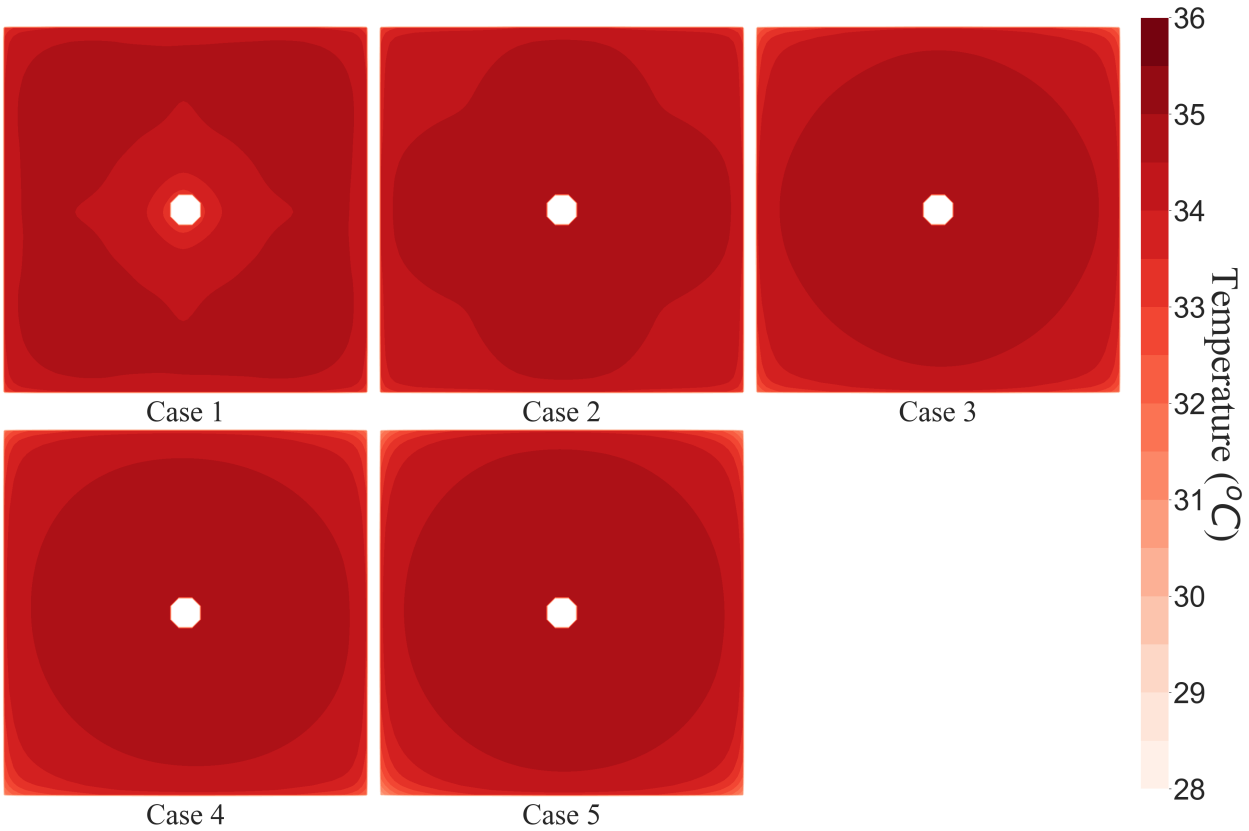

(b)

Figure C.1: Temperature at $z = 1$

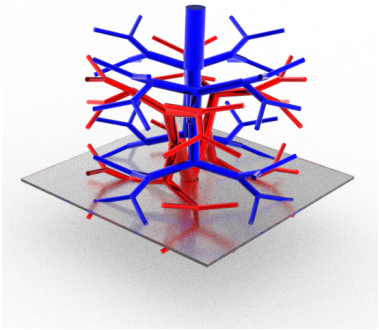

(a)

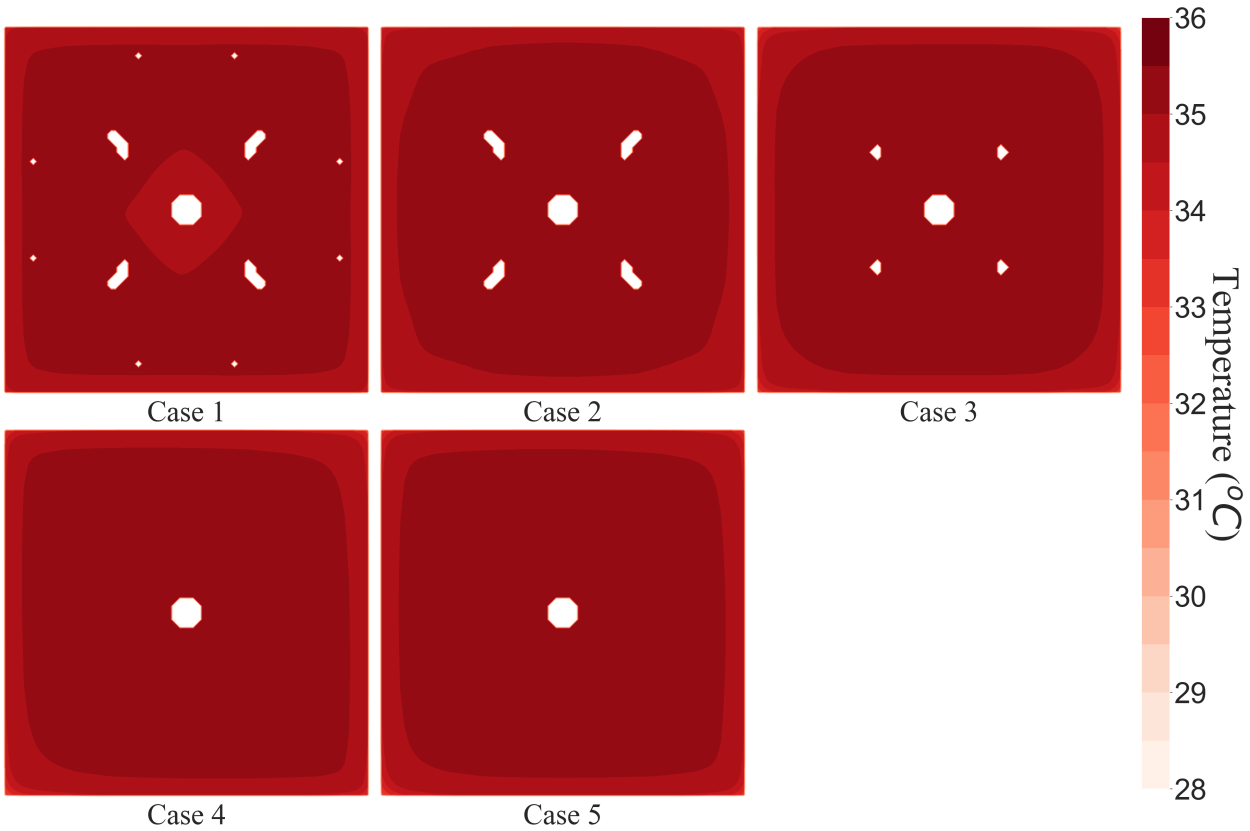

(b)

Figure C.2: Temperature at $z = 20$

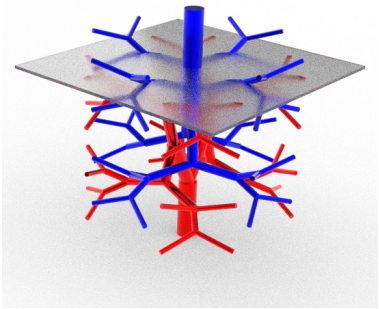

(a)

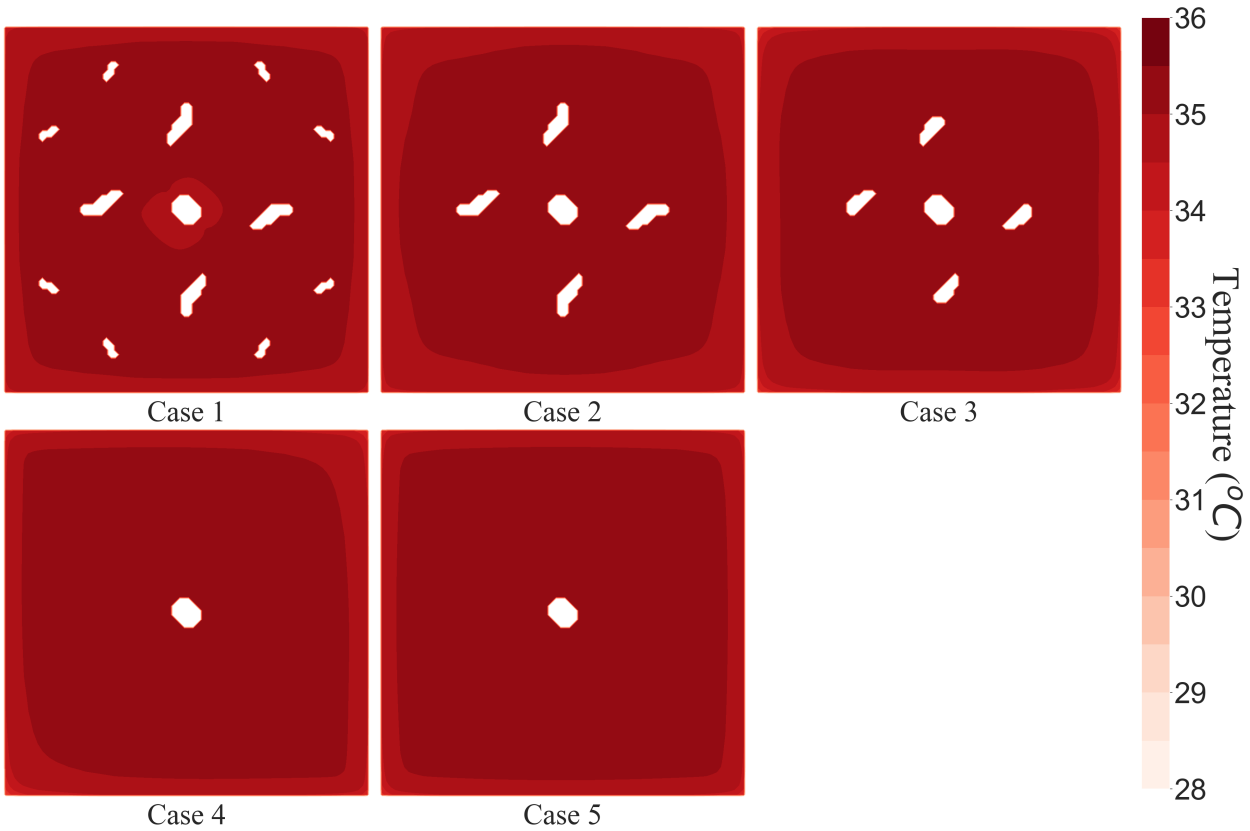

(b)

Figure C.3: Temperature at $z = 60$

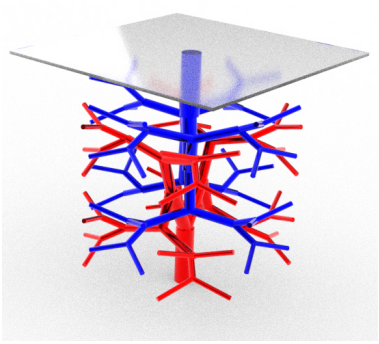

(a)

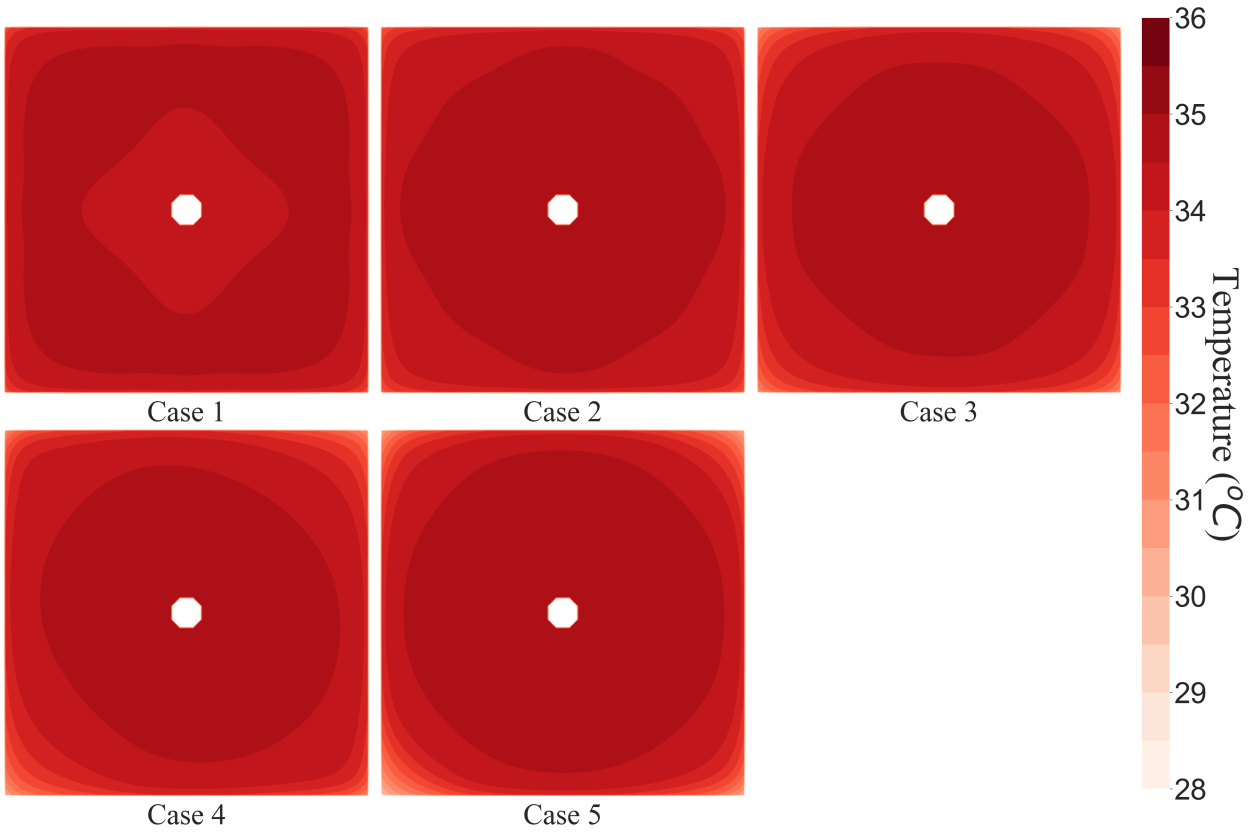

(b)

Figure C.4: Temperature at $z = 80$

Appendix D

Temperature Error Plots for 3D Analysis

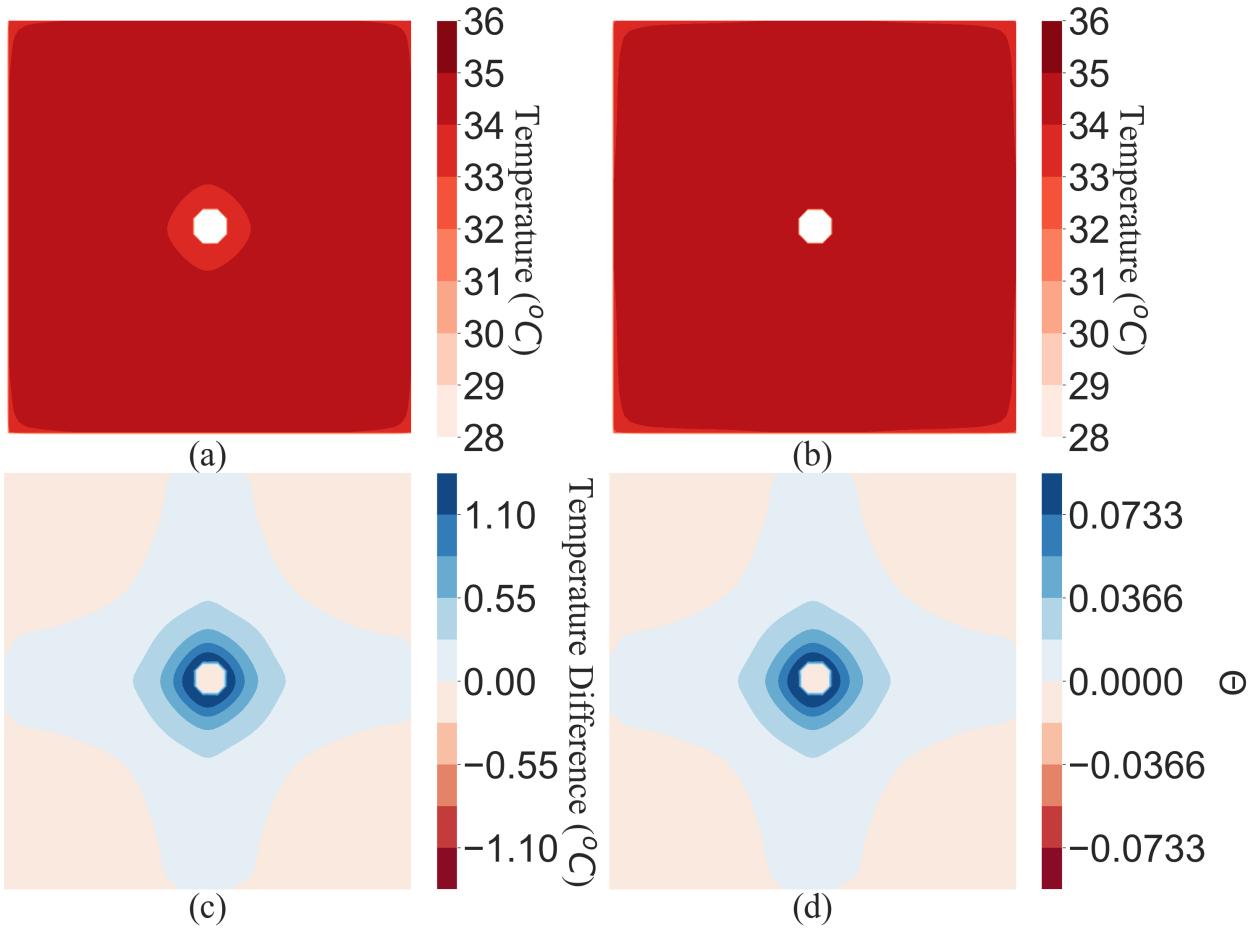

Figure D.1: Temperature Error in Case 2 at $z = 1$ (a) Temperature map of Case 1 (b) Temperature map of Case 2 (c) Temperature difference between Case 2 and Case 1 (d) Non-dimensional temperature error between Case 2 and Case 1

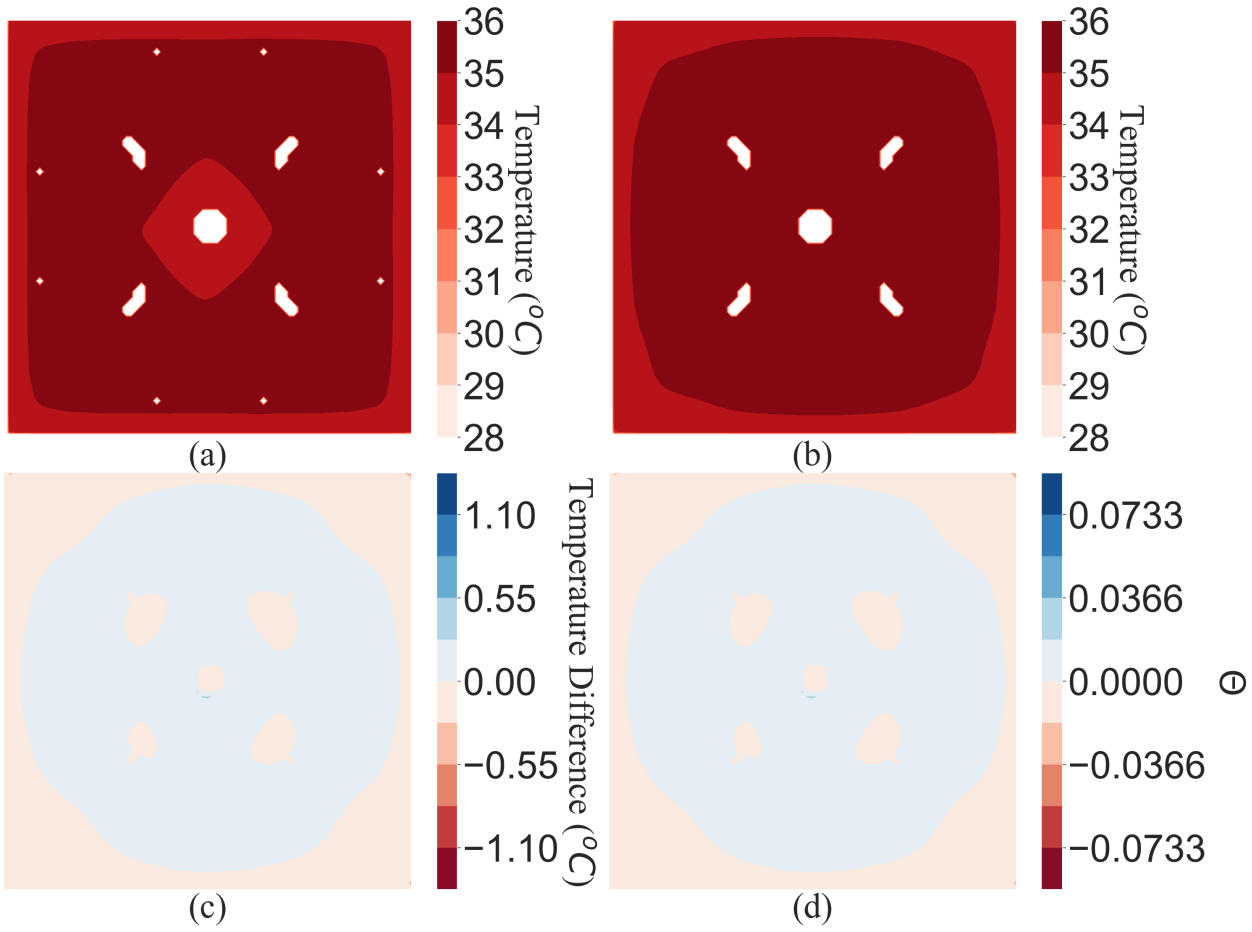

Figure D.2: Temperature Error in Case 2 at $z = 20$ (a) Temperature map of Case 1 (b) Temperature map of Case 2 (c) Temperature difference between Case 2 and Case 1 (d) Non-dimensional temperature error between Case 2 and Case 1

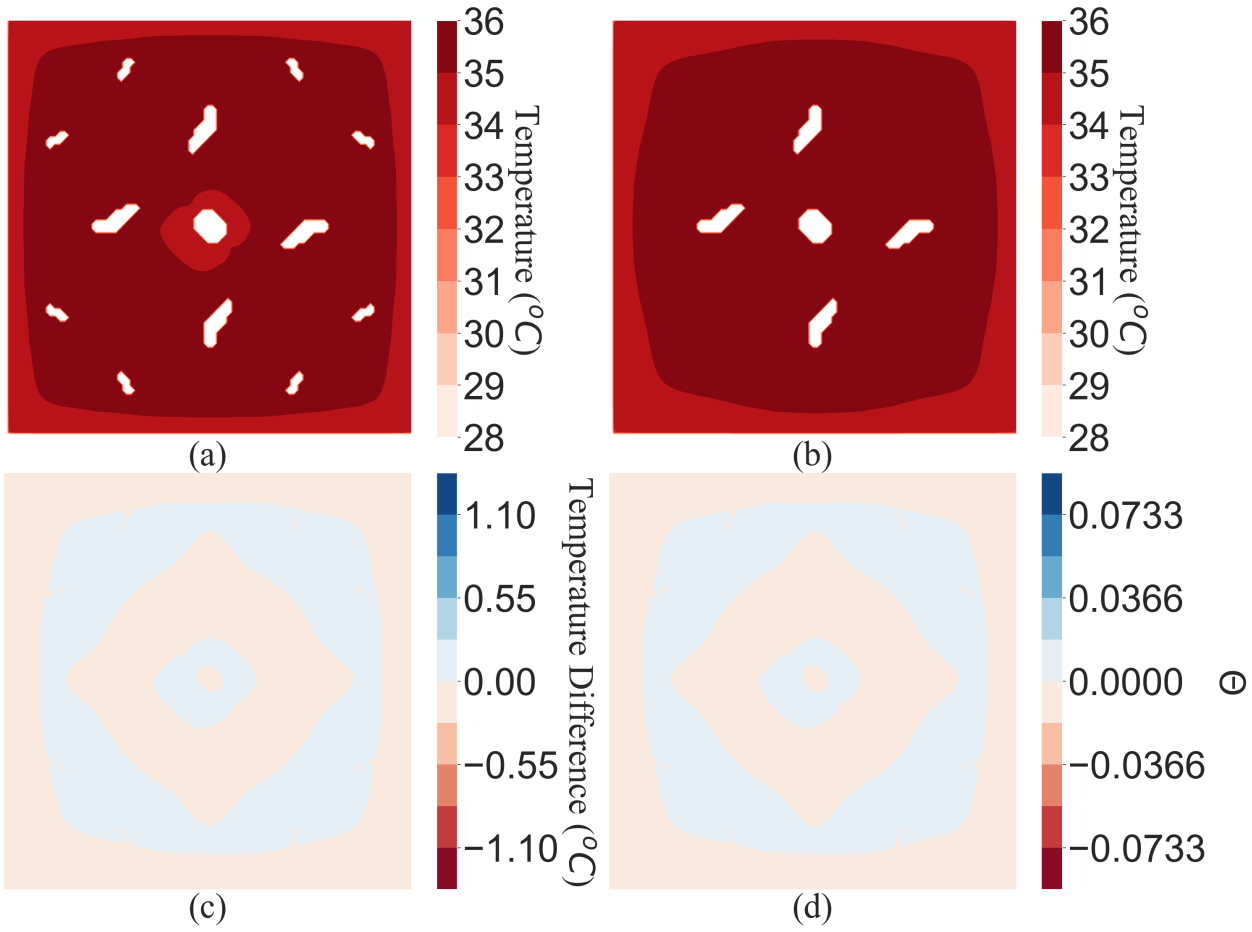

Figure D.3: Temperature Error in Case 2 at $z = 60$ (a) Temperature map of Case 1 (b) Temperature map of Case 2 (c) Temperature difference between Case 2 and Case 1 (d) Non-dimensional temperature error between Case 2 and Case 1

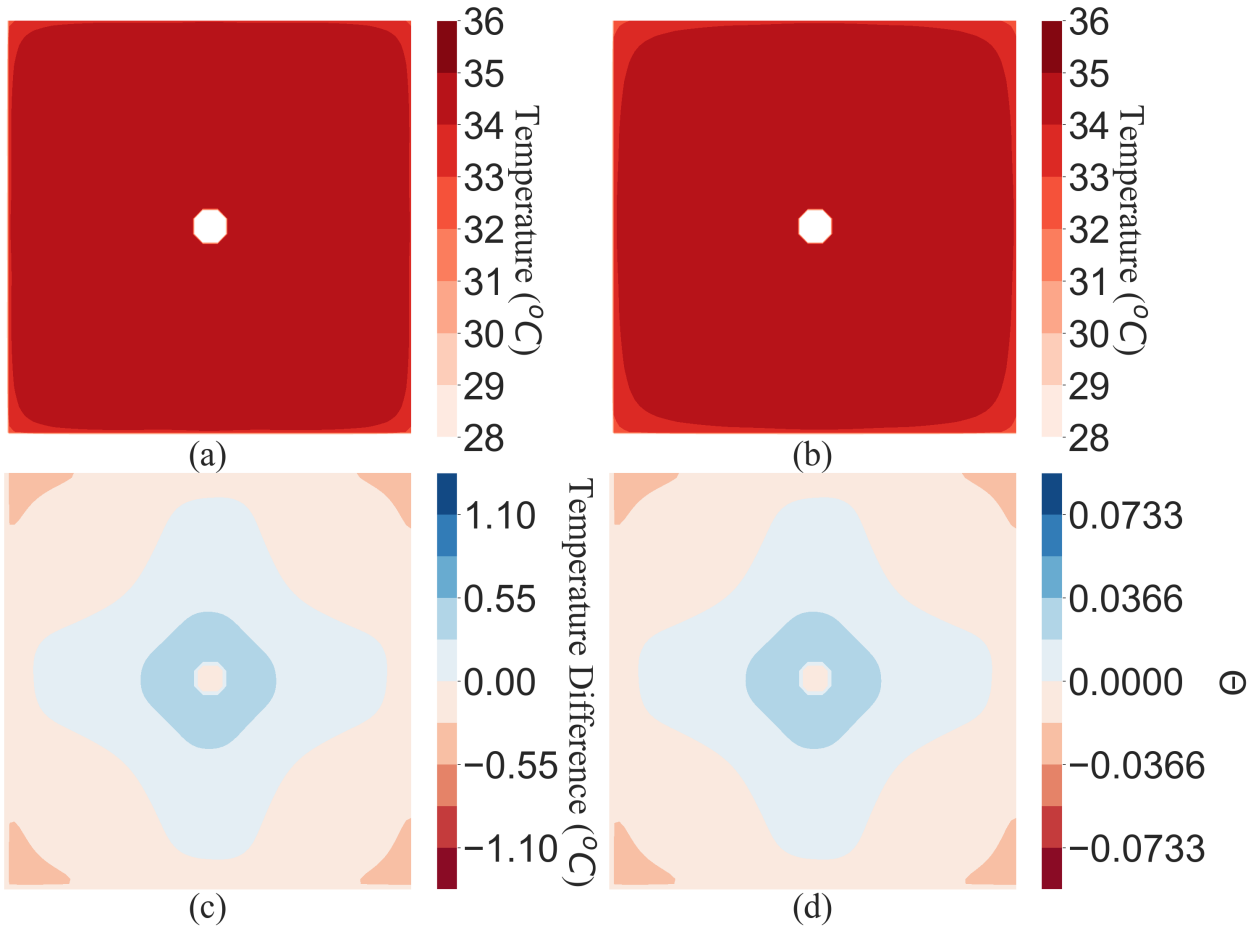

Figure D.4: Temperature Error in Case 2 at $z = 80$ (a) Temperature map of Case 1 (b) Temperature map of Case 2 (c) Temperature difference between Case 2 and Case 1 (d) Non-dimensional temperature error between Case 2 and Case 1

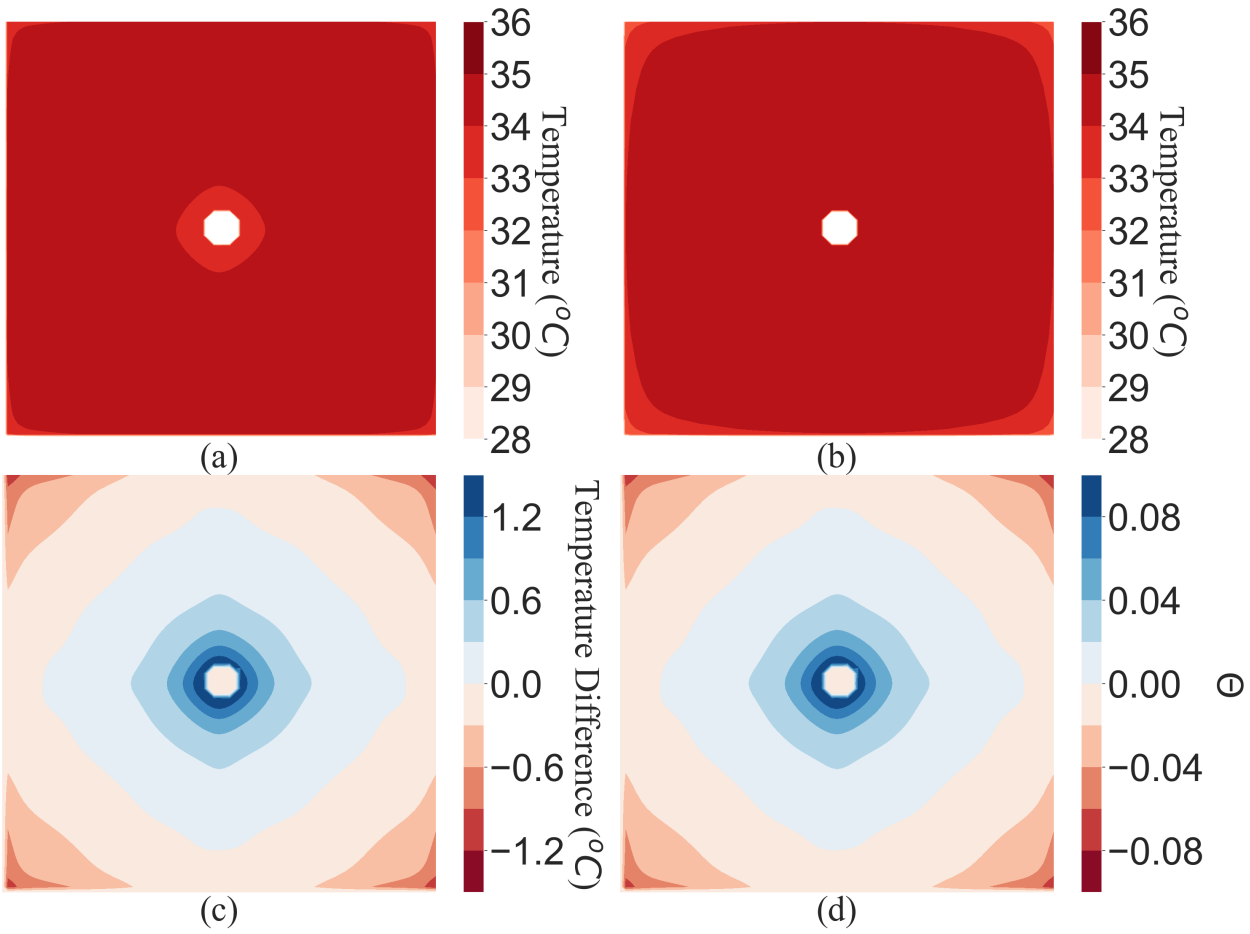

Figure D.5: Temperature Error in Case 3 at $z = 1$ (a) Temperature map of Case 1 (b) Temperature map of Case 3 (c) Temperature difference between Case 3 and Case 1 (d) Non-dimensional temperature error between Case 3 and Case 1

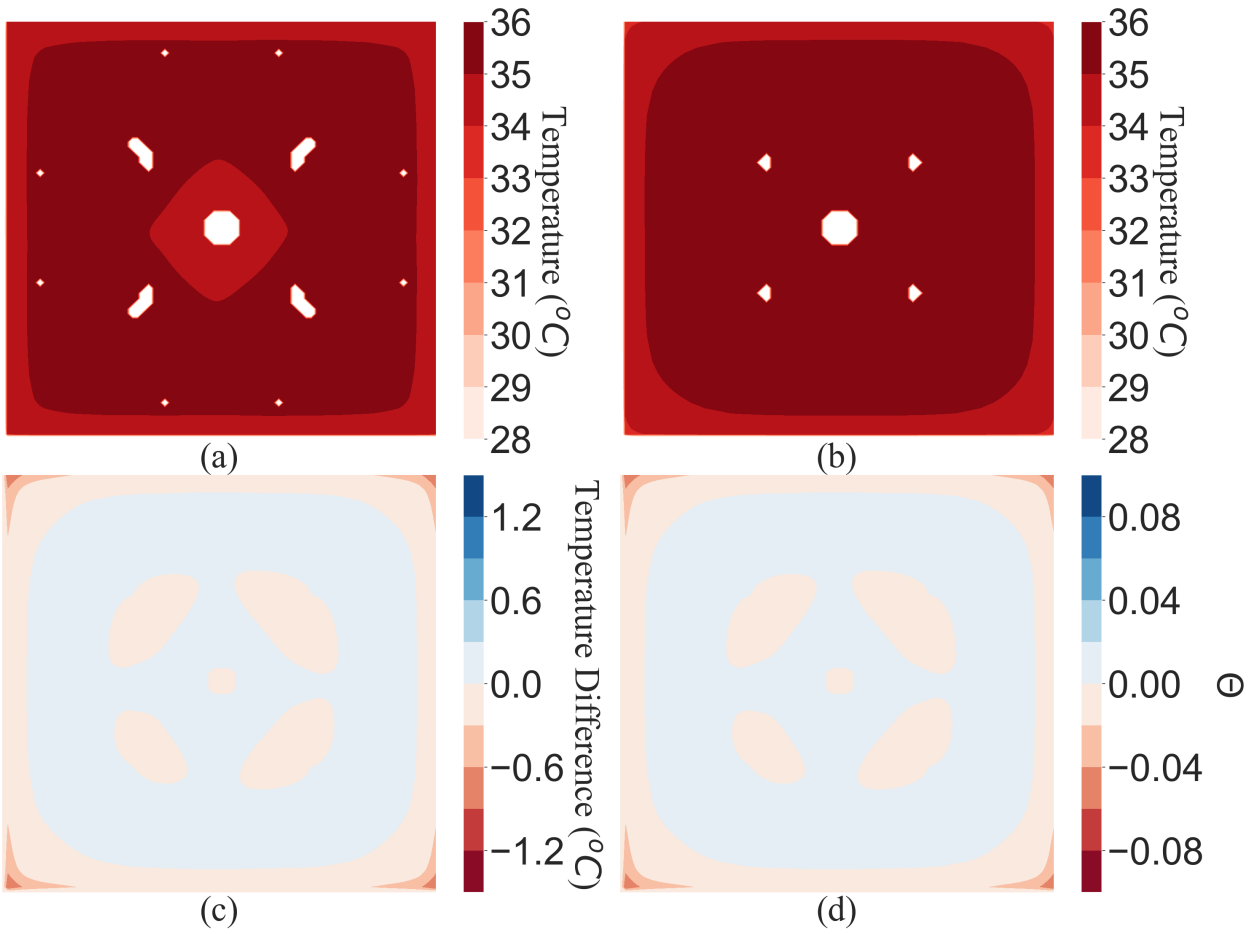

Figure D.6: Temperature Error in Case 3 at $z = 20$ (a) Temperature map of Case 1 (b) Temperature map of Case 3 (c) Temperature difference between Case 3 and Case 1 (d) Non-dimensional temperature error between Case 3 and Case 1

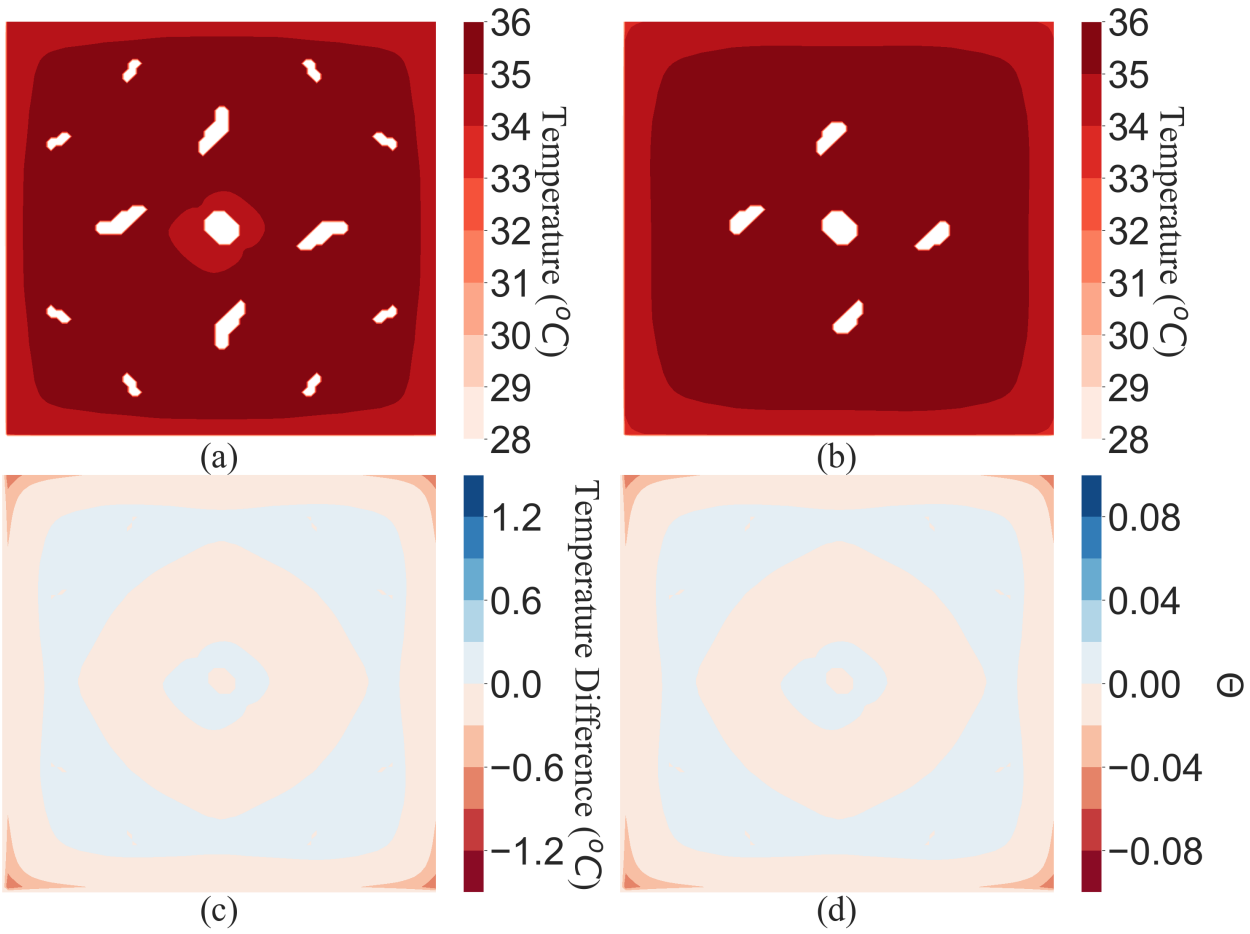

Figure D.7: Temperature Error in Case 3 at $z = 60$ (a) Temperature map of Case 1 (b) Temperature map of Case 3 (c) Temperature difference between Case 3 and Case 1 (d) Non-dimensional temperature error between Case 3 and Case 1

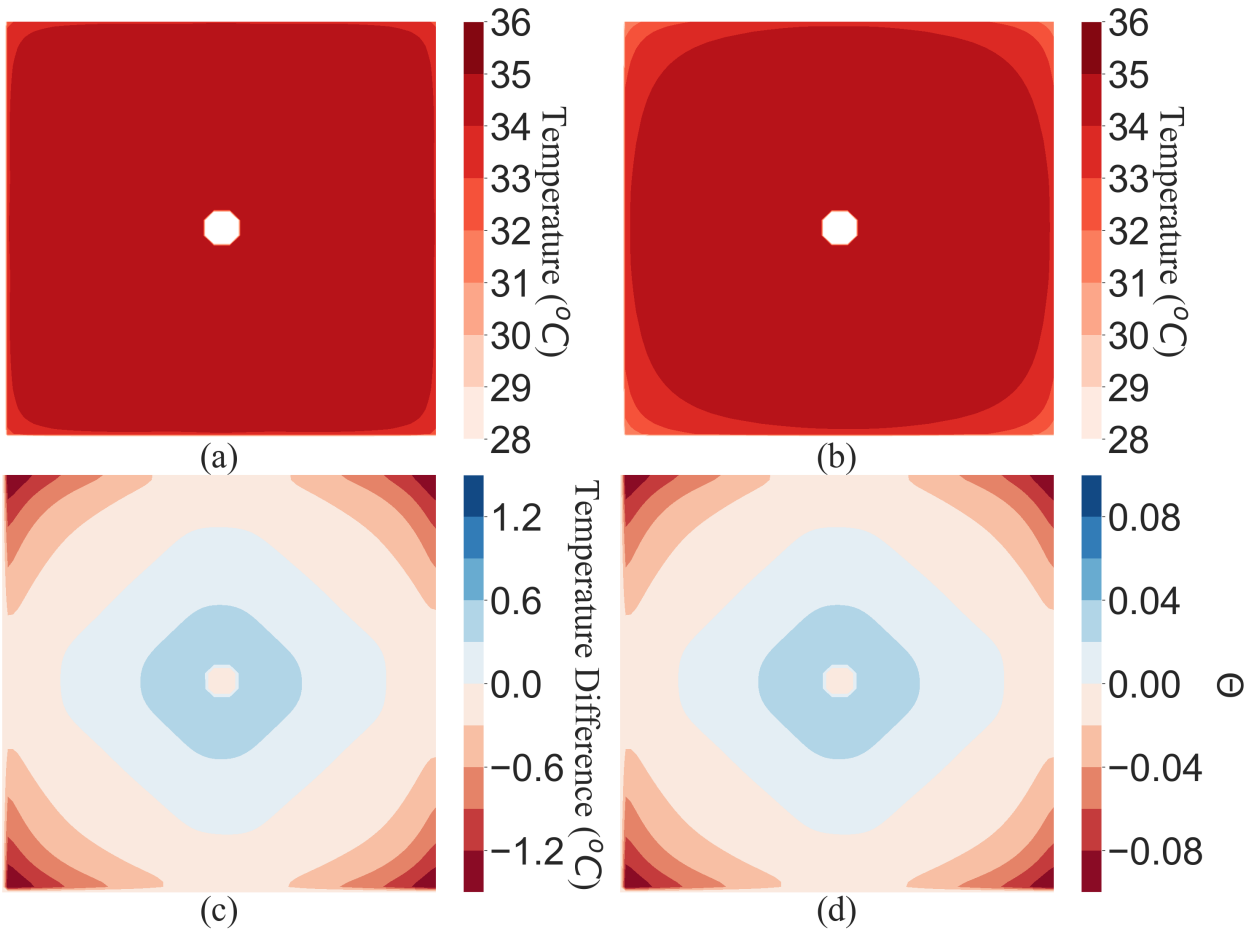

Figure D.8: Temperature Error in Case 3 at $z = 80$ (a) Temperature map of Case 1 (b) Temperature map of Case 3 (c) Temperature difference between Case 3 and Case 1 (d) Non-dimensional temperature error between Case 3 and Case 1

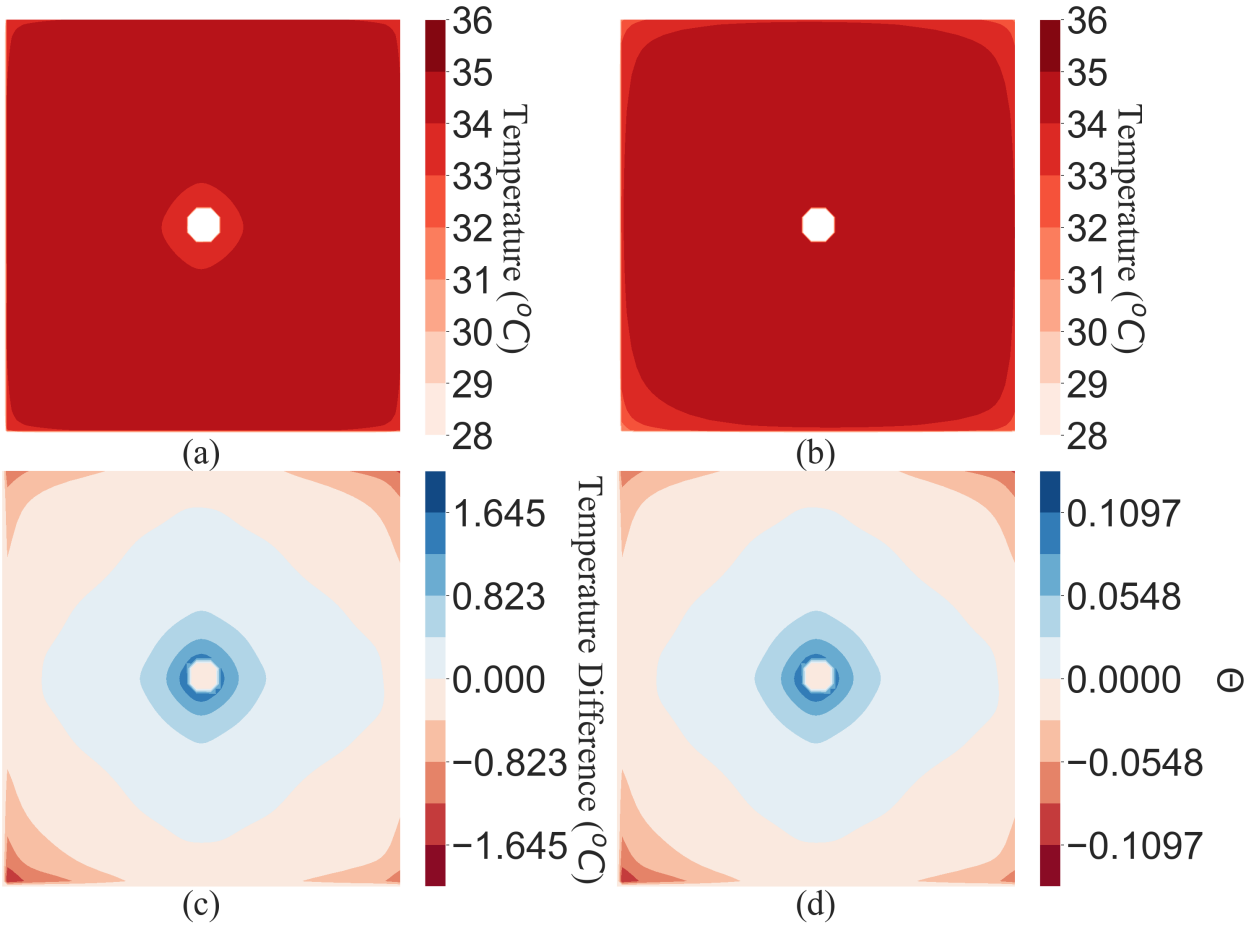

Figure D.9: Temperature Error in case 4 at $z = 1$ (a) Temperature map of Case 1 (b) Temperature map of Case 4 (c) Temperature difference between Case 4 and Case 1 (d) Non-dimensional temperature error between Case 4 and Case 1

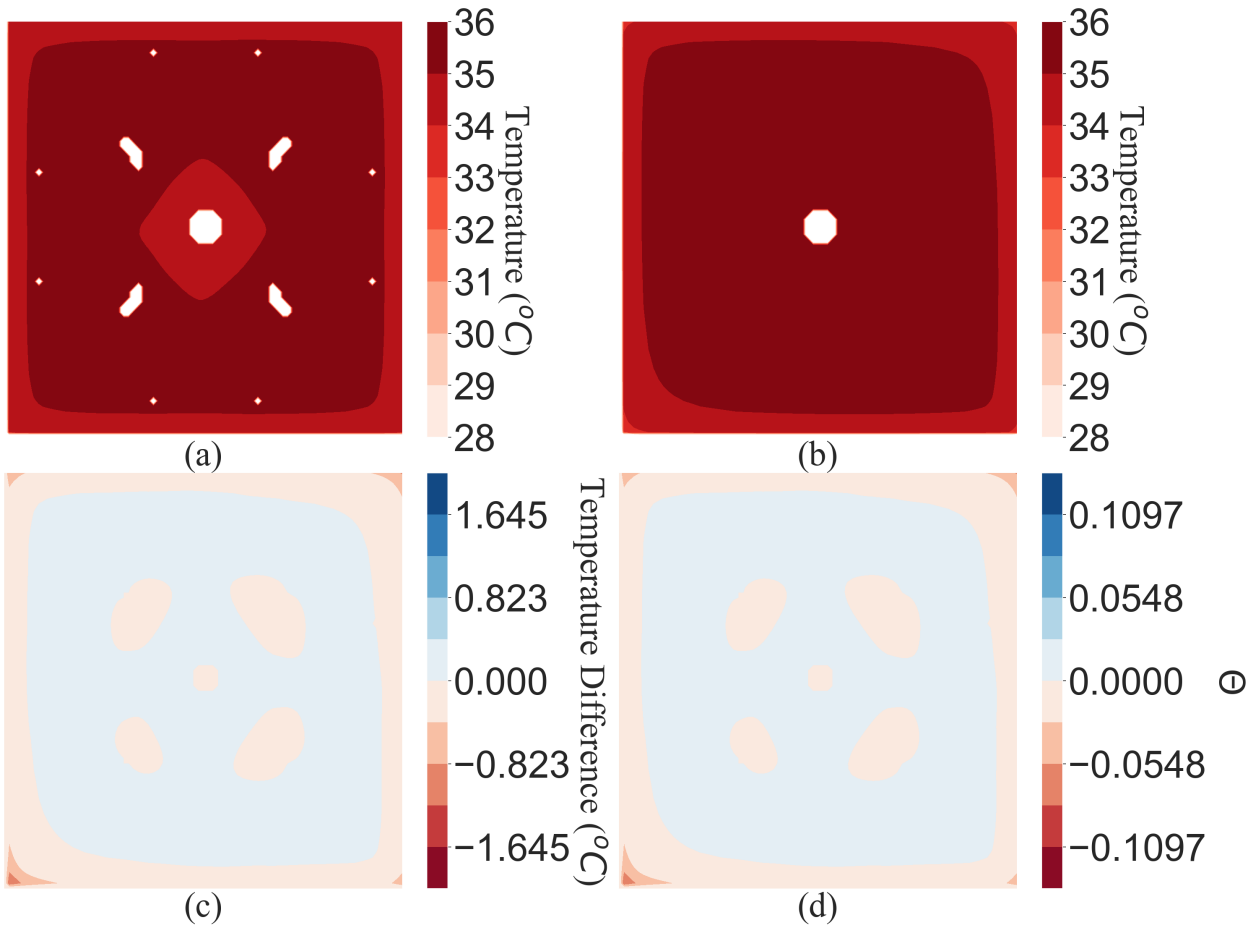

Figure D.10: Temperature Error in Case 4 at $z = 20$ (a) Temperature map of Case 1 (b) Temperature map of Case 4 (c) Temperature difference between Case 4 and Case 1 (d) Non-dimensional temperature error between Case 4 and Case 1

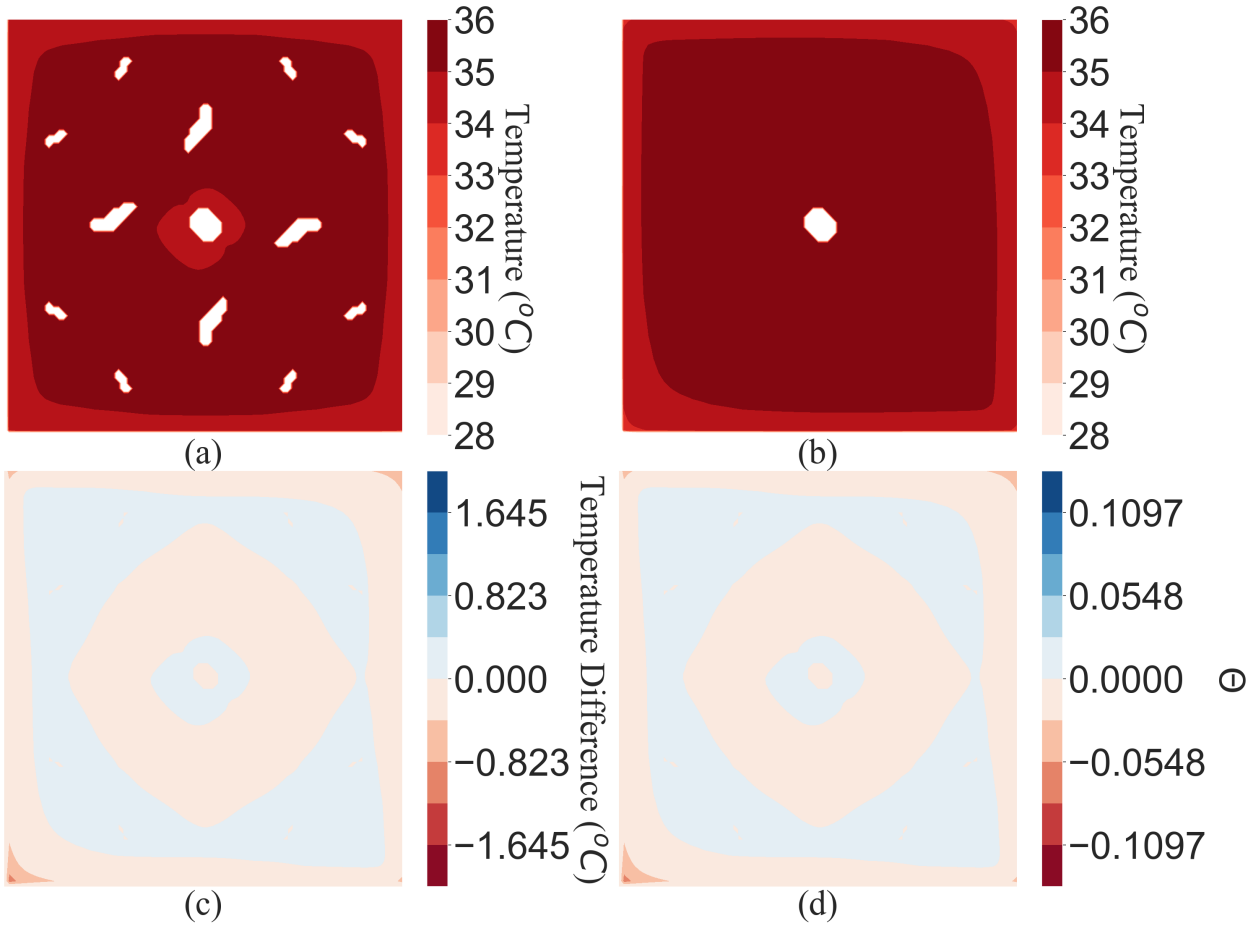

Figure D.11: Temperature Error in Case 4 at $z = 60$ (a) Temperature map of Case 1 (b) Temperature map of Case 4 (c) Temperature difference between Case 4 and Case 1 (d) Non-dimensional temperature error between Case 4 and Case 1

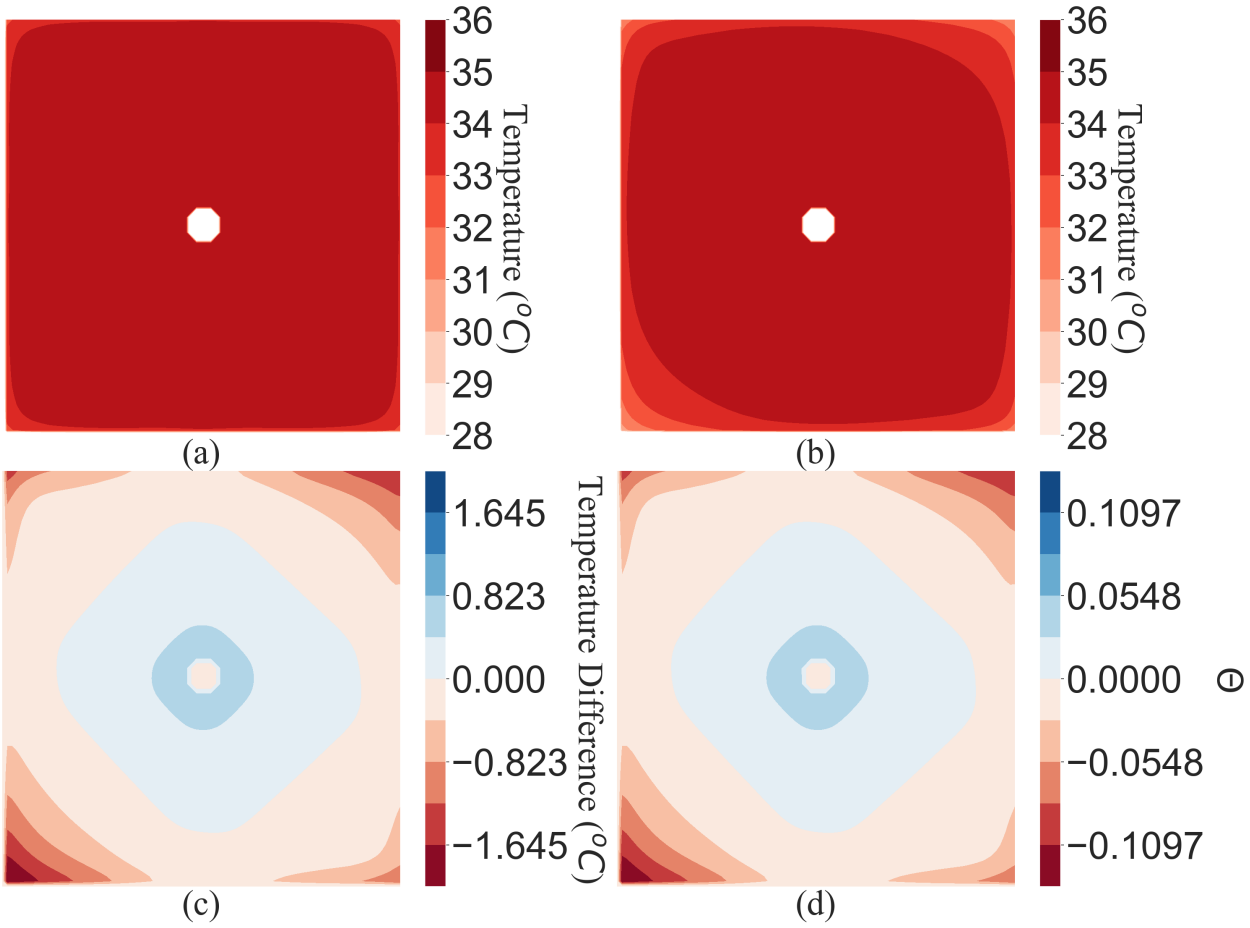

Figure D.12: Temperature Error in Case 4 at $z = 80$ (a) Temperature map of Case 1 (b) Temperature map of Case 4 (c) Temperature difference between Case 4 and Case 1 (d) Non-dimensional temperature error between Case 4 and Case 1

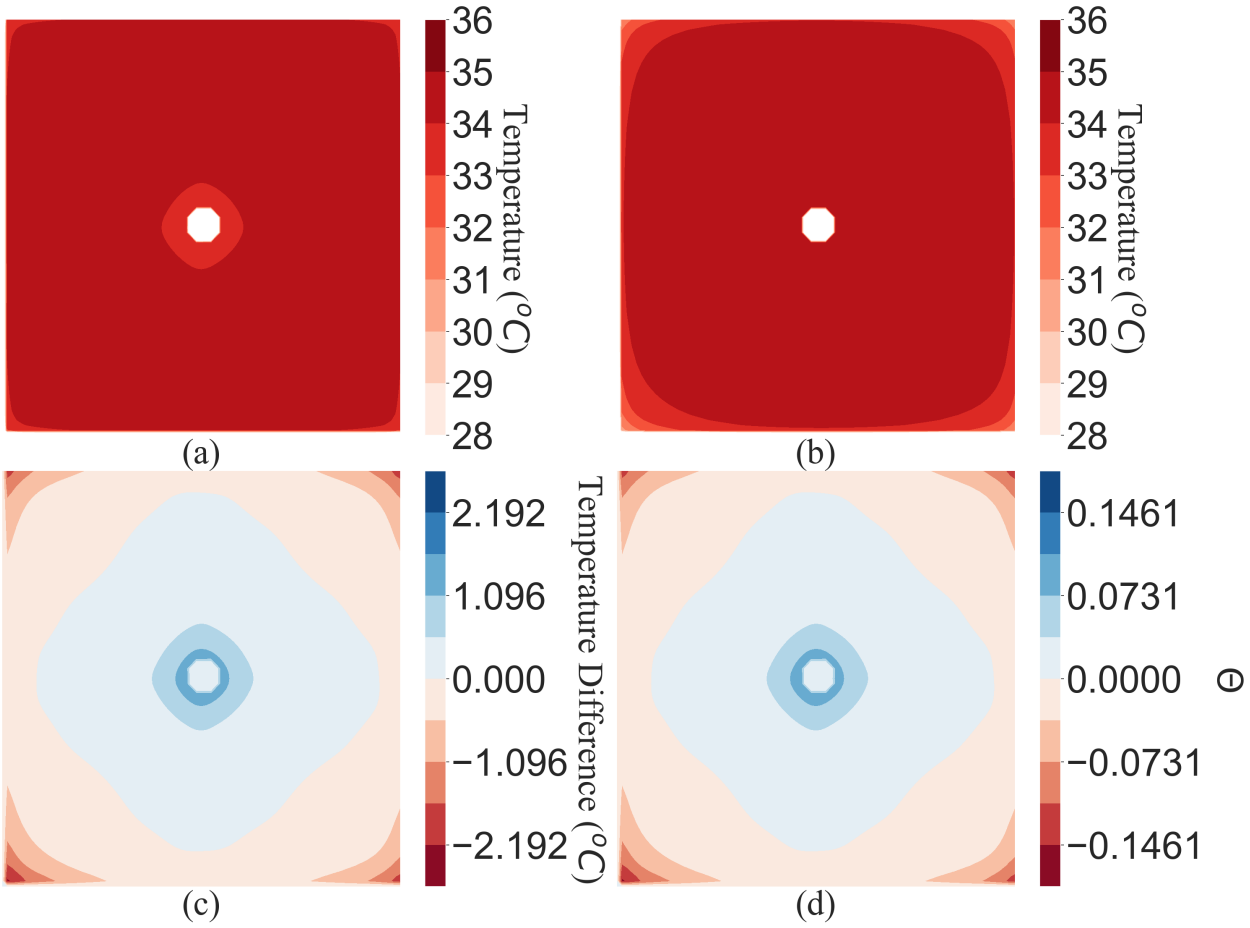

Figure D.13: Temperature Error in Case 5 at $z = 1$ (a) Temperature map of Case 1 (b) Temperature map of Case 5 (c) Temperature difference between Case 5 and Case 1 (d) Non-dimensional temperature error between Case 5 and Case 1

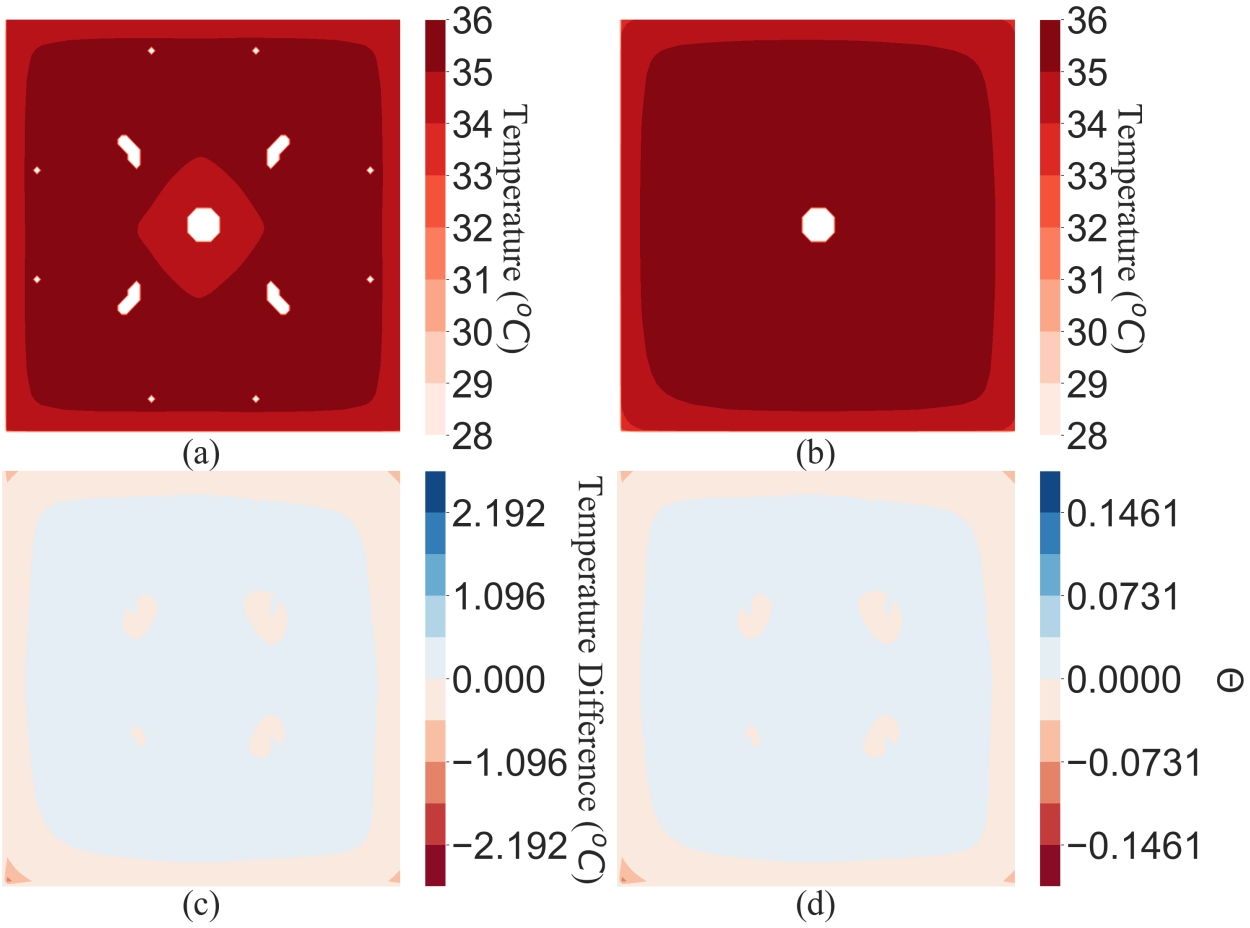

Figure D.14: Temperature Error in Case 5 at $z = 20$ (a) Temperature map of Case 1 (b) Temperature map of Case 5 (c) Temperature difference between Case 5 and Case 1 (d) Non-dimensional temperature error between Case 5 and Case 1

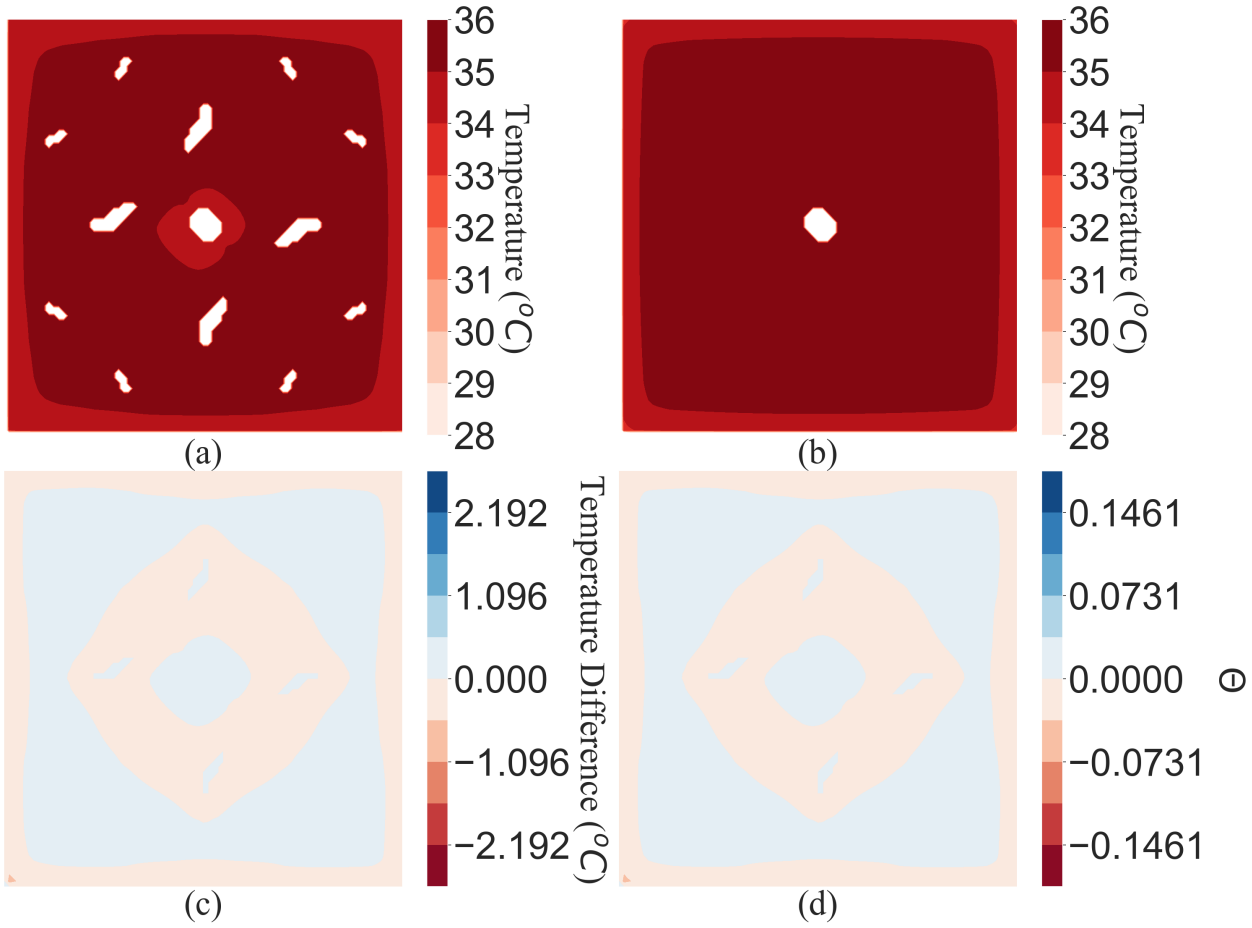

Figure D.15: Temperature Error in Case 5 at $z = 60$ (a) Temperature map of Case 1 (b) Temperature map of Case 5 (c) Temperature difference between Case 5 and Case 1 (d) Non-dimensional temperature error between Case 5 and Case 1

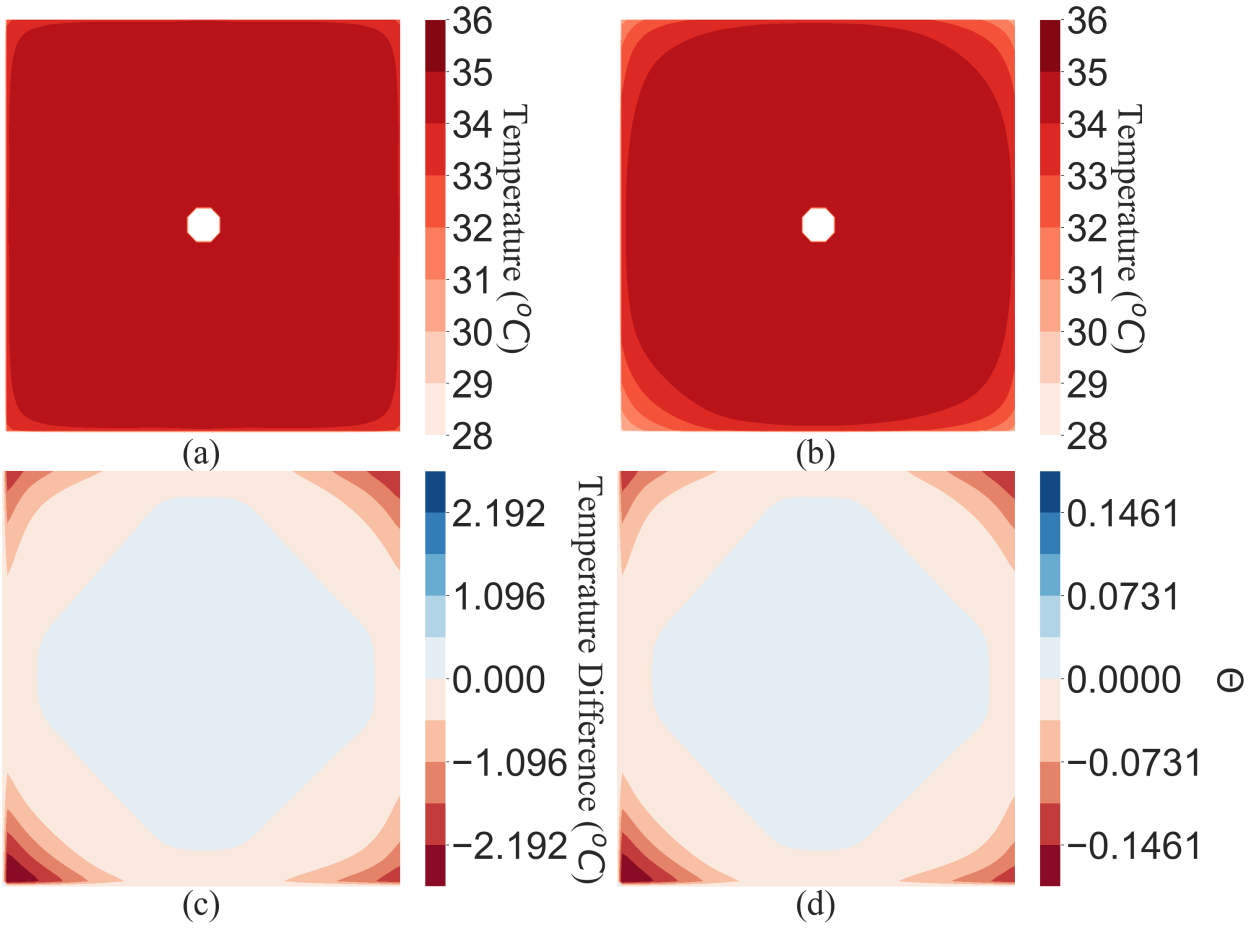

Figure D.16: Temperature Error in Case 5 at $z = 80$ (a) Temperature map of Case 1 (b) Temperature map of Case 5 (c) Temperature difference between Case 5 and Case 1 (d) Non-dimensional temperature error between Case 5 and Case 1

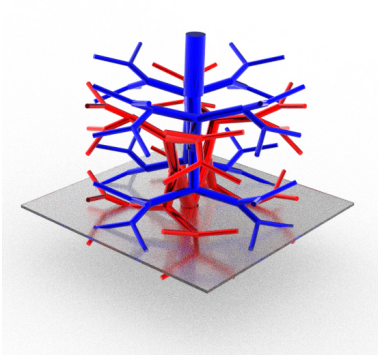

(a)

(b)

Figure D.17: Temperature error at $z = 20$

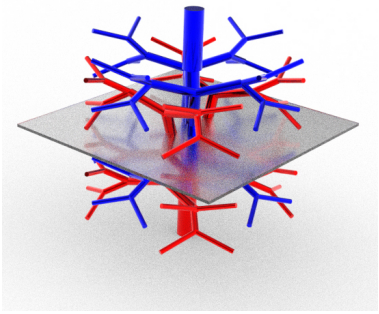

(a)

(b)

Figure D.18: Temperature error at $z = 40$

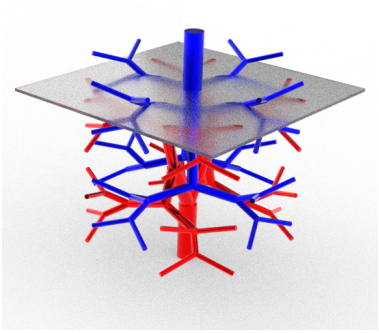

(a)

(b)

Figure D.19: Temperature error at $z = 60$

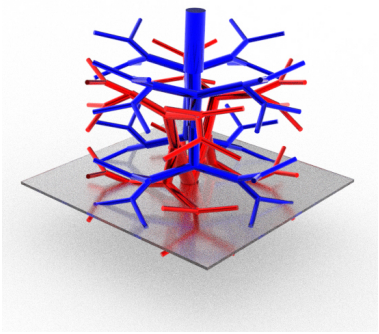

(a)

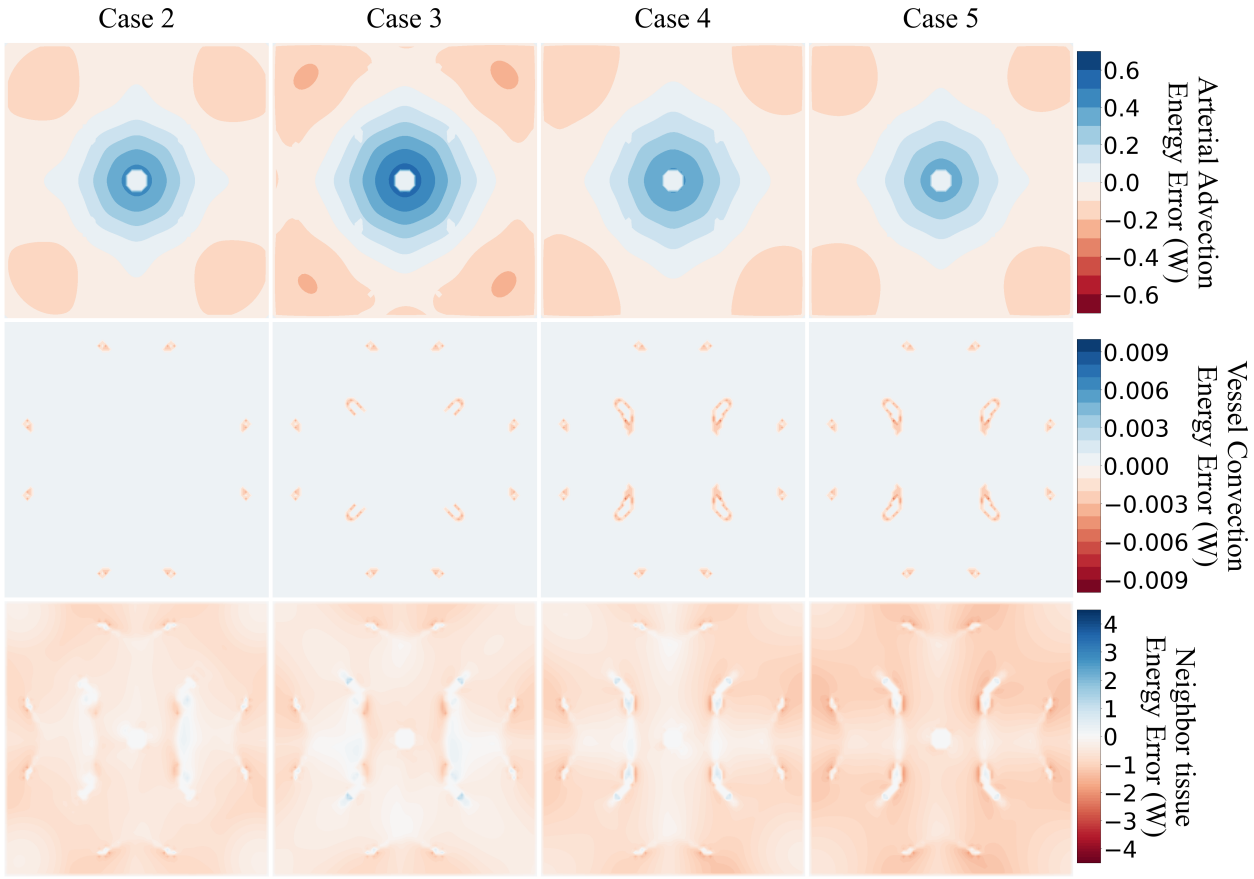

(b)

Figure D.20: Energy error analysis at $z = 20$

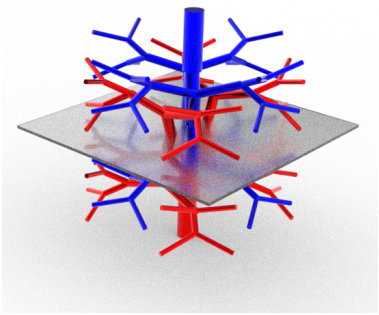

(a)

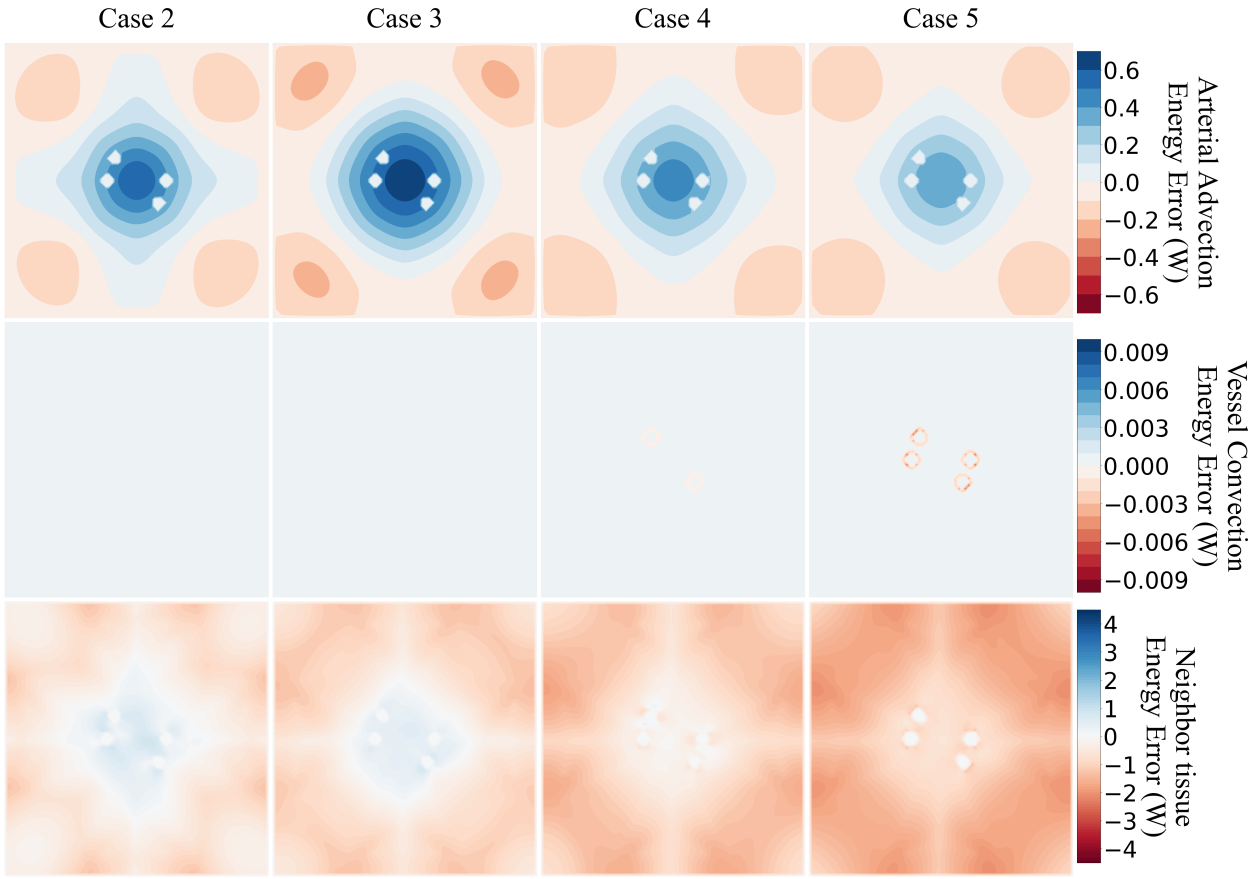

(b)

Figure D.21: Energy error analysis at $z = 40$

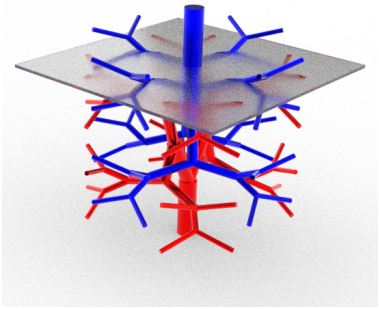

(a)

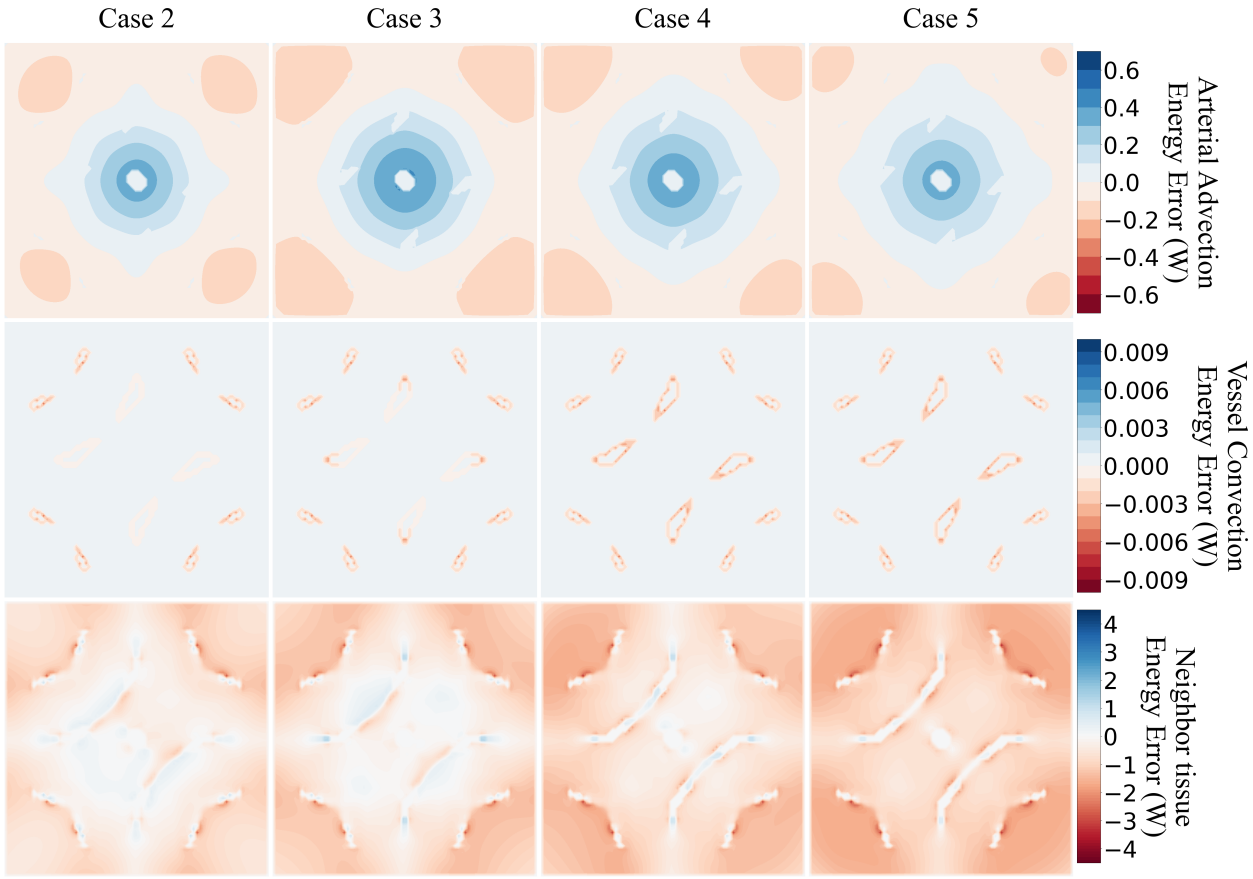

(b)

Figure D.22: Energy error analysis at $z = 60$

Appendix E

Effect of SoI radius and Thermal Conductivity on Temperature Error

Table E.1: Effect of larger SoI and tissue thermal conductivity on temperature error

ϵ	k_t	max ΔT_t	max abs(ΔT_t)	max abs(θ)	RMSE	$\sum \Delta T_t$
(mm)	($\mathrm{W\,m^{-1}\,°C^{-1}}$)	(°C)	(°C)		(°C)	(°C)
177.5	0.50	-2.74	2.78	0.183	0.128	-9750.9
187.5		-1.88	1.88	0.125	0.081	-2155.0
200.0		1.39	1.39	0.093	0.057	3194.7
212.5		1.39	1.39	0.093	0.055	6076.3
225.0		1.39	1.39	0.092	0.058	7760.6
237.5*		1.38	1.38	0.092	0.061	8835.9
250.0*		1.38	1.38	0.092	0.064	9573.0
262.5*		1.38	1.38	0.092	0.066	10106.3
177.5	0.75	-2.03	2.03	0.135	0.114	-9254.8
187.5		1.42	1.42	0.094	0.074	-2006.7
200.0		1.41	1.41	0.094	0.056	3150.2
212.5		1.41	1.41	0.094	0.056	5959.6
225.0		1.41	1.41	0.094	0.06	7615.1
237.5		1.41	1.41	0.094	0.063	8677.3
250.0		1.41	1.41	0.094	0.066	9407.6
262.5		1.41	1.41	0.094	0.068	9936.9

Table E.2: Effect of larger SoI and tissue thermal conductivity on temperature error

ϵ	k_t	max ΔT_t	max abs(ΔT_t)	max abs(θ)	RMSE	$\sum \Delta T_t$
(mm)	($\mathrm{W\,m^{-1}\,°C^{-1}}$)	(°C)	(°C)		(°C)	(°C)
177.5	1.00	-1.67	1.67	0.112	0.106	-8737.1
187.5		1.43	1.43	0.096	0.071	-1787.7
200.0		1.43	1.43	0.096	0.058	3196.8
212.5		1.43	1.43	0.095	0.059	5937.3
225.0		1.43	1.43	0.095	0.063	7562.7
237.5		1.43	1.43	0.095	0.066	8609.8
250.0		1.43	1.43	0.095	0.069	9331.7
262.5		1.43	1.43	0.095	0.071	9855.7
177.5	1.25	1.45	1.45	0.097	0.1	-8250.6
187.5		1.45	1.45	0.097	0.071	-1559.1
200.0		1.45	1.45	0.097	0.06	3273.2
212.5		1.45	1.45	0.097	0.062	5950.5
225.0		1.44	1.44	0.096	0.066	7547.3
237.5		1.44	1.44	0.096	0.069	8579.6
250.0		1.44	1.44	0.096	0.072	9292.8
262.5		1.44	1.44	0.096	0.074	9811.3
177.5	1.50	1.46	1.46	0.098	0.096	-7802.5
187.5		1.46	1.46	0.098	0.071	-1336.9
200.0		1.46	1.46	0.097	0.063	3360.0
212.5		1.46	1.46	0.097	0.065	5979.7
225.0		1.46	1.46	0.097	0.069	7549.8
237.5		1.46	1.46	0.097	0.072	8568.0
250.0		1.46	1.46	0.097	0.074	9272.8
262.5		1.46	1.46	0.097	0.076	9785.8
177.5	1.75	1.47	1.47	0.098	0.094	-7390.8
187.5		1.47	1.47	0.098	0.071	-1125.6
200.0		1.47	1.47	0.098	0.065	3449.7
212.5		1.47	1.47	0.098	0.068	6016.7
225.0		1.47	1.47	0.098	0.072	7561.9
237.5		1.47	1.47	0.098	0.075	8566.7
250.0		1.47	1.47	0.098	0.077	9263.5
262.5		1.47	1.47	0.098	0.078	9771.2